Biological Fate of Soft Nanomaterials: A Physico-Chemical and Translocation Study

Dissertation presented to the Polymer and Advanced Materials: Physics, Chemistry and Technology Department of the University of the Basque Country (UPV/EHU) for the degree of Doctor in Applied Chemistry and Polymeric Materials

Presented by
Marta Martínez Moro

Thesis Supervisor: Dr. Sergio E. Moya
University Tutor: Dr. Isabel Goñi

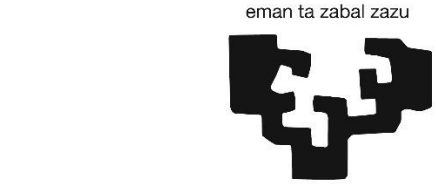

Universidad del País Vasco
Euskal Herriko Unibertsitatea

Donostia-San Sebastián, 2020

This PhD Thesis has been carried out at:

Soft Matter Nanotechnology Group
CIC biomaGUNE
Donostia – San Sebastian, Spain

Soft Matter Laboratory
Instituto de Investigaciones Fisicoquímicas Teóricas y Aplicadas (INIFTA)
Consejo Nacional de Investigaciones Científicas y Técnicas (CONICET)
La Plata, Argentina

Surflay Nanotec GmbH
Berlin, Germany

Universität Leipzig
Institut für Midizinische Physik und Biophysik
Leipzig, Germany

NanoBioMedical Centre, Adam Mickiewicz University, Poznań, Poland

Acknowledgements

These four years have been a roller coaster of emotions. Many mixing feelings with science, stress, but also really good moments. I learn a lot during my PhD. In all those moments, I am really happy to be surrounded by extraordinary people.

Firstly, I would like to thank Sergio, my supervisor, for giving me this opportunity. I have never believed anything better. Thanks for the extraordinary chance to work in different projects and countries. I really appreciate your support and the trust placed in me.

I am very thankful to CIC biomaGUNE. From maintenance to management, platform managers or IT people. All of you contributed to make my work easier.

I am also thankful to Isabel Goñi and Jon M. Matxain from the UPV/EHU for helping me with the bureaucracy at the university.

Also, a big thanks to our collaborators: Ana Sanchez from CIC biomaGUNE, Marco Monopoli and Eva Clemente at RCSI Chemistry Department in Ireland, Juan Giussi and Omar Azzaroni from Soft Matter Laboratory-INIFTA-CONICET in Argentina, Carolin Zillberfein, Julia Bottner, Tom Venus and Irina Estrela-Lopis from Institut für Medizinische Physik und Biophysik, Lars Dähne from Surflay GmbH in Germany and Jacek Jenczykb from NanoBioMedical Centre in Poland.

I don't forget my Soft Matter Nanotechnology labmates Cristian, Julia, Richard, Raquel, María, Elisa and Tanja, to be my scientific family in this last year. Thanks especially to my former labmates Ane, Patrizia, Desiré, Eleftheria, Nikos, María and Ángel. Without your support in scientific and personal issues, I doubt I would have been able to be here. Thanks to show me new things every day.

A special thanks to all the people I met over the world. Infinite patient developed by Caro, Julia, Joaco, Alessandro, Eleonora, Giussi, Laia, Alegretto, Muzzio, Tasca. Thanks!

No pueden faltar aquí Idoia, Elena, Vero, Silvia, Bea, Luchi y Dani por convertir en esta última etapa los días más grises en geniales.

Gracias a mis Santanderinos2.0, mis Chicas Viajeras y mi Big Pharma por el apoyo y ánimos durante todo este tiempo.

A mi familia, especialmente a vosotros papá y mamá. Porque os debo todo lo que soy. Por enseñarme que, con constancia, sacrificio y dedicación, todo se consigue. También mi hermano merece una mención especial por confiar tanto en mí. Y mi güeli. De verdad, mil gracias.

Y por último gracias, Edu. Sin tu apoyo diario... nada de esto hubiese sido posible. Your hand in mine, we walk the miles. Thanks to you, it will be done

Gracias por tanto

Table of Contents

List of figures

General Introduction

Chapter 1.

Chapter 2

Chapter 3

Chapter 4

Chapter 5

Appendix

List of tables

Chapter 3

Chapter 5

Summary

In recent decades, the use of nanomaterials in the biomedical field has increased considerably. Despite many efforts, the medical translation of nanomaterials is limited. The efficacy of nanomaterials in therapy is strongly correlated to their capacity to reach specific organs, or cells and tissues and deliver their cargo. However, nanomaterials may undergo transformations during translocation or circulation leading to their aggregation, degradation, or lose of integrity, which may compromise their therapeutic efficacy. Issues such as degradation or aggregation of nanomaterials in biological matrices are seldom considered in the design and synthesis of nanocarriers. Nanomaterials also interact with biomolecules such as proteins, which form a coating around them, the so-called bio or protein corona, which gives a biological identity to the nanomaterials impacting on their translocation and biodistribution. Understanding nanomaterial behaviour in biologically relevant conditions such as physiological pH, temperature, the presence of biomolecules, or how their cargo affects their properties is also of fundamental relevance for the design of successful nanocarriers.

In this thesis we aim to advance the understanding of the physico-chemical properties and transformations of nanomaterials in an intracellular environment and in biological relevant media. We have worked with different nanomaterials: hydrogels, metal nanoparticles engineered with polymer brushes, gold nanoparticles and supramolecular polymer nanoparticles. Each nanomaterial considered allows us to address a different aspect of the interaction of nanomaterials with the cellular environment.

Chapter 1 describes the impact of cationic biomolecules such as polyallylamine hydrochloride (PAH), spermine or spermidine and doxorubicin on poly(N-isopropylacrylamide co methacrylic acid) (P(NIPAM-co-MAA)) microgels. Which respond to temperature or pH with a change in size. Above 32 ℃, the PNIPAM transition temperature, hydrogels reversibly collapse losing water and volume. Carboxylate groups of methacrylic acid (MAA) bring responsiveness to pH. Hydrogels largely swell at basic pH values, while they collapse and lose volume at acidic pH values. Studies of the interaction of PAH with the hydrogels were conducted with PAH of different molecular weights and at temperatures below and above the transition temperature. Dynamic Light Scattering and zeta potential measurements at 20 ℃ show that PAH 15 kDa MW accumulates inside the microgel while, higher MW PAH is accumulated on the hydrogel's surface. At 40

°C, due to the partial segregation of the MAA moieties to the surface of the hydrogel microparticles, PAH accumulates on the surface of the hydrogel for all MWs considered. Confocal laser scanning microscopy (CLSM) and fluorescence lifetime imaging (FLIM) were applied to observe how PAH, spermidine, or spermine can affect the complexation of doxorubicin with carboxylate inside the microgel.

In **Chapter 2**, time lapse nuclear magnetic resonance (NMR) was employed to study changes at the molecular level of the hydrogel resulting from environmental changes and the complexation with cargo molecules. NMR allows to trace how environmental conditions affect the rotational freedom of functional groups in the hydrogel during changes in temperature, obtaining information on the kinetics of the phase transition. Molecules, such as, PAH, polydiallyldimethylammonium chloride (PDADMAC), spermidine, spermine, and doxorubicin were used to study their impact on the hydrogel hydration state. Changes in the intensity of the PNIPAM methyl group ^{1}H-NMR signal spectra during heating (up to 40 °C)/cooling (down to 20 °C) of the hydrogel will reveal how ionic strength, pH, and the presence of cationic molecules with different molecular weights affect the volume phase transition (VPT) of the hydrogel at the molecular level. Acidic pH values provoke a decrease in the charge of carboxylate groups of MAA and water content inside the particles, which results in a fast hydrogel dehydration. Conversely, at basic pH values the hydrogel remains highly hydrated without the polymer loosing conformational freedom. The ionic strength also has an impact on the hydrogel VPT producing a faster hydration. Small polycations, such as spermidine and spermine, have a larger effect on the hydrogel VPT than larger polyamines, probably due to their higher penetration compared to PAH, inducing a more pronounced dehydration of the hydrogel.

Chapter 3 addresses the interaction between the protein corona formed by human plasma on top of gold nanoparticles and two lectins present in the human diet. Wheat Germ agglutinin (WGA) from wheat binds to the glycans Neu5Ac and chitobiose (GlcNac1β-4GlcNac), while sambucus nigra (SNA) from elderberries binds to the Neu5Ac(α2–6)Gal/GalNAc glycan. The interaction of fluorescently labelled lectins with the protein corona glycans is studied by fluorescence correlation spectroscopy (FCS). Different associations between lectins and the protein corona is shown for soft and hard protein corona, with SNA displaying a higher affinity when compared to WGA. Removing glycans from the corona largely supresses the interaction of the corona with the lectins. We will show by means of FCS that the protein corona around nanoparticles interacts with lectins and that this interaction depends on the presence of glycosylated proteins.

Chapter 4 shows the surface functionalization of ZnO nanoparticles by the grafting from synthesis of spherical polymer brushes. These polymer brushes provide colloidal stability in aqueous media and protect the ZnO against degradation with pH. Reversible addition-fragmentation chain-transfer polymerization (RAFT) was employed for brush synthesis using the following monomers: acrylic acid (PAA), polyethylene glycol (PEG) and [2-(Methacryloyloxy)ethyl] trimethylammonium chloride (METAC), an example of negative charge, no charge and positive charge. A polymer density of 18% was obtained in the PAA coating, while PMETAC was 9%, and PEG was 3.57%. Confocal Raman Microscopy allows label free tracing of ZnO nanoparticles inside the cells, and an evaluation of the impact of the spherical brush on the stability and solubility of the ZnO NPs.

Chapter 5 deals the formation of PAH-siRNA complexes as gene delivery agents and their tracking inside the cell. Fluorescence Cross-Correlation Spectroscopy (FCCS) is used to study the formation and stability of the complexes at different pH values, and to establish the timeframe for the release of siRNA intracellularly, which is a necessary step for the actual silencing process. Shortly after endocytosis complexes form large aggregates inside cells with large diffusion times, probably as a result of their interaction with different cell components and compartments. After 12 h, faster diffusion times are obtained indicating the dissolution of the complexes, delivering the siRNA while cross-correlation between fluorescently labelled siRNAs and PAH decreases, implying complex breakage and siRNA release.

Resumen

En las últimas décadas, el uso de nanomateriales en el campo de la biomedicina ha aumentado considerablemente. En la escala nanométrica, las propiedades de los materiales cambian respecto a las del material a gran escala. Las propiedades singulares de los nanomateriales los hace atractivos para el desarrollo de sensores para el diagnóstico de enfermedades o como agentes de contraste de imagen, y como transportadores para liberación controlada o en la regeneración de tejidos.

La liberación controlada de fármacos es una de las aplicaciones más atractivas puesto que el hecho de transportar un agente terapéutico de forma controlada a un órgano o tejido concreto minimiza posibles efectos adversos que ese agente pueda tener sobre tejidos sanos. La fármaco-cinética de numerosos fármacos tradicionales resulta en la presencia no deseada de los fármacos en órganos sanos, una situación que en casos como la quimioterapia tradicional, resultan en efectos secundarios o malestar. Efectivamente, una aplicación de los nanomateriales en liberación controlada es el transporte de fármacos anticancerígenos con el objetivo de restringir su biodisponibilidad al tejido cancerígeno. Los fármacos o agentes terapéuticos pueden ser transportados en los nanomateriales de formas muy diversas tanto encapsulados dentro del nanotransportador como unidos a su superficie. Los agentes terapéuticos pueden unirse a la superficie de nanopartículas a través de enlaces covalentes o mediante interacciones electrostáticas o enlaces de hidrogeno. Normalmente el encapsulado de fármacos se realiza durante la síntesis o ensamblado de los nanomateriales.

La posibilidad de modificar la superficie de los nanotransportadores con moléculas con capacidad de reconocimiento celular permite direccionar los nanomateriales a tejidos específicos restringiendo la biodisponibilidad del nanomaterial y fármaco a los órganos. Además, la “decoración” de la superficie con diferentes moléculas permite reducir la toxicidad de algunos nanomateriales o incluso aumentar su tiempo de circulación en el torrente sanguíneo.

A pesar de los esfuerzos, la traslación de los nanomateriales a la medicina es limitada. La eficacia de los nanomateriales en terapia está fuertemente correlacionada con su capacidad para alcanzar órganos específicos o células y tejidos y liberar su carga. Sin embargo, los nanomateriales pueden sufrir transformaciones durante su circulación y en los diferentes procesos de translocación a nivel de tejido, órgano o células que conducen a su agregación, degradación o pérdida de integridad, lo cual compromete su eficacia terapéutica. Aspectos como degradación o agregación de nanomateriales en matrices

biológicas son raramente consideradas en el diseño y la síntesis de los nanotransportadores, pero tienen importancia fundamental en la evaluación de su potencial terapéutico.

Los nanomateriales interaccionan con biomoléculas presentes en medio biológico como proteínas, lípidos, enzimas, iones, etc. Las proteínas del medio forman un recubrimiento alrededor de las nanopartículas, la llamada biocorona o corona de proteínas, la cual da una identidad biológica a los materiales afectando su traslado y biodistribución. El estudio del comportamiento de los nanomateriales en condiciones biológicas relevantes como pH fisiológico, temperatura, presencia de biomoléculas o cómo los fármacos o agentes terapéuticos transportados en el nanomaterial afectan a sus propiedades también es de fundamental relevancia para el diseño de nanotransportadores exitosos.

En esta tesis, nos hemos propuesto avanzar en la comprensión de las propiedades físico-químicas y la transformación de nanomateriales en el ambiente celular y en medios biológicos relevantes. Hemos trabajado con diferentes nanomateriales: hidrogeles, nanopartículas metálicas modificadas con cepillos poliméricos, nanopartículas de oro y nanopartículas poliméricas supramoleculares. Cada material considerado, nos permite resolver diferentes aspectos de la interacción de los nanomateriales con el ambiente celular.

El **capítulo 1** se centra en el estudio de la interacción de biomoléculas catiónicas como la polialilamina hidroclorada (PAH), espermina o espermidina y la doxorrubicina con hidrogeles de poli(N-isopropilacrilamida-co-ácido metracrílico) (P(NIPAM-co-MAA)). Los microgeles, son partículas micrométricas formadas por cadenas poliméricas flexibles interconectadas que conforman una red tridimensional altamente solvatada en medio acuoso (hidrogeles) u orgánico (organogeles). En nuestro trabajo, los hidrogeles de P(NIPAM-co-MAA) responden a variaciones en temperatura o pH con cambios en su tamaño. Por encima de 32 ℃, que es la temperatura de transición de fase del PNIPAM, los hidrogeles colapsan perdiendo agua y reduciendo el volumen de una forma reversible. Los grupos carboxilato del ácido metacrílico (MAA) aportan capacidad de respuesta al pH. Los hidrogeles se hinchan a pHs básicos, mientras que colapsan y pierden volumen a pH ácido. Los estudios de la interacción de PAH con los hidrogeles fueron llevados a cabo con diferentes pesos moleculares de PAH y a temperaturas por encima y por debajo de su transición de fase. La dispersión de luz dinámica y el potencial zeta a 20 ℃ muestran que el PAH cuyo peso molecular es de 15kDa se acumula dentro del hidrogel pero que PAH con mayores pesos moleculares se acumula en la superficie del hidrogel. A 40 ℃, debido a la segregación de segmentos de MAA en la superficie de las micropartículas de

hidrogel, el PAH, independientemente del peso molecular, se acumula en la superficie. Las técnicas de microscopía confocal e imagen de fluorescencia de vida media fueron utilizadas para observar cómo el PAH, la espermidina o la espermina pueden afectar a la complejación de la doxorrubicina con grupos carboxilatos dentro del hidrogel.

En el **capítulo 2**, se estudiaron cambios a nivel molecular con la temperatura en las cadenas poliméricas de hidrogeles de P(NIPAM-co-MAA) en diferentes condiciones de pH, fuerza iónica, y en presencia de moléculas de carga positiva de diferente peso molecular mediante la técnica de resonancia magnética nuclear (RMN) de lapso de tiempo. Esta técnica de RMN permite monitorizar cambios en señales de RMN como consecuencia de variaciones en la libertad de flexibilidad conformacional a nivel molecular que ocurren durante cambios de temperatura. En particular hemos estudiado cómo cambios en el entorno del hidrogel (pH, fuerza iónica, etc.) que afectan la carga de los grupos carboxilatos de MAA y en consecuencia su estado de hidratación, impactan en la libertad conformacional de los grupos metilo del NIPAM durante cambios en la temperatura produciendo el colapso del hidrogel. Para esto se midió la intensidad de la señal ^{1}H-RMN de los grupos metilo de PNIPAM durante el calentamiento hasta 40 ℃, seguido por el enfriamiento de la muestra hasta los 20 ℃. A partir de las variaciones de señal de RMN con la temperatura se determinó la cinética y grado de deshidratación del hidrogel. A pHs ácidos disminuye la carga de los grupos carboxilato del MAA y el contenido de agua dentro de la partícula, resultando en una rápida deshidratación del hidrogel. Por el contrario, a valores de pH básico, el hidrogel permanece hidratado sin pérdida de libertad conformacional del polímero. El aumento de la fuerza iónica, de 50 a 500 mM, resulta en una mayor deshidratación del hidrogel y en una cinética de deshidratación más rápida. Poliaminas de bajo peso molecular como la espermidina y la espermina, inducen una mayor deshidratación del hidrogel que poliaminas de alto peso molecular, probablemente debido a su mayor penetración en el hidrogel y a una interacción más efectiva con los grupos carboxilatos.

El **capítulo 3** aborda la interacción entre la corona de proteínas formada a partir de plasma humano en la superficie de nanopartículas de oro y dos lectinas, la aglutinina de germen de trigo y la sambucus nigra, proveniente de las bayas de saúco. Las lectinas son proteínas que se unen a carbohidratos de forma específica. La aglutinina de germen de trigo se une a los glicanos Neu5Ac y la quitobiosa (GlcNac1lcNac1β-4GlcNac) mientras que la sambucus nigra se une al glicano Neu5Ac(α2–6)Gal/GalNAc. En la corona de proteínas hay glicanos, dependiendo de la composición proteica de la corona, de ahí que las dos lectinas estudiadas tengan una diferente interacción con la corona. Para formar la corona de proteínas

alrededor de nanopartículas de oro, se emplearán diferentes disoluciones de plasma humano (3%, 10%, 40% y 80% de plasma respecto del volumen total), así como diferentes pasos de centrifugado y lavado de tal manera que se formen las llamadas corona de proteínas dura y blanda. La primera, está formada por las proteínas con mayor afinidad con la superficie de las nanopartículas de oro, siendo más estable en el tiempo. La corona blanda, por otra parte, está formada por una nube de proteínas que están asociadas más débilmente con la superficie de las nanopartículas. Esta corona es más dinámica y está en constante cambio. Para estudiar la interacción de corona con lectinas, se utilizaron lectinas marcadas fluorescentemente. La asociación de las lectinas fluorescentes con la corona se estudió mediante espectroscopía de correlación de fluorescencia (FCS del inglés fluorescence correlation spectroscopy). Mediante esta técnica es posible monitorizar la difusión de moléculas fluorescentes permitiendo discriminar entre lectinas libres y asociadas en base a su tiempo de difusión. Se observó una mayor asociación de la lectina sambucus nigra con la corona tanto dura como blanda debido a que existe un mayor número de glicanos Neu5Ac con los que esta lectina posee una gran afinidad, al contrario que la aglutinina de germen de trigo cuya interacción con esos glicanos es débil. Además, se llevó a cabo la eliminación enzimática de los glicanos de la corona de proteínas para suprimir la interacción de la corona con las lectinas. Por medio de FCS se observó que, tras la ruptura de los glicanos, la lectina se encuentra libre en la disolución. Esto indica que la interacción entre las lectinas y la corona de proteínas se debe a la presencia en ella de proteínas glicosiladas.

En el **capítulo 4** se presenta la funcionalización de la superficie de nanopartículas de óxido de zinc (ZnO) mediante la síntesis de cepillos poliméricos. Estos cepillos poliméricos proporcionan estabilidad coloidal en medio acuoso y protegen al ZnO frente a la degradación por el pH. Esta degradación por pH produce la liberación de iones Zn^{2+} cuya abundancia en la actividad mitocondrial puede producir inhibición en la respiración celular. La modificación superficial de las nanopartículas de ZnO se llevó a cabo mediante polimerización por transferencia de cadena por adición-fragmentación reversible (RAFT) usando los siguientes monómeros: ácido acrílico (AA), polietilenglicol (PEG metacrilato) y cloruro de trimetilamonio
[2-(metacriloxi)etil] (METAC), como ejemplos de monómeros de carga negativa, neutra y positiva, respectivamente. Una densidad polimérica de 18% fue obtenida en el recubrimiento con PAA, mientras para el PMETAC fue de un 9% y para el PEG de un 3.57%. Se utilizó microscopía Raman confocal para visualizar las nanopartículas de ZnO dentro de las células, y la evaluación del impacto del cepillo polimérico en su estabilidad y solubilidad sin necesidad de marcaje fluorescente.

La señal Raman de las nanopartículas se monitorizó en el tiempo dentro de las células comprobando que la degradación de las nanopartículas es más lenta cuando están recubiertas de un cepillo polimérico.

El **capítulo 5** trata de la formación de complejos de PAH-siRNA como agentes de vectores para terapia génica y el estudio de su destino biológico dentro de la célula. Estos complejos se forman por interacción electrostática de los grupos fosfato del siRNA con los grupos aminos del polímero PAH. La espectroscopía de fluorescencia de correlación cruzada (FCCS del inglés fluorescence cross-correlation spectroscopy) permite estudiar la evolución temporal de la correlación espacial entre dos especies fluorescentes dentro de un volumen confocal. En nuestro caso, tanto el polímero como el siRNA están marcados fluorescentemente, cuyos fluoróforos tienen espectros de emisión no coincidentes. FCCS es utilizada para estudiar la formación y estabilidad de los complejos a diferentes pHs por medio de la correlación cruzada entre ambos componentes, y para establecer el periodo de tiempo necesario para la liberación del siRNA dentro de la célula. Mediante FCS/FCCS pudo observarse que después de la endocitosis, los complejos forman grandes agregados dentro de las células con tiempos de difusión muy largos, probablemente como resultado de su interacción con diferentes componentes o compartimentos celulares. Esto produce la pérdida de intensidad de fluorescencia de los fluoróforos tanto del PAH como del siRNA al estar durante mucho tiempo iluminados por el láser. Analizando la amplitud de la correlación cruzada entre el siRNA y el PAH, a tiempo cero se observa que esta disminuye después de 12 horas, lo que indica la ruptura del complejo y la posible liberación del siRNA. Analizando las funciones de correlación de los componentes por separado, vemos en la mayor parte de los casos, la principal especie encontrada es siRNA con tiempos de difusión algo mayores a los obtenidos para el siRNA en disolución debido a su posible asociación a otras biomoléculas dentro de la célula.

General Introduction

Nanomaterials in Medicine

Nanomedicine is the application of nanotechnology in the biomedical field. It makes use of nanomaterials (NMs) to improve conventional diagnosis and treatments of diseases.[1] In the last decade, interest in nanomedicine has increased enormously for the treatment of a large number of pathologies, i.e., cancer,[2] brain or cardiovascular disorders,[3,4] immune diseases[5] as well as tissue regeneration,[6] and for improving imaging procedures[7,8] or sensing.[9,10]

At the nanoscale, the properties of materials (optical, magnetic, etc.) are different from bulk. The gravitational forces are not significant at this scale in comparison with other forces, such as nuclear or electromagnetic forces, so it is necessary to replace classical mechanics by quantum mechanics to understand nanoscale properties. The surface-to-volume ratio also plays an important role at the nanoscale. As the size of materials decreases to the nano world the area displayed for the material increases. One distinct characteristic of nanomaterials is indeed their large surface to volume ratio. This results in materials with higher chemical reactivity, thereby making possible to 'decorate' the nanomaterials with a large number of functional groups, molecules or even other NMs.[11,12]

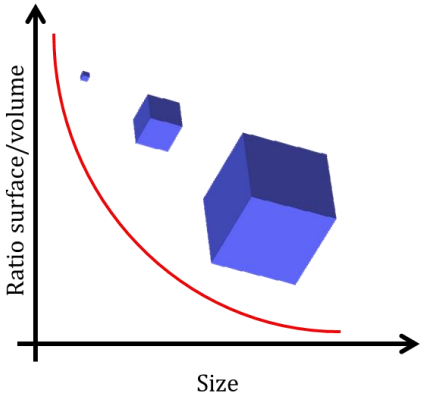

Figure 1. Dependence of ratio surface/volume with size

Many biological processes take place at the nanoscale. Biomolecules, e.g., proteins, can also be considered nano objects. The unique physico-chemical properties of NMs, such as superparamagnetism, plasmonic resonance, or controlled self-assembly have a large number of potential applications in different fields ranging from electronics,[13] cosmetic[14] and food products, amongst others.[15] The features of NMs in addition to the large surface to volume ratio, and a size comparable with biomolecules make them highly appealing for biomedical applications, in particular as drug delivery vehicles. Moreover, nanoformulations offer many encapsulation routes for otherwise insoluble payloads.[16] The surface modification of the NMs with peptides, antibodies, and other functionalities allows for colloidal stabilization and

targeted delivery.[17,18] Indeed, the surface engineering of NMs can be used to direct them to specific tissues or organs, and at the same time to increase circulation time avoiding early clearance through the mononuclear phagocyte system (MPS).[19] The MPS is responsible for identifying foreign bodies and guarantees their elimination through the macrophages via the liver or spleen.

Since 2016, 75 different nanocarriers are being evaluated for ongoing clinical tests with a further 18 new nanoformulations in clinical trials (17 of them related to cancer). The US Food and Drug Administration (FDA) and the European Medicines Agency (EMA) have approved 2 nanoparticles (NPs) and the European Market (CE Market) one for intratumoural administration.[20] Although we can find NPs used in the treatment of multiple diseases, a significantly large number of nanoformulations have been designed with the aim of treating or diagnosing cancer. Nowadays, chemotherapy is the most commonly used treatment for any kind of cancer.[21] However, chemotherapy faces a major drawback: the unspecific toxicity associated with the drugs employed, which produces adverse effects, such as hair loss, immunodeficiency, and/or nauseas.[22]

The use of NMs as carriers for chemotherapeutics aims to reduce the bioavailability of the drugs in healthy tissue, thereby restricting the drugs to the malign tissue. Cancer targeting can be achieved by the so-called Enhanced Permeability and Retention effect (EPR effect). This mechanism was discovered in 1986 by Maeda and Matsumura when they observed a high accumulation of certain proteins in solid tumour tissues.[23] EPR is a consequence of rapid tumour growth.[24] During the growth phase, tumours require a large amount of nutrients, realised by creating more blood vessels than in the healthy tissues. The disrupted and aberrant growth of the tumour and the secretion of nitric oxide synthase, or bradykinin inhibitors, produces higher endothelium permeability. All of these factors create fenestrations in the blood vessels allowing the penetration of the NMs and their accumulation in the tumour.[25] Nevertheless, clinical trials have shown that the EPR effect in humans is not as prominent as in rodent models.[26] However, a recent study has been published where the EPR effect is brought into question as the principal means of access for NPs to solid tumours.[27] Sindhwani and co-workers showed that tumour fenestration is less abundant than is generally thought. They estimate that 75 - 97% of NP extravasation is produced by transcytosis, or active transport mediated by vesicles. Complementary strategies are required to ensure that NPs accumulate in tumour tissue. As previously mentioned, this is achieved by the active decoration of the surface of NP with ligands, which have high affinity with specific motifs present in cells/tissues.[24–26] These ligand molecules may be carbohydrates, proteins, peptides, aptamers, or lipids.[28] As frequently targeted receptors we can mention transferrin receptors that are in charge of the iron transport and cell growth control[29] or folate receptors overexpressed in some tumours.[30,31] Other important receptors present in the membrane/cell surface are glycoproteins and lectins,[32,33] cluster of differentiation 44 receptors (CD44),[34,35] interleukin-4 receptor (IL-4R) expressed in lung tumour cells and tumour endothelial

cells[36] or integrins.[37] The combination of actively targeted NMs and the EPR effect allows for localised drug delivery at the tumour site. However, the specific binding between the ligand and the cell receptors can produce the accumulation of NPs in neighbouring cells close to the blood vessels resulting in the immobilisation of the NPs and preventing their diffusion to cancer tissue. This so called binding-site-barrier effect can decrease targeting efficacy.[38]

When NPs are administered, they will encounter different bodily fluids and environments, depending on the means of administration: intravenous, oral, inhalation, or topical. Following a specific exposure route, NPs will be subjected to multiple translocation processes, until they reach the cell interior, or are eliminated from the body. Through these processes they will interact with biomolecules, face changes in pH, be exposed to enzymes, and will also be "attacked" by the immune system. All of these processes can lead to nanocarrier degradation and eventually to the release of encapsulated drugs prior to reaching targeted organs, or in an undesired timeframe. The stability of NPs is therefore of prime importance during translocation and circulation in vivo, and in regards to the effective delivery of encapsulated drugs to targeted organs and cells.[39] NPs can also form aggregates inside biological fluids through interactions with biomolecules in the body, or through the changes in their structure, or as a consequence of degradation processes in biological fluids.

The properties of NPs have an impact on their biodistribution. Size, surface charge, shape, and stability are key factors influencing the biological fate of NPs, which must be taken into consideration in the material design for drug delivery.

Size

The influence of size on the distribution of NPs has been studied in animal models via advanced imaging techniques by Perez-Campaña *et al*. They showed that ^{13}N radiolabelled Al_2O_3 NPs with sizes varying from a few nanometres to microns with the same surface chemistry have a completely different biodistribution pattern as observed by positron emission tomography.[40] All their biodistribution studies were performed for a single time, 68 min. Larger nanoparticles (150 nm and 10 μm) accumulated in the lungs in a higher proportion than the smallest (10 nm and 40 nm). This fact can be explained by the accumulation of large particles or aggregates in the small lung capillaries. Due to their diameter larger nanoparticles are stopped in small capillaries producing a passive drug targeting.[41] 10 nm NPs showed less internalization than bigger ones. In fact, the small nanoparticles were located in the kidneys and the bladder suggesting that its excretion in urine. For sizes up to 300-500 nm, NPs tend to accumulate in the organs where the mononuclear phagocytes recognize and remove the particles. Early removal of nanocarriers may impede that they can perform the desire treatment, i.e, delivery of a drug to a specific organ.[42]

Using ICP-MS, Lopez-Chaves *et al*. studied the accumulation of gold NPs with different sizes (10, 30 and 60 nm) after intraperitoneal administration in different organs and their excretion after 9 days.[43] During this time smaller NPs were found in the kidneys and intestine, meanwhile the 60 nm NPs accumulated into the spleen. This situation suggests that the excretion of larger particles occurs via the spleen, and in the case of smaller NPs (10 and 30 nm) the elimination takes place via the intestine since the gold concentration was found to be higher in the feces. Experiments at longer times were performed by Li *et al*. in which gold NPs were used to study their biodistribution during 90 days but the administration route was intravenous in this case.[44] They employed sizes of 6.2, 24.3, 42.5 and 61.2 nm and obtained similar results. Again, larger particles were found in the liver and the spleen after 90 days and the smallest, which have faster clearance times (around 20 days), were found in different organs, such as the heart or lungs.

At cellular level, size plays an essential role in the uptake of NPs. A study of Pan *et al.* in 2018 concluded that in L929 cells (mouse fibroblast) the uptake of chitosan nanocapsules is more effective when size decreases.[45] Capsules loaded with rhodamine B were prepared with sizes from 25 to 200 nm. Cell uptake was monitored via Confocal Laser Scanning Microscopy (CLSM) and flow cytometer. CLSM images revealed higher fluorescence intensity in cells exposed to 25 nm NPs than those exposed to 45 nm or 125 nm NPs. This was confirmed with flow cytometry. A similar size dependence of uptake was observed by Wang *et al.,* but studying the different cell internalization pathways with NPs of different sizes.[46] Experiments revealed that NPs of 40 nm and 150 nm in diameter and equal ζ-potential do not follow the same endocytosis process. After endocytosis, larger particles are exocytosed by the cell meanwhile the smaller NPs are internalized and accumulate in the nucleus surroundings after 24 h. Cabral *et al*, observed a relation between size and the degree of tumour vascularization.[47] The authors employed polymer micelles ranging from 30 to 100 nm in diameter and found no differences in hipervascular tumours. The situation changes when the permeability of the tumour is lower where only NPs smaller than 50 nm accumulate in low vascular tumours.

Shape

Regarding intravenous administration, when a particle is present in the bloodstream, the shape of the particle will affect its flow due to the shear forces of blood circulation.[48,49] Spherical nanoparticles moves through the blood parallel to the vessel wall, while the non-spherical NPs follow a random path due to the combination between rotation and translation. Blood circulation times also seems to be influenced by shape. Filamentous polymer micelles remain in the blood vessels for more than a week, in contrast to the spherical NPs which only remain for 3 days.[50]

Biodistribution also is affected by shape. It has been shown that materials with discoidal forms accumulate preferentially in the lungs and heart,[49,51,52] while

elongated shapes, such as nanorods, agglomerate in the spleen and in the liver more than the spherical NPs.[52]

NP shape can also influence the cell internalization and retention. Nambara *et al.* studied the cell internalization of triangular and spherical NPs with different surface areas and volumes.[53] They concluded that shape and size modulate the NP cell uptake. For triangular NPs, higher internalization was observed for those NPs with higher surface area meanwhile for spherical gold NPs the higher uptake was found in the smaller ones. The high local curvature in the triangular NPs makes their cell internalization faster even in HeLa cells where the spherical gold NPs uptake is clearly not so efficient.

Once NPs come into contact with cells the available surface area for interacting with the cell membrane is important for cell uptake. In general, rod shaped NPs can reach more favourable contact with cell receptors than spherical particles because of their geometry, having a larger contact area.[51] It has also been shown that the orientation of the material during its first contact with the cell modulates the rate of NPs internalization.[54]

Surface charge and chemistry

The surface charge of NPs is an important parameter because it accounts on the colloidal stability of nanoparticle suspensions, the interaction between the NPs themselves and with the different components in blood, and the cell surface.[55] NPs with negative or neutral surface charge experience less absorption of proteins present in blood, which leads to a longer circulation lifetimes.[56,57] When NPs are in contact with the bloodstream, different proteins such opsonins, complements or immunoglobulins bind to the NPs surface. The presence of opsonins in the biocorona makes the NPs recognizable by phagocytes, which engulf them. This opsonization process ultimately leads to the clearance of the NPs from the body.[42] If opsonization is reduced or prevented, the MPS will not recognize the particles, thus, diminishing the degree of clearance from the blood. The phospholipid composition of cell membrane results in a negative charge on the surface of cells. Based on electrostatic interactions positively charged NPs are more likely to arrive to the cell surface as opposed to negatively charged ones.[56,58–60] Some of these positive coatings can further induce the endosomal escape of NPs, which will be later addressed. Amino functionalized materials with protonatable amines can induce the so called 'proton sponge effect' promoting the release of NPs and their cargo into the cytoplasm from endosomes.[61] Unprotonated amines can sequester protons from the medium producing a pump of protons into the endo-lysosomes (endosomes fused with lysosomes). The protonation of amines leads to a difference in proton concentration that, in turn, induces an osmotic swelling of the endo-lysosomes, causing defects in the endosomal membranes, through which NPs translocate to the cytoplasm.[62]

Colloidal stability

One of the crucial aspects to take into account in the design of nanocarriers is their colloidal stability.[63] Nanocarriers must have a stable size in aqueous solution to be used for biomedical applications, with minimal aggregation or sedimentation.[64] Stabilization of NPs is usually achieved by modifying them with functional groups, organic molecules or polymers that enhance their stability in an aqueous environment. Another fundamental goal of the surface modification of NPs is to minimise their interaction with biomolecules.[65,66] Undesirable interactions can also lead to aggregation of the nanocarriers. Besides, a coating with low levels of interaction with biomolecules, preventing opsonization, can be used to reduce recognition by the MPS. This can be achieved by the surface decoration of the NPs with a so called stealth coating, i.e. proteins, polymers, amphiphilic molecules with a low affinity for proteins found in blood. Among polymers, the most common stealth coating is polyethylene glycol (PEG), however other polymers are also effective as stealth coatings, e.g., polysaccharides, polyaminoacids, polyoxazolines, or poly(zwitterions).[67–70] Very often, stealth polymers are arranged around NPs as polymer brushes i.e, covalently grafted onto the particle surface from one end of the polymer chain while the other end remains free. The steric repulsions between the polymer chains compel them to stretch away from the surface creating a dense shell around the nanoparticle.[71] In some cases this polymer shell acts as anti-fouling coating preventing the adhesion of bacteria or proteins and conferring colloidal stability.[71,72]

Furthermore, nanocarriers interact with smaller molecules present in the bloodstream and with inorganic salts, which can affect their stability and lead to aggregation, affecting circulation and biodistribution. The evaluation of the stability of colloids in biological media is therefore extremely important in assessing their potential for biomedical applications. As mentioned before, if NP tend to form large aggregates it is highly probable that they will accumulate in the lungs and not arrive to the target organ.[73]

Composition

NMs can be classified according to their chemical nature as inorganic, organic, carbon based, and hybrid (Fig. 2).

Inorganic NMs are those composed of inorganic elements, such as metals or metal oxides. The synthesis methods of these NMs allows, in many cases, precise control over their size, shape and surface functionalization. Inorganic NPs display exceptional optical and magnetic properties. For example, some of them are used in sensing applications, e.g., quantum dots (QD), gold NPs, etc. QDs are colloidal nanocrystals that generally combine elements from groups II-V and III-V of the periodic table (i.e. CdSe, ZnS, InP, etc.), but they can be also fabricated with carbon (CQD). They are photostable and fluorescent and perform excellently as contrast agents or in

bioassays.[74,75] Gold and silver NPs are examples of inorganic materials used in sensing and diagnosis.[76] These NPs have extraordinary optical properties related to their characteristic surface plasmon resonance.[77] Gold NPs are of special interest in the biomedical field, not only for their optical properties, but also for their simple synthesis methods and their shape control (nanostars, nanorods, nanospheres, nanotriangles, etc).[78,79] In addition, gold NPs are easy to functionalize, usually through thiol exchange, which makes it possible to gain control over chemistry, not just size.[80] Gold NPs have found applications in photothermal therapy[81] and also for drug delivery by attaching drugs to the NP surface.[82,83] Metallic oxide NPs are also widely used in nanomedicine, especially iron oxide NPs, which present remarkable magnetic properties and high biocompatibility allowing their application in hyperthermia, MRI, or as drug delivery systems.[84] Moreover, metal oxides, such as ZnO, find applications as antimicrobials or high UV absorbents.[85,86]

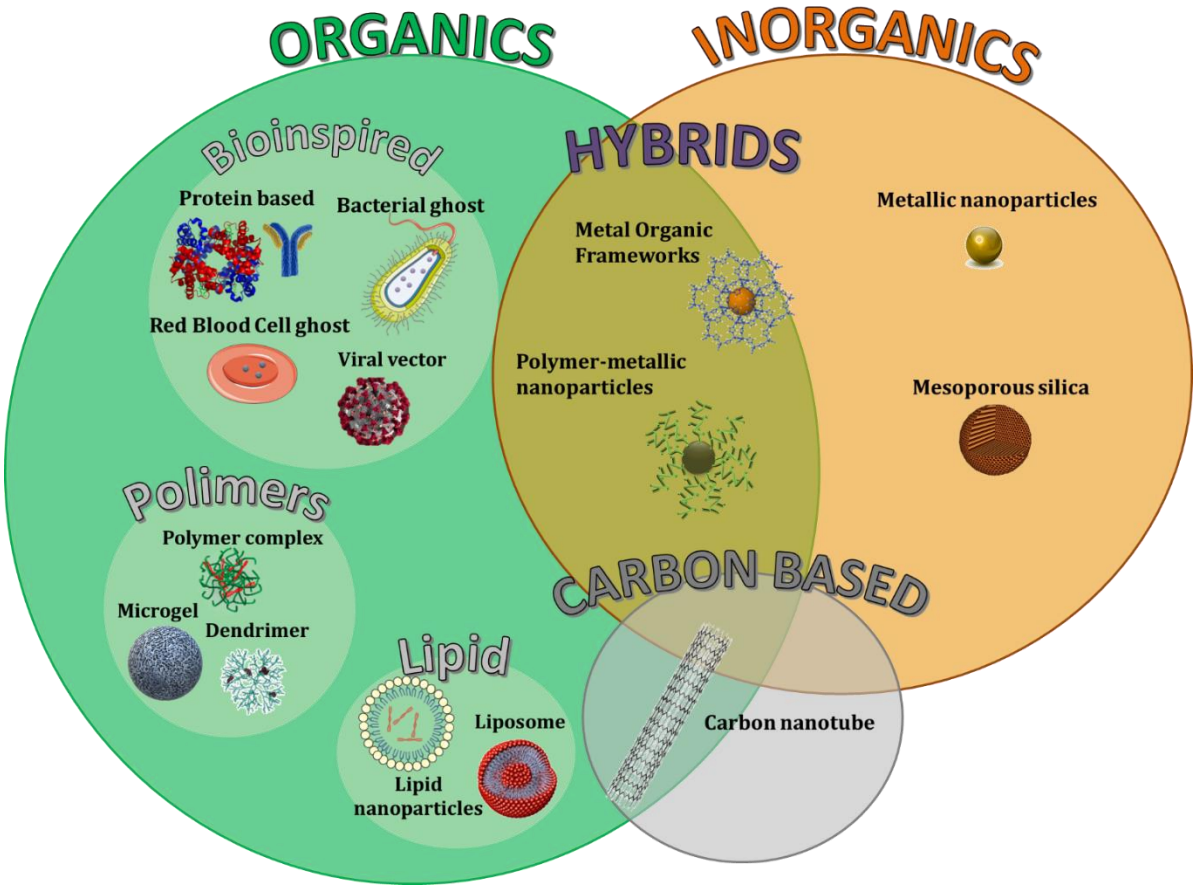

Figure 2. Nanomaterials classification based on their chemical nature.

Other interesting inorganic NMs for biomedical applications are mesoporous silica NPs, which are formed by an arrangement of organized pores with sizes in the nm range. Mesoporous NPs have been largely studied as drug delivery systems due to

their ease of functionalization, high porosity, and large surface area that allows the encapsulation of a large amount of drug inside the pores.[87,88]

Inorganic materials are usually modified with organic molecules to improve their colloidal stability, for targeting, and in many cases to load a cargo. The combination of inorganic and inorganic materials results in the formation of hybrid NMs.[89–93]

Carbon based materials are characterized by an array of carbon atoms, and show different properties depending on the carbon hybridization. Carbon materials comprise graphite, carbon nanotubes, carbon dots, diamond, fullerenes, and graphene. Carbon based NMs display unique mechanical, optical, thermal, and electrical properties that have led to their application in multiple fields, including biomedical sciences.[94]

Organic materials are the most widely used materials in nanomedicine. Organic NMs are based on organic molecules linked covalently, or through self-assembly into a nanostructure. The most frequently organic molecules used in biomedical applications are proteins,[95] polymers like chitosan (CHI),[96] poly(lactic-co-glycolic)acid (PLGA),[97] and lipids.[98]

Proteins are one of the most abundant macromolecules, consisting of one or more long chains of amino acids. They are amphiphilic molecules which perform a large variety of functions within organisms including molecule transport, specific chemical reactions, DNA replication, protection and structure to cells and tissues.[99–101] The production of artificial proteins with a *la carte* design has opened up new opportunities in the biomedical field.[102] Proteins find applications in biomedicine as therapeutic molecules (antibodies,[103] insulin[104]), or as structural components of nanocarriers (albumin,[105] hemoglobin,[106] etc.). To build protein NPs one of the most common protocol is protein crosslinking by desolvation, or co-precipitation.[107] Chaiwaree, *et al*.[105] used the co-precipitation method with $MnCl_2$ and Na_2CO_3 to entrap the protein inside the $MnCO_3$ NPs (used as a template). Then glutaraldehyde was added as a protein crosslinker agent prior to EDTA addition for the dissolution of the template. It was shown that these particles can be loaded with doxorubicin, which was released in the presence of Pronase® (protein-enzyme mixture) up to 40%.

Phospholipids formulated into liposomes are probably the most successful organic material used as a nanocarrier. It was in the early 1960s when liposomes were described for the first time, eventually becoming a powerful tool for drug delivery. Liposomes are vesicles formed by at least a single lipid bilayer. Multiple products based on liposomes have reached the pharmaceutical market, such as Doxil® (breast cancer), Abelcet® (fungal infections), or Marquibo® (lymphoblastic leukaemia).[108] Hydrophilic drugs can be encapsulated inside the aqueous phase cavity of the liposomes, while hydrophobic drugs can be embedded within the hydrophobic regions of the lipid bilayer.[109]

Analogous structures to liposomes are found in polymersomes, which are built by amphiphilic polymers arranged as polymer vesicles.[110] In spite of their similarities with liposomes, polymersomes present some additional advantages such as a higher stability and drug protection in comparison with liposomes.[111,112]

There are many polymers with synthetic and natural origins that have been used for drug delivery. Polymers for drug delivery formulations can be found in nature, in the chitin shells of crustaceans (chitosan), in the cartilage of some organisms (chondroitin), or in the cell walls of some algae (alginate). These polymers are biodegradable and biocompatible. In addition, polymer chemistry offers multiple possibilities for the synthesis of polymers with tailored properties that can be used to mimic natural polymers, or biomolecules like polypeptides,[113] polylysine (PLL), poly lactic acid(PLA), etc. Artificial polymers based on purely synthetic monomers, like polyallylamine hydrochloride (PAH), poly ethylenimine (PEI), etc., which have also been used for drug encapsulation in multiple formulations. Synthetic polymers can be designed with tailored properties for drug delivery. There are multiple routes for synthesis. Free radical polymerization is widely employed to obtain random copolymers and structures, e.g., hydrogels (Chapters 1 and 2). Better structural control can be achieved by using atom transfer radical polymerization (ATRP), or the reversible addition-fragmentation chain transfer polymerization (RAFT), which results in a narrow molecular weight distribution.[114,115]

Polymers can be formulated in different ways for drug delivery: as polymersomes, polymer micelles, solid NPs, capsules, scaffolds, complexes, etc. Among the most studied drug delivery vehicles based on polymers we find hydrogels[116,117] and polymeric NPs based on polyelectrolytes (PEs).[118–120]

PEs are polymers with ionizable units that dissociate in a polar solvent, and become charged.[121] The charge of the PEs can be positive (polycation), e.g., polyacrylic acid (PAA), chitosan (CHI), polyethyleneimine (PEI) and polyallylamine hydrochloride (PAH), or negative (polyanion), e.g., chondroitin (CSA), alginate (ALG), poly-[2-(methacryloyloxy)ethyl]trimethylammonium chloride (PMETAC). In addition, some polyelectrolytes, like proteins, can have both positive and negative charges (zwitterionic). In 1992, Decher *et al*. showed that it is possible to build thin films of polyelectrolytes, or polyelectrolytes multilayers (PMEs), with the alternating assembly of oppositely charged PEs, using the layer-by-layer technique (LbL).[122] PEMs are stable systems unless the polycations or polyanions lose their charge. Variations in pH, ionic strength, or temperature among others can trigger PEM degradation, or even complete dissolution.[123–125] Sukhorukov *et al*. built PEMs on top of colloids[126] instead of flat surfaces opening the possibility to encapsulate biomolecules between the PEMs. Using sacrificial colloids that could be removed after PEM assembly they showed the formation of nanocapsules.[127,128] Considering that some therapeutic agents are charged, it is also possible to build nanocarriers by the formation of complexes with the PEs. This approach is especially interesting in the

case of gene delivery. DNA and RNA are negatively charged biopolymers that can be used with a polycation: PEI, CHI, etc., to form complexes. The polymers protect the cargo reducing their degradation and will also trigger endosomal release and the delivery of the DNA/RNA to the cytoplasm.

A hydrogel is a 3-dimensional network of flexible polymer chains held together by crosslinking agents and highly solvated in water. The porous matrix in the hydrogel can be used to encapsulate molecules of different molecular weight. Depending on composition hydrogels can respond to pH, or temperature, or external stimuli such as a magnetic or an electrical field by shrinking or swelling. Stimuli responsive hydrogels are particularly attractive for drug delivery as they allow for the delivery of encapsulated molecules in specific biological environments or the release can be stimulated by external agents.[129]

Overall, soft materials are characterized by a high versatility in their design and offer many opportunities to develop a plethora of nanocarriers for applications in drug delivery.

Biological fate of nanoparticles

Protein corona

Independently of the administration pathways used for the delivery of NPs (parenteral, oral, topical), for most applications NPs must be stable when they come into contact with bodily fluids, e.g. blood and its components. Many biomolecules, such as as lipids[130] and proteins, can be adsorbed onto the surface of a NP. Proteins that attach onto NPs have a large influence on their biological fate. The proteins associated around NPs have been called 'protein corona' (PC). PC forms spontaneously around charged NPs within the first few seconds of contact with blood, or cell media.[131] PC formation is a competitive and dynamic process. Human plasma is composed of a complex mixture of nutrients/small molecules, cells, and a high concentration of free proteins. However, only 10-50 varieties of protein form the PC.[132] The most abundant are albumins, apolipoproteins, fibronectins and immunoglobulins.[133] These proteins are initially attached to the NPs, but over time they are replaced by less abundant proteins with higher affinity with the NP surface. Size, shape, surface functionalization, and the charge of NPs affect the process of PC formation. The local environment also must be considered since the biological milieu, pH, exposure time, and temperature influence PC formation.[134,135]

Despite the dynamic character of the PC there is a layer of proteins around the NPs, which is called the hard corona (HC), that is formed by proteins which bind strongly and which are very stable over time.[136,137] Surrounding the HC are other proteins with lower affinity that are weakly attached forming a soft corona (SC)[138] (Vroman effect[139]). The exchange between those proteins and the biomolecules of the environment is fast, and consequently more difficult to study in regards to composition, binding affinity or structure.[137] Therefore, the complete study of the PC

effect is limited due to the fact that the SC is the external and more dynamic layer and has a larger impact on biological milieu-material interactions than HC. The study of PC dynamics and its changes in real time, provides fundamental knowledge on NP biointeractions. The PC can be characterized by different techniques: Dynamic Light Scattering (DLS) (Appendix - I), Quartz Crystal Microbalance (QCM), Gel Electrophoresis (GE), and Transmission Electron Microscopy (TEM) among others.[140] In this thesis, the main technique employed for PC studies has been Fluorescence Correlation Spectroscopy (FCS) (Appendix - III) which allows to track the PC formation by measuring the diffusion of either fluorescently labelled NPs or proteins.[57] Most importantly, FCS allows the study of the PC inside cells.

The importance of the study of the PC, specially the HC with lifetime of many hours, lies in the biological identity that the corona brings to the NP.[141] The PC screens the surface charge of the NPs and in this way can impact on colloidal stability or affect their targeting capacity.[142] It has been observed that a pre-corona formation can prevent the agglomeration of NPs when their repulsive interactions are weak or their colloidal solubility is limited, but also can induce aggregation in other cases.[143–145] Not only is the stability of the NPs impacted by the PC, also the interactions with other biomolecules, such as apolipoproteins, involved in lipid transport or lipids, e.g., cholesterol, can produce NP destabilization.[131] The formation of a PC can also translate to changes in NP circulation lifetime.[146,147] Meanwhile certain proteins, e.g., HSA, can increase NP circulation time in blood, while other proteins cause NP phagocytosis.[42] PC formation can indeed influence NP uptake. Palchetti *et al*. showed that lipid NPs uptake is influenced by the PC and is also dependent on cell type.[148] The uptake of lipid NPs in MCF7 cells was shown to be reduced due to PC formation while their uptake in HeLa cells was shown to be higher with the same PC. Specific interactions between the cell membrane and the PC absorbed onto the NP certainly affect the cellular uptake.[149] In addition, the PC has the capability to enhance the biocompatibility of NPs. Some NMs are highly toxic, and the coating of proteins reduces their toxicity due to a limited direct exposure of the NP's surface to cells. This is the case for QDs, carbon nanotubes, or graphene.[150–152] The therapeutic effect of NPs can be also compromised due to the different biological identity.[142] To study NP-PC interactions and their changes, gold, polystyrene, and silica NPs are frequently used as models because it is easy to control their size, shape, and surface chemistry.[153–155]

To limit the adhesion of proteins onto NPs, polymers are commonly used as stealth coatings. Stealth coatings are designed to avoid electrostatic interactions between proteins and NPs. To achieve this goal, it is usually necessary to provide a neutral surface charge stabilized by hydrogen bonding with water or a zwitterionic coating, minimizing the interactions with proteins.[156] The most commonly used stealth coating is polyethylene glycol (PEG), a hydrophilic polymer, which is usually attached covalently to the surface of NPs from one end of the polymer chain.[157] It has been shown that the absorption of plasma proteins on PEG coatings is

dependent on the length of the surface density PEG chains. For example, coatings of 5000 MW PEG, with a 5% wt surface density have been shown to perform excellently as a stealth coating.[158] However, PEG antibodies have been shown in literature.[159,160] Lubich *et al.* confirmed the existence of IgM and/or IgG anti-PEG antibodies in healthy and hemophilic patients.[161] The discovery of antibodies against PEG has motivated the search for coatings to reduce the interaction of NPs with proteins and opsonization, e.g., zwitterionic polymers,[162] peptides,[163] or proteins[164] to increase the circulation lifetime.

Cellular uptake

Nanoparticles with a protein corona coating will face the microenvironment of the target tissue.[165] The interaction with the extracellular matrix, the action of enzymes and the microenvironment of the tissue (pH, salts, proteins, etc) among others are factors that could hinder the NP translocation in the tissue. It has been shown that the pH in the tumoural microenvironment lies at approximately 6.8. This fact can produce changes in the surface charge of the nanocarriers favouring, or hampering, cellular uptake.[166]

At the cellular level, NPs must translocate through the cell membrane. Different mechanisms can lead to NP internalization, with endocytosis being the most common. The endocytosis process involves NP trapping inside intracellular vesicles, thereby avoiding direct contact with the cytosol or other cell compartments.[18] There are different mechanisms of endocytosis depending on the cell type, but the most studied are clathrin-dependent endocytosis, caveolin-dependent endocytosis, clathrin-caveolin-independent endocytosis, phagocytosis, and micropinocytosis. The actual mechanism taking place will depend on the cell and NP characteristics.

Phagocytosis is the endocytic process characteristic of monocytes, macrophages, neutrophils, dendritic cells, M cells, and some endothelial cells.[167] Through this process, NPs covered with a PC attach to the phagocytes by the cell-surface receptors (light blue in Fig. 3), such as the Fc receptors, or the complementary receptors. The cell extensions surround the NP while forming anchoring points between the receptors and the NP, encapsulating the NPs in a phagosome. Overall, larger particles, above 0.5 μm, are internalized via phagocytosis.[54,168] Pinocytosis is another endocytic process that is used for the uptake of fluids and solutes. Pinocytosis is the most common process in mammalian cells, and it can be carried out by specific (receptor endocytosis) or non-specific (adsorptive pinocytosis) binding between receptors and NMs. The physico-chemical properties of the NMs and the receptors present in the cell membrane determine the internalization mechanism.[169]

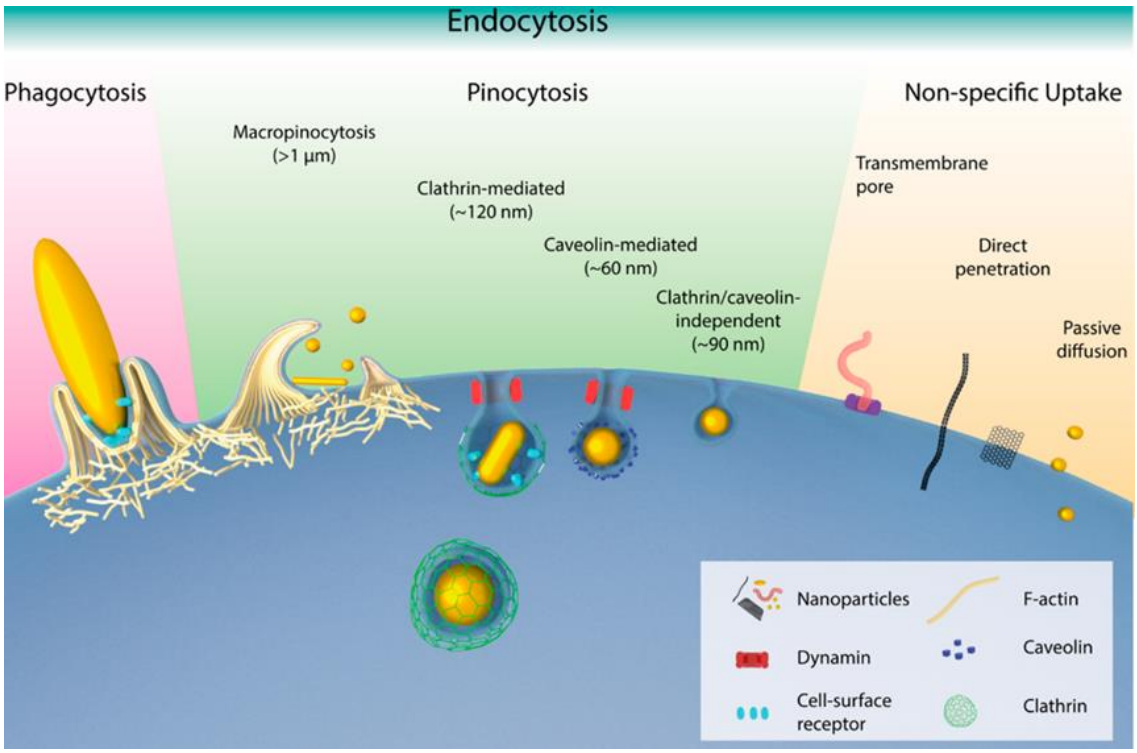

Figure 3. Different endocytosis pathways scheme. Reprinted with permission from Kinnear, C., Moore, T. L., Rodriguez-Lorenzo, L., Rothen-Rutishauser, B. & Petri-Fink, A. Form Follows Function: Nanoparticle Shape and Its Implications for Nanomedicine. Chem. Rev. 117, 11476–11521 (2017). Copyright 2020 American Chemical Society.

Micropinocytosis is the pathway employed by cells for the uptake of large extracellular fluids (composed of medium and the particles). In this case, there is no specific binding between the NPs and receptors, the material arrives to the cell surface, actin proteins are activated, and the membrane ruffles swallow it in the macropinosomes.[167]

Clathrin-mediated endocytosis is a receptor mediated endocytosis employed by cells to internalize nutrients, growth factor, and antigens.[170–173] This mechanism takes place in specific regions of the membrane, where clathrin is the most abundant protein, which in combination with other proteins organize to match nanoparticle shape to trigger internalization. This complex structure called coated pit corresponds to around 2% of the cells surface. The membrane produces an invagination, then GTP-binding proteins, e.g., dynamin induce the breaking of the coated pit from the membrane and form the endocytic vesicles with sizes between 80 and 150 nm depending on the cell type.[174] Clathrin is removed from the vesicle where the early endosomes are formed. The removed clathrin returns to the cell membrane to be reused in other clathrin-mediated endocytosis.[175]

Besides clathrin-mediated endocytosis there is another internalization mechanism via receptors called caveolar-mediated endocytosis. This type of endocytosis plays a role in the uptake of folic acid, bacterial toxins, regulation of lipids, or even diseases.[170,176,177] Additionally, different cells types, such as endothelium, muscle cells, fibroblasts, etc. use this internalization route. In this case, NPs are invaginated

by the membrane in vesicles formed by lipid rafts and covered by caveolae proteins. These proteins give the characteristic shape of the primary vesicle. The caveolae-vesicles are smaller than clathrin ones, with sizes between 50 and 80 nm and have a neutral internal pH.[176] The scission of the membrane is carried out by dynamin, as in clathrin-mediated endocytosis but this process is slower than in clathrin-mediated endocytosis. Usually, after uptake, lysosomes fuse with the vesicles and lead to the release of the caveolae-vesicle content. In caveolae-mediated invagination, vesicles do not follow the lysosome pathway, as is the case for virus or other pathogens, thus avoiding their degradation.[178]

In addition, there are other non-receptor mediated endocytic processes less common such as non clathrin-vacuole-mediated, passive diffusion, or direct penetration.[51,168–170,179]

Release of encapsulated drugs

Once the cellular uptake has taken place, the NM locates within the endosomes. These compartments inside the cell can be classified as: early endosomes, recycling endosomes, and late endosomes.[170] The early endosomes are the first vesicles formed after the release of coating proteins (clathrin or caveolae). The pH in the early endosomes is around 6 before their maturation to late endosomes where the pH drops to 5 when they are fused with the lysosomes.[167] This change in the pH is often taken into account in the design of drug delivery systems. As stated above, some aminated polymers with high buffering capacity can protonate at endosomal pH and induce changes in osmotic pressure inside the endosomes, the so called 'proton sponge effect'.[180] This osmotic swelling induces partial breakage of the membranes of the endosome and facilitates the escape of the NPs and the liberation of the drug into the cytoplasm. Another pathway followed by some lipids is fusion with the membrane, which also leads to the delivery of the encapsulated drug.[181] Very often, nanocarriers are designed to protect the cargo at neutral pH, whereas at acidic pH (as in endo-lysosomes) they disassemble, produce an osmotic swelling or fuse to the lipid membrane, liberating the cargo.[182] Another way to activate the drug delivery is the formation of pores in the endosomal membrane. The endosomal membrane is permeable, and some peptides can bind to the membrane producing tension changes on it.[180] The high affinity of these polymers produces membrane disruption and the consequent release of the nanocarrier payload.[181]

In this thesis we will focus on carriers for chemotherapeutic agents, which inhibit cell replication in diverse ways and on carriers for nucleic acids. An example of chemotherapeutics that we work with is doxorubicin, a widely studied anti-cancer drug. Cell growth inhibition in the case of doxorubicin is caused by the intercalation of the drug with DNA, interfering with the enzyme topoisomerase II, which is responsible for the transcription of the DNA.[183]

In recent years, gene therapy has been extensively explored due to the genetic or hereditary origin of a large number of human diseases.[184] Gene therapies are based on the modulation of gene expression by addition, deletion, regulation, repair or replacement of a particular genetic sequence in specific cells.[185,186] Gene technology is being implemented to target rare genetic disorders, cancer, and infectious diseases by delivering nucleic acids including short interfering RNAs (SiRNAs),[187] plasmid DNAs,[188] messenger RNAs (mRNAs),[189] CRISPR/Cas9 complexes.[190] Although, theoretically, gene therapy serves as a solution for the permanent eradication of the diseased genetic sequence, the translation of this technology to clinical trials has largely been limited due to the difficulty associated with the delivery of genetic material to the target site. Enzymatic degradation in blood, poor bioavailability at the targeted location, rapid clearance from the systemic circulation and immunological response are the major barriers towards the translation of this technology in practical application.

Aim and Objectives

Despite the large investment in nanomedicine , the translation of NMs to the medical sector is far from being realised.[19] This is, to large extent, because NMs are not capable of fulfilling their goal: i.e., the delivery of payloads in specific organs and cells in a programable way. Very often, research does not take into account the biological fate of NMs and how the NMs will evolve, or change, through contact with biomolecules, cells and through the different translocation processes that they will encounter in vivo. The state of aggregation, the degradation of the NMs, and the loss of targeting or protective coatings in biological fluids, cells and organs are issues that are seldom studied and are particularly important regarding the evaluation of the capacity of NMs to fulfil their therapeutic goal and deliver their cargo as designed. Translocation and biological fate both at the body and cellular level are very much dependent on the physico-chemical properties of NMs: i.e., their surface charge, size, colloidal stability, etc.

This thesis aims to address different issues related to the interaction between soft NMs and biomolecules and their translocation, aggregation, and degradation at the cellular level. We make use of NMs with different characteristics and composition that allow us to address specific problems of NMs translocation and fate, and bio interactions. We will advance on the understanding of how the physico-chemical properties of soft NMs are affected by their interaction with biomolecules, or by environmental conditions such as in biological fluids; pH, ionic strength; and we will aim to correlate the physico-chemical characteristics of the NMs studies with their translocation and fate.

The specific objectives can be summarised as:

Evaluate the impact of charged biomolecules and cargo on the responsiveness of pH and temperature sensitive hydrogel microparticles. Poly(N-isopropylacrylamide-co-methacrylic acid P(NIPAm-co-MAA) hydrogel is studied as a drug delivery system by taking the advantage of its responsiveness to changes in temperature and pH. An innovative use of time lapse NMR spectroscopy will be presented to understand P(NIPAm-co-MAA) hydrogel dehydration behaviour as a function of temperature in different environmental conditions. Changes in the intensity of ^{1}H-NMR signal spectra during heating/cooling of the hydrogel from 20 to 40 °C will reveal how the ionic strength, the pH, and the presence of cationic molecules with different molecular weights affect the volume phase transition of the hydrogel from a molecular perspective.

Characterize the protein corona surrounding NPs with lectins by means of Fluorescence Correlation Spectroscopy (FCS). The protein corona (PC) provides a

biological identity to NPs and influences their interaction with other biomolecules and cells. Here, we focus on the interaction of the PC with lectins, carbohydrate-binding proteins This interaction may be fundamental for cell uptake. FCS allows one to study the association between labelled lectins and the sugar moieties of the PC formed around gold NPs. By means of FCS, changes in the diffusion of fluorescently labelled lectins can be correlated to their association with the PC around gold NPs.

Evaluate the impact of polymer coatings on the degradation of ZnO NPs intracellularly by means of confocal Raman microscopy. ZnO NPs are known to dissolve intracellularly at endosomal pH values. Polymer coatings, such as polymer brushes, can act as barriers against NP degradation. We will show that Confocal Raman Microscopy (CRM) can be used to trace ZnO degradation intracellularly and to assess the protective effect of polymer brushes.

Determine the biological fate and dissociation of polymer complexes carrying siRNAs intracellularly by means Fluorescence Correlation and Fluorescence Cross-Correlation Spectroscopy. We will study the fate of polyamine complexes used as carriers for small interference RNA (siRNA). Carriers must release siRNAs in the cytosol. Translocation of polyamine complexes inside cells will be studied by CLSM. By means of Fluorescence cross-correlation spectroscopy (FCCS) we show that it is possible to trace the release of siRNA intracellularly and determine the timeframe of the delivery of siRNA in the cytosol.

Chapter 1

A study of the complex interaction between polyamines and negatively charged poly(N-isopropylacrylamide-co-methacrylic)

1.1. Motivation

Gels are crosslinked polymers forming a tridimensional network (Fig 1.1). A fundamental characteristic of gels is that the polymer matrix is capable of reversible swelling in a solvent, usually water. This process takes place via van der Waals forces, hydrogen bonds, electrostatic, and/or hydrophobic interactions depending of the nature of the polymer and solvent.[191,192]

Gels can be classified according to the solvent in which they swell.[193] When they swell in an aqueous media gels are called hydrogels. Polymer chemistry offers several routes to easily tune the hydrogel structure. By adjusting synthetic parameters (amount of cross-linker, monomers, reaction time, etc.) it is possible to control hydrogel porosity and swelling behaviour.[194] The porous structure of hydrogels has found multiple applications for the encapsulation of drugs.[84,195–199]

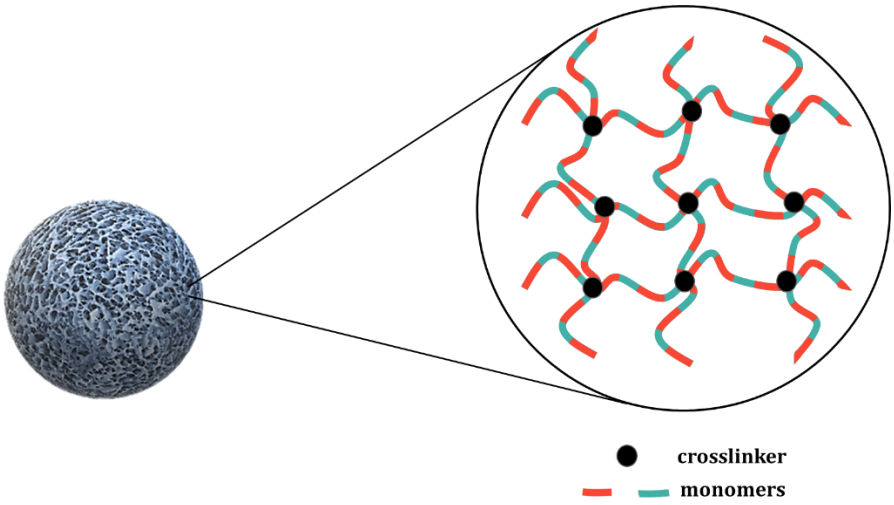

Figure 1.1. Microgel structure.

Micrometer-sized hydrogels, microgels, are highly-hydrated crosslinked polymer networks in the colloidal domain. Microgels are usually designed to undergo a volume

phase transition in response to specific stimuli, such as temperature, pH, ionic strength, or solvent nature. Microgels based on poly(N-isopropylacrylamide) (PNIPAm) are one of the most studied thermosensitive hydrogels. PNIPAm hydrogels exhibit a volume phase transition at 30℃–32℃, the so-called nominal lower critical solution temperature (LCST). Above this temperature, the cross-linked PNIPAm chains stabilized by hydrogen bonding with water dehydrate, resulting in a drastic decrease in particle size. Microgels with temperature sensitivity near physiological conditions have drawn increasing attention due to their potential application in sensing,[200,201] regenerative medicine,[202,203] and drug delivery.[204,205]

PNIPAm based microgels, though practically not charged, are highly solvated in water by hydrogen bonding interactions and provide an environment suitable for hydrophilic and charged drugs. However, the encapsulation and retention of charged drugs in PNIPAm-based microgels is limited and it is necessary to increase the loading capacity by introducing ionic co-monomers into the PNIPAm network that can trap oppositely charged molecules. Microgels based on PNIPAm and methacrylic acid (poly(N-isopropylacrylamide-co-methacrylic acid) (P(NIPAm-co-MAA)) are both thermoresponsive and pH-sensitive, while also being capable of complexing positively charged drugs through carboxylic groups. Besides drug delivery, P(NIPAm-co-MAA) microgels are increasingly employed in emulsion stabilization,[206,207] thin-film fabrication,[208,209] among other applications. Moreover, the distribution of ionizable groups in the microgels (random and core–shell) controls the interactions for the uptake and release of certain cargos.[210] Charged thermoresponsive microgels can also be assembled into films using the Layer-by-Layer (LbL) technique, which expands their potential applications to sensing and delivery. Indeed, P(NIPAm-co-MAA) microgels have been assembled with poly allyl amine hydrochloride (PAH) as a counter polyelectrolyte, polycation. The microgel is alternatively assembled with PAH up to a desired number of layers. Interestingly, it can be observed that during their assembly the microgels decrease their water content.[211] However, the LbL films retain thermoresponsiveness from the microgels and exhibit an increase in hydrophobicity, stiffness, and adhesion properties upon switching the temperature from below to above the LCST while the permeability of redox probes through the film remains unchanged. The physico-chemical properties of the microgel films can be explained by assuming that during the assembly of PAH, diffusion of the polyelectrolyte chains into the microgel takes place, at least partially.

Polyelectrolytes could indeed diffuse into the microgel porous structure in addition to adsorbing on their surface. Diffusion of polyelectrolytes inside charged hydrogels will depend on the pore size of the microgel and on the charge of both the diffusing polyelectrolyte and the microgel. Since PAH is positively charged, it will face attractive interactions with P(NIPAm-co-MAA) microgels that would facilitate diffusion inside the pores, and complexation with MAA negative charges inside the hydrogel core. At the same time, the presence of charges on the surface of the hydrogel can lead to PAH complexation on the surface of the microgel, which may also

lead to the recharge and blocking of pores and finally prevent additional PAH chains from entering the microgel core. Interesting results about the interaction of temperature and pH-sensitive P(NIPAm-co-MAA) microgels with polyelectrolytes have been already reported.[212,213] P(NIPAm-co-MAA)) microgels exposed to oppositely charged polyelectrolytes of different molecular weight showed different electrophoretic mobility and hydrodynamic radius depending on the molecular weight of the polyelectrolyte. Some authors postulated that the oppositely charged polyelectrolyte chains penetrate into the microgel structure,[214] while others suggested the accumulation of the polyelectrolytes on the microgel interface.[215] Whether the polyelectrolyte deposits on the microgel surface or penetrates the microgel has not been fully demonstrated. Dobrynin and Rubinstein have demonstrated that the surface adsorption of polyelectrolytes on an oppositely charged surface depends on the surface charge density, the fraction of the charged monomers on the polyelectrolyte and ionic strength.[216] Gelissen et *al*.[217] recently investigated a model core-shell PNIPAm-based microgel with a cationic core composed of N-(3-Aminopropyl) methacrylamide hydrochloride and an anionic shell composed of monomethylitaconate to study whether the presence of a negatively charged shell shields the cationic core while still enabling the uptake and release of anionic guest polyelectrolytes. These microgels were loaded with polystyrene sulfonate of different molecular weight to study the influence of their chain length on polymer uptake and release. Using small-angle neutron scattering, the authors evaluated the spatial distribution of polystyrene sulfonate within the microgels and found that the location of polystyrene sulfonate in the microgel depends on the molecular weight of the polymer.

In this chapter, we aim to advance on the understanding of the interaction between negatively charged PNIPAm microgels and positively charged PAH molecules. Our goal is to better understand how polyelectrolyte chains associate with the microgel, and to determine how this association is affected by the temperature-induced collapse of PNIPAm chains which leads to a redistribution of the charged moieties.

ζ-potential, DLS, flow cytometry, CLSM and FLIM have been employed to study the association between these two species DLS and ζ-potential allows to study the colloidal stability of the microgel above and before the LCST in the presence of PAH molecules. Flow cytometry helps to estimate the quantity of fluorescently labelled PAH, as a function of polymer MW, entrapped inside the microgel. By means of confocal microscopy information on the localization of fluorescently labelled PAH in the hydrogel will be obtained. In addition to the interaction of polyamines with the hydrogel, we study the complexation of small positively charged drugs with the carboxylate groups of the hydrogel. Doxorubicin, a positively charged chemotherapeutic is encapsulated in the hydrogel. The competition between polyamines, PAH and the oligomers spermidine and spermine, with doxorubicin to form complexes with the carboxylate groups of the hydrogel will be evaluated by CLSM and FLIM.

1.2. Experimental Section

1.2.1 Materials

N-isopropylacrylamide (NIPAm, 97%), N,N'-methylene-bis-acrylamide (BIS, 99%), ammonium persulfate (APS, 98%), polyallylamine hydrochloride of 15 kDa (PAH 15 kDa), polyallylamine hydrochloride of 50 kDa (PAH 50 kDa), and Methacrylic acid (MAA, 99%) and doxorubicin (DOX) were purchased in Sigma Aldrich. Polyallylamine hydrochloride of 140 kDa (PAH 140 kDa) was obtained in Alfa Caesar. Green rhodamine PAH (G-PAH) was provided by Surflay Gmbh in Germany.

1.2.2 Microgel Synthesis

P(NIPAm-co-MAA) hydrogels were obtained via free-radical precipitation polymerization.[218] 12 mmol of NIPAm and 0.28 mmol of BIS was added to 100 mL of Milli-Q water were heated up to 70 ℃under magnetic stirring and N2 bubbling during 1 hour. Then, 1.72 mmol of MAA was poured into the solution. After 5 min, 0.26 mmol of APS were added to start the polymerization and was stirred for 4 h. Microgels were collected by centrifugation and washed with water three times.

1.2.3 Microgel Characterization

Scanning Electron cryo microscopy (CryoSEM) was performed to characterize the microgel size, shape and surface. The equipment used was a Scanning Electron Microscope SEM Jeol 7001TTLS. Samples were frozen with liquid nitrogen and then introduced in the cryo chamber. There, a piece of sample was cut with a cold knife and the sublimation process started. By this process the water content of the microgel was remove retaining the microgel structure. Once the sublimation process is finished, the sample is moved to the cold stage and measured. Samples were not metal coated, and a lower acceleration voltage was employed (5 kV).

Via DLS, microgel size and ζ-potential as a function of temperature were measured in a Malvern ζ-Sizer Nano ZS in backscattering mode with a 173° scattering angle. 1 $mg \cdot mL^{-1}$ of microgel was dispersed in 5 mM KCl and PAH with different MW (15, 50 and 140 kDa) was added at different concentrations at 20 ℃. Measurements were performed at 20 ℃ and 40 ℃.

1.2.4 Polyelectrolytes internalization in microgel

Polyelectrolytes internalization was studied via CLSM and FACS.

Confocal microscopy imaging was performed with a Zeiss LSM 880 confocal microscope (Carl Zeiss Gmbh). Data acquisition and analysis are controlled with Zen black software. The excitation wavelength was 488 nm of an argon laser and the emission was collected using a GaASP detector coupled with transmission, TPMT. The objective used was a 100X EC Plan-Neofluar (oil, 1.3 NA) objective. Kinetic experiments were carried out by acquiring 1024 x 1024-pixel frames with 10X digital

zoom and 120 time series with a 1.2 s frame rate. The samples were stabilized for 10 minutes at different temperatures before time series acquisition using a temperature-controlled insert in the microscope stage.

For FACS experiments, microgel solution was placed in a 5 mL BD Falcon polystyrene round-bottom tube and G-PAH at different concentrations was added. G-PAH fluorescence was recorded in the PE-A channel (585/42 nm filter with a 556 nm long pass filter) of a BD FACSCanto II cytometer. Before the experiment, BDt CS&T beads were run to guarantee the correct performance of the instrument. As a control, microgel without G-PAH was measured to characterize the population in terms of the forward (FSC) and side scatter (SSC). This sample and microgel loaded with the maximum percentage of PAH were used to fix the PE-A voltage. The number of events recorded for each sample was 10000. Results were analyzed using FlowJo 7.5 software.

1.2.5 Doxorubicin Release via Fluorescence Lifetime Imaging Microscopy

Microgel solution was placed in a in NuncTM Lab-Tek Q5 Chambered Coverglass and observed in a confocal microscope. The measurements were performed in the NanoBiomedical Centre in Poznan, Poland and in CIC biomaGUNE. In biomaGUNE, the measurements were done in a Zeiss LSM 510 laser scanning microscope and in the NanoBiomedical Centre in a Scanning Fluorescence Laser Microscope system Olympus FV 1000 via the add-on system from PicoQuant. This system consists of two pulsed laser heads (185 nm and 635 nm) with a Multichannel Picosecond Diode Laser Driver PDL 828 'Sepia II', Time-correlated single-photon counting (TCSPC) and Time tagging unit PicoHarp 300, two photon detection units and the software to collect the data, Symphotime. Measurements were performed using an Olympus water immersion objective 60x/NA 1.2 and 485 nm laser. In the detection channel, an LP 505 filter was used to suppress reflected and scattered laser light.

DOX was added to reach a concentration of 10^{-5} M. After 5 min, 40% spermidine or spermine were added to observe changes in the DOXO lifetime.

1.3. Results and Discussion

Microgel Characterization

The ratio of NIPAm to MAA in the hydrogel was determined by ^{1}H NMR (Fig. 1.2). From NMR, an estimated ratio of 88% of NIPAM to 12% MAA (0.88:0.12) was determined.

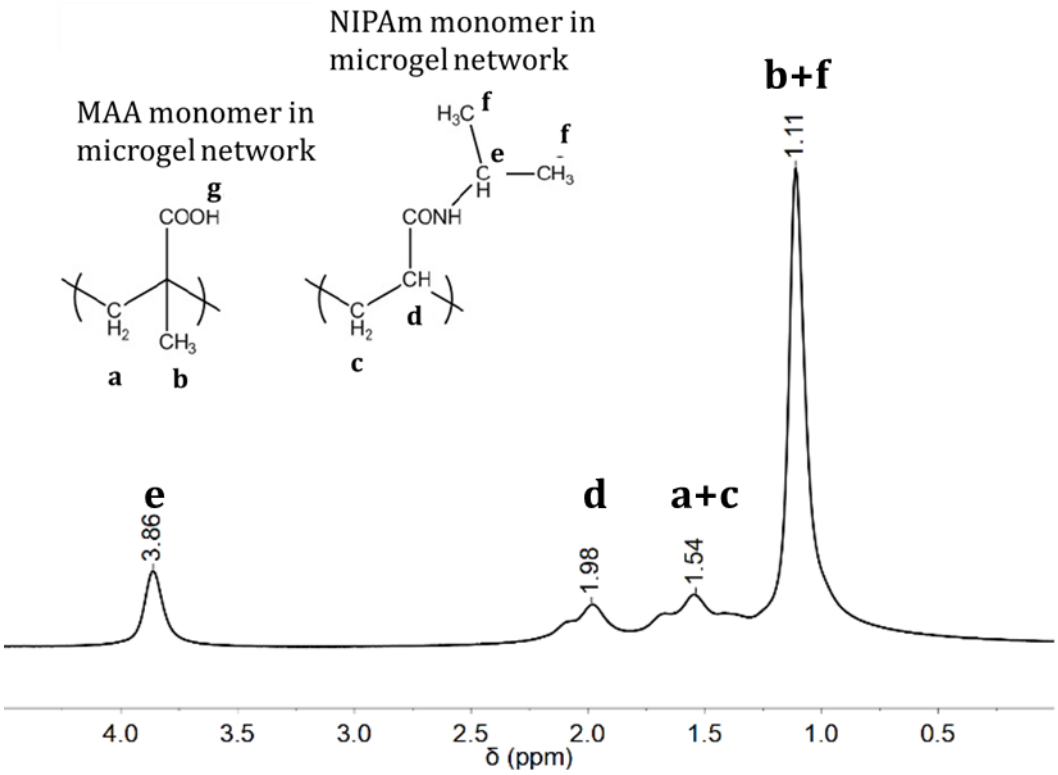

Figure 1.2. 1H NMR spectrum for poly(NIPAM-co-MAA) microgels.

Microgels were also characterized by cryo-SEM (Fig. 1.3). The microgel appearance is smooth and spherical with a diameter of approximately 500 nm. Filaments connecting the hydrogel microparticles can be observed, which are most likely non-sublimated water.

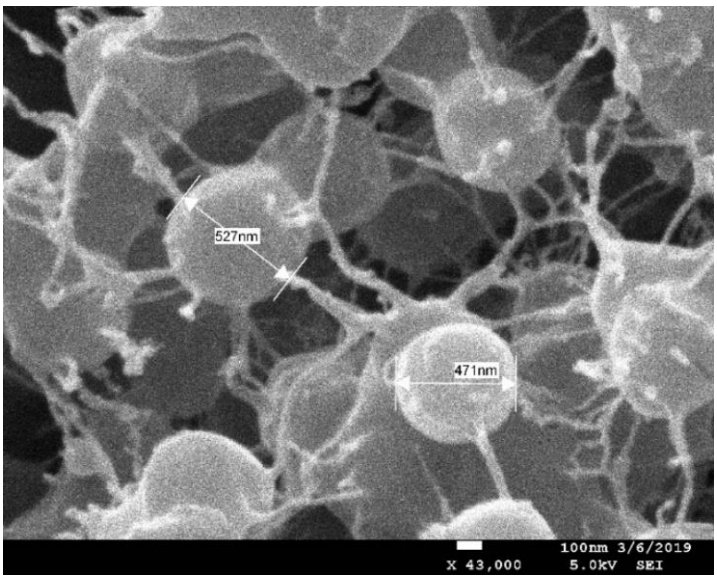

Figure 1.3. Cryo-SEM micrographs of PNIPAM-co-MAA microgels. Scale bar is 100 nm, magnification of 43.000 and voltage of 5 kV.

DLS and ζ- potential measurements were employed to study the changes in the surface charge and hydrodynamic diameter in the presence of PAH at 20 °C (below the LCST) and 40 °C (above the LCST). (Fig. 1.4). The mass of added PAH is calculated as percentage of the total microgel mass.

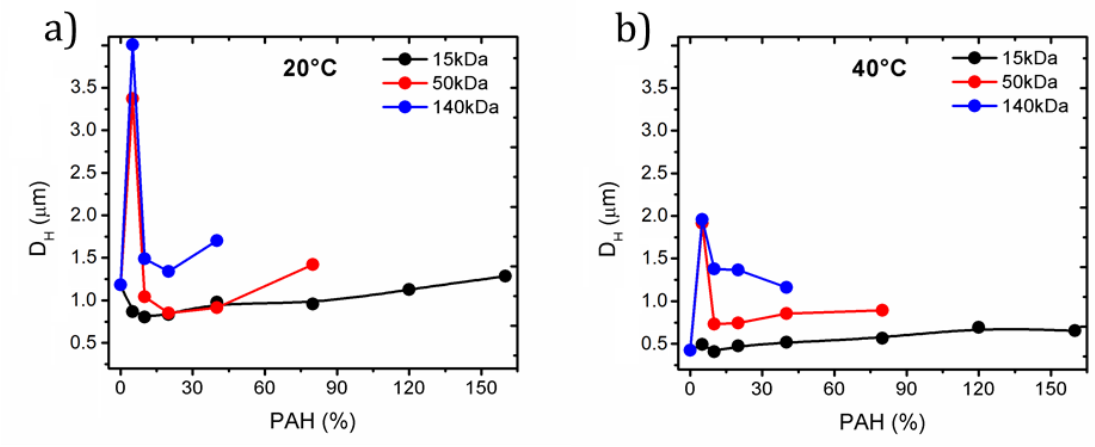

PAH → MW ↓ Amount (%)	15kDa				50kDa				140kDa			
	20°C		40°C		20°C		40°C		20°C		40°C	
	D_H	PDI	D_H	PDI	D_H	PDI	D_H	PDI	D_H	PDI	D_H	PDI
0	1181	0,298	424,2	0,034	1181	0,298	424,2	0,034	1181	0,298	424,2	0,034
5	865,9	0,152	494,1	0,061	3370	1	1917	0,329	4007	0,309	1956	0,27
10	805,1	0,095	407,7	0,029	1044	0,335	728,9	0,262	1488	0,243	1378	0,104
20	834,8	0,095	473,3	0,332	851,9	0,157	744,6	0,045	1340	0,303	1367	0,302
40	976,5	0,228	517	0,238	912,5	0,178	856,4	0,017	1701	0,198	1161	0,242
80	956,2	0,151	566,5	0,012	1421	0,238	891,1	0,065	Precipitation			
120	1129	0,211	691,9	0,096	Precipitation							
160	1284	0,321	652,9	0,062								

Figure 1.4. Microgel hydrodynamic diameter at different temperatures: A) below the LCST (20 °C) and B) above LCST (40 °C) with increasing amounts of PAH of 15 kDa (black), 50 kDa (red), and 140 kDa (blue), respectively. The table presents the data of the figures above. The units for the hydrodynamic diameter are nm.

As shown in the table, the diameter of the hydrogel without PAH decreases from 1.181 µm at 20 °C to 0.424 µm when the temperature is above the LCST. This result differs from that of cryo-SEM. This is because in the DLS measurements the microgel is composed by a polymeric matrix full of water, whereas the water is absent, due to sublimation, in the cryo-SEM measurements.

When PAH 15 kDa was added to the microgel solution at 20 °C the size of the hydrogel is reduced until the concentration of PAH reaches 10%. The hydrodynamic diameter changes from 1.2 µm to 0.8 µm for 0% to 10% PAH, respectively. Above 10% PAH we see that particle size increases slowly and linearly from 0.8 µm (10% PAH) to 1.3 µm (160% PAH). Above the LCST (40 °C), hydrogels with PAH 15 kDa show hydrodynamic diameters from 0.42 µm to 0.55 µm for PAH concentrations from 0 %

to 160 %, respectively. Concentrations of PAH 15 kDa over 160% result in the destabilization of the microgel solution and induce microgel precipitation.

In sharp contrast with the previous result, in the presence of PAHs with higher molecular weight a very different evolution of the microgel size was observed. The microgel exhibited a marked increase in size with 5% PAH of 50 kDa and 140 kDa both at 20°C and at 40°C, with more pronounced changes at 20°C. This increase in size is probably indicative of aggregation. However, at 20°C with the PAH concentration over 5%, and up to 15%, both MWs resulted in a particle size comparable to the initial value, close to 1.2 μm. Above 15% PAH concentration, the particle size increases slowly and linearly from 1.0 to 1.4 μm in diameter with addition of PAH 50 kDa, up to 80% of PAH, and from 1.5 to 1.7 μm with the addition of PAH 140 kDa, up to 40% of PAH. Over the upper percentages of PAH, 80% for PAH 50 kDa and 40% for PAH 140 kDa, the microgel precipitates. At 40 °C, the microgel with both PAH 50 and 140 kDa displays a larger diameter than the naked microgel (0.24 mm). The differences in diameter between the naked microgel were more prominent for PAH 140 kDa than for PAH 50 kDa. In fact, after the initial large size values at 5%, probably due to microgel aggregation, the microgels displayed sizes of 1.4 μm for 15% of PAH 140 kDa and maintained that value until 40% PAH before precipitation. Similar behaviour is observed in the case of PAH 50 kDa: at 40°C for 15% PAH the particle size was 0.7 μm.

These results evidence that the size and stability of P(NIPAm-co-MAA) microgels is largely affected by the presence of PAH below and above the LCST and that the molecular weight of PAH plays a substantial role in the microgel behaviour. In order to gain more insight into the interaction of PAH with microgels ζ-potential measurements were performed. To acquire a comprehensive knowledge of the mechanism (swelling/deswelling behaviour), ζ-potential measurements for 1 mg/ml microgel dispersions in 5 mM of KCl with an increasing amount of PAH at the three molecular weight studied, i.e., 15, 50, and 140 kDa were performed. Fig. 1.5A shows that at 20 °C the ζ-potential of the naked microgel is close to 0 mV decreasing to around -20 mV at 40 °C. This decrease in ζ-potential can be attributed to the reduction in particle volume above the LCST that favours the increase in the density of negatively charged MAA monomers on the hydrogel surface. Additionally, charge segregation to the surface can occur, because the collapse of PNIPAm with temperature triggers its aggregation forming a hydrophobic structure, which avoids the interaction of water by exposing the MAA monomer to the bulk. Such rearrangement would also help maintain the colloidal stability of the microgel in aqueous mediabehaviour.[219]

The 0 mV value of the microgel ζ-potential at 20°C was gradually increased with the addition of PAH 15kDa reaching a plateau close to + 25mV at 100 % PAH, approximately. For PAH 50 kDa, the ζ-potential at 20°C also gradually increased with the addition of PAH, reaching +50 mV for 80 % PAH without reaching a clear plateau

before destabilizing the system. On the contrary, the microgel-PAH 140kDa system appears to reach a plateau more steeply at around + 48 mV with only 10% of polyelectrolyte.

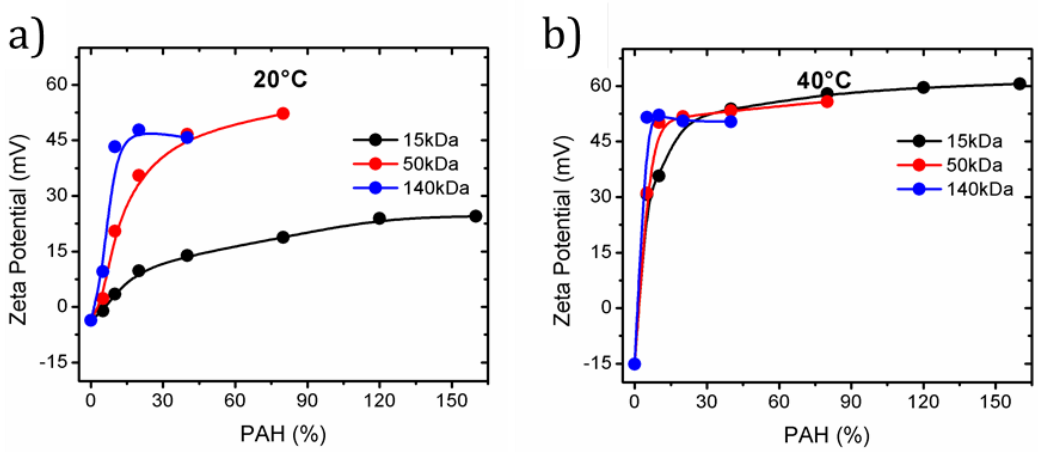

Figure 1.5. ζ-potential measurements of PNIPAM-co-MAA microgels in the presence of PAH 15 kDa (black), 50 kDa (red) and 140 kDa (blue) at: A) 20 ℃ and B) 40 ℃.

Fig. 1.5 B illustrates the ζ-potential results of the system at 40 ℃. A similar profile to the 20 ℃ case is observed, but the plateau (~50 mV) is reached with the addition of less PAH. Only 5 % of PAH 140 kDa is needed to achieve the highest potential values, whereas for 15 kDa and 50 kDa the plateau is reached at 30-40% and 10-15%, respectively. Based on the evolution of the microgel size and ζ-potential with the concentration PAH of different molecular weight, we can hypothesize that the low-molecular-weight polyelectrolyte can be incorporated inside the microgel with a high loading capacity, reaching up to a 160% increase in mass through incorporation of PAH. The loading capacity of the microgel (the capacity of the microgel to associate with the PAH without destabilizing and precipitating) decreases when the molecular weight of PAH increases, 80 % for PAH 50 kDa and only 40 % for PAH 140 kDa. Based on the comparison of ζ-potential values, we can argue that PAH accumulates more on the particle surface when its molecular weight increases, preventing its incorporation inside the microgel particle. Due to pore size considerations, the penetration of 50 kDa PAH into the microgel is limited and even more so in the case of 140 kDa PAH. Also, adding PAH with the highest molecular weight results in a plateau in ζ-potential at much lower amounts of PAH added, though yielding higher ζ-potential values due to overcompensation of charges in the microgel. Conversely, low-molecular-weight PAH is able to penetrate into the microgel, compensating internal charges in the microgel. The large sizes observed at 5 % PAH for 50 kDa and 140 kDa PAH evidence that PAH is depositing on the surface rather than being loaded inside the hydrogel, and that at low concentrations PAH is not fully recharging the microgel surface, causing aggregation.

CLSM and Flow cytometry studies of PAH internalization.

To gain further insight into the location of PAH in the microgel, we exposed the microgels to fluorescently labelled PAH 15, 50 and 140 kDa and imaged them using Confocal Laser Scanning microscope (CLSM) (Figure 1.6). From CLSM images we expect to discriminate if the PAH is located on the surface of the hydrogel particles or is distributed inside them. Figure 1.6A illustrates a micrograph of a microgel with 30% of labelled PAH 50 kDa. This micrograph shows that the hydrogel particles lose volume to a greater extent than the changes in the hydrodynamic radii observed with DLS. Since the hydrogel displays diameters below 500 nm, it is not possible to determine the location of the labelled chains. A homogenous distribution of fluorescence in the particles in presence of the labelled PAH is observed. Images taken at 20°C and 40°C do not show significant differences. In order to confirm that the interaction between the microgel and PAH is restricted to the negatively charged methacrylic acid group, core-shell microgels were prepared. In contrast to random co-polymerization, in the core shell microgels the core was synthesized only with the NIPAm monomer, while NIPAm and MAA monomers were used for the shell.

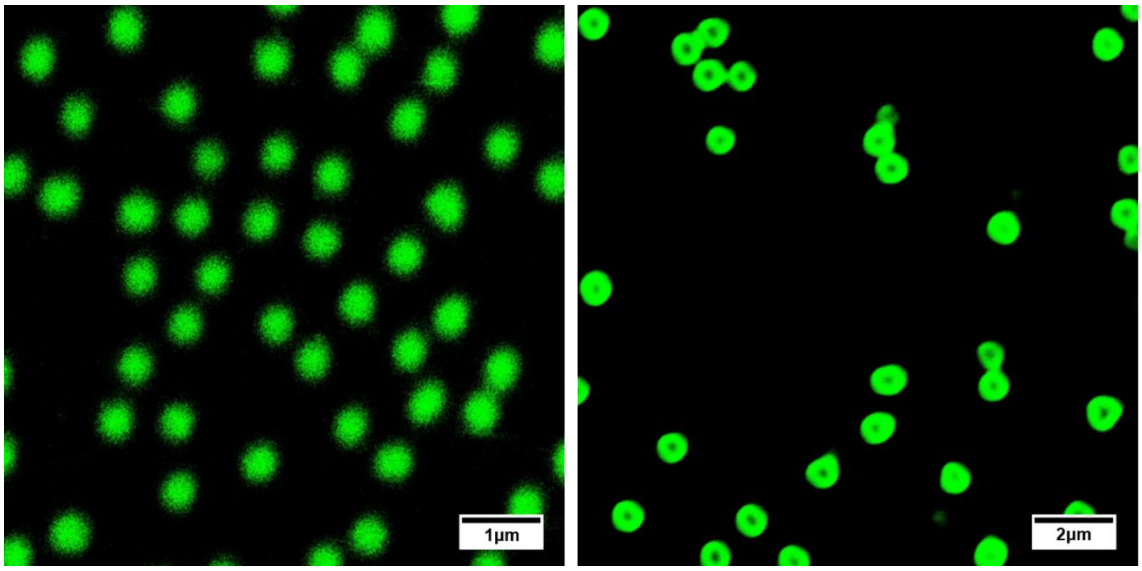

Figure 1.6. Confocal micrographs for: left) random microgel, right) core-shell microgel when they are in contact with 50 kDa G-PAH at 30% of concentration.

Flow cytometry studies were done in order to quantify the G-PAH uptake by the microgels (Fig. 1.7). Flow cytometry allows for the measurement of fluorescence per hydrogel particle as a function of the concentration of labelled PAH in bulk. In these experiments, the microgel was exposed to an increasing amount of labelled PAH 15 kDa and 50 kDa. Experiments were not performed with PAH 140 kDa to avoid instrumental problems, due to the low stability of the formed complexes and precipitation issues. Figure 1.7a and 1.7b display the maximum intensity of hydrogel dispersion as a function of increasing. For PAH 15 kDa the normalized intensity increases to 30-35 % of PAH addition in microgel dispersion. Above 35 %, the normalized intensity appears to remain constant with increases of PAH in the system.

For PAH 50 kDa, the plateau is reached before, and the normalized intensity does not change above 10% PAH.

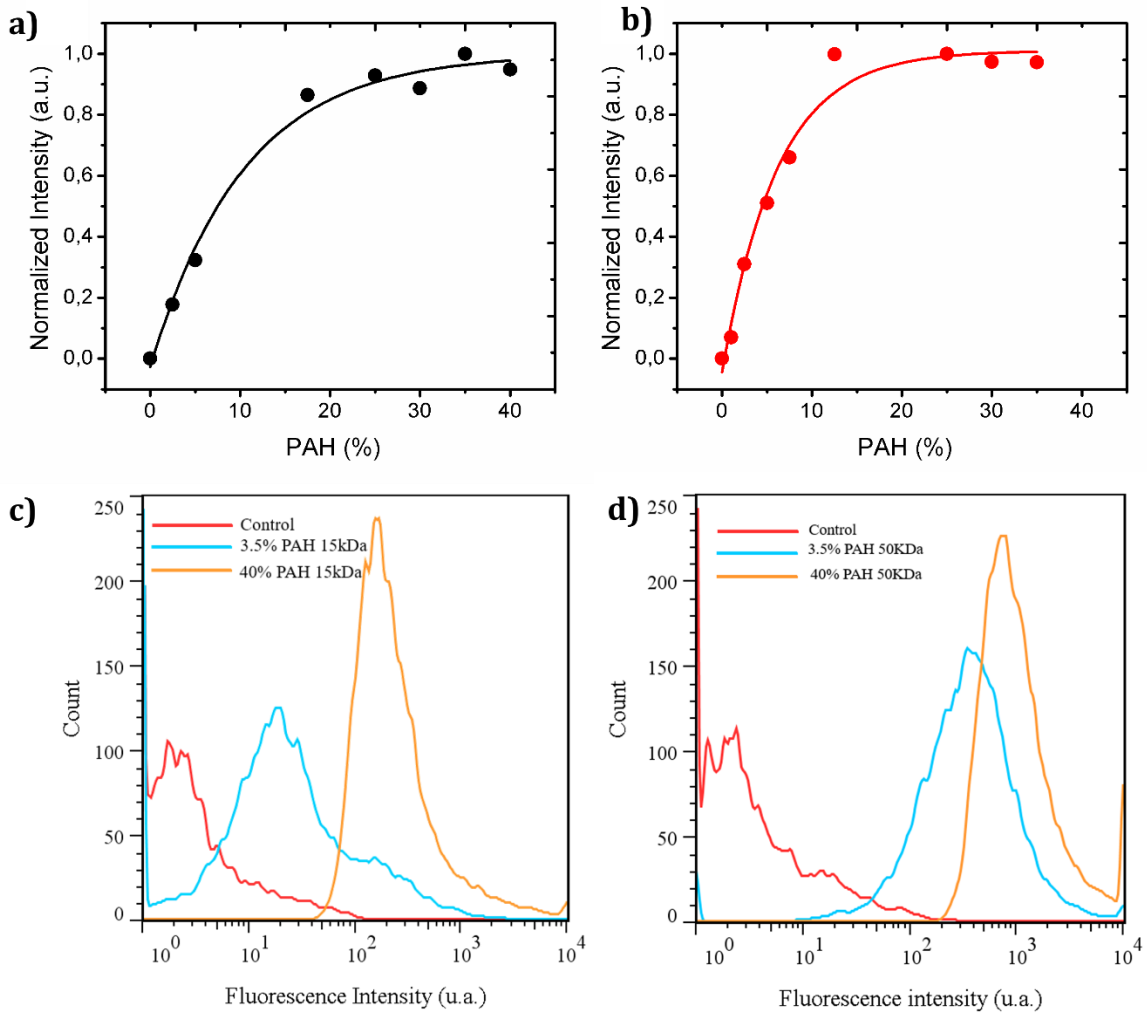

Figure 1.7. Intensity maximum of hydrogel dispersion vs the addition of G-PAH of: a)15 kDa (black) and b)50 kDa (red). Fluorescence intensity vs microgel number distribution for microgel without labelled PAH (control) and microgel with 3.5 % and 40 % of G-PAH C) 15 kDa and D) 50 kDa.

Flow cytometry data are in agreement with ζ-potential and DLS measurements and confirm that 50 kD PAH remains, at least partially, on the hydrogel surface, while PAH 15kDa is able to accumulate inside. This difference in uptake behaviour between the two MW PAH is indicative of the large PAH chains being stopped by the pore sizes in the hydrogels. However, it cannot be concluded that, for 50kDa, chains are only located on the surface of the hydrogel. 50kDa is an average weight, and there are smaller chains present that could get into the core. In addition, the interface of the hydrogel has fuzzy characteristics, and pores may change size from the surface to the inner core, so a partial penetration of PAH chains may also be possible.

Doxorubicin Release in the Presence of Polyelectrolytes

As mentioned in the introduction chapter, microgels are used as drug delivery systems due to their capacity to load and release drugs in response to a stimuli.[204,220] Since microgels are able to transport positively charged drugs , we chose as a model drug, doxorubicin (DOX) which is not only positively charged, but also fluorescent.

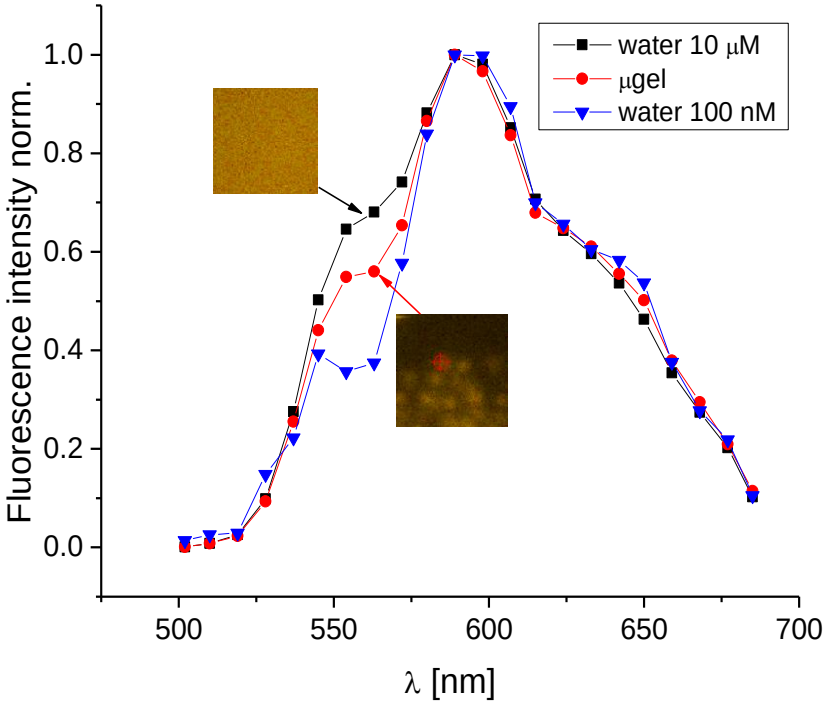

Figure 1.8. Normalised fluorescence emission for DOX: in water at concentrations of 10 μM (black) and 100 nM (blue), respectively and inside the microgel (red) obtained by CLSM.

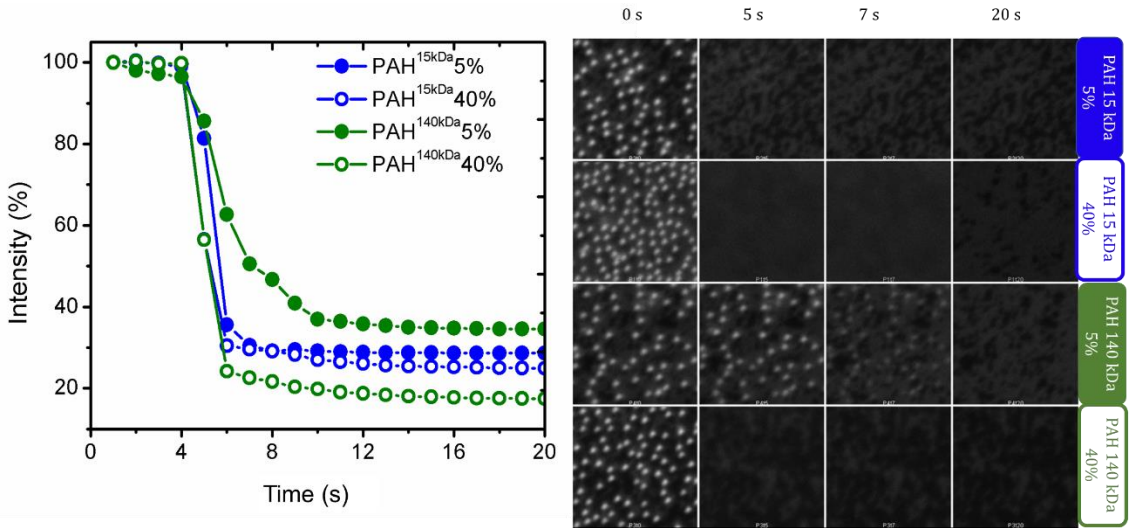

Figure 1.9. Release the DOX by the presence of different MW PAH: 15kDa in blue and 140 kDa in green. On the left, fluorescence emission at the wavelength of maximum intensity as a function of time. On the right, confocal micrographs of microgel pre-loaded with DOX at different exposure times: 0, 5, 7, and 20 seconds.

Fig. 1.9 (left) shows the variation in fluorescence emission at 20 °C as a function of time for the microgels preloaded with DOX after the addition of 5 % and 40 % of PAH 15 kDa and 140 kDa. The results show that independently of the PAH concentration, 5 seconds after the addition of PAH, the fluorescence intensity of DOX decreases.

Independently of the concentration of PAH the fluorescence intensity of the microgels loaded with DOX reaches its minimum after 5 seconds. The change in fluorescence intensity after the addition of PAH 140 kDa reveals a slower replacement of DOX, more dependent on the PAH concentration. For 5 % PAH 140 kDa, the fluorescence intensity decreases to 35 % 10 seconds after the addition of PAH. However, for 40 % PAH 140 kDa, the fluorescence intensity decreases to 20 % after 6–8 seconds of exposure to the polymer. The differences observed in the decrease in fluorescence depending on the PAH molecular weight and concentration hint at different kinetics in the release of pre-loaded doxorubicin in the microgel.

Fig. 1.9 right shows the confocal micrographs of the microgel pre-loaded with doxorubicin at different exposure times, 0, 5, 7, and 20 seconds with 5 % and 40 % of PAH 15 kDa and 140 kDa. For 5 % PAH of 140 kDa, the hydrogels still show fluorescence 7 seconds after the addition of the polymer. It is likely that in this case the penetration of PAH 140 kDa inside the microgel is limited, but then increases as the polymer concentration increases. It is worth highlighting that the decrease in intensity is not homogeneous among all microgels.

Fluorescence Lifetime Imaging (FLIM) was applied to study if the interaction of spermidine and spermine with hydrogels loaded with DOX also leads to the drug replacement. Both spermine and spermidine are positively charged with a few amines, 3 and 4, per chain. They can diffuse more easily in the hydrogels than PAH, but at the same time they can only interact with a few carboxylate groups and therefore their interaction with the hydrogel and capacity to replace DOX is expected to be more limited.

The fluorescent lifetime of DOX is sensitive to the polarity of the surrounding environment. Lifetime values of 1 ns are typical for free DOX in water solution meanwhile lifetime increment correspond a hydrophobic media i.e. conjugated.[221]

Fig. 1.10 shows the lifetime of DOX in solution, in the microgel, and in the presence of two concentrations of spermine (in and out of focus). As a control, the lifetime of DOX (10^{-5} M) in water is measured. A lifetime for DOX in water of 1.04 ns was measured, in agreement with that reported in literature.[221] Lifetime imaging of encapsulated DOX was performed inside the microgel (in focus) and on the microgel surface (out of focus). Subsequently, spermidine, 2.5 % and 40 % was added to the microgel solution and DOX lifetime imaging performed, again in and out focus. All the lifetime graphs were analysed applying a two components fitting model.

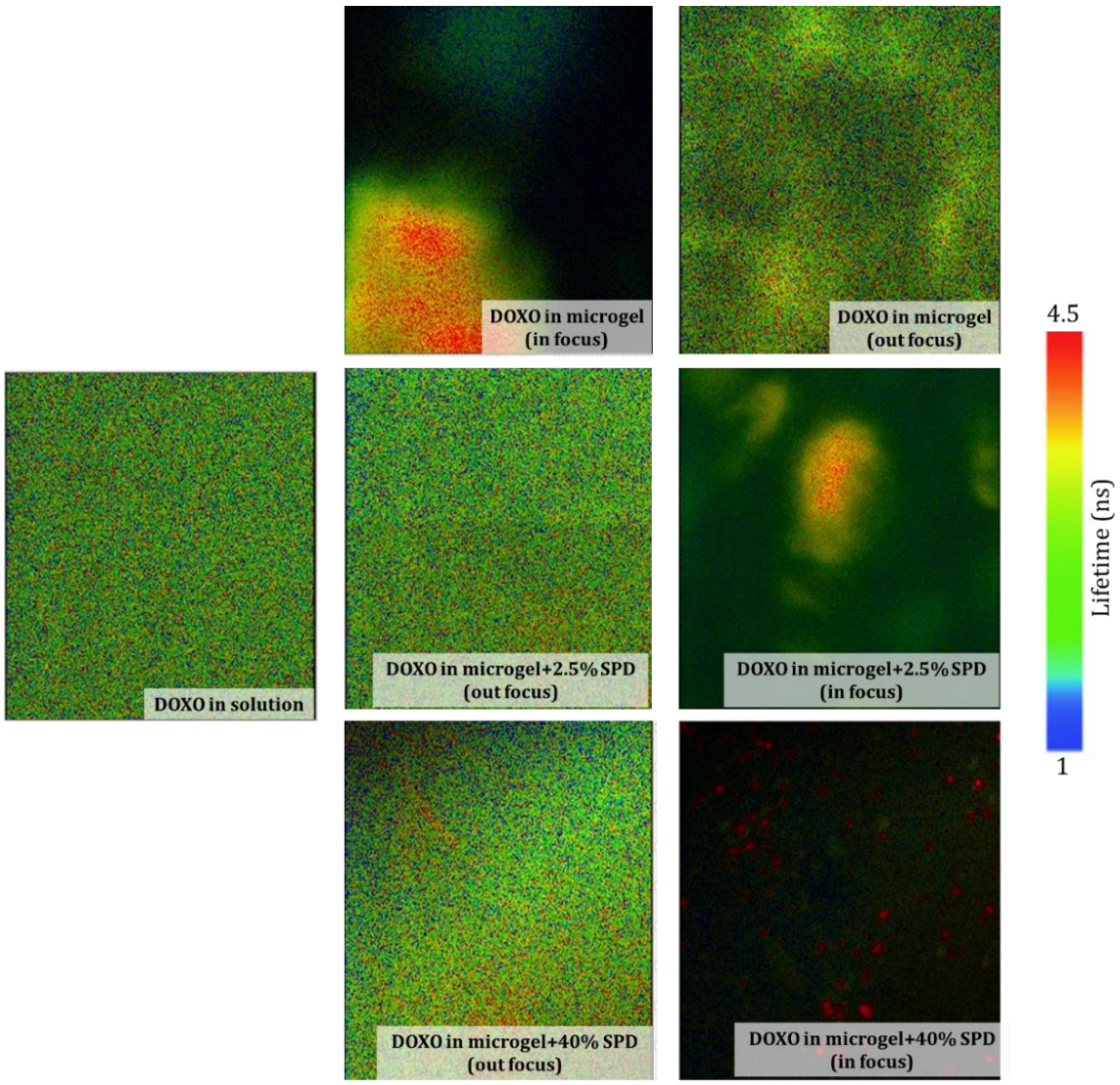

Figure 1.10. FLIM results for DOX in solution and in the microgel in the presence, or absence, of different amounts of spermidine (SPD) lifetime.

When we focus inside the microgel, the lifetime obtained is 1.4 ns, which is higher than the lifetime of free DOX in water, revealing that DOX is in a different environment, i.e. not dissolved in water and interacting with the hydrogel. Moving to the surface of the microgel (out of focus) the lifetime obtained is 1.1 ns which indicate a more hydrophobic environment than water, but less than inside the microgel. The addition of spermidine, 2,5 %, induces a change in the amount of DOX associated to the hydrogels and free DOX, which can be estimated by the fractional contribution of the different lifetime components of DOX. Out of the focus, 97% of DOX is in solution with a lifetime of 1.04 ns meanwhile 3% reports a lifetime of 2.99 ns, probably due to the association of DOX with the microgel. Focusing inside the microgel, two components are also recorded, one of them with a lifetime of 1.4 ns (66%) corresponding to the DOX inside the microgel but facing a more polar environment, i.e. water or associated to carboxylate groups, and a second component, 4.3 ns (34%), typical of a hydrophobic environment. The increase in DOX lifetime due to the

presence of spermidine indicates a change in the polarity of the microgel as a result of the compensation of negative charges of hydrogel by the positively charged spermidine. The amount of DOX in solution does not change with an increasing concentration of spermidine. At 40 % spermidine the same results as at 2.5% spermidine were obtained, most of the DOX is free in solution (98%) and only 2% is in a different environment (2.90 ns). However, inside the microgel, 15% of the DOX is in a hydrophobic environment (3.34 ns), with remaining fraction reporting a lifetime similar to that for DOX on the surface of the microgel (1.1 ns).

Experiments were also conducted with spermine which also replaces DOX in the microgels (Fig. 1.11). Before adding the spermine, inside the microgel we observe a lifetime of 1.5 ns, which is similar to the previous results. Outside of the microgel, the lifetime of the drug is 1.0 ns meaning the DOX is free in solution.

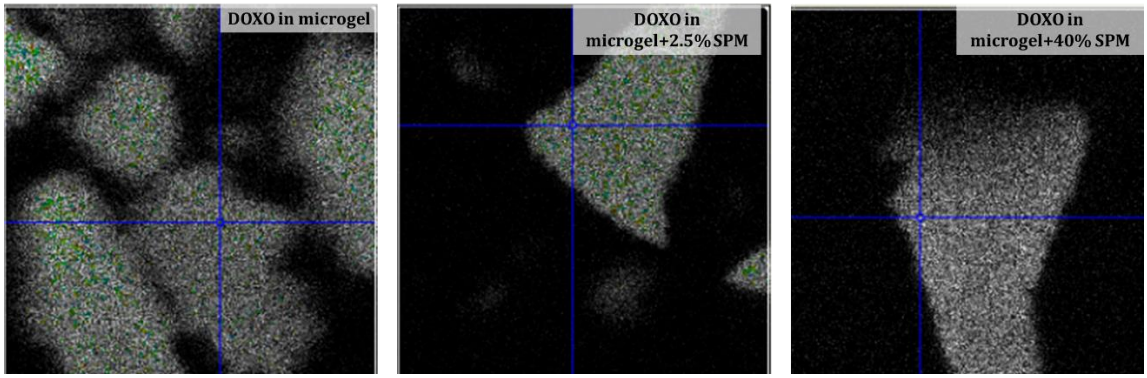

Figure 1.11. FLIM results for DOX in solution and in the microgel in presence or absence of different amount of spermine (SPM).

After adding 2.5% w/w of spermine to the microgel dispersion we observe two lifetime components inside the microgels. 89% of DOX is present with a lifetime of 1.77 ns while the rest has a lifetime of 1 ns for the component characteristic of the free DOX. Out of focus, at the surface of the microgel, the lifetime obtained was 1.5 ns, suggesting that the DOX is associated to the surface of the particles, but facing an aqueous environment. Increasing the amount of spermine to 40% w/w the hydrophobicity of the hydrogel increases and 48.7 % of the DOX inside shows a lifetime of 1.4 ns and a 51.3 % a lifetime of 3 ns.

1.4. Conclusions

We have shown that P(NIPAm-co-MAA) microgels and PAH chains interact in a complex way, which depends on both the molecular weight of the polymer and temperature. We observe different trends in the size and ζ-potential of hydrogels in the presence of PAH, which suggests that at 20 °C there is accumulation of PAH inside the hydrogel for PAH of low MW, 15 kDa, and deposition of PAH on top of the hydrogel surface for high MW, 50 and 140 kDa. The interaction between the microgel and PAH is also highly affected by the LCST, above which there is accumulation of positive charges on the microgel surface. Above the LCST, the partial segregation of the MAA

moieties to the surface leads to PAH accumulation on the surface of the hydrogel for all MWs of PAH considered. PAH molecules preferentially replace doxorubicin complexed to the MAA inside the microgel. Though the kinetics and extent of removal of doxorubicin depends on the molecular weight and concentration of PAH the phenomenon can be observed for all MW and concentrations of PAH employed. This observation implies that for PAH 140 kDa there is partial penetration of the polymer chains in the microgel. For smaller polyamines, spermine and spermidine, the removal of doxorubicin from the hydrogel is not as complete as for PAH behaviour.

Chapter 2

Kinetics of the thermal response of poly(N-isopropylacrylamide co methacrylic acid) hydrogel microparticles under different environmental stimuli: A time-lapse NMR study

2.1. Motivation

Microgels based on poly(*N*-isopropylacrylamide) (PNIPAm) exhibit a VPT at 30-32°C, the so-called nominal lower critical solution temperature (LCST).[222] Below this temperature the microgel particles are in a swelling (hydrated) state and the interactions monomer-solvent prevail. Above this temperature, the hydrogen bonds between the cross-linked PNIPAm chains and water break, resulting in a drastic microgel particle size decrease[223] to the deswelling (dehydrated) state. Micro- and nanogels with a transition temperature near physiological conditions have drawn increasing attention due to their potential application in sensing,[200,224,225] regenerative medicine,[226] and drug delivery.[227–229]

For drug delivery applications, below LCST PNIPAm based hydrogels provide an environment suitable for the encapsulation of hydrophilic and charged drugs, since PNIPAm is highly solvated in water by hydrogen bonding interactions (although it itself is practically not charged). However, to improve the loading capacity and retention of charged drugs in PNIPAm-based microgels it is often necessary to introduce ionic co-monomers into the PNIPAm network.[230,231] Microgels formed by copolymers of PNIPAm and methacrylic acid (MAA), poly(N-isopropylacrylamide-*co*-methacrylic acid) (P(NIPAm-*co*-MAA)), retain the thermoresponsive characteristics from PNIPAm while the negative charges of MAA can complex positively charged drugs.[232] The carboxylate groups also bring pH sensitivity to the system. Small changes in pH can have a large effect on the LCST of the hydrogel. This feature can be useful for drug delivery, where physiological temperature and local pH differences can both act as stimuli to facilitate molecular switching over a desired pH range.

The presence of carboxylate groups in P(NIPAm-*co*-MAA) hydrogels can significantly alter the hydration of the hydrogel.[233–235] Indeed, carboxylate groups in MAA are

known to be highly hydrated and their hydration largely depends on pH. At acidic (low) pH, the protonation of the carboxylates reduces hydration while at basic pH, hydration is increased.

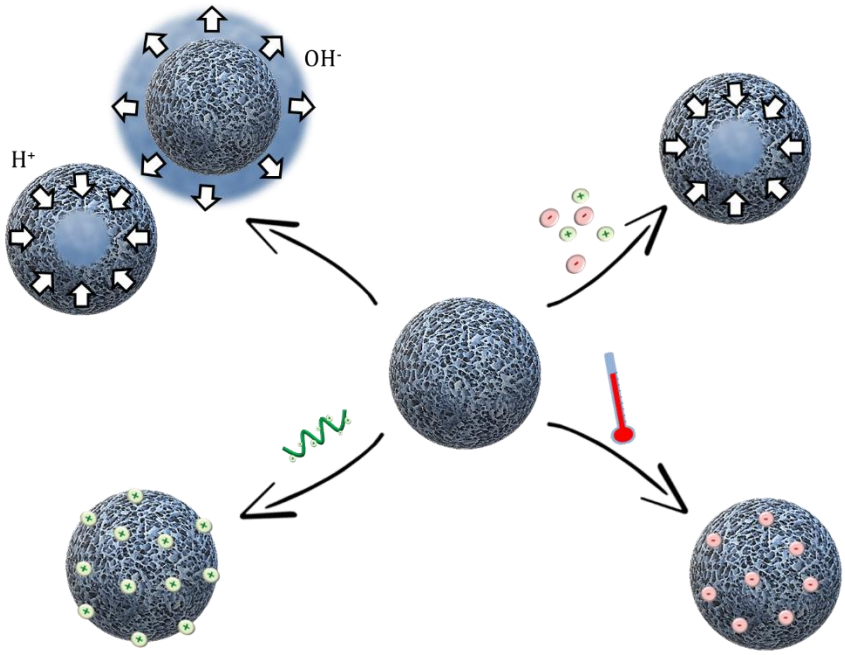

Figure 2.1. P(NIPAM-co-MAA) hydrogel behaviour to environmental stimuli: pH, ionic strength, polyamines or temperature.

The complexation of the carboxylate groups with positively charged molecules can alter their hydration and depending on the nature of the positively charged molecules (i.e., primary amine, quaternary ammoniums, or small or large molecular weight), the effect on dehydration may be more or less pronounced. Hydration of carboxylate groups can also be affected by the ionic strength, which can screen charges in carboxylates and weaken hydrogen bonding with water. Carboxylates can also form hydrogen bonds with the NIPAm monomers, altering their hydration as well.[236]

Overall, the variations in water content in the hydrogels, through the hydration of carboxylate groups triggered by changes in pH, ionic strength, or the presence of oppositely charged molecules, should affect the environment of NIPAm monomers and their thermal transition from a hydrophilic to a hydrophobic material.

Nuclear magnetic resonance (NMR) spectroscopy is one of the most powerful methods to study thermoresponsive polymers, and in particular the VPT.[237] Since NMR is very sensitive to polymer dynamics and the local chemical environment of studied nuclei, the coil-globule transition at LCST can be clearly observed in NMR spectra and it is possible to trace its evolution over time. Accordingly, comprehensive analysis of NMR data provides a thorough picture of the rearrangement of polymer chains at the molecular level, which makes this approach unique in comparison to commonly used light scattering techniques. Indeed, there are a number of studies that

exemplify the exceptional efficiency of NMR methods for monitoring thermoresponsive materials.[238–241]

To study the impact of the MAA groups on the phase transition of NIPAm hydrogels at the molecular level, we performed time-lapse NMR measurements,[242–245] which allowed us to follow the evolution of the NMR signal over time with changes in temperature. As temperature increases over the phase transition, NIPAm dehydrates becoming a more solid-like material with limited conformational degrees of freedom. Dehydration thus leads to a decrease in the overall chain dynamics and accordingly to an increase in residual dipolar coupling. Consequently, the NMR signal decays faster due to a substantially reduced spin-spin relaxation time (T_2). A significant fraction of immobilized protons generates extremely broadened NMR signals which are beyond detection by conventional high-resolution NMR probes. Therefore, eventually an apparent signal intensity drop can be observed during VPT. By tracing changes in the intensity of the NMR signal with time sweeping temperatures from 25 to 40 °C, we were able to study the kinetics of swelling and deswelling of P(NIPAm-*co*-MAA) hydrogels at different pH values and ionic strengths, and in the presence of small positively charged molecules such as doxorubicin; medium-sized oligomers like spermine and spermidine; or larger polymers such as PAH or polydiallyldimethylammonium chloride (PDADMAC).

Time-lapse NMR studies provide insight into the molecular changes in the P(NIPAm-*co*-MAA) hydrogel during temperature collapse and show how the presence of negatively charged and highly hydrated carboxylate groups impact collapse at the molecular level. To our knowledge, this is the first time that time-lapse NMR has been used to study the temperature-induced collapse of a PNIPAm hydrogel co-polymerized with a second monomer, in this case MAA, that conveys additional sensitivity of the system to environmental conditions, especially pH and the interactions with polyamines. Time-lapse NMR provides unique information on the polymer chain dynamics during hydrogel collapse and shows how the phase transition is affected by various environmental stimuli, which cannot be assessed by other means.

In this chapter, time lapse RMN measurements were performed from 25°C to 40°C in order to study the hydration kinetics of P(NIPAm-co-MAA) hydrogel. For that purpose, different pH, ionic strength values and positively charged molecules as doxorubicin (DOX), spermine, spermidine, polyallylamine hydrochloride (PAH) or polydiallyldimethylammonium chloride (PDADMAC) were used in this thesis.

2.2. Experimental Section

2.2.1 Materials

N-isopropylacrylamide (NIPAm, 97%), N,N'-methylene-bis-acrylamide (BIS, 99%), sodium dodecylsulfate (SDS), ammonium persulfate (APS, 98%), methacrylic acid (MAA, 99%), polyallylamine hydrochloride of 15 kDa (PAH 15 kDa), polyallylamine

hydrochloride of 50 kDa (PAH 50 kDa), doxorubicin hydrochloride 98.0-102% (HPLC), polydiallyldimethylammonium chloride average (high molecular weight 20%wt in H2O, PDADMAC), spermine tetrahydrochloride, spermidine trihydrochloride, sodium chloride (NaCl), hydrochloric acid (HCl),), sodium hydroxide (NaOH) and deuterium oxide (D_2O 99.8%) were purchased from Sigma Aldrich. Poly-allylamine hydrochloride of 140 kDa was obtained from Alfa Aesar.

2.2.2 Hydrogel synthesis

P(NIPAm-co-MAA) hydrogels were obtained via free-radical precipitation polymerization.[246] In a 100 mL milliQ water solution, 16 mmol of NIPAm, 0.14 mmol SDS and 0.31 mmol of N,N'-methylene-bis-acrylamide (BIS) were dissolved and heated up to 70°C under magnetic stirring and N_2 bubbling during 1 hour. Then, 2.12 mmol of MAA was added and stirred for 10 min. To start the reaction, 0.26 mmol of APS solution was introduced to the mixture which was kept during 3 hours under magnetic stirring. Following the synthesis, hydrogels were collected by centrifugation and washed with milliQ water three times.

2.2.3 Samples characteristics

In all samples the microgel concentration was 1 $mg \cdot mL^{-1}$ in water for DLS, or deuterated water for NMR experiments. pH was varied by adding HCl or NaOH, 1 M in D_2O, until the desired pH was obtained. PAH, PDADMAC, spermine or spermidine were added to the hydrogel solutions at 20% of hydrogel mass. The pH was measured with a pH meter. The hydrogel solution was transferred to the NMR tubes using a syringe.

2.2.4 DLS characterization

The hydrogel size and ζ- potential at different conditions was studied by dynamic light scattering (DLS). The experiments were performed in a Malvern ζ-Sizer Nano ZS in backscattering mode with a 173° scattering angle. All the samples were prepared as mention before (section 2.2.3.) and introduced by a syringe in the cuvette. All the samples were done by triplicate, using the temperature control at 25°C and 40°C and waiting 20 minutes at the indicated temperature before measurement.

2.2.5 Time Lapse NMR studies

Sample preparation was the same as in the DLS experiments and introduced in 5 mm NMR tube by a syringe. The NMR equipment used is an Agilent NMR 400 MHz spectrometer equipped with a double channel X{^{1}H} OneNMR probe. Before the experiment was performed, the temperature inside the NMR probe was set to 40°C (above LCST) and stabilized for at least 20 min. Dry air (dew point ~ -70 °C) was used as a heating/cooling medium. Subsequently, the fully hydrated sample, having a temperature equal to 20 °C, was transferred directly to the probe using air cushion lift. The total time required to transfer the sample to the probe (using the air cushion lift) and start acquisition was approximately equal to 0.75 s. Immediately after

transfer, NMR spectra were acquired according to a predetermined time sequence. The time interval between each acquisition was 2.5 s. Short excitation pulses were applied (45°).

2.3. Results and discussion

P(NIPAm-co-MAA) hydrogels

Dynamic light scattering was used to trace the swelling behaviour of P(NIPAm-co-MAA) hydrogels. Measurements at 25 ℃ and 40 ℃ were carried out to characterize the behaviour of the hydrogel above and below its LCST. Increasing the temperature above the LCST causes the PNIPAm chains to dehydrate and interact with each other forming hydrophobic regions with a smaller volume than in the hydrated phase. As a consequence, the hydrogel decreases in size. However, since the density of charges from MAA often decreases too, the repulsion among hydrogel microparticles decreases, leading to their aggregation (Fig. 2.2).[232,247]

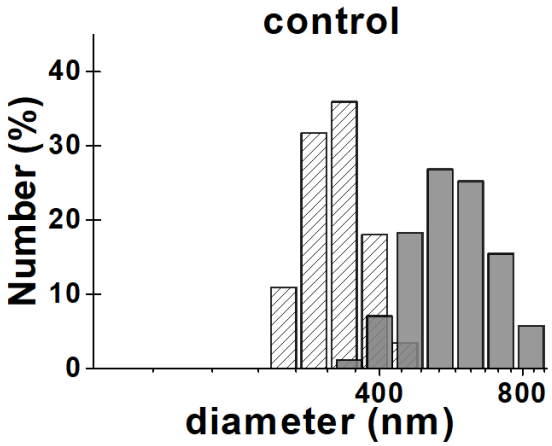

Figure 2.2. Dynamic light scattering histograms of hydrogels in water (pH 6.8). Stripe columns represent hydrogel distribution size at 25°C and for 40°C in grey.

The average hydrogel diameter is 357 ± 10 nm at 25°C but when the temperature increases to above the LCST until 40 °C, changes in size are induced.

Variable-temperature time-lapse NMR experiment[242–245] were conducted to obtain insight into the collapse and swelling/deswelling processes with temperature at molecular level in P(NIPAm-co-MAA) hydrogels, and to investigate how swelling and deswelling are affected by the presence of carboxylates.Keeping the same sample conditions as in DLS experiments but with D_2O as solvent, NMR signals were monitored from 20°C to 40°C to get information about the hydrogel P(NIPAm-*co*-MAA) collapse at molecular level studying the VPT. This information is provided by the changes in the signal of the methyl protons in the NIPAm isopropyl group marked with letter *a* in Fig. 2.3.

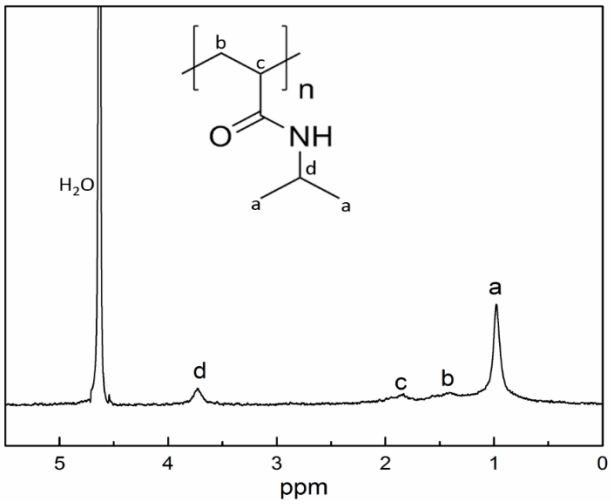

Figure 2.3. PNIPAM ^{1}H NMR spectra at room temperature.

Figure 2.4 shows the variation in the methyl protons of the NIPAm isopropyl group when the hydrogel is heating until 40°C and then cooling to 20°C.

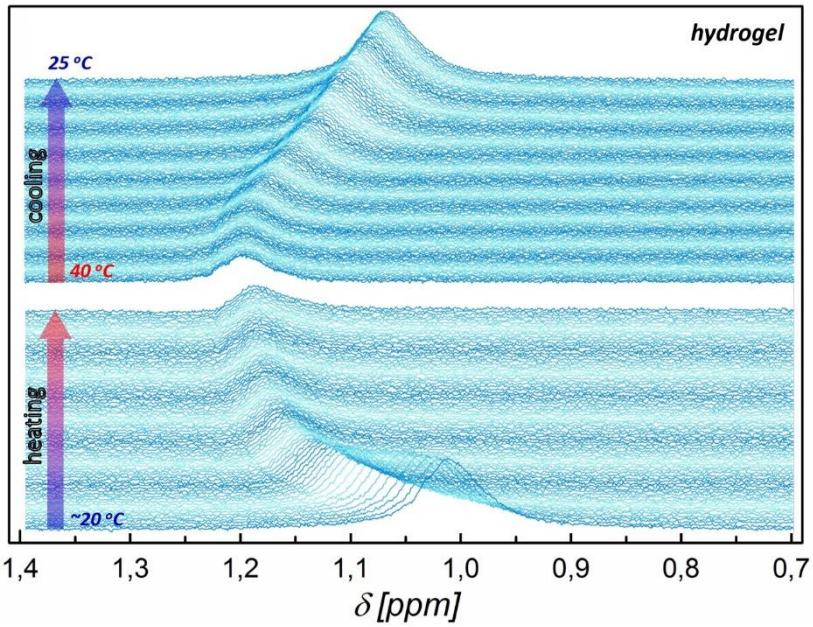

Figure 2.4. ^{1}H-NMR spectra evolution of methyl protons signal during heating and cooling experiments.

As mention before, when the hydrogel is above the LCST the polymer-polymer interactions increase and limitations in the conformational degrees of freedom are produced. This variation in amplitude of the NMR signal results from a gradual stiffening of the polymer network above LCST and accompanying reduction of spin-spin relaxation time T_2 (Fig. 2.4). In the collapsed state the hydrogel resembles a solid-like material characterized by significantly reduced polymer dynamics. Accordingly, the NMR free induction decay signal involves a fast decaying component, which is not fully accessible by high-resolution NMR probes. Consequently, an apparent decrease in signal amplitude takes place upon dehydration. This decrease can be employed to

probe the kinetics of the VPT. To prove reversibility of dehydration-hydration processes, an additional cooling experiment was performed. It is worth pointing out that the cooling experiment reveals the opposite effect of the heating experiment. Upon swelling, the intensity of the NMR signal increases indicating higher mobility of polymer chains. It is also important to emphasize that the intensity variations in NMR signal $I(t)/I_0$ observed in both cooling and heating experiments are of the same magnitude. Therefore, NMR data nicely reveal the reversibility of the VPT for the thermoresponsive gel. A chemical shift variation can also be appreciated with the variations in temperature. According to Sun et al.,[243] Tanaka et al.,[248] and Tang et al.,[245] this change is directly related to the deshielding effect upon VPT. Nevertheless, we believe that this specific phenomenon is predominantly related to the temperature dependence of the chemical shift of the lock signal[249], which is D_2O signal in this particular case. The software of the NMR equipment assigns a constant position to the lock signal, which results in the shift of the signal of the methyl groups (and other signals from the hydrogel), to the same extent as the D_2O shift. Therefore, the observed variation of the hydrogel signal position is solely apparent (Fig. 2.5).

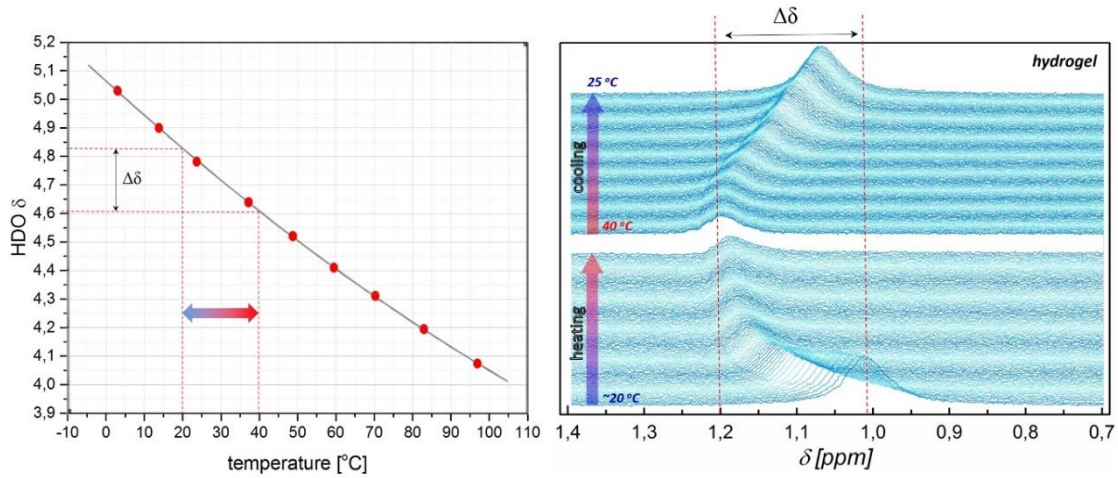

Figure 2.5.Temperature dependence of D_2O chemical shift.[250] On the right hand side the apparent NMR line shift observed for hydrogels is illustrated.

This signal is defined for each particular type of solvent and its frequency position is defaulted in the NMR software. It is well known that temperature can significantly affect the chemical shift of the solvent. Nevertheless, the NMR software does not take this effect into consideration and it invariably references to the defaulted signal position. Accordingly, one can observe an apparent shift of all NMR signals on the spectrum except the signal attributed to the solvent, which is stable. It is known that for the interval from 20 to 40°C the signal of D_2O displays a linear shift with temperature of $\Delta\delta \sim 0.2$ ppm.[250] Assuming that the shift of the methyl groups mirrors that of D_2O, it is possible to estimate the temperature variations of the sample during the time-lapse experiment.

It is worth mentioning that the cooling experiment is strongly affected by the significant heat capacity of the NMR probe. It must be considered that the NMR probes are not optimized so specific heat/cooling ramps performance is not possible. Besides their heat capacity influence the cooling experiment the reason why the heating and the cooling spectra are not symmetric. As the protocol samples preparation is the same independently the experiments, variations in heating/cooling experiments are assumed by the pH, ionic strength or polyamines.

To observe the evolution of the NMR spectra during cooling we simply switch off the heater and subsequently record the spectra until the probe reaches 25 °C. The large heat capacity of the NMR probe is manifested by the sigmoidal character of variations of the chemical shifts during cooling. In Fig. 2.5, the very first spectrum (bottom panel) represents the moment when the sample is just lifted down to the NMR probe and hence its temperature must be close to ~20 °C. Accordingly, subsequent spectra exhibit quite an abrupt change in chemical shifts and this change reveals an exponential character. The whole heating experiment lasted nearly 100 s. Before the cooling experiment was started, the sample remained in the probe for another several minutes. Therefore, the chemical shift observed in the very first spectrum from the cooling experiment (bottom panel) is slightly higher than the chemical shift observed for the very last spectrum from the heating experiment. In fact, the very first NMR spectrum from the cooling experiment represents the stage where the sample is already in equilibrium at 40°C. It is shown that the total chemical shift changes from ~20°C to 40°C equals $\Delta\delta \sim 0.2$ ppm. Assuming that our initial NMR peak position represents ~20°C we can easily recalculate the actual temperature of the sample throughout the time-lapse experiment relying on the linear dependence between temperature and D_2O chemical shift. Since there is certain finite time (~3 to 4 s) required to transfer the sample to the probe using air cushion lift and start acquisition, the initial temperature can slightly differ from 20°C. Therefore, in the figures representing evolution of the temperature versus time, there are error bars included of ±1°C.

Impact of pH in P(NIPAm-co-MAA) hydrogels

P(NIPAm-co-MAA) hydrogels are sensitive to pH due to the carboxylate groups of the MAA. The pK_a of MAA is 4.8 which means that is deprotonated at physiological pH. In acidic conditions, below its pK_a, the number of anionic charges decrease inducing a decrease in hydrogel size. Attending the DLS results at 25°C, the hydrogel size is reduced from 357 $\pm$ 10 nm (Fig. 2.6 b)) at pH 6.8 to 280.4 ± 11.31 nm (Fig. 2.6 a)) at pH 2.8. The opposite situation occurs when the pH is increased with the expansion of the hydrogel until 455.6 ± 24.5 nm (Fig. 2.6 c)). At pH 2.8 and 6.8, the size of the hydrogel increases at 40°C due to the growth of the polymer-polymer interactions that cause the aggregation except in the pH 8 data where the size remains stable. At this pH, the effect of the temperature is less dominant than in acidic conditions,

because methyl groups of NIPAm maintain the conformation dynamics avoiding the hydrogel precipitation as in other cases.

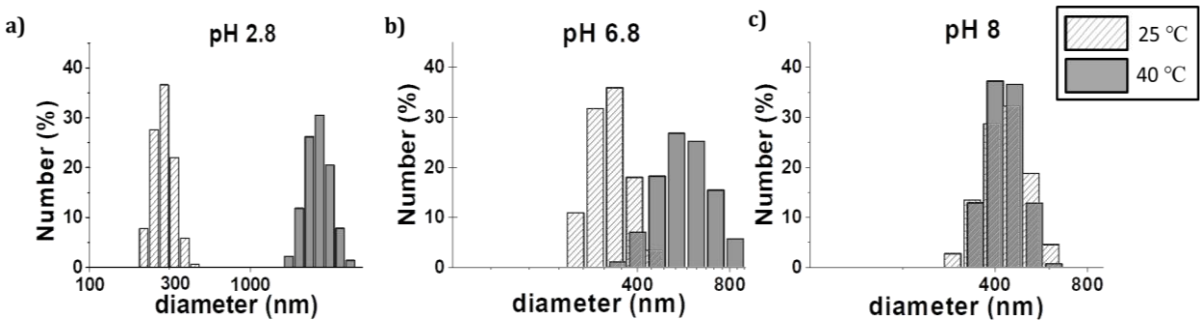

Figure 2.6. P(NIPAM-co-MAA) hydrogel DLS measurements at different pH: a) acidic pH below pKa, b) neutral pH, c) basic pH.

Similar results as in the DLS were obtained from the NMR experiments. Collapse is produced at acidic conditions below the pK_a and hydrate at neutral and basic pH (Fig. 2.6).

In Fig. 2.7 the hydrogel swelling and deswelling kinetic is represented by the $I(t)/I_0$ of methyl signal. This intensity ratio shows how fast the collapse of the hydrogel take place. The highest absolutes slope values the fastest the collapse process occurs. In the sample pH 6.8 consider as control because is the pH of the hydrogel dispersed in D_2O, the relation between intensities decrease by half in the first 50 s before remaining stable. When the pH is modified to acid values, the decay is higher (around 70%) being in the pH 2.7 faster (Fig.7 a)) after 40 s. The pH 6.3 and 6.8 samples arrive to the plateau 10 seconds later.

For pH values of 7.6 and 8 (green and blue colours I Fig. 2.7 a)), the methyl protons intensity signal is practically stable over temperature and time without significant changes from the first signal values. These results agree with those obtained in the DLS (Fig. 2.7 c)) where the size remains stable with temperature. At basic pH, the repulsion between the MAA carboxylic groups produce the size increase and higher hydrogel water content than at lower pH. The level of hydration of the hydrogel will have a direct impact on the conformational freedom of the methyl groups in NIPAM monomers. The plateau is reached at the lowest intensities for pH 2.7 at which the carboxylates are less hydrated and the water content of the hydrogel is smaller than at higher pHs.

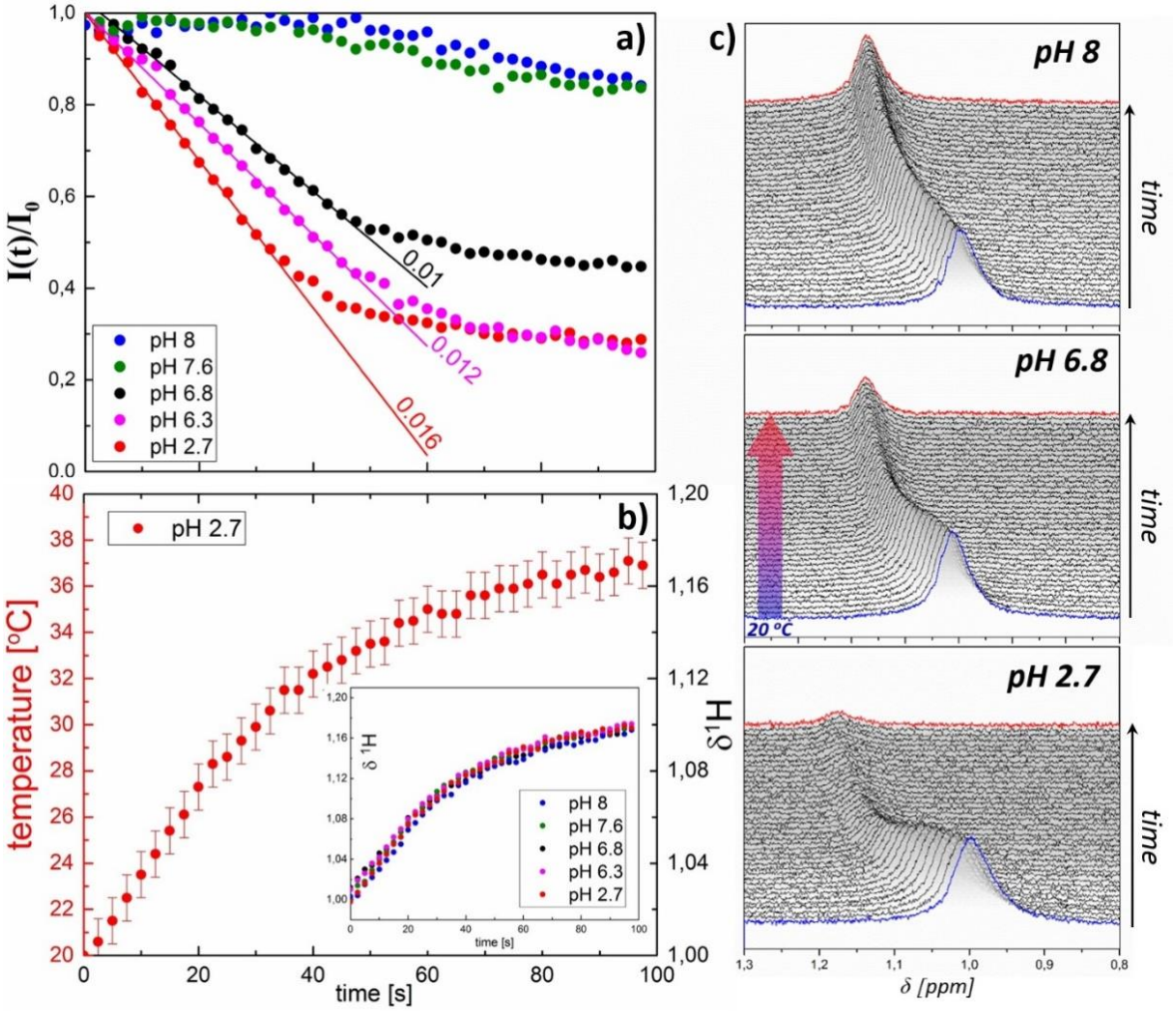

Figure 2.7. Deswelling kinetics of P(NIMPAm-co-MAA) hydrogel at different pH: 2.7, 6.3, 6.8, 7.6 and 8. a) I(t)/I₀ methyl proton signal with time. b) Temperature of the sample versus time. c) Evolution of methyl proton signal.

The *plateau* reached in the methyl proton signal evolution reveals the VPTT, where the collapse of the hydrogel is complete. $I(t)/I_0$ values decrease linearly until reaching a plateau with the exception of the very first values measured, which do not seem to follow a lineal regime. The reason for the deviation of these points from linearity is probably related to the finite heat capacity of the NMR tube. Indeed, if one looks at the initial points of the curves showing the temperature evolution in the tube they seem to follow a linear regime and not the exponential trend of the rest of the temperature curve.

Ionic strength impact

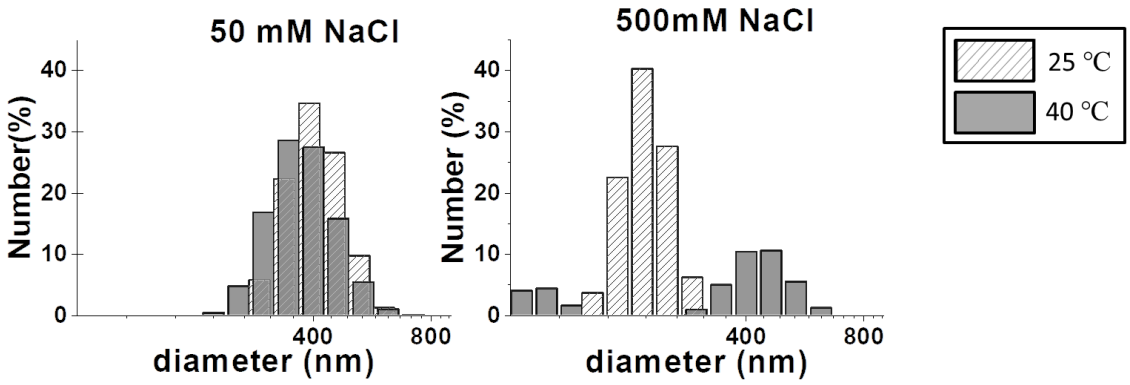

Figure 2.8. Dynamic light scattering intensity distributions of hydrogels in 50mM NaCl (left) and 500 mM NaCl (right) at 25°C (stripes) and for 40°C (solid).

The ionic strength affects in the hydration of the carboxylate groups of the P(NIPAm-co-MAA) hydrogel.[236] The increase in the ionic strength produced the shielding of the hydrogel charges meaning the dehydration of the hydrogel even its precipitation as occurs at 500 mM NaCl (Fig. 2.8).

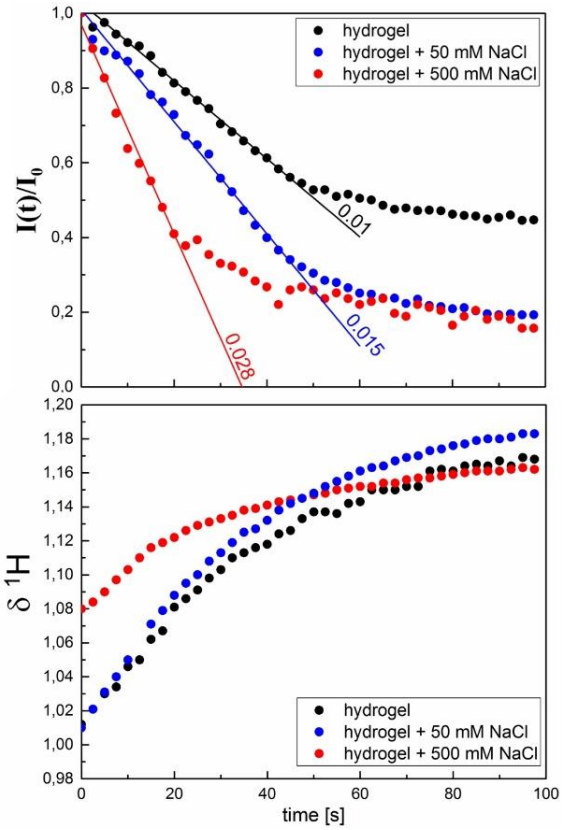

Figure 2.9. $I(t)/I_0$ evolution over time for the hydrogel dissolve in water and in the presence of 50 mM or 500 mM NaCl. The bottom graph presents the chemical shift of methyl groups in the same situation. The pH in all the samples was 6.8.

From NMR spectra, it is possible to see changes in the intensity peaks and therefore in the VPT. Although both ionic strength results arrive to the same value at 40°C the time to reach this value differs (Fig. 2.9). From the slope is possible to obtain information about the VPT kinetics. In the 500 mM NaCl solution, the slope value is higher (0.028 vs 0.015) than in the 50 mM and faster (20 s vs 60 s).

At the higher ionic strength, we expect the hydrogel to be less hydrated at room temperature, which would account for the faster kinetics. Increasing ionic strength decreases the charge of the hydrogel and consequently the hydration of carboxylates. The ionic strength can also alter the hydration shell around the NIPAm monomers, which may account for the more effective dehydration than with pH. Indeed, we observe a significant difference for the time at which the *plateau* starts between 50 and 500 mM NaCl, which must be associated with a lower phase transition temperature for 500 mM NaCl as it could be expected that the larger the salt concentration, the more the formation of hydrogen bonds between NIPAm and water molecules will be reduced. We cannot estimate in this case the temperature from the shifts of the methyl groups as the evolution of the chemical shifts with time does not follow the same trend as for the samples in D_2O and 50 mM NaCl. The reason for the completely different chemical shift variation here is the modified temperature dependence of the chemical shift for D_2O due to the presence of a relatively large concentration of salt. In the case of 50 mM NaCl the shifts follow the same trend as D_2O without addition of NaCl. There is practically no shift for the temperature at which the plateau starts in 50 mM NaCl. Results at 500 mM NaCl may be affected by a change in the heat capacity of D_2O at this salt concentration. Further experiments are needed to have a clearer picture of the response of the hydrogels with high ionic strengths.

Hydrogel-polyamines interactions

As we noticed in previous studies,[116] the P(NIPAm-co-MAA) response in deswelling depends on the molecular weight (MW) of the hosted molecules. Aiming to establish a relationship between MW of the polyamines and their influence on the swelling state of the hydrogels we studied polyamines of different MW: spermine (348.18 g/mol), spermidine (254.63 g/mol), PAH (15 kDa, 50 kDa and 150 kDa) and PDADMAC (450 kDa) (Fig. 2.10).

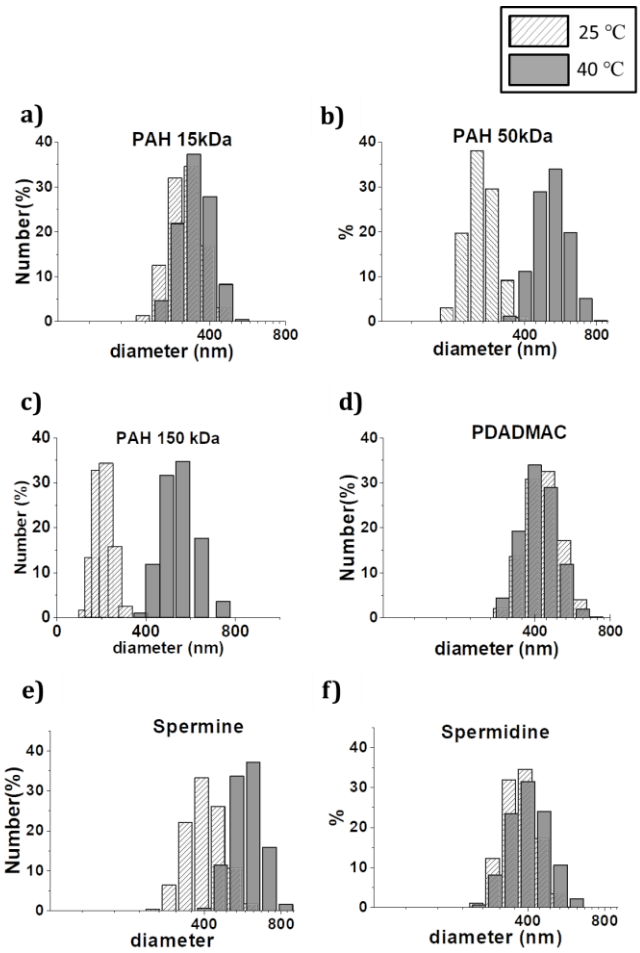

Figure 2.10. DLS results of hydrogel in presence of: a) PAH 15 kDa, b) PAH 50 kDa, c) PAH 150 kDa, d) PDACMAC, e) Spermine, f) Spermidine at 25°C (stripes) and 40°C (grey).

At 20% in hydrogel weight polymer concentration, PAH 15 kDa is inside the hydrogel[116] and no changes were observed in the hydrogel size above and below the LCST. The hydrogel possesses negative charge due to the carboxylic groups of the MAA that interact with the amine groups from the PAH. The absence of size changes is explained considering that PAH is acting as electrostatic crosslinker avoiding the hydrogel collapse. Several carboxylate groups in the hydrogel complex with one PAH chain, which limits the hydrogel collapse. For 50 kDa PAH, in addition to the diffusion of PAH inside the hydrogel, there is also deposition of the polymer on the hydrogel surface. In these conditions, the complexation of carboxylate groups is less pronounced, and the hydrogel can change size.

For microgels exposed to PDADMAC is possible to observe that DLS at 25°C and 40°C Fig. 2.10d) is practically the same, which can be interpreted as a result of PDADMAC acting as electrostatic-crosslinker. After interaction with spermidine (Fig. 2.10f)), a low molecular weight, microgels show a similar DLS behavior as PDADMAC, practically no changes in size with temperature. This behavior can again be understood as the small cationic molecule entering in the hydrogel and acting as an electrostatic-crosslinker that restricts changes in the microgel. In case of spermine

(Fig 2.10e)), also a small cationic molecule but with four amine groups, we observe that the sizes of the hydrogels at 25°C are smaller than for spermidine. We interpreted this as the spermine having a more dehydrating effect on the hydrogel due to a larger number of amines interacting with carboxylates. When the hydrogel with spermine collapses at 40°C the size of the hydrogel increases as a result of additional aggregation.

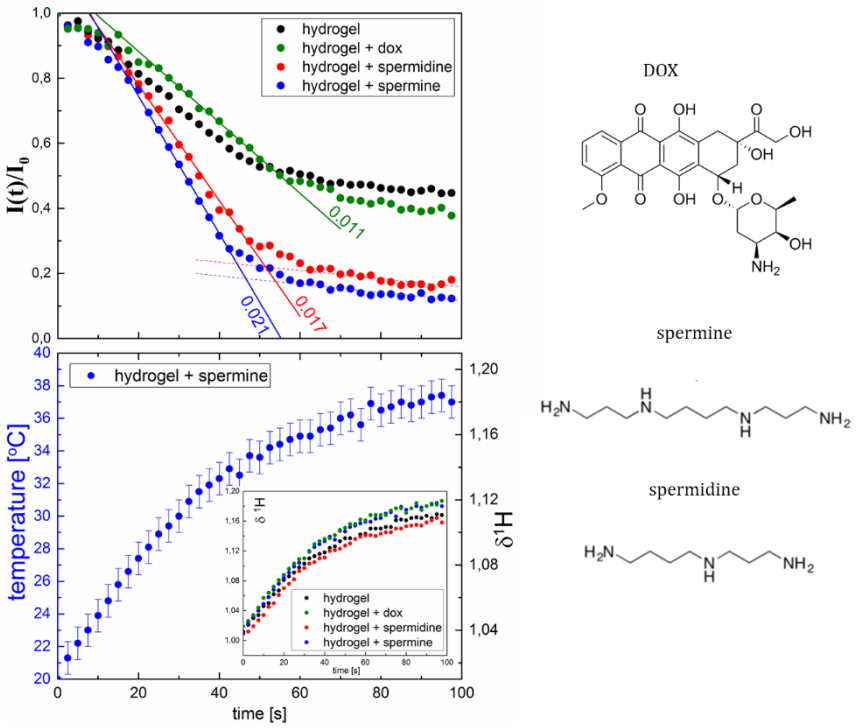

Figure 2.11. Dehydration kinetics observed for PNIPAm microspheres in the presence of a small positively charged molecule (doxorubicin) and medium-sized oligomers (spermidine and spermine). Top, dotted lines show the evolution of the I(t)/I₀ of the methyl proton signal over time for the hydrogel alone, and in the presence of doxorubicin, spermidine and spermine. All experiments were recorded at pH 6.8. Bottom, temperature of the sample versus time for the hydrogel with spermine. The inset graph represents the chemical shift variation over time for all samples presented in top figure.

P(NIPAm-co-MAA) hydrogels have potential applications in drug delivery of positively charged drugs, which can be complexed to carboxylate groups present in the hydrogel. Doxorubicin, a widely studied chemotherapeutic agent, is positively charged and can be encapsulated in the hydrogels by electrostatic interactions. We performed deswelling/swelling experiments with time-lapse NMR after doxorubicin encapsulation. In these experiments, neither the decay of intensity over time of the hydrogel nor the phase transition temperature are affected, indicating that doxorubicin does not change the hydration environment of the methyl groups of PNIPAm, and their rotational freedom is not affected (Fig. 2.11). A very different situation is observed for spermidine and spermine, which are molecules of intermediate MW displaying 3 and 4 amine groups, respectively. These amine groups permit both spermidine and spermine to interact with more than one carboxylate group at the same time. Indeed, spermidine and spermine can complex several carboxylates restricting their mobility; however, these molecules should not have a

direct impact on the methyl groups of PNIPAm. Most likely the spermine and spermidine also have a dehydrating effect on the carboxylates, reducing water content in the hydrogel, and we cannot rule out the possibility that the amines of the two molecules do not form hydrogen bonds with NIPAm monomers, altering their mobility. Therefore, we observe a decrease of up to 80% of the original signal (Fig. 2.11), comparable with the decrease in intensity seen when increasing the ionic strength. Spermine induces a slightly larger decrease in intensity than spermidine. This is probably due to the presence of one additional amine group in spermine which can link more carboxylate groups in the hydrogel resulting in effectively greater conformational freedom of the methyl group than spermidine. Practically no shift for the starting temperature of the plateau can be observed, which can be understood as none of the two molecules interacting directly with NIPAm and should not affect its interaction with water.

Furthermore, we performed time-lapse NMR after exposing the hydrogels to larger polyamines, PAH of two MWs, 15 kDa and 50 kDa, and PDADMAC in the same conditions described for DLS experiments. The addition of polycations displays abrupt dehydration kinetics for the systems studied (Fig. 2.12).

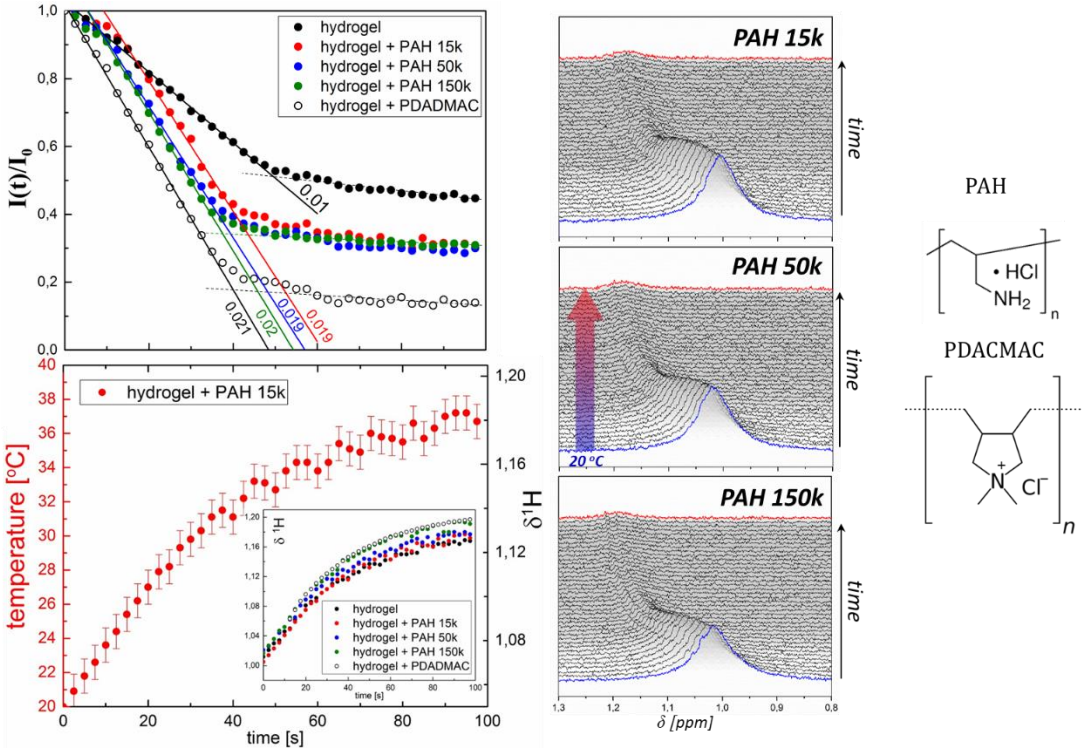

Figure 2.12. Dehydration kinetics in the presence of PAH and PDADMAC. a) Evolution of the I(t)/I0 over time for PAH of different MW and for PDADMAC. b) Temperature of the sample versus time for the hydrogel + PAH 15 k. The inset graph represents the chemical shift variation over time for PAH of different MW and for PDADMAC c) Change in the methyl proton NMR signal during deswelling for the three MWs of PAH studied. All experiments were recorded at pH 6.8.

Especially remarkable are the results obtained with PDADMAC, similar to spermine and spermidine.

It is likely that the small polyamines (spermine/spermidine) are more effective at complexing carboxylate groups as they can penetrate more easily in the hydrogel and reach the hydrogel core. The larger polyamines (PAH, PDADMAC) are more likely to stay at least partially on the hydrogel surface due to molecular weight considerations.[245] Taking into account the MW of PDADMAC, we could expect that the polymer would remain predominantly on the surface of the hydrogel. However, in addition to a cross-complexation effect, quaternary ammoniums can generate a more hydrophobic environment than primary amines, which can lead to a decrease in the hydration of the carboxylates at room temperature as we have previously shown. This behaviour would explain why PDADMAC is more effective than PAH at decreasing the intensity of the NMR signal during hydrogel deswelling and consequently the conformational freedom of the methyl groups.[248] Despite the more pronounced decrease in intensity in the presence of PDADMAC, the temperature at which the plateau starts remains the same as for PAH, shifted anyway to lower values than the D_2O at pH 6.8. Probably, we observe here that both PAH and PDADMAC have a similar effect on the water environment around NIPAm, which determines the actual phase transition temperature.

2.4. Conclusions

Time-lapse NMR studies of P(NIPAm-co-MAA) hydrogels with temperature show a faster dehydration of the hydrogel at acid pH due to a decrease in the charge of carboxylates and water content. Notably, at basic pH no collapse can be inferred from the time-lapse NMR as the signal intensity is not affected by the increase in temperature. Although the hydrogen bonds of NIPAm with water are broken with temperature, the methyl groups of NIPAm remain in a highly hydrated environment due to the water brought by the carboxylates. Increasing the ionic strength results in faster dehydration kinetics as both carboxylate and PNIPAm groups dehydrate in the presence of NaCl below LCST. Positively charged oligomers, spermine and spermidine result in faster dehydration kinetics, which can be correlated with the oligomers complexing several carboxylate groups. Oligomers have a larger effect on the dehydration kinetics than PAH, probably due to a more effective penetration in the hydrogel, while PAH is largely retained on the hydrogel surface. PDADMAC, despite its high MW, shows dehydration kinetics similar to the oligomers because of the strong dehydrating effect of quaternary ammoniums on carboxylate groups.[248] Previous work has shown how the P(NIPAm-co- MAA) hydrogels respond to pH, exposure to polyamines[248] and temperature but without relating the temperature-induced swelling/deswelling of the hydrogel to the conformational freedom and hydration of NIPAm at the molecular level. Our results provide novel insight into these stimuli-induced responses of the hydrogel and give a molecular explanation for how the behaviour of PNIPAm hydrogels is altered by the responsiveness of MAA monomers to the environment. Our time-lapse NMR experiments advance the understanding of the mechanism of collapse of P(NIPAm-co- MAA) hydrogels with

temperature, and of how the sensitivity of MAA charges to various stimuli (pH, ionic strength, presence of charged molecules), can affect hydrogel collapse at the molecular level, which has not be demonstrated previously. This work opens new perspectives for using time-lapse NMR to study other hydrogels or smart thermoresponsive systems that respond to multiple stimuli, by examining the polymer dynamics in the hydrogel. Furthermore, time-lapse NMR has strong potential for studying the impact of molecular cargo in thermal transition for hydrogels designed for drug delivery.

Chapter 3

Study of lectin-protein corona interaction on top of gold nanoparticles by fluorescence correlation spectroscopy

3.1. Motivation

In biological fluids many different biomolecules i.e. lipids, proteins, etc., are present that can be adsorbed onto the nanomaterial's surface. These molecules form a "new" interface on the nanomaterials and provide a biological identity to the nanomaterial, which plays a key role in the interaction of the nanomaterials with other biomolecules, cells, tissues and in translocation processes.[251,252] Understanding the interaction between the nanomaterials and the biomolecules adsorbing onto their surface has relevance for toxicological studies and in biomedical applications of nanomaterials.

Human blood is composed of plasma, erythrocytes, leukocytes and platelets.[253] Plasma is consists of water (92%), proteins (7%) and other components, such as lipids, electrolytes, ions, gases, aminoacids, glucose, or vitamins (1%) (Fig. 3.1).

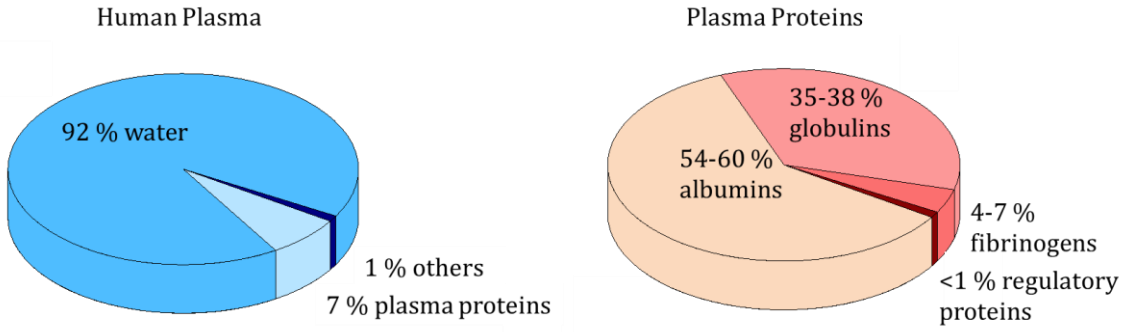

Figure 3.1. Scheme of Human Plasma and Plasma Proteins composition.

When a nanocarrier is administered by intravenous injection, proteins adsorbed on the nanoparticle surface forming the so-called protein corona (PC) or biomolecular corona (BC). As mentioned in the introduction, size,[254] shape[255] and surface charge[256] of nanomaterials impact on the characteristics of the PC formed around the nanoparticles.[257–261] Moreover, external factors such as blood pressure or protein

gradients can also affect protein corona formation.[262–264] The protein corona, which is formed in a few seconds, has a dynamic nature.[256] Those proteins, which are most abundant in plasma attach first to the nanoparticle surface. However, these proteins are replaced over time by other proteins present in lower concentrations, but with higher affinity for the nanoparticle surface.[265] The protein corona can be divided in to two 'layers or regions' (Fig. 3.2). An inner layer called the hard corona (HC), which is the most stable over time due to the high affinity between proteins and the nanomaterial surface.[266] The external layer of protein, called the soft corona (SC), is formed by a cloud of weakly bound proteins and constantly interacts and changes with the surrounding biomolecules.[138]

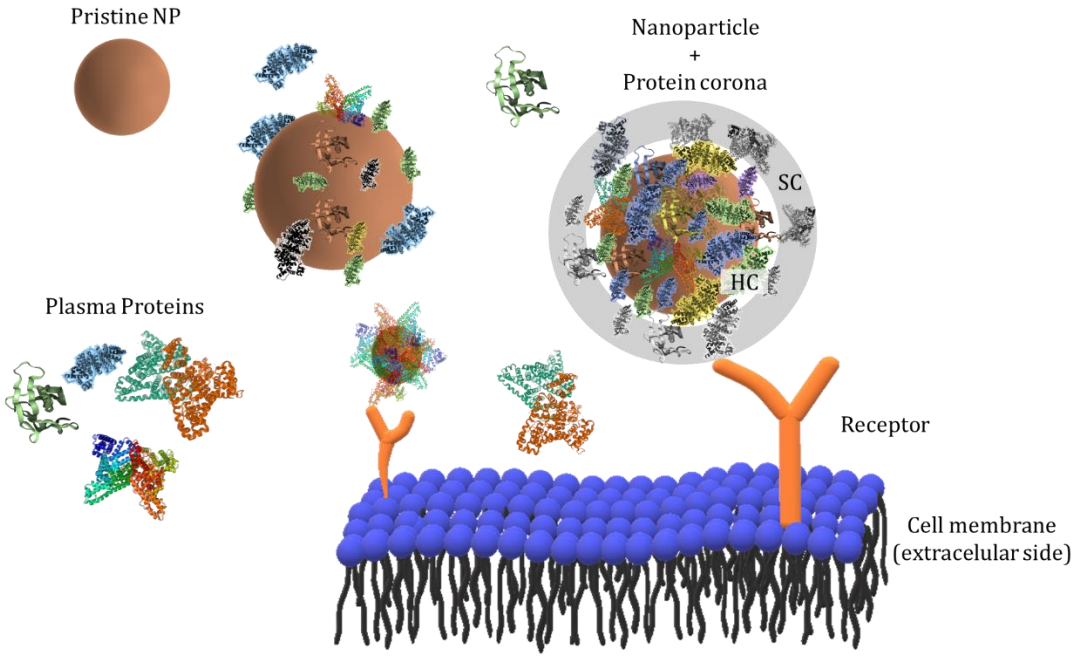

Figure 3.2.Protein corona formation on top of nanoparticles in a biological environment.

The protein corona changes the properties of the nanoparticles since it confers them new surface characteristics and a biological identity to interact with cells and with other biomolecules. At first, the adsorption of proteins onto the nanomaterial surface produces changes in size and surface charge.[267] PC formation affects the surface charge of nanoparticles, and depending on the initial charge and concentration of the nanoparticles and the proteins adsorbed on the nanoparticle surface charge can decrease or increase, thus impacting on colloidal stability. In some cases the PC helps to stabilize nanoparticles by reducing aggregation, in other cases the opposite situation takes place and after PC formation nanoparticles aggregate.[143,268] Increasing nanoparticle stability after PC formation helps to increase nanoparticle's half-life in the blood stream facilitating the arrival at the desired tissue. However, for active targeting therapies where different ligands are placed on the nanomaterial surface, the PC may compromise their function, masking the ligands and preventing specific ligand cell interactions.[269,270]

Due to the new biological identity acquired, the cytotoxicity, nanoparticle uptake, and trafficking inside the cell can be affected by the PC. As an example, there are nanomaterials such as carbon nanotubes that are capable of inducing cell death by the disruption of the cell membrane. For these nanomaterials, the PC acts as a natural coating, diminishing the damage of the pristine nanomaterials on the membrane and increasing the nanomaterial biocompatibility.[150–152,271]

Up to 50 % of the proteins in plasma are glycosylated which means that they display an oligosaccharide in their structure.[272] Sugar moieties present in oligosaccharides are key elements of cells and they change not only the protein structure, but also their function or solubility. Protein glycosylation is carried out between the endoplasmic reticulum (ER) and the Golgi apparatus in the presence of glycosidases and glycotransferases.[273] Glycosylated proteins are involved in many cellular process such as immune response, cell recognition, differentiation, etc., and are highly important for clinical medicine.[274] Glycans are also present in the protein corona but their role in nanoparticle-cell interactions is unknown.[153,275]

Lectins are carbohydrate-binding proteins, capable of highly specific interactions with sugar groups. Lectins take part in numerous biological recognition phenomena with cells, carbohydrates, and proteins. In addition, bacteria, viruses and fungi make use of lectins for attachment to intended targets. Lectins have also analytical applications, being used to recognize carbohydrates due to their binding with high specificity to sugar groups.[276] Lectins have their origin in bacteria, viruses, plants, and animals. Lectins are present in humans through their diet, specially through grains, some vegetables, and dairy products.[277] Lectins are resistant to human digestion and they enter the blood unchanged. In blood they can then interact with glycosylated proteins and reach different tissues and cells to which they can bind also through glycan recognition. In a similar fashion they can bind to glycosylated proteins found in the protein corona around nanoparticles. Lectin binding to the PC can in turn affect the interaction of PC with cells, trigger specific recognition events, and plays a role in the internalization process of nanoparticles. Nonetheless, to date there has not been a study of the recognition of PC by lectins and the role of glycosylated proteins in this interaction.

In this chapter, gold nanoparticles have been employed as a template to form a protein corona with human plasma and study its interaction with lectins. Two fluorescently labelled lectins have been chosen: Wheat Germ Agglutinin (WGA) and Sambucus Nigra (SNA), both from plant origin and bind glycans linked to Neu5Ac and chitobiose (GlcNac1β-4GlcNac) -linked residues and Neu5Ac(α2–6)Gal/GalNAc respectively.[278,279] Lectin binding to protein corona is studied via Fluorescence Correlation Spectroscopy (FCS), which provides information on the diffusion of fluorescence molecules by monitoring fluctuations of fluorescence intensity in a confocal volume. From the diffusion of labelled lectins, the percentage of lectins binding to the protein corona is determined. Moreover, we prove by means of FCS

that the interaction of lectins with PC takes places to the glycosylated proteins via removal of the glycans from the proteins with an enzymatic assay.

3.2. Experimental Section

3.2.1 Materials

Gold nanoparticles (GN) were provided by Ana Sánchez from Colloidal Nanofabrication Platform from CIC biomaGUNE (San Sebastián-Spain). Plasma was supplied by the IBTS (Irish Blood Transfusion Service). Wheat germ agglutinin (WGA), Bradford reagent and Phosphate buffer saline tablets were obtained from Sigma-Aldrich. Sambucus Nigra Lectin-Cy5 (SNA) was purchased from Vector Laboratories. PNGase-3F (CarboClip) was bought from Asparia Glycomics.

3.2.2 Protein Corona-Lectin Association

Different amounts of plasma were added to a PBS solution to obtain final protein concentrations of 3%, 10%, 40% and 80% v/v (250 µL). Gold nanoparticles (GN) (0.15 mg·mL^{-1}) were incubated in the different plasma concentrations for one hour at 37 °C with orbital shaking (220 rpm).

Following incubation, samples were centrifuged to remove proteins not adsorbed onto the GN. After this first step, different centrifugation protocols were applied to obtain either the soft, or hard corona, around nanoparticles. The proteins forming the soft corona are weakly adsorbed onto the surface, meaning that they can be easily removed by centrifugation.[280] For this reason, just one wash step was applied to remove excess protein in solution and maintaining the proteins weakly attached to the surface. On the other hand, proteins in the hard corona are strongly attached to the GNP surface remaining unchanged faced to washing steps. To obtain the hard corona samples were washed and centrifuged 3 times, removing the soft corona completely.

For both GN with SC or HC, 30 nM of fluorescently labelled lectin (WGA or SNA) were added in the solution with the GN with protein corona. Then, the binding between the protein corona and the lectin was studied by FCS. Samples were placed in NuncTM Lab-Tek Q5 Chambered Coverglass (Thermo Fisher Scientific, USA). FCS experiments were carried out with a Zeiss LSM 880 confocal microscope with Zen Black, and the confocal volume estimated using 25 nM ATTO633 solution, with a well-defined diffusion coefficient in water. The fluorescence from the lectin was detected by a photomultiplier tube (PMT) detector in the range 650-710 nm. As a control, the diffusion time of unbound lectin was obtained by measuring 30 nM of lectin in PBS. The objective used was a water immersion Zeiss C-Apochromat 40x with a numerical aperture of 1.2. All the samples were measured 20 times during 10 s and analyzed with Quick Fit 3.0 software.[281] Data was fit with a 3D normal diffusion model with two components, one referred to the free lectin and the other to the lectin associated to the GN.

3.2.3 Glycan Removal

N-linked glycans of the proteins forming the corona were removed using the PNGase-F (Carbo-Clip) kit from Asparia Glycomics. Following the protocol, for each 50-200 µg of protein, 1 µL of Carbo-Clip is required. To estimate the amount of protein attached to the nanoparticle surface, Bradford reagent was used.[282] The Bradford reagent is based on recording absorbance changes of the Coomassie Brilliant Blue G-250 due to its binding with proteins. BSA solution was used as a standard for protein quantification of the first centrifuge supernatant. The subtraction of these amounts gives us an estimation of the protein mass in the surface of the nanoparticles.

PNGase-F was added to the different solutions and incubated for 1 h at 60 ℃ with orbital agitation. 30 nM of lectin was added and measured by FCS following the same procedure as in section 1.2.2.

3.3. Results and Discussion

Gold Nanoparticle Characterization

GN were stabilized with sodium citrate in water. Fig. 3.3. shows the results for the sample characterization via UV-spectroscopy and TEM.

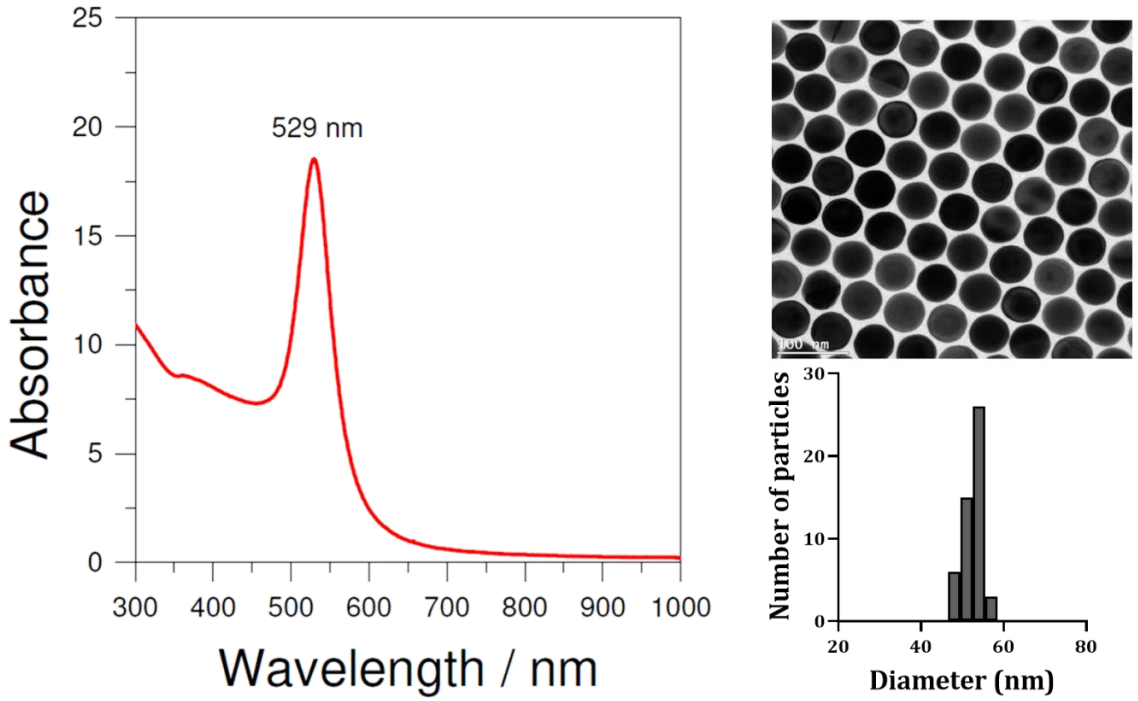

Figure 3.3. Characterization results of gold nanoparticles. On the left, the UV-visible absorbance spectrum shows a single absorbance peak at 529 nm characteristic for spherical gold nanoparticles on this size. On the right TEM micrographs of gold nanospheres. Data provided by Ana Sanchez from Colloidal Nanofabrication Platform at CIC biomaGUNE.

In metal nanomaterials, the electrons in the conduction band interact with specific wavelengths of incident light, producing a collective oscillation, a so-called localized

surface plasmon resonance (LSPR). The plasmon resonance frequency is dependent on the NP characteristics (size, shape, etc.) and their environment, being the maximum optical absorption at this frequency. Consequently, by UV-Vis spectroscopy it is possible to determine the type, size or shape of metal nanomaterials depending on the position and width of the maximum absorption.[283] The LSPR of gold nanoparticles is in the visible region around 500-600 nm depending on their size.[284,285] Fig. 3.3. shows a maximum absorbance at 529 nm which correspond to particles with diameter around 50 nm. This value is confirmed by DLS and TEM measurements, showing a hydrodynamic diameter of 53.58 ± 0.13 nm in water and 53.8 ± 2.1 nm size distribution (by FiJi software) respectively (Fig. 3.3).

Protein Corona-Lectin Association

Plasma was diluted in 150 mM PBS to obtain different protein concentrations: 3%, 10%, 40% and 80% v/v. Gold nanoparticles were added to the plasma dilutions reaching a final concentration of nanoparticles of 0.125 $mg \cdot mL^{-1}$. After incubation, samples were centrifuged and washed to remove excess protein. For soft corona formation samples were washed 1 time, while for hard corona formation they were washed 3 times. Then, 30 nM of labelled lectin was added to the sample cuvette with GN (250 µL, 0.1 $mg \cdot mL^{-1}$) for the FCS studies. Such a low concentration of fluorescence species is due to the optimal ratio signal to noise is addressed in the nanomolar range.

We use FCS to evaluate the interactions between lectin and proteins. The technique records fluctuations in the fluorescence intensity of molecules within a confocal volume, from which the diffusion time of the molecules can be obtained. In our study, if fluorescently labelled lectins associate to the glycans in the protein corona, lectins will diffuse similarly to nanoparticles with a protein corona, i.e., more slowly than the free lectin, which is not attached to the protein corona (Fig. 3.4). This is in fact observed, for both lectins used. When lectins are mixed with GN with protein corona either SC or HC there is a change in the autocorrelation function of the lectin which now displays a longer diffusion time compared with that for free lectin. From data fitting, assuming that the lectin could be either free or bound and knowing the diffusion time of free lectin it is possible to estimate the percentage of free and bound lectins.

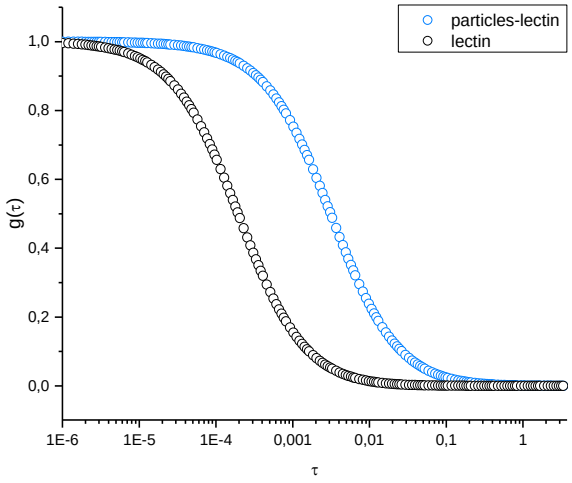

Figure 3.4. Example of normalized FCS results for free WGA lectin (black) and WGA lectin associated to glycans in the protein corona (blue). Changes in the lectin diffusion time reflects the association NPs-lectin.

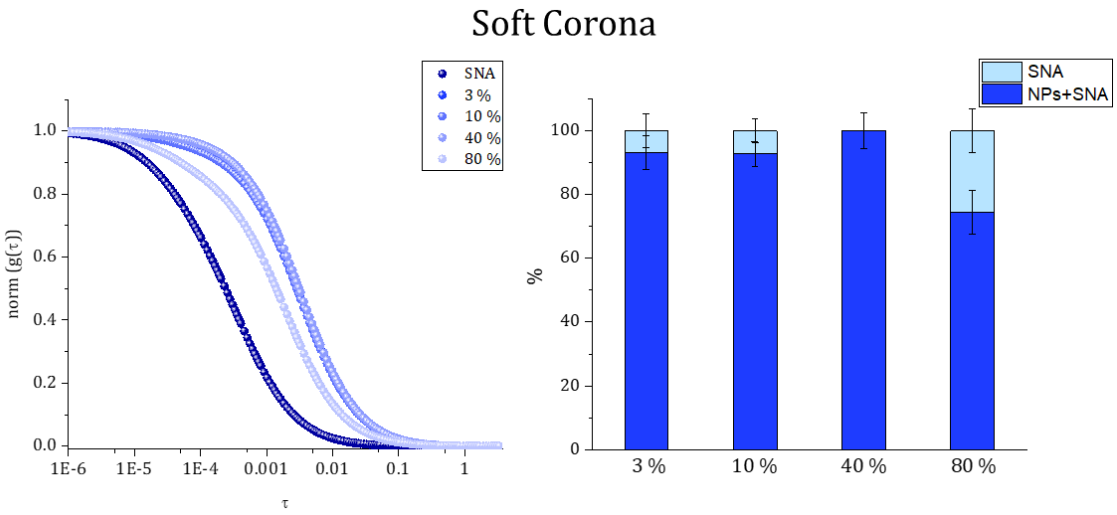

Figure 3.5. FCS results for the binding of SNA lectin with the soft protein corona for plasma percentage 3%, 10%, 40% and 80%. On the left side, the normalized correlation function and on the right side the percentage of free SNA and NPs SNA.

Fig. 3.5. shows the results obtained by FCS for soft corona binding of lectins. The analysis reveals that some measurements (around 5%) must be excluded due to large aggregates of nanoparticles, sometimes exceeding the technique detection limit. The normalized correlation function of the SNA lectin in PBS and the SNA lectin associated to the gold nanoparticles are shown in Fig. 3.5. As expected, the diffusion time of free SNA in PBS 150 mM is shorter than the diffusion time of lectin in the presence of GN with a soft protein corona. Free SNA has a diffusion time of 428 ± 8 μs while the values for the diffusion time of the gold NPs with SC are around 3000 μs. The diffusion time depends on the size of the complexes formed by the lectin with the nanoparticles with the PC coating. Since there are no significant differences among the diffusion time of

nanoparticles for protein concentrations from 3 to 40 % one can conclude that protein concentration does not affect the corona composition for the soft corona and there are no large differences in the number of binding sites for the lectins as a function of concentration. The hydrodynamic diameter of lectin-NP SC complexes is shown in table 3.1 together with their diffusion coefficients. The hydrodynamic diameter of complexes has been obtained via the Stokes-Einstein equation from the diffusion coefficient, as expected these are also quite similar. For the 80 % protein solution the diffusion time is around 10% smaller than in the other percentages, which results in approximately a 10 nm smaller diameter. Considering that a lectin has a diameter of 6 nm, a 10 nm difference in diameter may indicate several lectins not binding to the nanoparticles. However, one must also take into account that since only the lectins are fluorescent we cannot estimate the size of the nanoparticles with the protein corona beforehand and therefore the difference in hydrodynamic diameter that we observe may also be due to a smaller protein corona around the NPs when the protein concentration is 80 %.

	τ [µs]	D_c [µm²·s⁻¹]	d_C [nm]
Free SNA	428 ± 8	33.5 ± 0.6	6.41 ± 0.23
GN- 3%SC-SNA	3314 ± 210	4.3 ± 0.3	99.17 ± 0.79
GN- 10%SC-SNA	3344 ± 154	4.29 ± 0.20	100.09 ± 2.34
GN- 40%SC-SNA	3263 ± 195	4.40 ±0.26	97.59 ± 5.79
GN- 80%SC-SNA	3055 ± 186	4.7 ±0.3	91.362 ± 5.85

Table 3.1. FCS data obtained from the fitting of the autocorrelation curves. τ is the diffusion time, D_c the diffusion coefficient and d_c the hydrodynamic diameter of the fluorescence species. All the samples were evaluated with a 3D diffusion model with two fluorescence species (SNA lectin and lectin associated with GN-PC).

In order to gain a clearer picture of the interaction of the lectins with the PC we looked at the percentage of bound and unbound lectin at each protein concentration. Indeed, if one now considers the percentage of unbound lectin and lectins binding to the nanoparticles SC (Fig. 3.5), when the amount of protein added in solution is 3% or 10% the association is around 93% meaning that 7% of SNA is unbound. Increasing the protein concentration to 40%, we see that all the lectins bind with the PC. However, when the protein concentration increases to 80% only 75% of lectins bind to the protein corona. This increase in the amount of free lectin for 80 % is consistent with a decrease in the number of lectins binding to the SC for 80 % protein in media.

When we look at the binding of SNA to the hard corona we observe that, independently of the protein concentration in the initial solution, all the SNA is attached to the PC, except for the 40% plasma concentration, where we observe around 7% of unbound SNA.

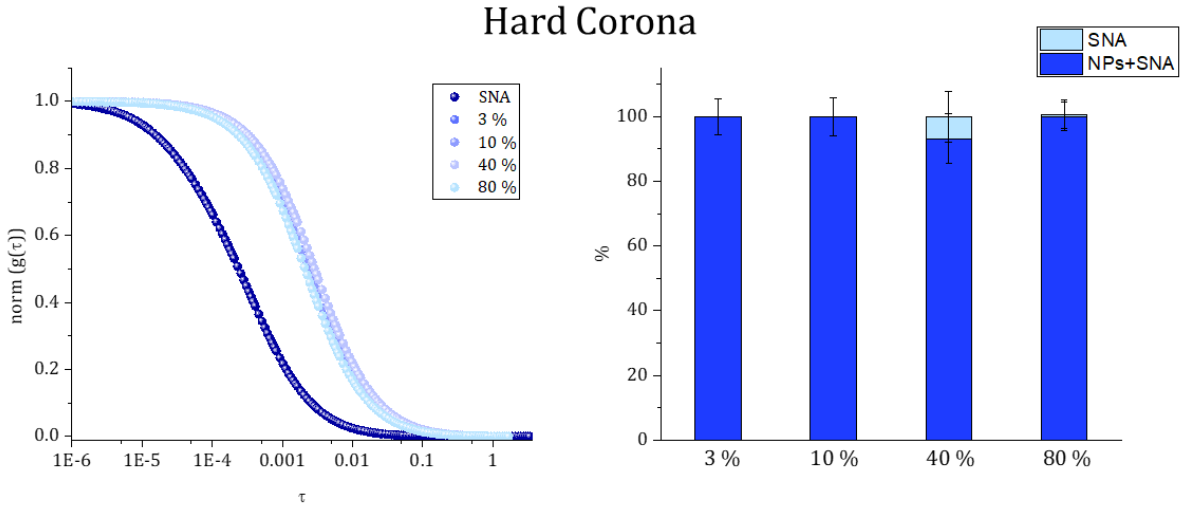

Figure 3.6. FCS results for SNA lectin association with the hard protein corona for plasma percentages 3%, 10%, 40% and 80%. On the left, normalized correlation function and on the right side the percentage of free SNA and NPs SNA.

	τ [μs]	D_c [μm²·s⁻¹]	d_C [nm]
Free SNA	428 ± 8	33.5 ± 0.6	6.41 ± 0.23
GN- 3%HC-SNA	2356 ±142	6.09 ±0.37	70.5 ± 4.33
GN- 10%HC-SNA	2365 ±132	6.07 ± 0.37	70.74 ± 4.33
GN- 40%HC-SNA	2954 ± 183	4.86 ± 0.30	88.35 ± 5.47
GN- 80%HC-SNA	2139 ±143	6.72 ± 0.45	63.90 ± 4.30

Table 3.2. Data obtained from the fitting of the correlation function for SNA association with the hard corona. τ is the diffusion time, D_c the diffusion coefficient and d_c the hydrodynamic diameter of the fluorescence species. All the samples were evaluated with a 3D diffusion model with two fluorescence species (free SNA and lectin associated with GN-PC).

The apparent higher affinity of SNA for the hard corona rather than for the soft corona may reflect a different composition of the hard corona with a larger amount of sugar groups with affinity for the lectin. A different composition of hard and soft corona can be explained by the different affinity of the nanoparticle surface for certain proteins. Those proteins with larger affinity will form the HC, whilst the composition of the soft corona is more influenced by the proteins present in larger concentrations in plasma. Regardless, all SNA bind to the HC at all protein concentrations, approaching 100 %, we observe interesting differences in the sizes of the lectin HC complexes as measured by FCS. Size can be only measured when the lectin is bound to the corona as this is the only fluorescent molecule in the complexes. For all protein concentrations the size of the complexes is smaller than for the corresponding soft corona. At 3% and 10 % protein concentration the sizes are the same, around 70 nm in diameter. At 40 %

protein size increases up to 88 nm in diameter but then decreases to around 64 nm for the 80 % protein. The increase in diameter to 88 nm at 40% of protein concentration corresponds to the only protein concentration with some free lectin in the media. Therefore, the larger size of the complexes cannot be explained by more bound lectin than for the other protein concentrations. Since all measurements were performed with the same GN the reason for the larger size for 40% must be in a different size of the HC, larger than at 3 and 10 % protein. The same explanation can be given to the 80 % protein but in this case the HC is smaller. Differences in size in the HC can be explained by differences in composition of the corona depending on amount of proteins available in solution.[286]

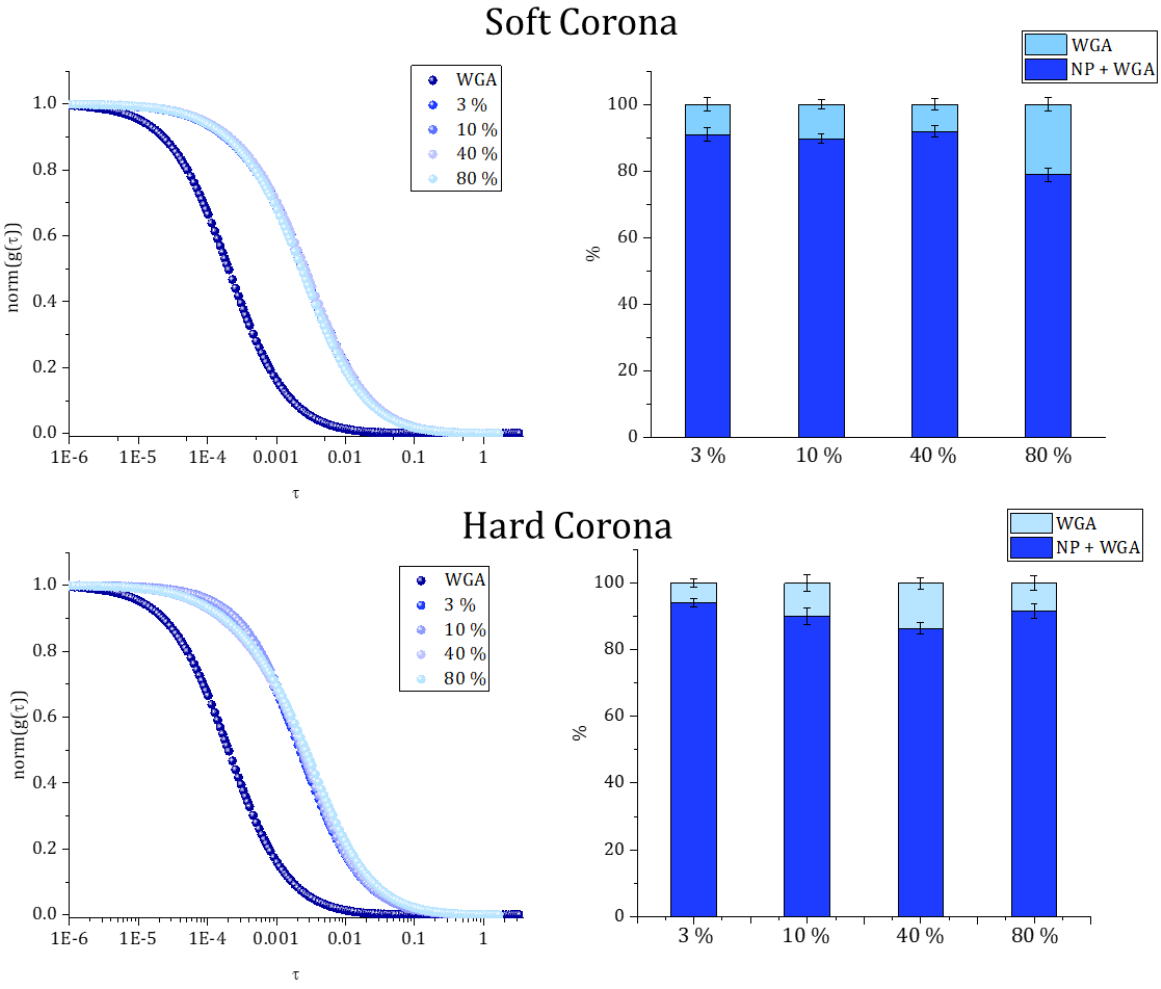

Figure 3.7. FCS results for WGA behaviour in a solution of 3%, 10%, 40%, 80% of plasma after one washed (soft corona) and three washes (hard corona). The histograms present the amount of free WGA (light blue) and the lectin associated with the different kinds of PC of particles obtained after the results were fitted.

In the case of WGA, which binds to glycans Neu5Ac and GlcNac1β-4GlcNac, the interaction with the SC has similar outcomes as SNA. Unbound lectin is present at all protein concentrations, around 10 % up to a 40 % protein and approximately 21 % for 80 % protein.

		τ [μs]	D_C [μm²·s⁻¹]	d_C [nm]
Free WGA	**-**	206.6 ± 1.5	75.6 ± 0.5	2.83 ± 0.38
GN- 3%PC-WGA	**SC**	3171 ± 112	4.93 ± 0.17	87.10 ± 3.00
	HC	2484 ± 58	6.29 ± 0.15	68.27 ± 1.63
GN- 10%PC-WGA	**SC**	2967 ± 61	5.27 ± 0.11	81.48 ± 1.70
	HC	2397 ± 76	6.52 ± 0.21	65.86 ± 2.12
GN- 40%PC-WGA	**SC**	3096 ± 72	5.05 ± 0.12	85.03 ± 2.02
	HC	3074 ± 81	5.08 ± 0.17	84.52 ± 2.83
GN- 80%PC-WGA	**SC**	3226 ± 101	4.84 ± 0.15	88.72 ± 2.75
	HC	2469 ± 85	6.32 ± 0.17	67.94 ± 1.82

Table 3.3. Diffusion time (τ), diffusion coefficient (Dc) and hydrodynamic diameter (dc) of the fluorescence species obtained from fitting curves for WGA association with soft (SC) and hard corona (HC). All the samples were evaluated with a 3D diffusion model with two components (free WGA and WGA-GN-PC association)

For the hard corona the association of WGA with the corona is not as complete as for the SNA, and some lectins remain unbound, between 5 and 15 % depending on the protein concentration. The smaller association of WGA lectin in equal conditions as for SNA is indicative of a smaller amount of sugar ligands available for interacting with WGA in the HC.

This binding difference shown by FCS between the SNA and the WGA are sustained on the glyco-profile. The amount of exposed Neu5Ac (N-Acetylneuraminic acid), one of the sialic acids predominant in humans, for which the SNA has major affinity, is very high in the HC. On the other hand, GlcNAc (N-acetyl-glucosamine) is a less prominent sugar, for which the WGA lectin has a high affinity. That is the reason why SNA affinity is higher compared to the WGA, i.e., the carbohydrate predominance of the Neu5Ac in the protein corona.

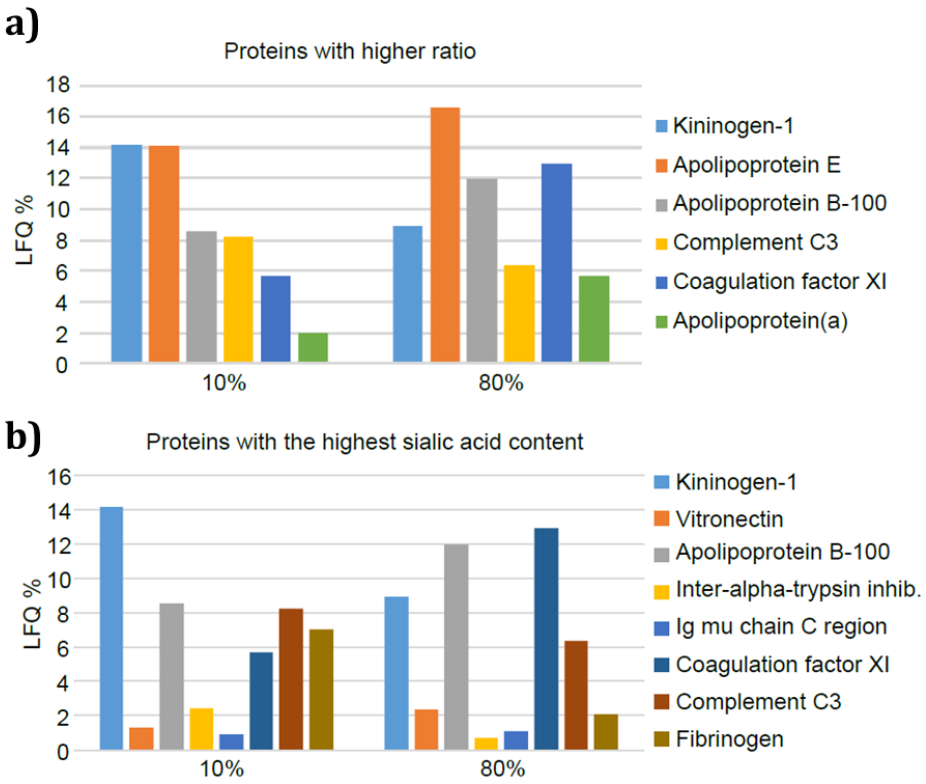

Figure 3.8. Histograms: a) Proteins in the 10% and 80% PC with highest ratio in the map and therefore the more abundant in the PC. b) Proteins with the highest content of Neu5Ac glycans

N-linked Oligosaccharide Removal

In order to prove that the interaction of lectins with the protein corona takes place through the glycan in glycosylated proteins we proceed to remove glycans from the corona using the PNGase-F enzyme. This enzyme separates N-linked carbohydrates at the junction between the GlcNAc and Aspargine residues from N-linked glycoproteins (Fig. 3.9).[287]

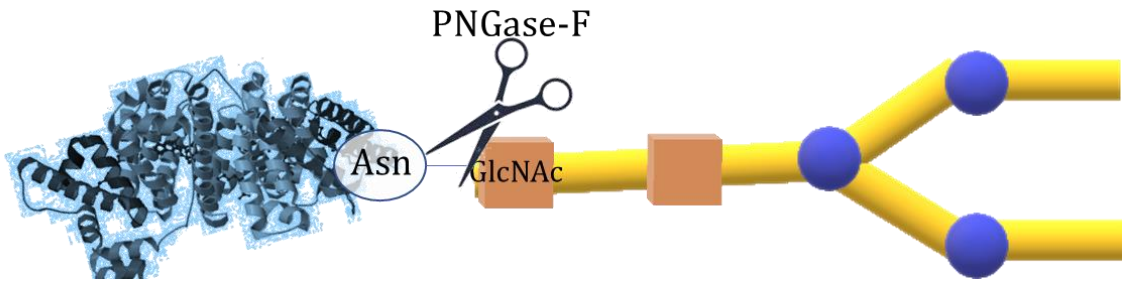

Figure 3.9. Scheme of the cleavage od PNGaseF between the Asn of the protein and the GlcNAc of the oligosaccharide

A Bradford assay was first performed to estimate the protein amount in the corona to calculate the amount of PNGase-F necessary in the solution. For that propose, a calibration curve with BSA in the range 0.05- 1.5 mg·mL^{-1} was carried out.

The initial protein amount in PBS and the supernatant of the first centrifugation were calculated. This estimation uses only the first centrifuge supernatant as most of the proteins in solution are removed in this centrifugation. The results obtained are listed in table3.4

	3 %	10 %	40 %	80 %
Protein in solution (mg)	0.75 ± 0.19	1.35 ± 0.34	5.38 ±1.34	9.27 ±2.30
Protein in supernatant (mg)	0.61 ±0.15	1.13 ± 0.30	4.70 ± 1.17	8.91 ± 2.20
Protein corona estimation (mg)	0.13 ± 0.03	0.22 ±0.005	0.68 ± 0.18	0.36 ±0.09

Table 3.4. Protein estimation in mg of the initial solution, the supernatant of the first centrifuge and in the protein corona. Calibration curve was done with BSA concentrations from 0.05 to 1.5 mg·mL^{-1}. Linear fitting was applied to obtain the equation $y = mx + d$ where y is x is the concentration of the protein, m the slope of the fitting, y the absorbance of the sample and d the fitting y-intercept with the zero. On our case, the fitting provides the equation: $y = 0.19355 \cdot x + 0.29657$.

After estimation of the amount of protein in the PC, 2 µL of PNGase-F was added and the samples were incubated at 60 °C for one hour. Once the glycans are cut, 30 nM of fluorescently labelled lectin (WGA or SNA) were added as in the previous experiments and FCS measurements were repeated. These experiments were done with hard corona due to their stability, especially in the 10% and 80% PC concentration.

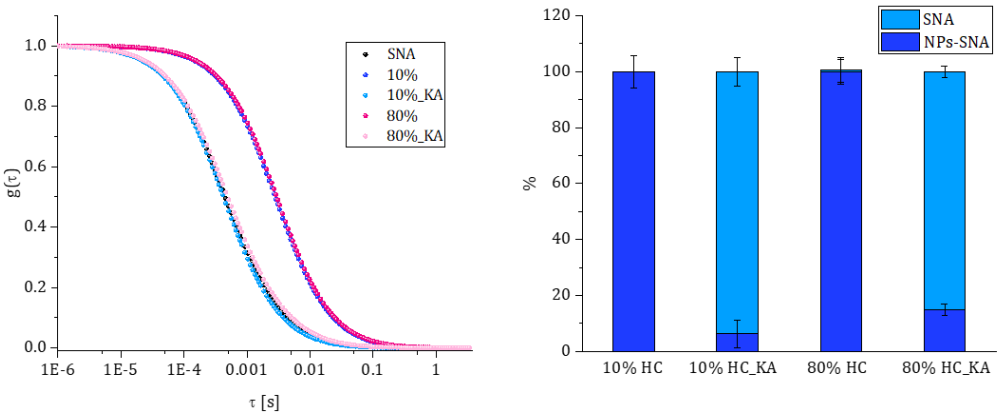

Figure 3.10. FCS data for SNA before and after glycan removal with the PNGase-F for hard corona on gold nanoparticles prepared from10% and 80% protein. KA refers to Kit Asparia.

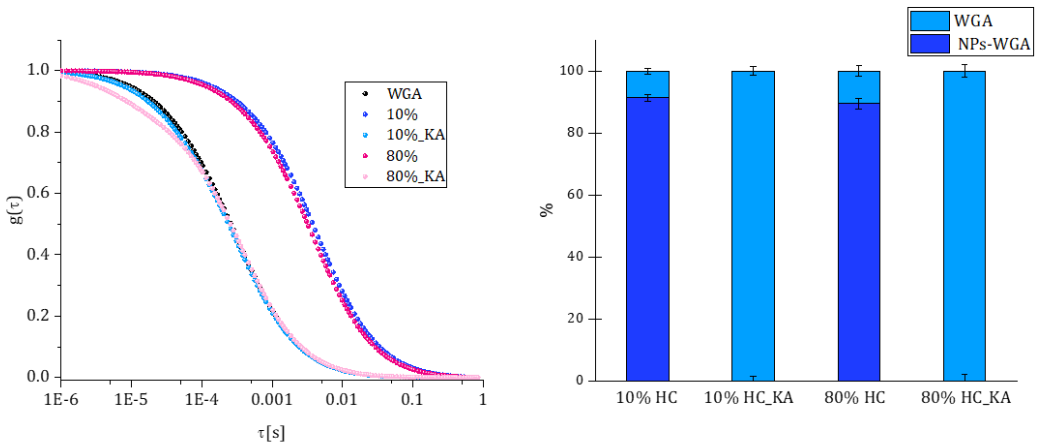

Figure 3.11. FCS data for WGA before and after glycan removal with the PNGase-F for hard corona on gold nanoparticles prepared from10% and 80% protein. KA refers to Kit Asparia.

Fig. 3.10 and 3.11 shows the results of the association of lectin with nanoparticles after the application of the PNGase-F assay. While for WGA (Fig. 3.11) all the lectin is free in solution after the enzyme application, in the SNA (Fig. 3.10) case some of lectin remains attached to the protein corona, 6% in 10% concentration of proteins and 10% in the 80% sample. SNA shows a 100 % binding to the PC before PNGase. Probably some Neu5Ac glycan remains in the corona or some SNA molecules binds unspecifically to the proteins.

3.4. Conclusions

In this chapter we have studied the association of two different lectins, WGA and SNA, with the protein corona around NPs by means of FCS.

Lectins have specific interactions with sugar groups that produce differences in their association with proteins. FCS studies reveals that WGA lectin shows that there are no significant differences between SC and HC for the interaction with WGA lectin. On the contrary, SNA exhibits different affinity for HC and SC. For the SC, some SNA remains free lectin in solution while for the HC all SNA bounds to the corona.

The different affinities between the lectins and the corona may be caused by the different protein composition and consequently different glycan profile around the nanoparticles. SNA has a predominant monosaccharide affinity with Ne5Ac present a higher amount in the HC according to the glycol-profile. WGA on the other hand, has a lower affinity for this sugar so the interaction between WGA and the protein corona is inferior than for the SNA.

Chapter 4

Impact of polymer coatings on the intracellular degradation of ZnO nanoparticles by means of confocal Raman microscopy

4.1. Motivation

Polymer and organic surface coatings of nanoparticles (NPs) designed for biomedical applications play a fundamental role in providing aqueous stability, as well as a mean to control the interaction of NPs with biomolecules, and to reduce toxicity.

Biomolecules are often used as coatings to enhance the biocompatibility of NPs through decoration of their surface. PEG, or zwitterionic, coatings are used to decrease interactions with proteins and to prevent recognition by the reticuloendothelial system, thereby preventing early clearance of NPs and prolonging circulation. In addition, coatings bring targeting functionalities and are responsible for guiding NPs to specific organs or tissues. In certain instances, the coating may also carry the drug/drugs to be delivered.

The coating can also reduce the toxicity by creating a barrier between the interface of the nanoparticle and the environment, which prevents the direct interaction of the nanoparticle and biomolecules, or cells. An organic coating, especially a polymeric one, can also prevent, or delay, nanoparticle degradation as it protects the nanoparticle surface from the environment. This is, for example, the case of some metal oxide NPs, such as ZnO or CuO, that degrade at endosomal pH. Both ZnO and CuO are known to be toxic because of their degradation in the endosome inducing a high concentration of ions, which alters cellular homeostasis. By coating these oxides with polymer chains the dissolution of the NPs can be slowed down, or even prevented. There are two ways to modify NPs with polymers.[288] These can be grafted or assembled on the NPs (grafting to)or they can be synthesized from the NP surface forming a polymer brush coating (grafting from) (Fig. 4.1). The synthesis of a brush from initiator molecules anchored on the surface of the NPs usually results in denser coating.

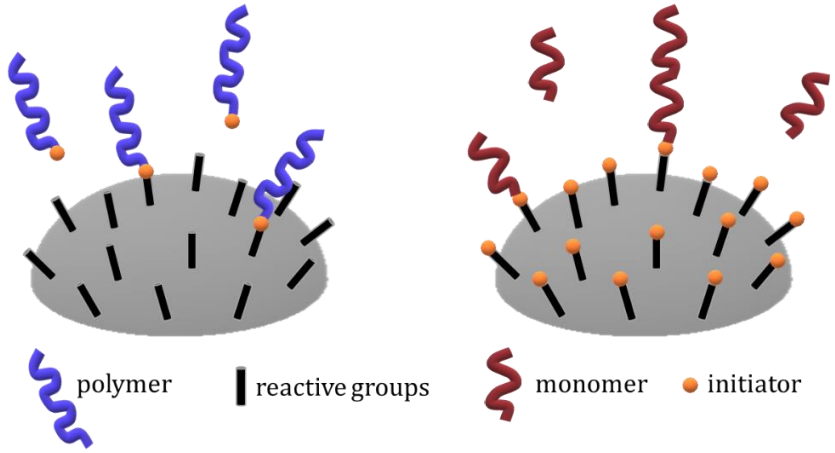

Figure 4.1. Scheme of polymer brushes synthesis: grafting to (left) and grafting from (right)

One of the most common techniques for the synthesis of brushes is radical polymerization. It is based on the consecutive addition of monomers to the polymer chain triggered.[289] Four steps take place: initiation, propagation, transfer, and termination. By controlling the ratio between them, it is possible to tune the polymer properties, e.g.: molecular weight.[290] For the in situ synthesis of polymer chains, initiators must be first anchored to the nanoparticle surface. The initiators generate free radicals which react with vinyl groups from the monomer forming new radicals that add monomers to the polymer chain.[291]

There are many different means of radical polymerization such as Nitroxide-Mediated Polymerization (NMP),[292,293] Atom Transfer Radical Polymerization (ATRP),[294,295] and Reversible Addition-Fragmentation Chain-Transfer (RAFT) Polymerization.[296–298] RAFT polymerization offers advantages over other controlled radical polymerizations.[115] RAFT can be performed in organic, or aqueous solutions at low temperatures, thereby avoiding the use of toxic metals used in ATRP and high temperatures required for NMP. It is also possible to employ different monomers, thereby allowing a degree of control over the molecular characteristics. In RAFT polymerization, the presence of a chain transfer agent (CTA) regulates the radical transference (low concentration CTA), or limits the molecular weight and the termination process (high concentration CTA).[299]

In this chapter we will show the modification of ZnO with polymer brushes synthesized *in situ*. We will prepare brushes with different charges: positive, negative, and neutral. The functionalization of the NPs with polymer brushes ensures colloidal stability. Moreover, we will show that polymer brushes protect the ZnO NPs by delaying their dissolution inside cells. For this we will use Raman Confocal Microscopy that will allow us to trace the intensity of bands related to ZnO inside the cell, which disappear following dissolution of the ZnO NPs.

4.2. Experimental Section

4.2.1 Materials

ZnO NM110 NPs were purchased from Joint Research Center (JRC). [2-(Methacryloyloxy)ethyl] trimethylammonium chloride (METAC) solution 80 wt. % in H_2O, acrylic acid (AA), anhydrous, contain 200 ppm MEHQ as inhibitor (99 %), poly(ethylene glycol methacrylate) average M_n 360 contains 500-800 ppm EHQ as inhibitor (PEG methacrylate), (3-Aminopropyl) triethoxysilane (APTES, 99%), Bis(carboxymethyl)trithiocarbonate (CTA, 98%), N,N'-Dicyclohexylcarbodiimide (DCC, 99%),(4-Dimethylamino) pyridine 99% (DMAP), 4,4′-Azobis(4-cyanovaleric acid) (CVA), (≥98 %) were purchased from Aldrich. The solvents, N,N-Dimethylformamide (DMF, 99.80%) and tetrahydrofuran (THF), purchased from ACROSS and ThermoFisher respectively, and nanopure water were used in the synthesis. FBS was purchased from Capricorn Scientific GmbH (Ebsdorfergrund, Germany). Trypsin and RPMI 1640 medium were purchased from Biowest (Nuaille, France).

4.2.2 Synthesis and characterization of polymer brushes

Synthesis of polymer brushes

Polymer brushes composed of PAA, PMETAC and PEG were synthesized on the surface of ZnO NPs via RAFT polymerization.

The synthetic procedure was the same for all the monomers. In order to immobilize the CTA and initiate the RAFT polymerization, APTES was used to anchor silane groups on the ZnO surface. For each polymer coating 150 mg of particles were suspended in DMF (2%w/v) before the addition of 1 mL of APTES. The reaction was carried out at 70℃ for at least 12 h. After this time, NPs were washed by centrifugation three times in order to remove excess reagents. CTA was bonded to the amines on top of ZnO NPs, in the presence of the carbodiimide (DCC), monomers and cyanovaleric acid (CVA, initiator) were stirrer at 70℃ under inert atmosphere during 12 h. The ratio between the reagents was:

[NPs]=[CTA]=[DCC]=[DMAP] [1] = [0.83] = [1] = [0.17] moles.

The amount of polymer was 10 times the molar amount of NPs. Three washes were done to remove the excess of reagents

Characterization of polymer brushes

In order to characterize the polymer brush coatings different techniques were used. Firstly, the coating process was followed by ζ-potential. At each preparation step, a few microlitres of the reaction mixture were taken and resuspended in 10 mM NaCl. Measurements were performed in a folded capillary Zeta Cell (DTS1070) in a Malvern ζ-Sizer Nano ZS at 25 °C. TEM images, for surface coating characterization, were obtained with a JEOL JEM 1010 transmission microscope at an acceleration voltage of

100 kV. Samples were prepared by pipetting 5µL of NPs (0.01 mg·mL^{-1}) onto a carbon film and dried. Additionally, thermogravimetric analysis (TGA) was performed to measure the percentage of polymer on the NP surface. The equipment used was a TGA/SDTA 851 Toledo (TA Instruments) with a heating rate of 10°C/min from room temperature to 800°C.

4.2.3 *In vitro* confocal Raman microscopy internalization

Confocal Raman microscopy (CRM) measurements were carried out using an Alpha300 R microscope (WITec GmbH, Ulm, Germany) with a charge-coupled device (CCD) detector cooled down to -60 °C. 75000 A549 cells were seeded in glass bottom petri dishes from WillCo. After 24 h of incubation, cells were washed three times with PBS. Then, 2 mL of PBS were added to the petri dish and samples were excited with a 532 nm laser to be observed through a 63x water immersion objective (W Plan-Apochromat 63x/1.0 Zeiss). Oscilloscope mode was employed to find the optimal position with the highest intensity of CH_2 signals from the cell, which means that the confocal volume is completely inside the cell and thus allows the maximum yield of cellular signals. Finally, 15 µg/mL of NPs (pristine or coated by polymers) were added to the cell cultures to monitor the cellular uptake in real time.

The data acquisition was accomplished in time series operational mode with 0.03 s integration time per pixel and a resolution of 4 pixels per nm. During the experiment, cell temperature is controlled and fixed at 37 °C. Data were analyzed using Project Four 4.0 WITec GmbH software. Data were obtained by Tom Venus, Carolin Zilberfain and Julia Böttner from the Institut für Medizinische Physik und Biophysik in Leipzig, Germany.

4.3. Results and discussion

Coating characterization

The different surface modification steps leading to the brush coating of the NPs were followed via ζ-potential.

Before ζ-potential measurements, the dispersion of ZnO NPs was ultrasonicated for 10 min to reduce aggregation. Fig. 4.2. illustrates the results of the different steps of the synthesis. Pristine ZnO NPs have a ζ-potential centered at 25.1 ± 2.55 mV, which matches with the data provided by the supplier (20.8 ± 0.8). After APTES functionalization, the zeta potential increases to 33.0 ± 3.2 mV due to the amines from the silane. The CTA grafting reduces the surface charge to 19.4 ± 2.47 mV. The substitution of amine groups on the surface with CTA carboxylate groups is responsible for the charge decrease produced in this synthesis step. After that, the zeta potential values vary depending on the monomer used. PAA polymer brushes results in a negative charge owing to carboxylate groups. The opposite situation was found in the case of PEG or PMETAC whose zeta potential remain positive

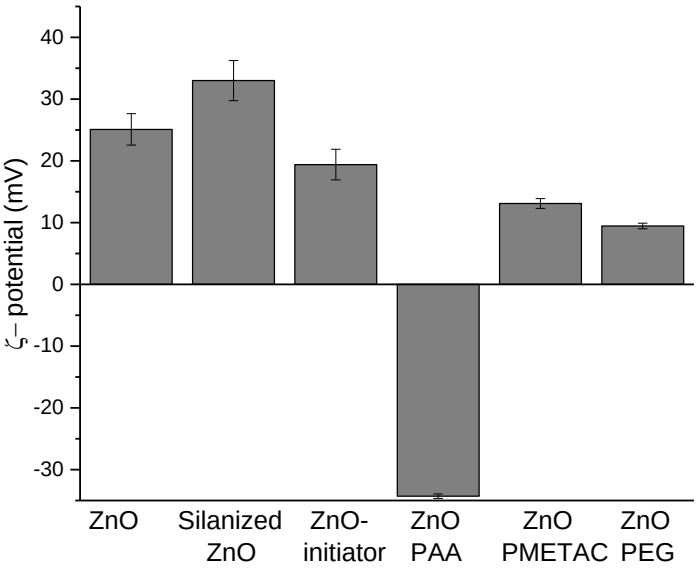

Figure 4.2. ζ potential measurements of the different steps in the ZnO NPs surface modification with PAA, PMETAC and PEG polymer brushes. The error bars range is 2-20%

TEM micrographs show the polymer brushes on the ZnO NPs surface (Fig. 4.3). These images reveal a polymeric coating thickness of around 20 nm in PAA, 8 nm for PMETAC, and around 2 nm for PEG.

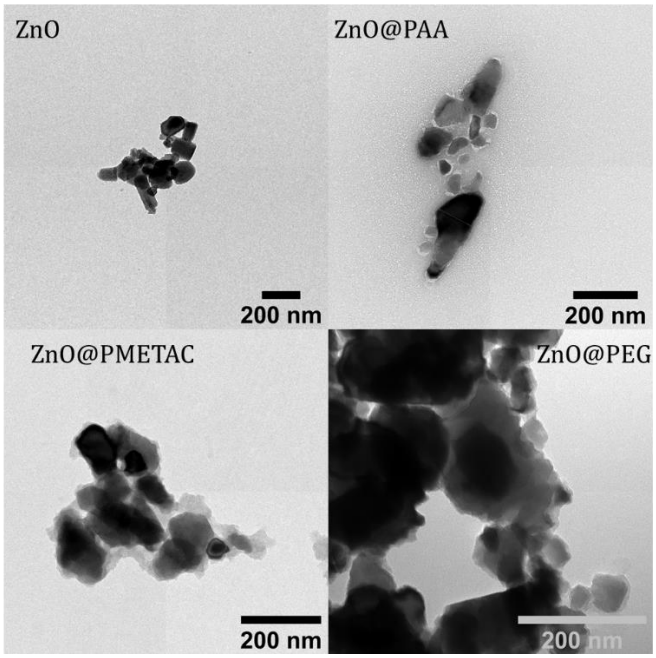

Figure 4.3. TEM micrographs of ZnO and ZnO with: PAA, PMETAC and PEG polymer brushes

TGA was performed in order to evaluate the percentage of polymer attached to the ZnO surface. TGA allows an estimation of the percentage of organic matter attached to the NP surface by monitoring the sample weight versus temperature under air or N_2 atmospheres. The weight loss corresponds to the organic matter (polymer brushes in our case) of the sample burned between 100°C and 800°C.[300] ZnO has a fusion

temperature above 1975 °C[301] so its mass remains invariant through this temperature range. As a control we performed TGA for the three polymers employed, showing a 100 % loss of weight, as expected, for a fully organic matter sample. The data (Fig. 4.4) indicate a successful grafting of the PAA polymer on the ZnO with 17.98 % of weight loss and with some differences with PMETAC (9.21%) and PEG (3.57%).

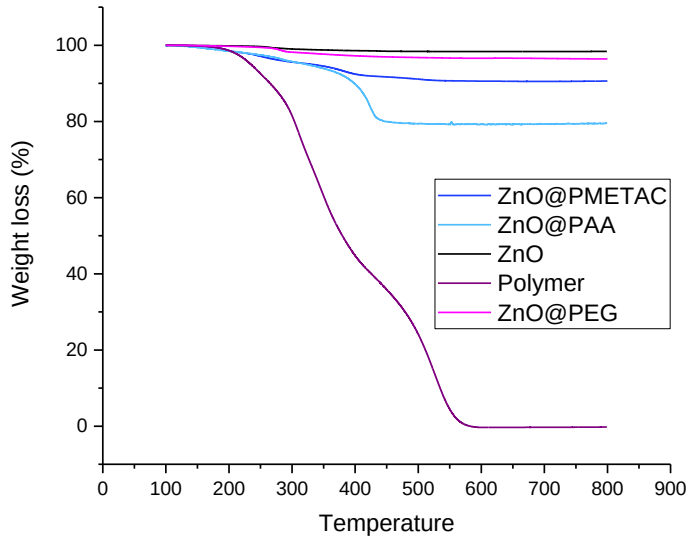

Figure 4.4. TGA measurement of: polymer, ZnO, ZnO@PMETAC, ZnO@PAA and ZnO@PEG showing the weight loss depending on the coating.

ZnO nanoparticles internalization

In Raman spectroscopy, ZnO NPs exhibit a dominant peak known as E_2, the Raman active optical phonon mode. This characteristic peak of ZnO NPs is observed at 437 cm^{-1}.[302] Lipids, proteins, and nucleic acids have characteristic Raman signatures that allow for their discrimination and make it possible to identify different regions inside the cell: lipid droplets (or bodies), the cytoplasm, or the nucleus. The position and the ratio between the peak areas allow to recognize the different compartments. Independently of the cell location illuminated by the laser, Raman bands corresponding to CH_2 and CH_3 signals correspond to lipids and proteins respectively and they are found at higher wavenumbers (2800-3050 cm^{-1}). The intensity of these band depends on the lipid and protein composition of each cellular compartment.[303] The lipid bodies can be distinguished due to the high content of CH_2 groups where the largest peak appears at 2850 cm-1, meanwhile the cytoplasm, with a higher amount of protein (and thus CH_3 groups) is characterised by the 2935 cm^{-1} band. Other signals characteristic of lipids can be found at 1754 cm^{-1} (C=O), 1656 cm^{-1} (C=C), 1440 cm^{-1} (CH_2 bend) and 1300 cm^{-1} (CH_2 twist).[304] In the cytoplasm, the contribution of proteins shows a characteristic fingerprint at 1656 cm^{-1} (amide I), 1100-1375 cm^{-1} (amide III) and 1004 cm^{-1} (phenylalanine). The nucleic acid signals at 730 cm^{-1}, 780 cm^{-1}, and 1082 cm^{-1} allow for the identification of the nucleus (Fig. 4.5).

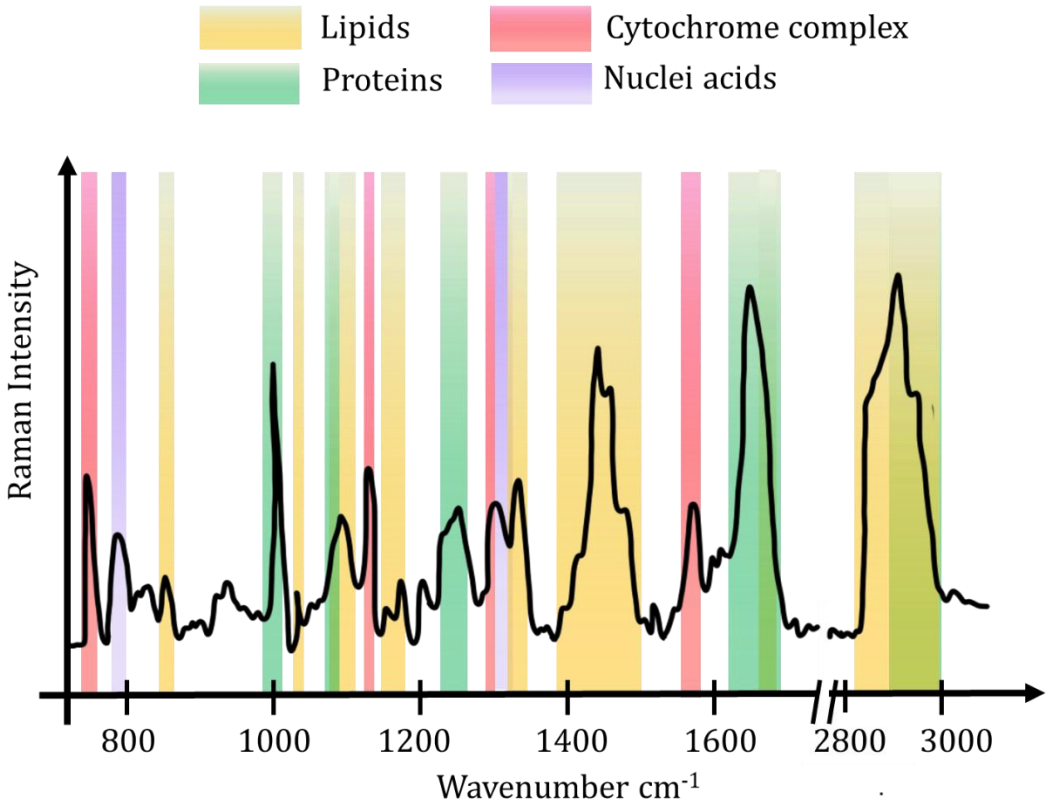

Figure 4.5. Raman spectra of A549 cells. The main contributions in the cells are due to proteins (green), lipids (yellow), cytochrome complex (red) and nuclei acids (purple). The 2800-3000 peak, which correspond to the CH_2-CH_3 signals is reduced by 3 in size in comparation with the other signals for a better visualization of the spectrum.

The Raman spectrum of cells does not overlap with the ZnO signals in the spectrum, which makes it possible to track ZnO by Raman imaging. This technique combines a confocal microscope with a Raman spectrometer. The microscope scans the cell, or the group of cells, and records a Raman spectrum of every single pixel, thereby allowing for the identification of the specific bands of ZnO, nucleus, proteins and lipids.

In our particular case, live imaging was performed. A single cell was studied at different times to monitor ZnO nanoparticle uptake. The scan time is dependent on the size of the cell and is a function of the integration time 0.03 s/pixel multiplied by the resolution of 4 pixels/nm.

Fig. 4.6. Shows a characteristic Raman spectrum between 300 and 3050 cm^{-1} for cells (green) and ZnO NPs inside the cells (red). On the cell spectrum (green) it is possible to distinguish the different signals of the cell components as shown in Fig 4.5. Peaks found at 747.68 cm^{-1} and 1082 cm^{-1} correspond to DNA. Protein signals were detected at 930-942 cm^{-1}; 1006.24 cm^{-1}, 1027.45 cm^{-1}, 1127.45 cm^{-1}, 1249.45 cm^{-1}, and 1582.65 cm^{-1} along with the lipid bands at 1254.60 cm^{-1}, 1305.94 cm^{-1}. The peaks at 1274-1500 cm^{-1}, 1650-1679 cm^{-1}, and 2800-2050 cm^{-1} correspond to different protein and lipid Raman modes.

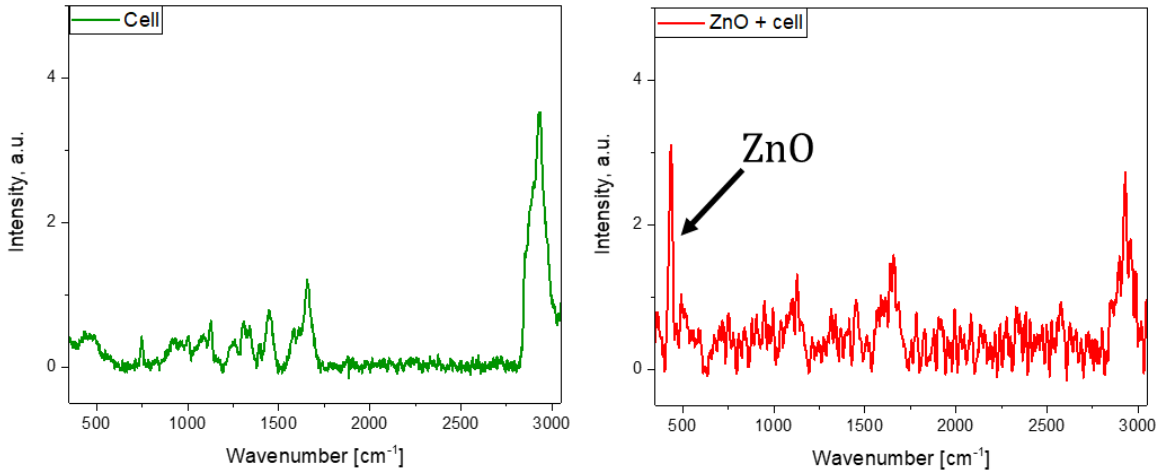

Figure 4.6. Raman spectra for A549 cytoplasm (green) and ZnO inside the cell (red). The noisy spectra are due to the short interaction time of the laser per pixel to avoid the cell death.

In the red spectrum, the ZnO Raman signal at 438.45 cm^{-1}can be identified as well as cell bands.

To trace the intracellular degradation of ZnO NPs we performed Raman cell imaging of A549 cells exposed to 15 µg/mL of NPs The NPs dissolution can be traced by the decrease in the ZnO Raman signal. Experiments were performed with pristine (unmodified) and brush coated ZnO NPs. A maximum dissolution rate was observed when living cells are exposed to pristine ZnO NPs (Fig 4.7).

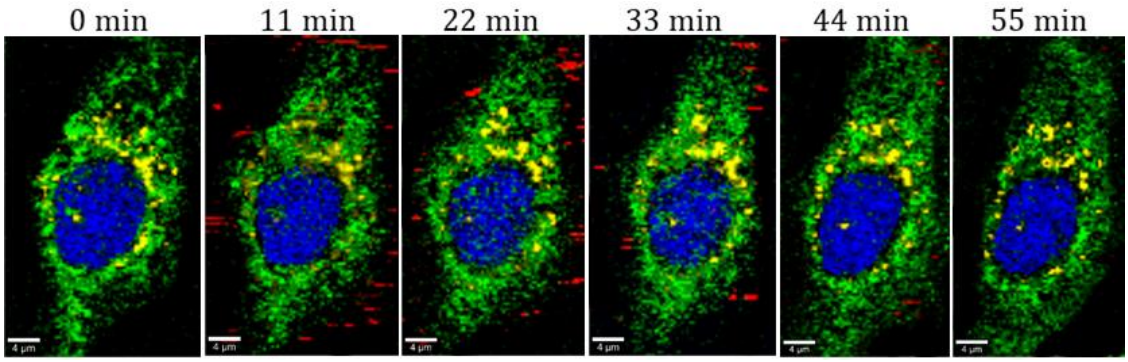

Figure 4.7. CRM life imaging results for pristine ZnO NPs. After analysis applying the pertinent filters, each element is presented in different colours: red for ZnO NPs, green for the cytoplasm, blue for the nucleus and yellow for lipid droplets. All the measurements were performed at the same z position.

The fate of pristine ZnO NPs was followed from uptake. A time series of images focusing on an individual cell were obtained (see Fig. 4.7). At time zero, i.e. 0 min, it can be seen that no ZnO NPs are observable inside the cell, however, spectral data revealed there to be a small of ZnO in the focal plane. After 11 mins, some ZnO NPs

can be detected inside the cell. Some minutes later, dissolution takes place as evidence by the lack of ZnO Raman signal at 55 min.

As in the case of pristine ZnO NPS, imaging of ZnO NPs coated with polymer brushes of PAA, PMETAC and PEG was performed. All three coatings form a barrier around the NPs, but at the same time confer the nanoparticle different surface charge: negative, positive and neutral charge respectively.

In contrast to the experiment with pristine ZnO, negatively charged PAA coated ZnO display a reduced dissolution rate. After 60 minutes, it is still possible to identify PAA coated ZnO NPs inside the cell (Fig 4.8) while it is not possible to detect bands from pristine ZnO at this same timepoint (Fig 4.7). Indeed, PAA coated ZnO NPS were still identifiable even 70 minutes after initial exposure.

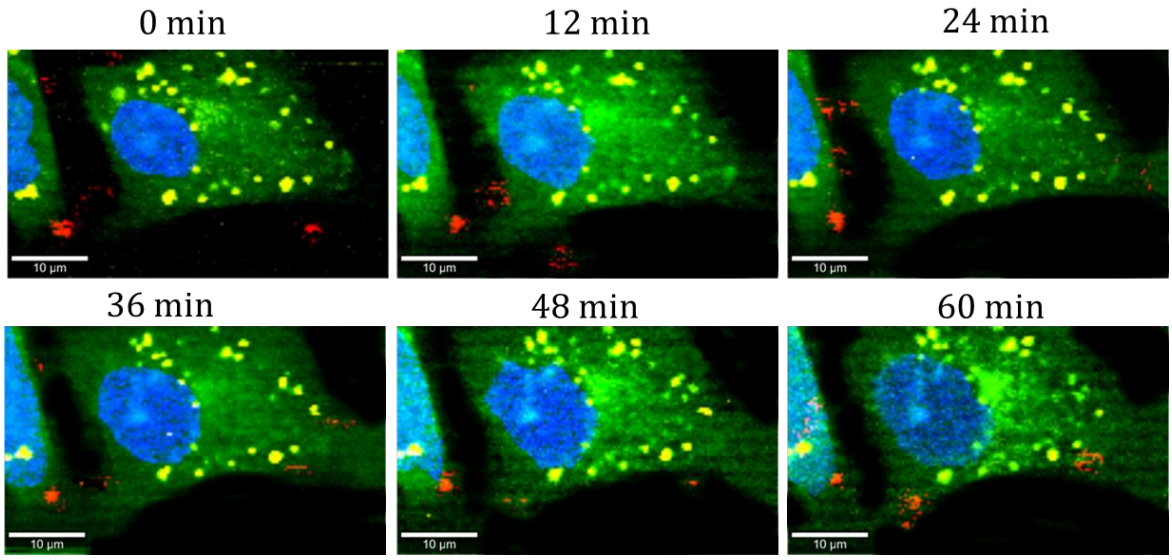

Figure 4.8. CRM life imaging results for ZnO NPs with PAA polymer brushes on their surface. In the analysis stage, different colours were used to show the different elements. In red ZnO/PAA NPs and the cell components: blue nucleus, yellow lipid droplets and green for the cytoplasm.

A neutrally charged PEG coating was employed to study the NPs internalization inside the cell. PEG is one of the most employed coatings due to its neutral charge, hydrophilicity, and flexibility reduce opsonin adhesion. Following the internalization of ZnO coated with PEG polymer brushes the dissolution of ZnO into Zn^{2+} ions is observed to be faster than PAA coated ZnO NPS, but slower than pristine ZnO NPs (Fig. 4.9). TGA and TEM show that the PEG coating is thinner than that of PAA and PMETAC. Therefore, the effectiveness as a diffusion barrier between the cell and the ZnO NPs is lower, which leads to faster dissolution times of ZnO core. Despite this fact, ZnO-PEG NPs are still found inside cells after 68 min.

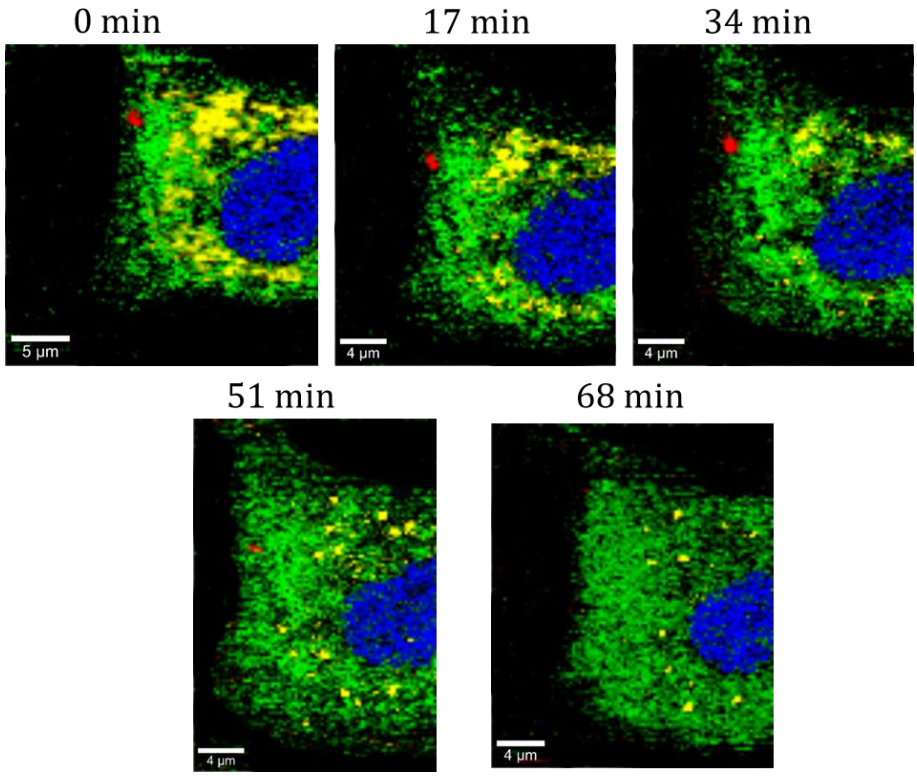

Figure 4.9. CRM life imaging results for ZnO with PEG brushes. In red ZnO/PEG NPs and the cell components: blue nucleus, yellow lipid droplets and green for the cytoplasm.

Finally, PMETAC was employed to compare the previous results with a positive charge on the surface of the ZnO NPs. Fig. 4.10, shows higher uptake than the PEG and PAA coatings. This result is expected since the interaction between PMETAC coated ZnO particles and the negative charge of the cell membrane enhances internalization.[60]

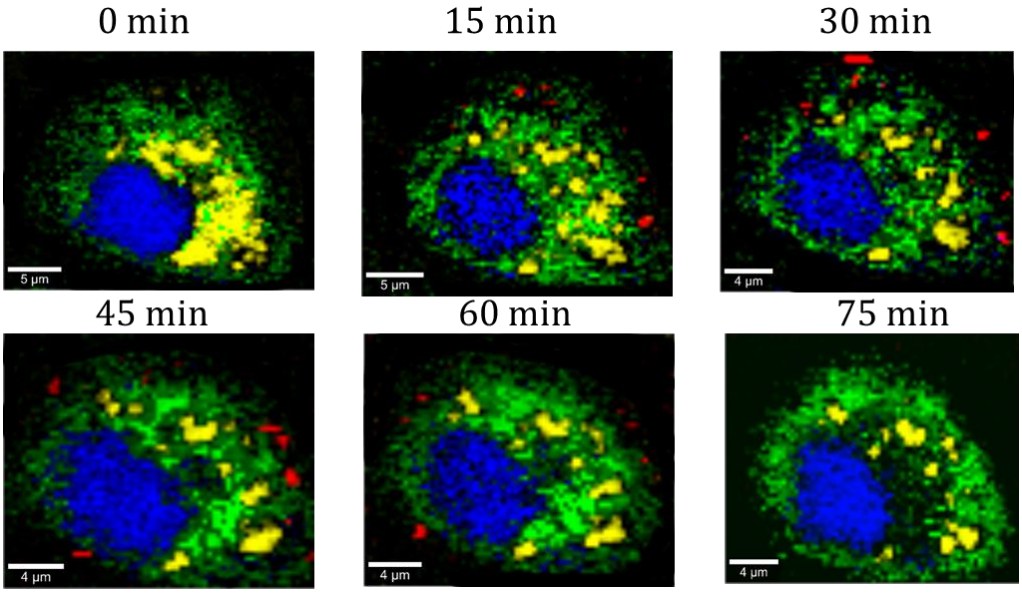

Figure 4.10. ZnO with PMETAC brushes CRM life imaging micrographs. The ZnO/PEG NPs are presented in red and the cell components: blue nucleus, yellow lipid droplets and green for the cytoplasm.

Raman analysis for the live imaging of ZnO-PMETAC NPs shows the dissolution of ZnO takes place between 60 min and 75 min.

4.4. Conclusions

In this chapter we synthesized different polymer brushes on top of ZnO NPs to study the dissolution kinetics of the ZnO core intracellularly. To characterize the materials, TGA, TEM and ζ-potential measurements were performed. Confocal Raman Microscopy was used to follow the uptake and dissolution of the materials.

The results show that independently of the polymer brush used, brush coatings drive the NP core dissolution. The characterization indicates that the shell formation around the NPs delays the degradation, i.e. a thicker polymer shell delays the dissolution of the NP core. The degradation timeframe is slower for higher density coatings such as PAA, as they act as a stronger diffusion barrier.

Chapter 5

Intracellular Fate of poly(allylamine)/siRNA Nanoparticles and siRNA Delivery

5.1. Motivation

Gene therapy is a therapeutical approach that uses genes to treat or prevent diseases.[305] Gene therapies make it possible to replace, inactivate, modify, or introduce different nucleic acids (DNA or RNA) to alter the patient's genetic sequence and mitigate a specific disease. It can be used not only in hereditary diseases, but also in cardiovascular disorders, cancer, and immune deficiencies.[184,306–309]

Four strategies can be performed in gene therapy: gene addition, gene edition, gene replacement or gene expression alteration.[310,311] The first of them, the gene addition, is carried out when a reduced expression of the gene or a dysfunctional gene produce a disorder. In this case, the addition of the functional version of the gene copy in the cell reverts the situation and leads to its correct working. This strategy its commonly used in some cardiologic diseases or cystic fibrosis among others.[312–314] Occasionally, the edition of the gene is enough to the cell correct operation. CRISPR-Cas9[315] is the most promising editing procedure and has been first probed in humans in 2016 to edit cells for lung cancer treatment.[316] In this clinical trial, Lu *et al*. modify the *PD1*-gen to improve efficacy of T cells immunotherapy.[317] Nevertheless, some diseases, especially those related with retinal degeneration, are caused by a particular gene defect being the gene replacement the best treatment.[318,319] Lastly, it exists the gene interference therapy where interference RNA (RNAi) is capable of inhibiting gene expression by blocking messenger RNA (mRNA), which is in charge of the transfer of the genetic sequence from DNA.[320,321] The mRNA codes the amino acid sequence of a protein, being therefore the pattern for its synthesis. Among the RNAi, the small interference RNA (siRNA) has been applied for the treatment of a large number of diseases such as cancer, viral infections, or brain disorders.[3,322–328] siRNA is usually composed of a double stranded chain composed of 20-25 nucleotides, which is formed from long double stranded RNA (dsRNA) chopped in small pieces by the Dicer enzyme. siRNA forms a complex with certain proteins called RNA-induced silencing complexes (RISC). One of these proteins is the argonaute (Ago), which is responsible for unwinding the siRNA. The RISC helps one of the siRNA single strands to recognize its mRNA counterpart, which results in mRNA's cleavage, meanwhile the complementary single strand can be degraded or cleaves other mRNA.[329]

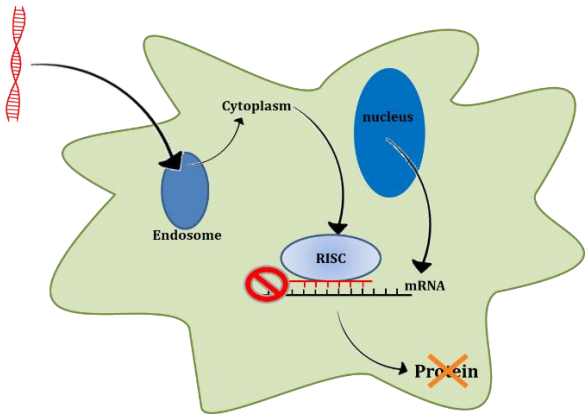

Figure 5.1. Scheme of siRNA intracellular pathway

Despite its potential, the delivery of unprotected siRNA *in vivo* is limited. siRNA molecule size is about 13 kDa, which means high possibilities to be removed by renal clearance.[330] In addition, the intracellular internalization of siRNAs is restricted due to its strong anionic nature as a result of ~40 phosphate groups. Nonetheless, siRNA can produce an immunogenic response if they interact with specific receptors such as Toll-like receptors.[331] A protection against enzyme degradation (ribonucleases or RNAses) is also needed in order to arrive to the cytoplasm.[332] The acidic pH in the lysosomes (~4.5) can also induce siRNA degradation.[333] For this reason, robust carriers are needed to protect siRNAs to guarantee, intracellular uptake, and to ensure their release from the endosome to the cytosol.[334] The most effective carriers for siRNAs are viral vectors, e.g., like lentivirus, which takes advantage of the natural mechanism of viral infection and shows high cell specificity. However, viral vectors are expensive, not always easy to produce, and are usually more associated with diseases than with treatment. Non-viral vectors have been developed as an alternative. These are usually based on cationic lipids and positively charged polyelectrolytes (polycations), which can form complexes with negatively charged nucleic acids. These vectors usually display primary amines, for promoting endosomal release.[335–339] The amines of the carrier prompt the complex through the cell membrane allowing it to arrive to the endosome where, ideally, the degradation of the complex will take place and the siRNA should be released.[340,341] When siRNA complexes have translocated to the endosomes, the complexes should degrade, and the siRNAs should be released to ensure that silencing will take place.

It is important to bear in mind that the efficacy of silencing will not only depend on the uptake of siRNA complexes, but also on their stability as complexes. They must disassemble in order to release the siRNAs following cellular uptake.[338] The intracellular fate of the liposome/siRNA and polycation/siRNA complexes is a largely unknown aspect of siRNA delivery, as it is not easy to trace the individual components, siRNAs and lipids or polymers, individually in cells. Fluorescence correlation spectroscopy (FCS) and fluorescence cross-correlation spectroscopy (FCCS) provide a means to trace the fate of both the complexes and their individual

components. FCS is a spectroscopic technique used to study the diffusion time of fluorescent molecules and objects in different matrices, including cells.[342]

In FCS, fluctuations in the intensity of fluorescence coming from molecules, or objects, at nanomolar concentrations are recorded inside a femtolitre confocal volume. Diffusion times are derived from the correlation analysis of the fluctuations in fluorescence intensity.[343] FCCS, a variation of FCS, studies the dynamic interactions between two molecules or objects labelled with spectroscopically different species.[344,345] FCCS provides the time correlation between two fluorescent objects in the confocal volume. The technique has been widely applied to study protein-protein interactions inside live cells,[346–350] and to analyse the association of oligonucleotides and polymers, both in bulk solution and in cells.[351–353]

We apply transmission electron microscopy (TEM), and dynamic light scattering (DLS) to study the formation of PAH/siRNA complexes and their structural changes depending on the nitrogen/phosphate molar ratio (N/P ratio). To gain further understanding of the mechanism of siRNA delivery, we investigate the complexation and stability of PAH/siRNA nanoparticles first *in vitro* and then intracellularly by FCS and FCCS. The biological fate and intracellular translocation of the PAH/siRNA nanoparticles was also studied by FCS/FCCS and confocal laser scanning microscopy (CLSM). Fate studies revealed that PAH/siRNA nanoparticles have a dynamic nature, which is influenced by the ratio of PAH to siRNA and the environmental conditions. Free siRNA was detected after 24 h, indicating dissociation of the nanoparticles. From our results it is possible to estimate the time scale for the disassembly of PAH/siRNA complexes inside the cell, which is a fundamental component for evaluating the efficacy of siRNA delivery and gene silencing.

5.2. Experimental Section

5.2.1 Materials

Poly(allylamine hydrochloride) salt (PAH) (17.5 x 10^3 g/mol), Cy5-siRNA, hydrochloric acid (HCl), and sodium hydroxide (NaOH) were purchased from Sigma-Aldrich, USA. PAH labelled with green rhodamine (G-PAH) was provided by Surflay GmbH, Germany. Human lung adenocarcinoma cell lines (A549 CCL185) were obtained from the American Type Culture Collection (ATCC), USA. UltraPure DNase/RNase-Free Distilled Water and Nunc™ Lab-Tek™ Chambered Cover glasses were purchased from ThermoFisher Scientific, USA. RPMI 1640 medium was purchased from Lonza, USA. HyClone™, fetal bovine serum (FBS) was purchased from ThermoFisher Scientific, USA, and penicillin and streptomycin from Sigma Aldrich, USA. RPMI medium without phenol red and Leibovitz's L-15 medium without phenol red were purchased from ThermoFisher Scientific, USA.

5.2.2 PAH-siRNA Complexes synthesis and characterization

To synthesize the complexes, PAH (17.5 kDa) and siRNA (13 KDa) were mixed in RNase-free water at room temperature. The one-step synthesis is driven by electrostatic and hydrogen bonding interactions between the amines of PAH and the phosphate groups of siRNAs. Throughout the study the complexes are named according to the molar ratio of nitrogen groups from PAH to the phosphate groups from siRNA(N/P).
Nitrogen/phosphate (N/P) molar ratios from 0.5 to 40 were tested.

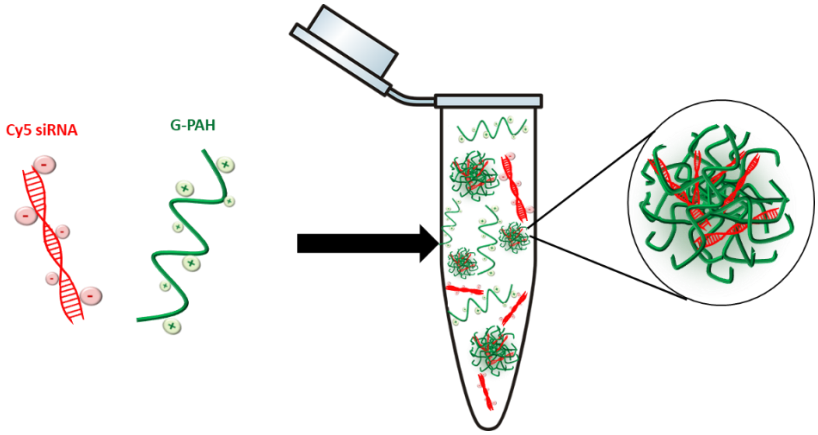

Figure 5.2. PAH/siRNA complexes synthesis.

The size of the complexes for the different N/P molar ratios was studied by dynamic light scattering (DLS) and transmission electron microcopy (TEM). For DLS measurements a Malvern ζ-Sizer Nano ZS in backscattering mode was used with a 173° scattering angle. Samples were measured in 1 mL polystyrene cuvettes in triplicate at 25 °C. For TEM imaging 5 µL complexes were placed on an ultrathin plasma coated carbon film. Then 3 µL of ammonium molybdate (20 mg·mL^{-1}) serving as a negative stain was added. The carbon film was washed 3 times with nanopure water and left to dry for at least one hour. TEM images were obtained on a JEOL JEM 1010 transmission microscope with and acceleration voltage of 100 kV.

5.2.3 Complex Stability

For the stability studies, complexes with ratios N/P = 40, 4, 2 and 1 were synthetized using green rhodamine labelled PAH (GPAH) and cy5.5 labelled siRNA. The equilibration time was 30 min at room temperature. Fluorescence cross-correlation spectroscopy (FCCS) is the technique chosen to study the complex formation and stability. A Zeiss LSM 880 confocal microscope with Zen black software was used to carry out the experiments. Samples were placed in NuncTM Lab-Tek Q5 Chambered Coverglass (Thermo Fisher Scientific, USA). The confocal volume was determined using 25 nM Rhodamine 123 solution. Fluorescence was detected in GaASP and PMTr detectors simultaneously in the range 500-560 nm and 650-710 nm, respectively. Measurements were performed with a Zeiss C-Apochromat 40x, numerical aperture 1.2 water immersion objective. Stability

studies were performed at different pHs. To change the pH of the medium, 1 M HCl and 1 M NaOH solutions were used. For each sample 20 runs of 10 s were performed. Data analysis was carried out using QuickFit 3.0 software.[281] A 3D normal diffusion model was applied to fit the data with 2 components. In case 2 components data was not effective a 1 component 3D normal diffusion model was implemented. From the diffusion coefficient, we can then calculate the hydrodynamic radius applying the Stokes-Einstein equation: $r_H = \kappa_B T (6\pi\mu D_C)^{-1}$

Complex stability was also studied in non-fluorescent RPMI 1640 enriched with 10% of FBS and 1% of antibiotics (100 units/mL penicillin, 100 mg/mL streptomycin; P/S) to evaluate the complex stability.

5.2.4 Cell Culture

A549 epithelial cells from a human lung carcinoma were cultured in RPMI 1640 medium with 10% FBS and 1% P/S (full RPMI) at 37°C and 5% CO_2 in an incubator. GFP-A549 cells were cultured in Ham's F-12 K medium supplemented with 10% FBS, 1% P/S and blastidicin at 10 µg/mL in the same incubator.

5.2.5 Cellular Uptake of Complexes

Cell uptake of complexes was studied with flow cytometry for complexes with N/P ratios of 2 and 4. A549 cells were exposed to complexes and incubated for between 3 and 24 h at 5% CO_2 and 37 °C. Afterwards, cells were washed and tripsynized Measurements were done in duplicate, up to around 10000 events/sample in a BD-FACs Canto II cytometer. A549 cells were used as a control in the uptake experiments where the cy5-siRNA fluorescence was quantified.

5.2.6 Biological Fate of Complexes via FCCS

Approximately 40000 A549 cells were seeded in each well with 500 µL of full RPMI. After 24 h cells were washed three times with PBS and incubated with 200 µL of N/P 2 complexes with full RPMI. One hour later the time zero wells were washed 3 times with PBS in order to remove the non-internalized complexes. 200 µL of free serum L15 medium was added to perform the experiments in the microscope. Same process was carried out for the 24h wells. In all cases, data were recorded for at least 3 cells in different positions within each cell and 20 runs of 10 seconds each.

5.2.7 Co-localization of Complexes via CLSM

Cell samples were prepared as previously described for FCCS and imaged with a Zeiss LSM 510 confocal microscope with Zen black software. Samples were placed in NuncTM Lab-Tek Q5 Chambered Coverglass (Thermo Fisher Scientific, USA) were measured with a 63 x oil objective (NA 1.4). As in FCCS, the detectors employed to measure fluorescence simultaneously were GaASP and PMTr in the range 500-560 nm and 650-710 nm respectively.

Co-localization analysis was carried out with JACoP plugin from ImageJ. The Otsu Thresholding plugin was also used.[354]

5.2.8 In vitro siRNA transfection

For the siRNA transfection experiments, GFP-A549 cells and non-fluorescent complexes were used. Approximately 30000 GFP-A549 cells were seeded in a 24 well plate with full RPMI 24 h before doing the experiments. Once the cells grow, they were washed with RPMI 3 times. As controls, lipofectamine RNAiMAX and PEI/siRNA nanoparticles were used. These nanoparticles and the complexes formed by PAH/siRNA were transfected and followed over a 96 h period. To quantify the silencing efficacy, the cells were PBS washed and trypsinized before measuring their fluorescence in the flow cytometer as in the uptake experiments. All the samples were measured in triplicate.

5.3. Results and Discussion

Complex characterization

To evaluate the complexation of the PAH and siRNA, the amount of siRNA was fixed while the concentration of PAH was varied. In this way it is possible to establish the best N/P molar ratio for complex formation. Best results were obtained with N/P ratio of 2.

Results from DLS and TEM for N/P = 2 complexes are presented in Fig. 5.3. The diameter distribution histogram by intensity shows a hydrodynamic diameter of 98 ± 4 nm with a 0.23 ± 0.03 nm polydispersity index. TEM results confirm the DLS results and show rounded nanoparticles with a size of 80 ± 22 nm.

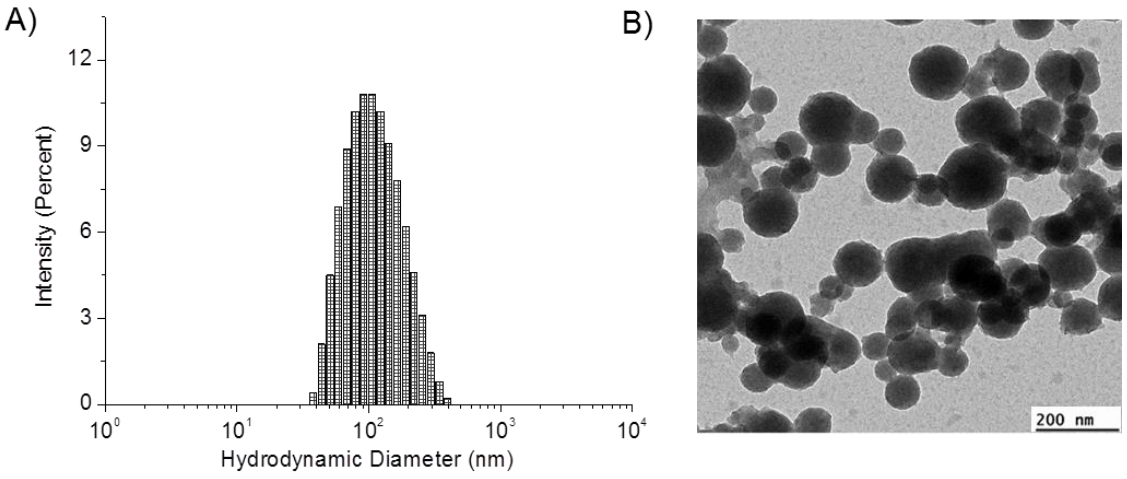

Figure 5.312. A) DLS and B) characterization of PAH/siRNA complexes at molar ratio N/P 2

For FCCS measurements, first it is necessary to carry out controls with G-PAH and R-siRNA (Fig. 5.4) in order to confirm that there is no cross talk between the detection channels. The cross-correlation function (in black) and the autocorrelation function

of the non-present species in the solution (red in Fig. 5.4A and green in Fig. 5.4B) are zero indicating that the PAH fluorescence does not interfere in the siRNA fluorescence detection and vice versa. The diffusion coefficients obtained for the single species were: $D_{G\text{-}PAH}$ = 48.5 ± 6.01 $\mu m^2 \cdot s^{-1}$ and $D_{R\text{-}siRNA}$ = 22.55 ± 2.05 $\mu m^2 \cdot s^{-1}$.

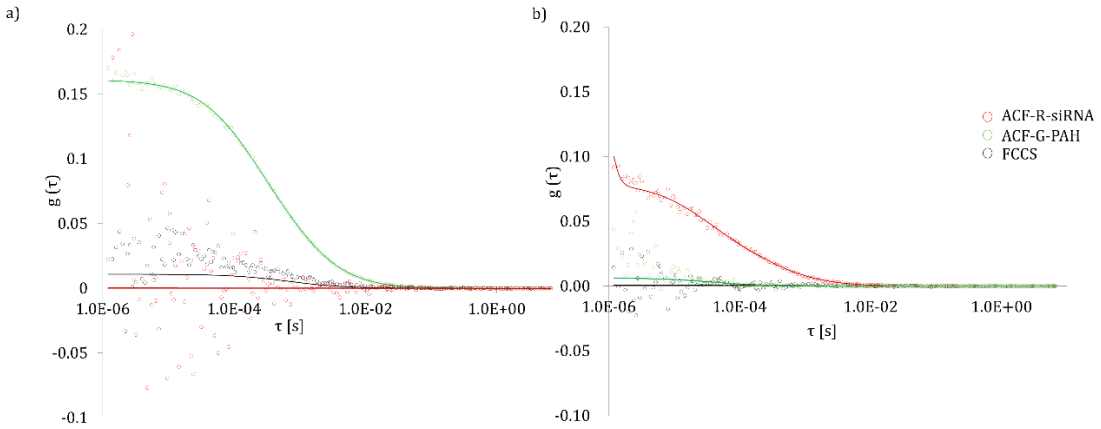

Figure 5.4. FCCS results of: a) G-PAH and b) R-siRNA as control.

Once the control measurements were done, different ratios of N/P were used, an excess of amines to phosphates (N/P>1), the same amount of amines and phosphates (N/P~1) or small amount of amines in relation to phosphates (N/P<1). The differences in PAH/siRNA complexes composition can be observed by the relative cross-correlation (Table 5.1). With some simplifications, the relative cross-correlation is the ratio between the cross-correlation amplitude at time zero and the autocorrelation amplitude of each specie at time zero, which reveals the fraction of single species in the sample. It may have the values from 0 to 1 where 0 indicates no association between the two species and 1 the complete association.

	FCCS/ACF_G-PAH	FCCS/ACF_R-siRNA	D_c [$\mu m^2 \cdot s^{-1}$]	R_C [nm]
G-PAH	-	-	45.1±4.1	4.6±0.4
R-siRNA			97.1±12.2	2.1±0.2
N/P 0.6	0.04	1	28.5±0.2	7.5±0.1
N/P 1.2	0.1	1	9.5±0.1	22.6±0.2
N/P 2.4	0.4	0.2	5.2±0.1	41.3±0.8
N/P 4	0.2	0.3	3.5±1.2	61.2±23.8

Table 5.1. FCCS data obtained from the fitting of the curves. FCCS/ACF_G-PAH and FCCS/ACF_R-siRNA are the relative cross-correlation, D_c and R_c the diffusion coefficient and hydrodynamic radius of the complexes, except in the cases G-PAH and R-siRNA where D_c and R_c indicates the diffusion coefficient and the hydrodynamic radius of the free G-PAH and R-siRNA.

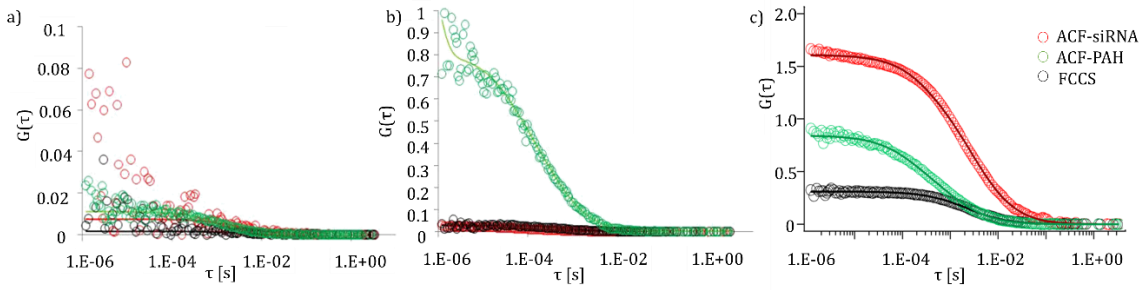

Figure 5.5. FCCS results from: a) N/P 0.6, b) N/P 1.2 and c) N/P 2. Red and green circles represent the autocorrelation function (ACF) of siRNA and PAH respectively. Black circles refer to the cross-correlation between both species.

Complexes with a slight excess of phosphates (ratio N/P 0.6) (Fig. 5.5a) are the smallest with a hydrodynamic radius of approximately 7.5 ± 0.1 nm. Regarding its relative cross-correlation, all the siRNA is associated to the complexes (FCCS/ACF-siRNA = 1) as in the case of ratio NP 1.2. Increasing the N/P ratio to 1.2 (Fig. 5.5b) the complex is formed, and the size grows to 22.6 ± 0.2 nm. In this case, the relative cross-correlation (Table 5.1) indicates that R-siRNA is completely associated (FCCS/ACF-siRNA = 1) to the complexes and there is an excess of free G-PAH (FCCS/ACF-PAH = 0.1). This G-PAH has a diffusion coefficient of 48.5 ± 6.0 $\mu m^2 \cdot s^{-1}$, 10 times faster than the nanoparticle diffusion coefficient 4.75 ± 0.05 $\mu m^2 \cdot s^{-1}$. Increasing the amount of amine groups to a molar ratio N/P 2.4, larger complexes with free species of R-siRNA and G-PAH were found (Fig. 5.5c). The diffusion coefficient of the complexes in this case is 2.6 ± $\mu m^2 \cdot s^{-1}$ which results in a hydrodynamic radius of 41.3 ± 0.8 nm. The values of relative cross-correlation (Table 5.1) indicate that complexes are in equilibrium with free G-PAH (FCCS/ACF-PAH = 0.4) and R-siRNA (FCCS/ACF-siRNA = 0.2). Cross-correlation for N/P ratios with a higher excess of G-PAH is zero, meaning that it is impossible to form complexes (Fig. 5.6).

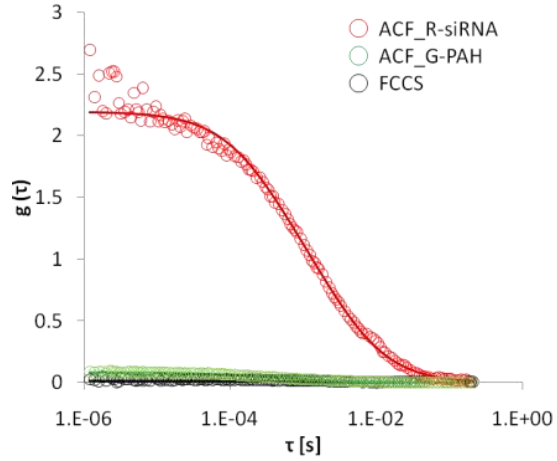

Figure 5.6. FCCS results for N/P = 4. Red and green circles represent the autocorrelation function (ACF) of siRNA and PAH, respectively. Black circles refer to the cross-correlation between both species.

Complexes stability in cell media

As previously mentioned, nanoparticle stability needs to be studied to understand the behaviour of the complexes in the local environment of the cell.

For that propose, complexes at different N/P ratios (N/P > 2, N/P = 2 and N/P < 2) were prepared in RNAse free water. After 30 min they were diluted in complete RPMI (10% FBS and 1% antibiotic) without phenol red and incubated for a further 30 minutes.

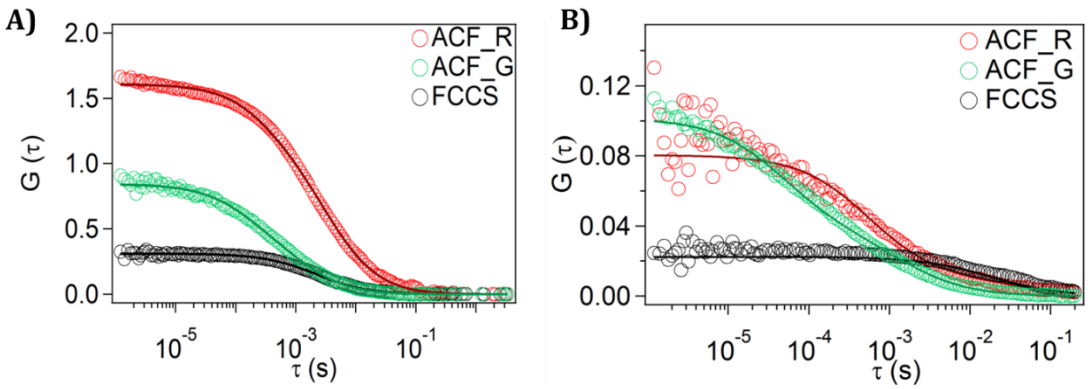

Figure 5.7. FCCS results for: A) complexes N/P 2 in RNAse free water and B) complexes N/P 2 diluted in full RPMI

With a ratio of N/P = 2 the complexes retain the cross-correlation (Fig 5.7B), but doubled the diffusion coefficient and the size in relation to previous results, obtaining: D_C = 2.1 ± 0.1 $\mu m^2 \cdot s^{-1}$ and R_C = 102.2 ± 4.9 nm The relative cross-correlation remains close to 0.3 for siRNA and PAH (Table 2), similarly to the case without proteins (Table 1) indicating that complexes are in equilibrium with the free molecules of G-PAH and R-siRNA.

For complexes with N/P different than 2 (Table 5.2), especially with the excess of amines, form aggregates with diffusion times exceeding the temporal resolution which is limited to the millisecond time producing the stoppage of the system (Fig 5.8).[355]

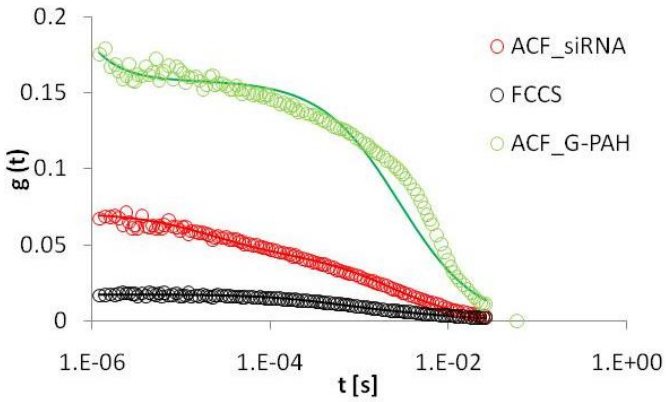

Figure 5.8. FCCS results for complexes with a molar ratio of N/P = 4 where it is possible to see that the green curve corresponding to G-PAH exceeds the technique limit

These changes in diffusion time may be due to the presence of proteins resulting in the formation of a protein corona, or the association of nanoparticles with proteins which affect the stability of the complexes.[356,357] It could also be attributed to conformational changes in the free molecules.[358] RPMI medium is composed of different salts (~ 150 mM NaCl) and phosphate ions (~ 5 mM Na_2HPO_4) that can interact with the G-PAH and replace the R-siRNA molecules.[339] This situation is not seen in the case of N/P = 2 meaning that the complexes are stable in full RPMI

Analysing the autocorrelation function of G-PAH and R-siRNA separately in RPMI full media, it is possible to obtain information about the stability of these species in RPMI. The diffusion coefficient of the siRNA remains stable around 43 $\mu m^2 \cdot s^{-1}$, the opposite is seen for PAH were the diffusion coefficient changes from 12.9 ± 0.6 $\mu m^2 \cdot s^{-1}$ to 97.1± 12.2 $\mu m^2 \cdot s^{-1}$. It seems that PAH, which is a flexible polymer, undergoes a conformational change due to changes in the ionic strength, the pH and the RPMI components.[359]

	D_c ACF_G-PAH	D_c ACF_R-siRNA	D_c FCCS
G-PAH	97.1 ± 12.2	-	-
R-siRNA	-	43.0 ± 2.6	-
N/P 0.6	6.9 ± 0.5	3657 ± 335	1358 ± 96
N/P 1.2	0.7 ± 0.1	6905 ± 603	20009 ±2520
N/P 4	Exceeds the technique limit	5.9 ± 0.5	1.3 ± 0.1

Table 5.2. Diffusion coefficients for free species of G-PAH and R-siRNA and different N/P complexes

Complex stability at different pHs

The stability of PAH/siRNA nanoparticles at biologically relevant pH values was studied to assess their potential for the intracellular delivery of siRNA. The ideal nanocarrier for siRNA drug delivery should provide protection against degradation before arriving to the target, with long blood half-time and efficient endosomal release. It basically means that at physiological pH (7.4) it should be stable and disassemble at endosomal pH (~5). Therefore, the R-siRNA can be released and delivered in the cytoplasm and start the siRNA pathway.[359,360] Stability studies were done at different pH values, from 7.4, where particles are assembled to acid and basic environments for complexes N/P = 2 (Fig. 5.9). While the pH acidifies, the cross-correlation amplitude at time zero decreases indicating that the complexes are rearranging or/and even disassembling before reaching pH 2. The amplitude of the

autocorrelation functions at time zero is inversely proportional to the number of particles. Regarding the autocorrelation function of the G-PAH (Fig. 5.9B) and R-siRNA (Fig. 5.9A) their amplitudes decrease, pointing out the number of free species in the confocal volume in both cases increases supporting the complex disassembly. This hypothesis is confirmed with the decrease in the cross-correlation amplitudes (Fig. 5.9C) which is directly related to the number of complexes displaying both labels.

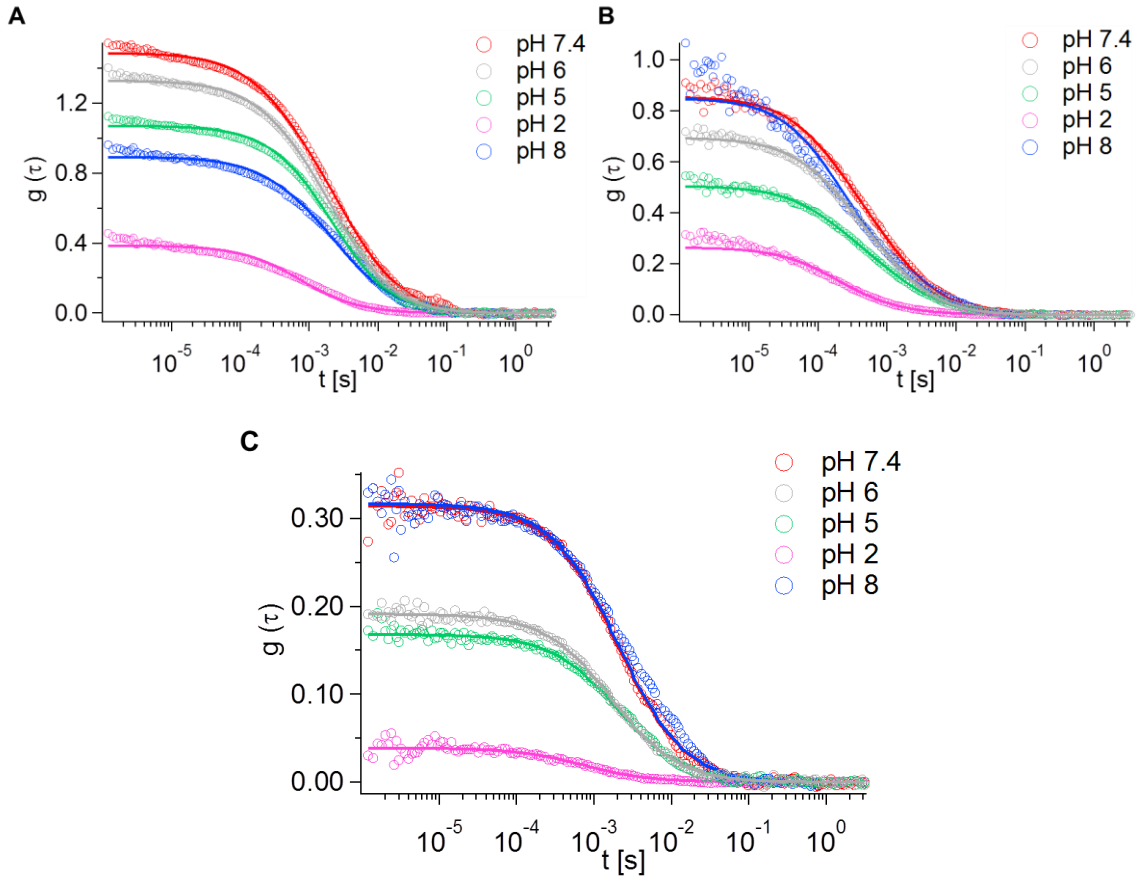

Figure 5.9. Autocorrelation function of: A) R-siRNA, B) G-PAH, C) cross correlation of complexes (N/P 2) at different pH.

The nanoparticle size is also affected by the decreasing pH (Table 5.3). The hydrodynamic radius decreases from 41.3 ± 0.8 nm (Dc = 5.2 ± 0.1 $\mu m^2 \cdot s^{-1}$,) at pH 7.4 to 11.1 ± 0.2 nm at pH 2 (Dc = 19.3±0.3 $\mu m^2 \cdot s^{-1}$).

Once the G-PAH/R-siRNA complexes are at pH 2, NaOH is added to increase the pH (blue dots) and the possible changes observed. All the amplitudes at time zero increase, indicating a higher complexation than at pH 2. The increase of the G-PAH and R-siRNA autocorrelation amplitudes at time zero means that there are less free species in the confocal volume. Complementary, the cross-correlation amplitude at time zero grows which indicates the complexation of the species. Regarding the hydrodynamic radius, the values increase with increasing pH to 107.4 ± 2.6 nm, 30% larger than at pH 7.4 (Table 5.3).

	pH 7.4	pH 6	pH 5	pH 2	pH 8
FCCS/ACF_G-PAH	0.4	0.3	0.3	0.1	0.4
FCCS/ACF_R-siRNA	0.2	0.1	0.2	0.1	0.4
t_D [µs]	2973±73	2707±128	2192±103	799±13	3888±140
D_C [µm²/s]	5.2±0.1	6.0±0.3	7.5±0.3	19.3±0.3	4.0±0.1
r_H [nm]	41.3±0.8	35.8±1.8	28.6±1.1	11.1±0.2	53.7±1.3

Table 5.3. FCCS data obtained from the fitting curves when complexes are exposed to different pH. FCCS/ACF_G-PAH and FCCS/ACF_R-siRNA are the relative cross-correlation, D_c and R_c the diffusion coefficient and hydrodynamic radius of the complexes, except in the cases G-PAH and R-siRNA where D_c and R_c indicates the diffusion coefficient and the hydrodynamic radius of the free G-PAH and R-siRNA

Observing the results for the single species of PAH and siRNA we can that their autocorrelation functions remain stable for changes in pH (Fig. 5.10).

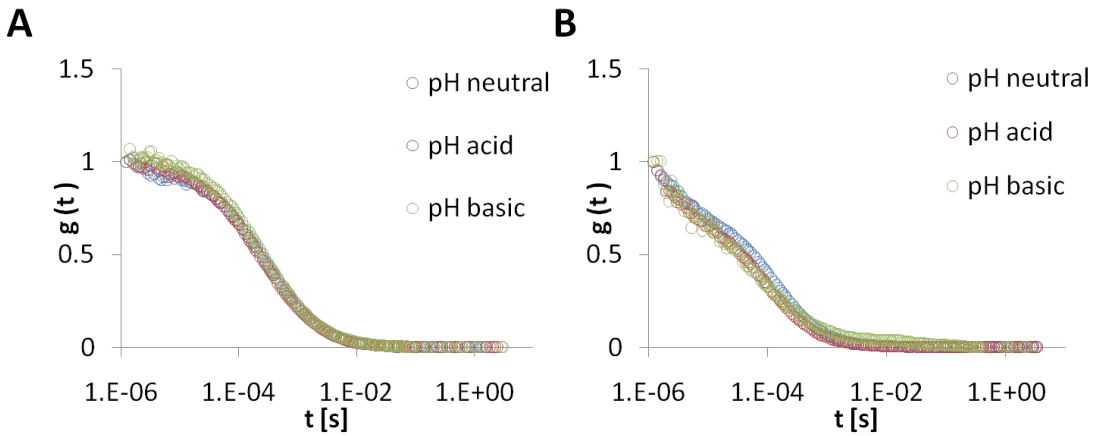

Figure 5.10. Autocorrelation function of: A) G-PAH and B)R-siRNA at pH basic, acid and neutral. Not differences were noticed.

In summary, pH changes can produce the re-assembly of the species as nanoparticles with different diameter. pH induces charge variations of the components, with siRNA phosphate groups loosing charge in acidic pH conditions, thereby inducing the disassembly of complexes. At basic pH, the amine groups of the PAH presumably retain enough charges to form complexes with the siRNA, however, the electrostatic repulsion between the PAH chains of the same charge decreases, which allows the nanoparticles to grow in size.

This data obtained by FCCS supports the system stability in solution. The system is stable at physiological pH and can be disassembled at acidic pH hinting at the potential release of siRNA inside the endosomes.

Intracellular flow cytometer studies: Complex uptake

The uptake of complexes with different N/P molar ratios was studied in A549 cells via flow cytometry using cy5 labelled siRNA. In this way, it is possible to compare the changes in mean fluorescence intensity at different time points and different N/P ratios. Cells were washed and tripsynized in order to obtain cell suspensions 3 h and 24 h after incubation. In Fig. 5.11 the mean fluorescence per cell is shown as a function of the incubation time for control, N/P = 2 and N/P = 4. The control measurements for the cells was performed with untreated A549 to see possible autofluorescence from the cell line.

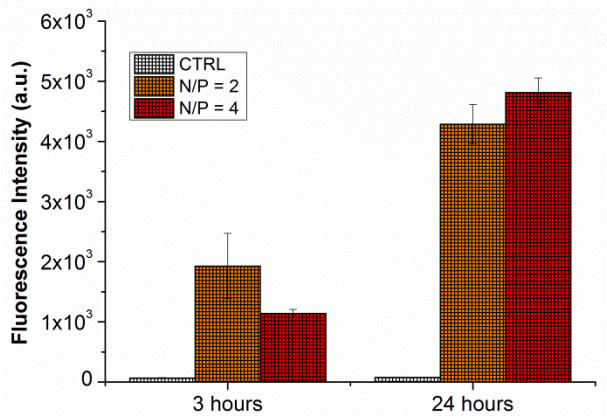

Figure 5.11. Mean fluorescence intensity of A549 cells, PAH/R-siRNA complexes N/P 2 y N/P 4 as function of incubation time 3 h and 24 h

Increasing the incubation time, the fluorescence intensity increases independently of the N/P ratio. For both ratios, there are no significant changes possibly due to the relative cross-correlation for PAH and siRNA the values at N/P 2 and N/P 4 are really similar (Table 5.1).

Intracellular FCCS studies: Trafficking in live cells

One of the main objectives of this chapter is the intracellular tracking of the complexes and the single species over the time. FCCS allows us to study this intracellular trafficking at distinct locations within A549 live cells at different time points. Experiments at 1 h, 6 h, 12 h and 24 h were performed, with results from 1h and 24 h being the most relevant results.

In the FCCS experiment, confocal images were taken in order to select different points in the cell, such as cell membrane surroundings, nucleus, cytoplasm, etc. The selected points inside the cell were measured 20 times for 10 seconds. For samples incubated for 1 h we observe photobleaching as shown below in Fig. 5.12. It can be seen that the count rate drops from an initial value of approximately 45 kHz to 20 kHz over the 10 s measurement time.

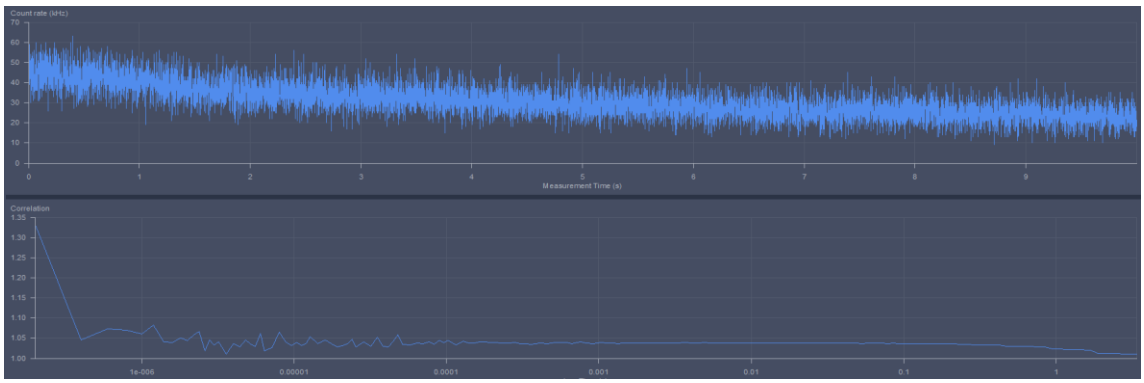

Figure 5.12. Screenshot of acquisition window in Zen 3.0 black software. In the image above is possible to see the count rate (average intensities) which starts at 45 kHz and decrease close to 20 kHz. The lower panel corresponds to the resulting autocorrelation function with long difussion times due to the association with large molecules.

When bleaching occurs in one of the three channels, or in all of them, the first 20 s were reported separately from the rest of the averaged data (solid and empty dots in Fig. 5.13, respectively). After 1 h of incubation, PAH and siRNA were associated with big cell machineries and/or fixed structures that prevented their free diffusion in cell compartments.[361] This observation is supported by the detection of many events of fluorescence bleaching (Fig. 5.13). Since the large and slow-diffusing complexes remain longer in the confocal volume, they are irradiated longer and experience bleaching. Once these large aggregates are bleached, the fluorescence intensities in the confocal volume are significantly lower, making it possible to detect fluorescence fluctuations from fast-diffusing species.[362] Only a small part of these "fast" species showed cross-correlation (7% of the total of the measures). A total of 79% of the fast-diffusing species were G-PAH (Fig. 5.14). After 24 h, bleaching events were significantly reduced and individual PAH and siRNAs are detected (Fig. 5.13). This observation suggests a decrease in co-localization of siRNAs and PAH. Interestingly, at this time-point 83% of the individually diffusing species are R-siRNA molecules. The diffusion times of these molecules varied significantly from 300 µs to10^4 µs The wide distribution of diffusion times can be ascribed to the R-siRNAs interacting with several cellular proteins or machineries, or experiencing environments of different viscosity inside the cells.[361] It is plausible that R-siRNAs showing diffusion times of ~ 300 µs might be localized in the cytoplasm where the viscosity is similar to that of RPMI cell medium 83% of the individually diffusing species is R-siRNA molecules.

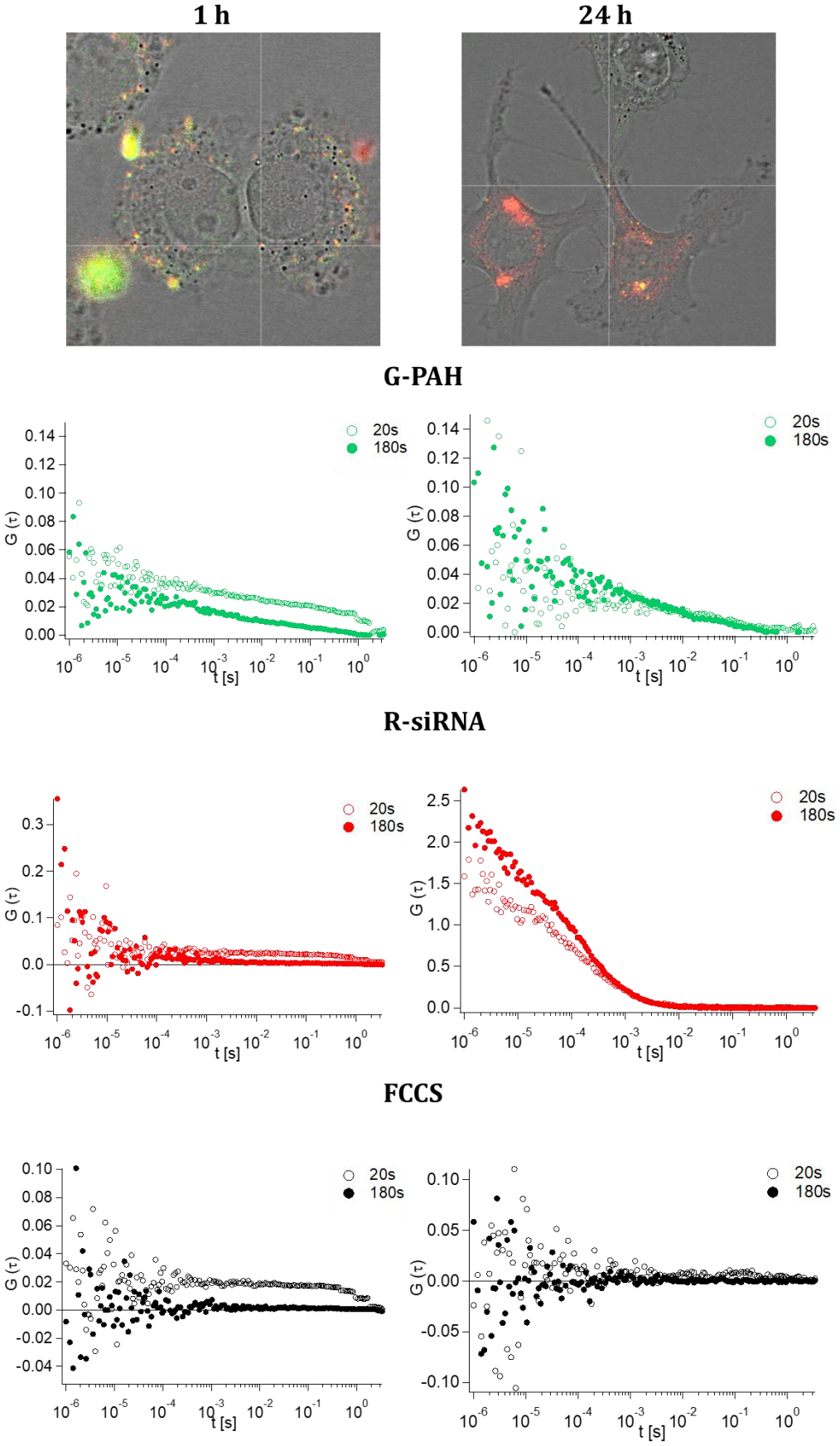

Figure 5.13. Confocal images of A549 cells at 1 h and 24 h later for G-PAH/R-siRNA complexes and their autocorrelation function in the red (R-siRNA) and green (G-PAH) channel and the cross-correlation function.

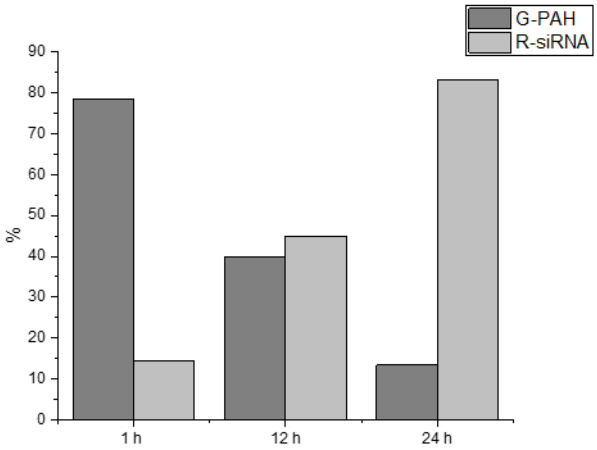

Figure 5.14. Percentage of free G-PAH and R-siRNA at times 1 h, 12 h and 24 h for 44 measurements.

Co-localization studies via CLSM

Co-localization experiments were performed at different time points to corroborate our FCCS findings. To evaluate statistically the colocalization, two indexes were used Pearson's coefficient (r) and Mander's coefficients (M1 and M2).[363] Pearson's coefficient measures the correlation between two variables showing values from 1 to -1 where 1 means total correlation between the intensities of two images and -1 absence of correlation.[364] On the other hand, Mander's coefficients based in Pearson's coefficient indicate the percentage of overlapping between two images. In this case, the values vary from 0 to 1.[365] *M1* definition is the ratio between "summed intensities of pixels from the green image for which the intensity in the red channel is above zero" to the "total intensity in the green channel".[366] *M2* has same definition but for the red channel.

In Fig. 5.15 is possible to appreciate the diminish in the co-localization of species after 24 h with a reduction of 50% of all the coefficients. The decrease in co-localization corroborates the FCCS results and is attributed to the intracellular disassembly of the PAH/siRNA complexes.

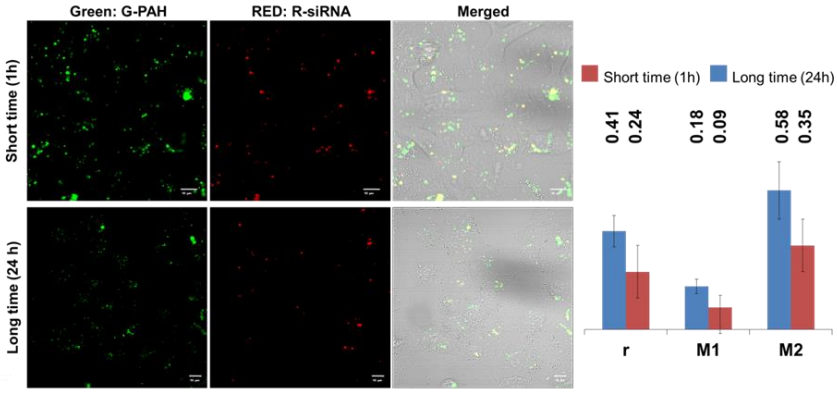

Figure 5.15. CLSM images for G-PAH, R-siRNA and merge of them with the confocal transmission image. Micrographs were done after 1 h and 24 h after incubation with N/P =2 complexes.

The fate of the nanoparticles inside cells is sketched in Fig. 5.16. After cellular uptake, complexes are translocated to endosomal compartments displaying acidic pH that favours their spontaneous dissociation and the diffusion of siRNA in the cytoplasm.

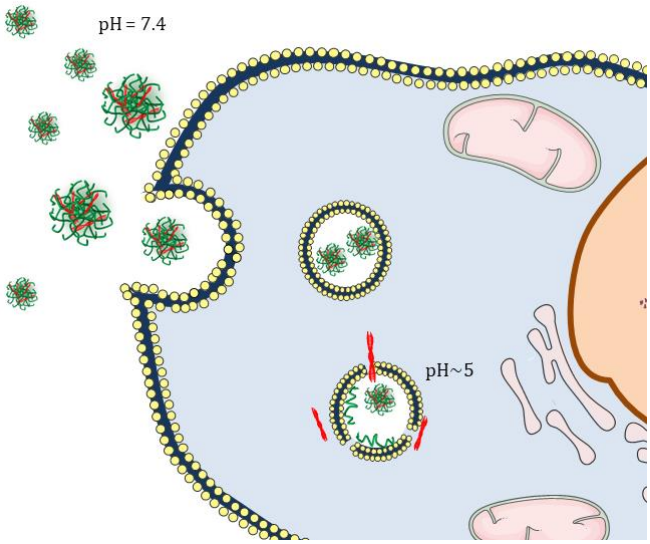

Figure 5.16. Scheme of the uptake and intracellular fate of PAH/siRNA complexes. The degradation of the complexes in the endosome is shown by the presence of free PAH (green) and siRNA (red) at low endosomal pH. The translocation of the siRNAs from the endosomes to the cytoplasm is indicated by the presence of free siRNA outside endosomal compartments

siRNA Transfection

The GFP-A549 cell line was used for silencing experiments because it has a stable expression of GFP that can be knocked down by the delivery of specific siRNAs. Flow cytometry analysis was carried out to quantify the efficacy of siRNA delivered by PAH/siRNA nanoparticles. It allows the evaluation of the efficacy of GFP silencing by measuring the fluorescence intensity per cell after transfection (Fig. 5.17). Transfections were performed using different N/P ratios. The expression level of GFP in GFP-A549 cells, decreased by ~ 55% in cells treated with N/P = 2 compared to untreated cells. For N/P = 4, the fluorescence intensity of the cells decreased by up to 75%, indicating good silencing efficiency of PAH/siRNA nanoparticles. When naked siRNA was used as a control, no inhibition of GFP expression was observed.

The higher efficacy shown by PAH/siRNA could probably be attributed to the better complexation by PAH, a linear polymer with only primary amines, to siRNA with a relatively small excess of amine groups to phosphate. PAH/siRNA nanoparticles have the advantage of being highly stable in neutral environments and disassembling at endosomal pH values, which favours the liberation of the siRNAs. At this pH, PAH molecules protonate and can induce endosomal breakage, which can also trigger the translocation of siRNAs into the cytosol.

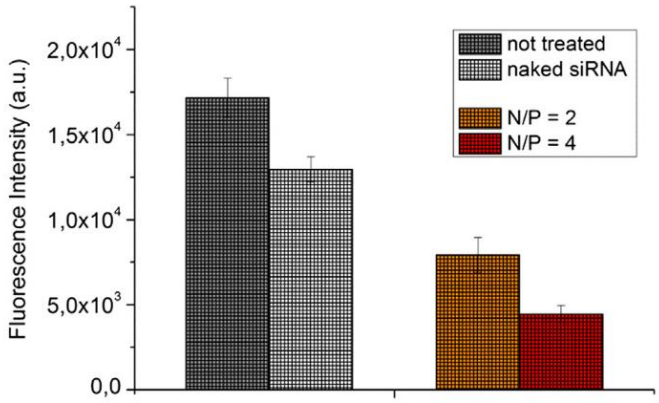

Figure 5.17. Fluorescence intensity (u.a.) via flow cytometry in: not treated cells (dark grey), naked siRNA (light grey) and NP2 (orange) and NP4 (red) complexes

It is possible to see in Fig. 5.17 that naked siRNA does not produce effective silencing, meanwhile GFP-A549 expression decreases by around 55 % when complexes N/P =2 were transfected.

5.4. Conclusions

In this chapter we have studied the formation, stability, and in vitro biological fate of PAH-siRNA complexes. Different physico-chemical techniques were employed to study the PAH/siRNA nanoparticle formation, such as DLS, TEM, FCS, and FCCS. By means of FCCS, we obtained detailed information on the complexation of PAH and siRNA, which showed that the complexation, formation, and stability of PAH/siRNA nanoparticles is dependent on the ratio of charged amines in PAH to charged phosphate groups in siRNA(N/P), and on environmental conditions such as pH, and the presence of phosphates and/or proteins in media.

With FCCS we have also shown that the most stable nanoparticles are formed by complexation of PAH and siRNA in water with N/P = 2. PAH/siRNA nanoparticle reorganization is triggered by variations in pH. The nanoparticles disassemble in moderately acidic pH similar to that found in the endosomal environment, around pH 5.5. PAH/siRNA nanoparticles have a dynamic nature, being able to reassemble from molecular components into nanoparticles by increasing the pH from acidic to moderately basic pH.

Intracellular studies by FCCS and FCS revealed that at early stages, PAH/siRNA nanoparticles rearrange inside cells forming large aggregates, probably by interacting with cell structures and proteins, but later they disassemble liberating the siRNAs. Cytosol translocation of siRNAs is confirmed by CLSM imaging. Our experiments demonstrate a timescale for the endocytic release of siRNAs from the nanoparticles: association between PAH and siRNA in the form of slowly diffusing species could be detected for up to 12 h (early and late endosomes). After 24 h, a significant decrease in PAH and siRNA co-localization was observed, and free siRNA (characterised by

faster diffusion times), could be detected, indicating an effective endosomal release in the cytoplasm. The combined use of FCS and FCCS enabled us to analyse the reorganisation and compositional changes of nanoparticles in different environments, including in cell media and inside cells, and to demonstrate nanoparticle degradation intracellularly.

Moreover, FCS/FCCS allowed us to trace the molecular components PAH and siRNA individually both in bulk and intracellularly, which cannot be assessed by other experimental techniques. Our work also brings insight into the translocation process of the nanoparticles and the mechanism by which the siRNAs are delivered to the cytosol, which is fundamental for designing effective delivery systems for nucleic acids based on charged polymers.

General conclusions

This PhD thesis aims to study the interaction between biomolecules and nanomaterials, their translocation, aggregation and intracellular degradation. We have addressed different issues related to protein corona formation, intracellular stability of nanomaterials, therapeutics delivery, and how the physico-chemical properties of nanomaterials are affected by biologically relevant conditions. For addressing these issues, we have chosen different nanomaterials based on their suitability for the problem to tackle. Summing up the results from each chapter, the following conclusions can be drawn.

- In chapter 1, we have studied the interaction of poly (isopropyl amide co methacrylic acid P(NIPAM-co-MAA) microgels with polyamines and the chemotherapeutic drug doxorubicin and how this interaction is affected by the temperature. P(NIPAM-co-MAA) displays multiple carboxylate groups that bring pH sensitivity to the microgel and a negative charge, while the NIPAM monomers make the hydrogel thermoresponsive. We have observed that the molecular weight of the polyamine poly allyl hydrochloride (PAH) determines if the polyamine diffuses, or not, inside the hydrogel. At 20℃, low molecular weight PAH (15k Da) accumulates inside the microgel, while for higher molecular weights (50 and 140 kDa), PAH is preferentially retained on the microgel surface. The interaction between the microgel and the PAH is affected when the temperature is above the LCST. Above 32℃, deposition of the PAH occurs on the hydrogel surface independently of the molecular weight of the polyamine, due to the partial segregation of the MAA moieties on the surface and the decrease in size of the hydrogel pores as result of the collapse of NIPAM.

  Confocal studies show that when doxorubicin is complexed to the microgel, and the microgels are exposed to PAH, doxorubicin is released from the microgel and replaced by the PAH. In presence of 140 kDa PAH, doxorubicin is replaced more slowly than for 15 kDa PAH. Fluorescence lifetime imaging microscopy (FLIM) measurements reveal that smaller polyamines, like spermine or spermidine, which can diffuse inside the microgel but bear only a few charges, also remove doxorubicin. However, this replacement is not as complete as for PAH, which may not diffuse as easily into the microgel, but provides multiple amine groups capable of interacting with the carboxylate groups of the hydrogel simultaneously.

- In chapter 2, the impact of charged biomolecules and cargo on the responsiveness of pH and temperature sensitive P(NIPAM-co-MAA) hydrogel was studied by Time-lapse NMR. By Time-lapse NMR the evolution of the

intensity of the NMR signal as a function of time is followed. Above the LCST, the hydrogel collapses causing restrictions in the chain mobility, which means longer relaxation times and the decrease of the whole hydrogel signal intensity. The timescale over which changes in signal intensity occur, and the final decrease of the NMR signal, provides information of the conformational freedom of the polymer molecules.

We have shown that Time-lapse NMR experiments provide more detailed information on the collapse mechanism of P(NIPAm-co-MAA) microgels with temperature, and of how the collapse is affected at the molecular level by the sensitivity of MAA charges in pH, ionic strength, presence of charged molecules), temperature

Changes in the intensity of ^{1}H-NMR signal spectra of methyl groups of NIPAM during heating/cooling of the hydrogel were recorded from 20 to 40℃ Changes in temperature at pH 2 show faster hydrogel dehydration due to a decrease in the charge of the carboxylates, which in turn affects the overall water content of the microgel, resulting in more pronounced and faster dehydration compared to at neutral pH. Most interestingly, at basic pH 8 the signal intensity is not affected by the temperature changes due to the methyl groups of NIPAM remaining highly hydrated owing to the water brought by the carboxylates. Though hydrogen bonds of NIPAM with water break during the phase transition, the large water content inside the hydrogels at this pH provides an environment where the methyl groups retain the same conformational freedom as at 20℃. The presence of NaCl produces carboxylate and PNIPAM dehydration leading to faster hydrogel dehydration. On the other hand, positively charged oligomers (spermine and spermidine) produce fast dehydration kinetics, probably by complexation with several carboxylate groups. However, PAH effect in the hydrogel collapse, is lower than oligomers due to the presence of PAH on the surface as we showed in chapter 1. PDACMAC, which has a higher MW than PAH, exhibits comparable dehydration to spermine or spermidine due to the strong dehydrating effect of quaternary ammoniums on the carboxylate groups.

- In chapter 3, we study the interaction of lectins with the sugar moieties of the protein corona formed around gold nanoparticles by means of Fluorescence Correlation Spectroscopy (FCS). Fluorescently labelled wheat germ agglutinin (WGA) and sambucus nigra (SNA) lectins are used for their different glycan affinities. By means of FCS we look at the diffusion of free and bound lectin and we are able to determine the percentage of bound lectins. Experiments are performed for gold nanoparticles coated with a soft corona (SC) and a hard corona (HC). WGA interaction with the SC and the HC do not show relevant differences. On the other hand, SNA presents higher affinity for the HC where

all lectin is bound to the HC rather than the SC where some free lectin is found in solution.

The differences between the interaction of lectin and the protein corona suggests different protein compositions and therefore different glycans profile. The HC glycan profile reveals a prevalence of Neu5Ac monosaccharide to which SNA has high affinity and WGA low affinity.

To verify that lectin interaction with the protein corona depends on the glycans present in the corona we remove the glycan moieties. FCS results show that most of the lectins are free in solution confirming that the lectin interaction with the protein corona takes place through the glycan moieties of the glycosylated proteins of the biocorona.

- In chapter 4, ZnO nanoparticles were coated with polymer brushes composed of (polyacrylic acid (PAA), poly(2-methacrylolyloxyethyltrimethylammonium chloride) (PMETAC) and polyethylene glycol (PEG)) synthesized from the nanoparticle surface by reversible addition–fragmentation chain-transfer polymerization (RAFT). The impact of the polymer coating on the degradation of ZnO nanoparticles intracellularly was studied via confocal Raman microscopy by looking at changes in the ZnO Raman band at different positions within cells. The dominant ZnO peak in Raman is the active optical phonon mode (E_2 high), located at 437 cm^{-1}, which differs from that of lipids, proteins, and nucleic acids. It is possible to trace ZnO dissolution intracellularly via decrease in the associated Raman signal following ZnO dissolution. From the time evolution of this band we can evaluate the degradation time of the nanoparticles and the protective effect of the polymer brushes

  All the polymer brushes provide protection against ZnO degradation, with high density PAA being the most effective. This is seen as a result of PAA coated ZnO requiring a further 30 minutes to dissolve, implying that the PAA brushes act as a more effective diffusion barrier.

- In chapter 5, The complexation of PAH and silencing RNA (siRNAs), and nanoparticle formation are studied by transmission electron microscopy (TEM), dynamic light scattering (DLS), fluorescence correlation spectroscopy (FCS) and fluorescence cross-correlation spectroscopy (FCCS). FCCS shows that the formation and stability of PAH/siRNA nanoparticles is dependent on the ratio (N/P) of charged amines (from PAH) to charged phosphate groups (from siRNA), with 2 being the most stable ratio.

  Changes in the autocorrelation and cross-correlation amplitudes at time zero in FCCS studies corroborate that pH plays a fundamental role in nanoparticle

stability. At pH 2, the labelled PAH and siRNA amplitudes decrease which means higher concentrations of these species in solution. At the same time, the cross-correlation amplitude at time zero decreases, which denotes that the nanoparticles have disassembled. Increasing the pH from 2 to 8, the situation changes completely. At time zero the autocorrelation and cross-correlation amplitudes are higher, indicating complex reassembly when the pH increases to basic values.

Intracellular studies by FCCS and FCS reveal that at early endocytic stages, PAH/siRNA nanoparticles rearrange inside cells forming large aggregates, probably by interacting with cell structures and proteins, but later they disassemble liberating the siRNAs. Cytosol translocation of siRNAs is confirmed by confocal laser scanning microscopy (CLSM). Our experiments demonstrate a time-scale for the endocytic release of siRNAs from the nanoparticles: association between PAH and siRNA in the form of slow diffusing species could be detected for up to 12 h (early and late endosomes). After 24 h, a significant decrease in PAH and siRNA co-localization was observed, and free siRNA (characterized by faster diffusion times), could be detected, indicating an effective release.

Appendix: Methods

I. Dynamic light scattering (DLS) and ζ-potential

Dynamic Light Scattering (DLS) is the most common technique to characterize the size of colloids. Colloidal particles move randomly in a liquid dispersion following Brownian motion that depends on temperature, size and concentration of the colloids and solvent properties.[367] If a laser hits a particle, light is scattered in all directions. It is possible to record the intensity fluctuations of this scattered light over time.[368] The autocorrelation function of intensity fluctuations over the time determines how fast the scattering intensity fluctuates and from there the diffusion coefficient of the particles can be calculated. Applying the Stokes-Einstein (eq I.1) equation it is possible to obtain the hydrodynamic radius (r_H) of the colloid.

$$D = \kappa_B T (6\pi\mu r_H)^{-1} \quad [I.1]$$

A DLS system will typically have detectors at different positions. In this study, for all measurements, a back scattered detection system at 173° was employed (MALVERN Nano-ZS, U.K) in order to avoid rotational diffusion effects in the autocorrelation function.

This equipment also allows the measurement of the ζ-potential of a charged particle. When a particle is in solution, an electric potential is created between its surface and the ions present in the liquid. Charged particles attract charged ions in the aqueous solution forming the so-called electrical double layer (EDL). The first layer is known as Stern layer where oppositely charged ions are absorbed on the NP surface. Close to this zone it is the diffusion layer where like and opposite charged ions are present.[369] Its composition is dynamic and depends on pH, temperature, ionic strength etc. Applying an electric field, it is possible to estimate the potential difference in the EDL, which is related to the charge with which the particle will move under the applied field.

Zeta potential gives information on the colloidal stability. Small zeta potential absolute values, below 5-10 mV, are related to unstable dispersions, while high zeta potentials are associated to better colloidal stability.

II. Confocal laser scanning microscopy (CLSM)

Confocal Laser Scanning Microscopy (CLSM) is a optical technique used to generate fluorescence images of materials, cells or tissues in a specific plane in z-direction (focal plane) which enhance the resolution allowing three dimensional reconstructions.[370]

In CLSM the sample is illuminated by coherent light and focused in a very small spot in the focal plane by the objective lens (Fig. I). The emitted fluorescence light passes through the dichromatic mirror until the pinhole aperture in front of the photomultiplier (PMT) which acts as detector. The pinhole aperture can attenuate out of focus light collecting only the light from the focal plane. The smaller the pinhole, the less out of focus light reaches the PMT detector. 2D images are obtained by the reconstruction of the different signals taken point by point and line by line scanning within the confocal plane.

The confocal optical system allows increased lateral resolution and a unique optical sectioning capability thus, it is possible to get a 3D image of thick specimens with good spatial resolution. Depth scans are performed by selecting different focal planes along the Z-axis. A series of 2D images are collected and can be used to reconstruct the 3D structure of the specimen.

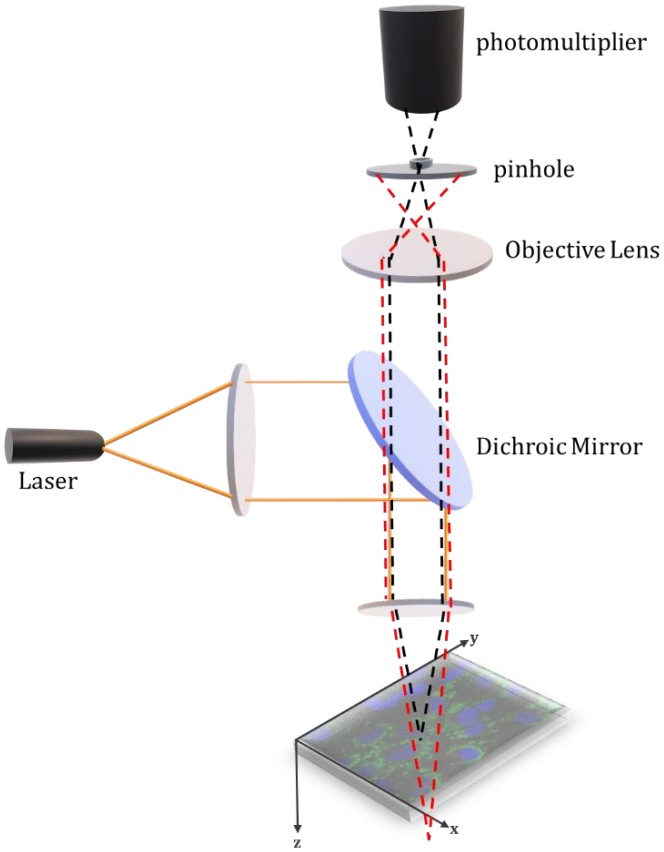

Figure I Scheme of a Confocal Laser Scanning Microscope typical configuration

III. Fluorescence correlation spectroscopy (FCS)

Fluorescence Correlation Spectroscopy[371,372] (FCS) is based on the statistical analysis of fluorescence intensity fluctuations arising from a fluorescent molecule inside a confocal volume. Due to Brownian motion, molecules are moving into and out of the confocal volume producing fluctuations over time. The intensity fluctuations are

dependent on the number of fluorescence molecules/particles in this volume. Fluorescence intensity must be higher than the background signal but not high to avoid quenching effects. It is not possible to record fluctuations for high fluorescence intensities. For that reason, the optimal signal-noise ratio occurs at nanomolar concentration when a few numbers of fluorescence molecules are in the confocal volume making FCS a single molecule technique.

The deviation of the signal from its temporal average fluorescence gives us the fluctuation signal (Fig. II).[57]

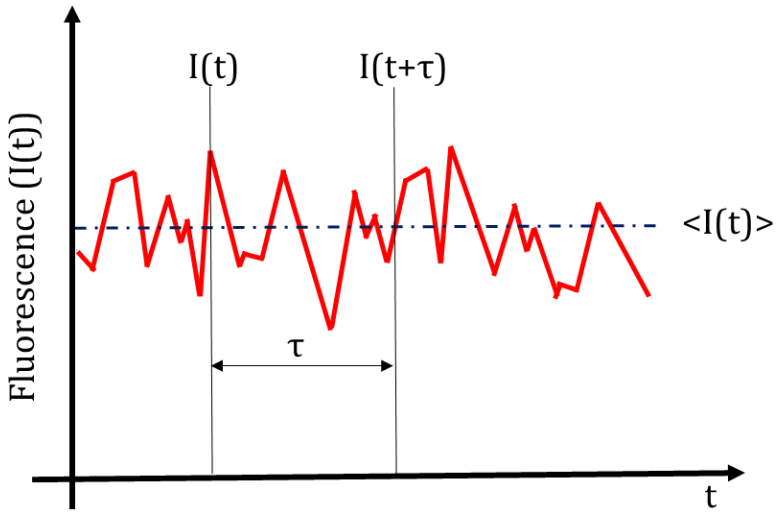

Figure II. Fluorescence fluctuation over the time obtained during the measurement. <I(t)> present the average intensity of the sample

$$\delta I(t) = I(t) - \langle I(t) \rangle \qquad [I.2]$$

$$\langle I(t) \rangle = \frac{1}{T} \int_0^T I(t) dt \qquad [I.3]$$

This fluorescence signal is correlated over the time, resulting the autocorrelation function (ACF or G(τ)):

$$G(\tau) = \frac{\langle I(t) I(t+\tau) \rangle}{\langle I(t) \rangle^2} \rightarrow G(\tau) = \frac{\langle \delta I(t+\tau) \delta I(t) \rangle}{\langle I(t) \rangle^2} + 1 \qquad [I.4]$$

It is possible to obtain I(t) and δI(t) through the detection efficacy of the setup and the changes in the local concentration of the sample on the space of the observed volume ($\vec{r} = (x, y, z)$):

$$I(t) = \kappa \int_V I_p(\vec{r}) \cdot S(\vec{r}) \cdot CEF(\vec{r}) \cdot C(\vec{r}, t) d\vec{r} \qquad [I.5]$$

$$\delta I(t) = \kappa \int_V I_p(\vec{r}) \cdot S(\vec{r}) \cdot CEF(\vec{r}) \cdot \delta C(\vec{r}, t) d\vec{r} \qquad [I.6]$$

κ detection efficacy

I_s excitation energy

$CEF(\vec{r})$ collection efficiency function of the system

$S(\vec{r})$ optical transfer function objective-pinhole

$C(\vec{r}, t)$ distribution of fluorophore

Equation [I.4] can be written as:

$$G(\tau) = \frac{\iint I_p(\vec{r}) I_p(\vec{r}\prime) S(\vec{r}) S(\vec{r}\prime) CEF(\vec{r}) CEF(\vec{r}\prime) \langle \delta C(\vec{r}\prime, t+\tau) \delta C(\vec{r}\prime, t) d\vec{r} d\vec{r}\prime \rangle}{\langle C \rangle^2 \left(\int I_p(\vec{r}) \cdot CEF(\vec{r})\, d\vec{r} \right)^2} + 1 \qquad [I.7]$$

Taking in account that the emission light distribution reaches a maximum at the beam center in the focal plane and the light from outside the focal plane is not taken into consideration, we can define $\omega(\vec{r})$:

$$\omega(\vec{r}) = I_p(\vec{r}) \cdot S(\vec{r}) \cdot CEF(\vec{r}) = cte \cdot e^{-2x^2/{w_0}^2} e^{-2y^2/{w_0}^2} e^{-2z^2/{z_0}^2} \qquad [I.8]$$

where, w_0 and z_0 the distance where the intensity decay $1/e^2$

Obtaining the correlation function $G(\tau)$:

$$G(\tau) = \frac{1}{N} \left(1 + \frac{4\tau D}{w_0^2}\right)^{-1} \left(1 + \frac{4\tau D}{z_0^2}\right)^{-1/2} + G_\infty \qquad [I.9]$$

D diffusion coefficient

N number of particles

G_∞ offset of the correlation function

τ time

From the amplitude of the correlation function at $\tau = 0$ it is possible to obtain the number of fluorescence molecule/particles inside the confocal volume:

$$G(0) = N^{-1} \qquad [I.10]$$

which is thereby dependent on the dimensions of the confocal volume (V_{eff}) that can be obtained from a dye with a known diffusion coefficient and the concentration.

The concentration of the particles can be determined by equation [I.11]:

$$[C] = N \cdot {V_{eff}}^{-1} \qquad [I.11]$$

Furthermore, the diffusion coefficient (D) is related with the hydrodynamic radius by the Stokes-Einstein equation:

$$D = \kappa_B T (6\pi\mu r_H)^{-1} \qquad [I.12]$$

κ_B Boltzmann's constant

T Absolute temperature

μ viscosity of the medium

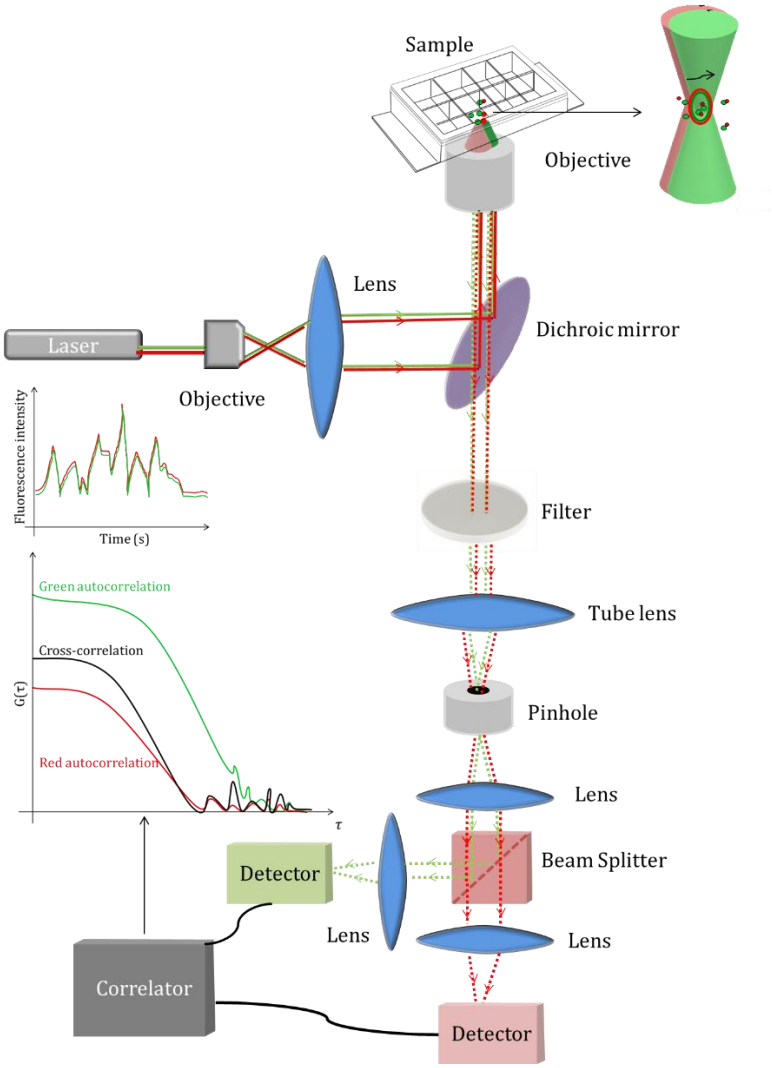

Figure III. FCCS setup. Lasers illuminate the same confocal volume (sample) without overlapping. Light travel through the filters and mirrors until arrive to the objective which focus into the sample. The emitted fluorescence go through the sample objective and it is split from the excitation light by the dichroic mirror and center in the pinhole which collect only the fluorescence from the focal plane. After that, the fluorescence arrives to the detector for its correlation analysis.

IV. Fluorescence cross-correlation spectroscopy (FCCS)

Fluorescence Cross Correlation Spectroscopy (FCCS) is a variant of FCS.[345] In this case, two lasers with different wavelengths excite the sample aiming to study the interaction of the two species labelled with two different fluorophores.[373] The fluorophores must be spectroscopically different to avoid signal overlapping, cross excitation, or cross talk.[374] FCCS allows recording not only the autocorrelation function of the two species, but also the correlation function between them. As such, it is possible to study species that are not distinguishable from their diffusive properties. The cross-correlation signal is highly sensitive providing information on The interaction of small species as proteins in solution[375] but it is also possible to obtain information of particles inside the cells.[376]

The equation [I.4] becomes:

$$G(\tau) = \frac{\langle I_a(t) I_b(t+\tau) \rangle}{\langle I_a(t) \rangle \langle I_b(t) \rangle} \quad [I.13]$$

being a and b the two different species.

In this case, the concentration can be estimated by the auto and cross correlation curves at time zero:

$$\frac{G_{ab}(0)}{G_a(0) \cdot G_b(0)} = \langle C_{ab} \rangle V_{eff} \quad [I.14]$$

V. Fluorescence lifetime imaging microscopy (FLIM)

The fluorescence lifetime of a molecule is the average time the molecule spends in the excited state before returning to the ground state by emission of a fluorescence photon.[377] The fluorescent lifetime is dependent on the local environment. By studying changes in fluorescent lifetime of a fluorophore it is possible to determine if the fluorophore is inside a cell, pH changes or binding between proteins, amongst other processes.[221,378]

There are two principle measurements domains employed for FLIM, time domain and frequency domain. In this thesis we employed the most common time domain-based method time correlated single photon counting (TCSPC).[379] A pulse monochromatic source excites the sample and the photons emitted are detected by a photomultiplier. As such, TCSPC measures the time between a detected fluorescence photon and the excitation pulse, the data is recorded in the TCSPC histogram which can be analysed with different mathematical models (Fig. V.B). FLIM images are created with the location of the laser beam in the selected area and attributing different colour to the arrival time of the photon (Fig. IV.A).

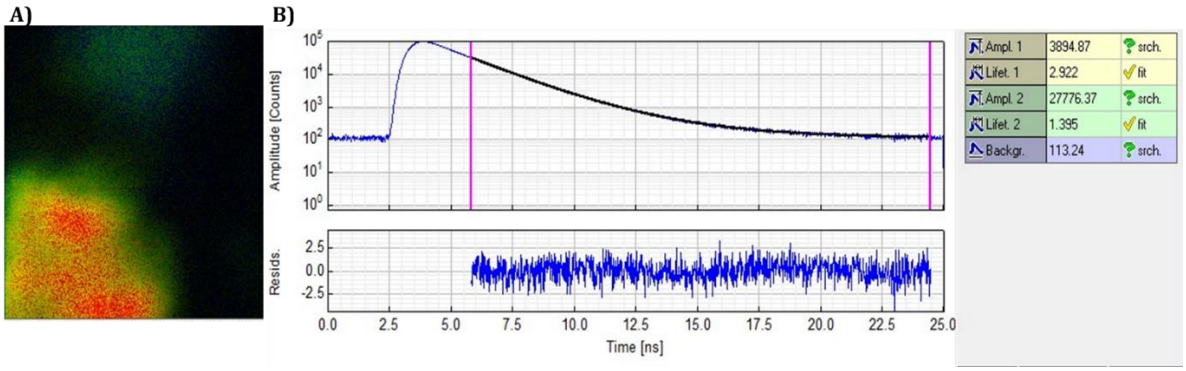

Figure IV. FLIM results for microgel loaded with DOXO. A) image where each photon is represented by a pixel with different colours that represent the DOXO lifetime being red higher lifetime and blue the lowest. B) TCSP histogram correspond to the microgel. Mathematic analysis provides the lifetime of each species and their amplitude.

VI. Flow cytometry (FCM)

Flow cytometry is an analytical method developed to measure fluorescence or light scattering of a colloidal dispersion (cells, particles, etc.).[380]

A flow cytometer is composed by three elements: the fluidic system, the optical system and the electronics. The fluidic system transports the sample to the optical system. The fluidic system is designed to flow a single event (cell/particle) into the optical system intersecting individually the laser (Fig. V). The light scattered with an angle <20° in the same axis as the laser is collected in the Forward Scatter Channel (FSC). FSC is collected by the forward scatter photodiode and provides information on the size of the particle/cell. Scattered light and fluorescence are also recorded at 90° In this case, the data (Side Scatter Channel (SSD)). give information about the complexity of the sample.[381] SSD and fluorescence are guided by the mirrors to one of the photomultiplier tubes (PMTs) which collect the signal. The signal from the detectors is transformed in digital signal by the electronic system and sent to the PC for analysis.[382]

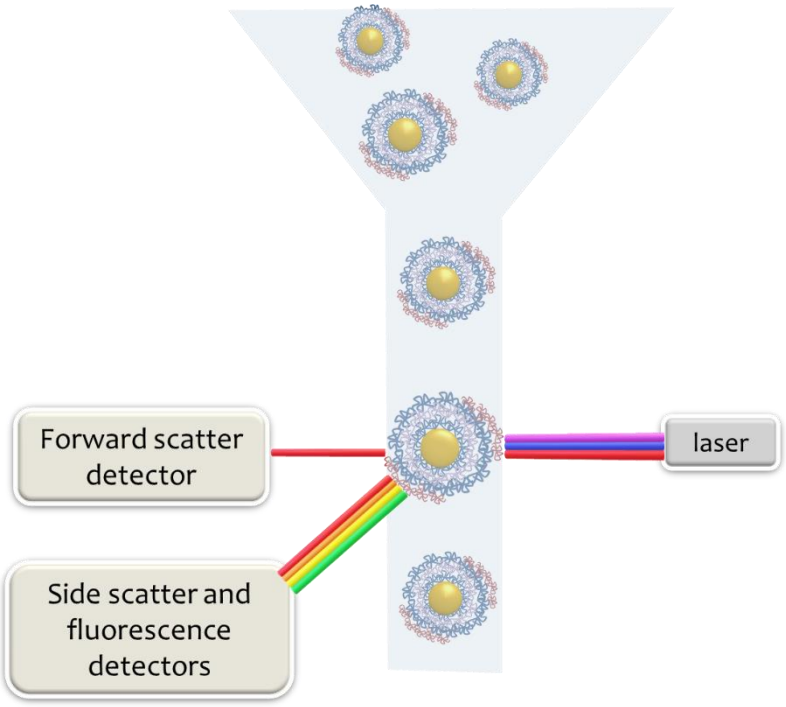

Figure V. Scheme of the working principle of flow cytometer

The equipment used during this work is the BD FACS Canto II.

VII. Confocal Raman microscopy (CRM)

When a monochromatic light hits a sample, the light can be absorbed, reflected or scattered. The induced dipole ($\vec{\mu}$) by the external electric field $\vec{E}$ can be express by:

$$\vec{\mu} = \alpha\vec{E} \qquad [I.15]$$

where $\vec{\alpha}$ is the polarizability a physic concept that relates the changes in the charge distribution in the equilibrium with an external electric field. Expanding in Taylor series the equation of polarizability and introducing in eq[I.15], equation [I.16]:

$$\mu(t) = \alpha_0 E_0 \cos(\omega_0 t) + \frac{1}{2}\left(\frac{\partial \alpha}{\partial q}\right) q_0 E_0 \cos[(\omega_0 - \omega_q)t] + \frac{1}{2}\left(\frac{\partial \alpha}{\partial q}\right) q_0 E_0 \cos[(\omega_0 + \omega_q)t]$$

being q_0 the normal coordinate in equilibrium, ω_0 oscillating frequency, $\omega_q$frequency at q normal coordinate can be excited.

In the equation [I.16] the first summand is due to Rayleigh scattering, the second to Stokes scattering where the photon generated has a smaller frequency than the incident photon and the third to anti-Stokes when the frequency of the photon emitted is higher than the incident one.

In the scattered case, most of the photons are elastically scattered (Rayleigh scattering) but a small fraction (0.001%) the scatter is inelastically. From this interaction, the 1% interact with optical phonons producing an energy shift, the frequency is not the same as the incident one. This effect is called Raman scattering.[383]

A molecule active in Raman should be capable of changing polarizability $\left(\left(\frac{\partial \alpha}{\partial q}\right) \neq 0\right)$.

This effect is complementary to infrared spectroscopy where the polarizability is constant and the dipole moment change (Fig VI).

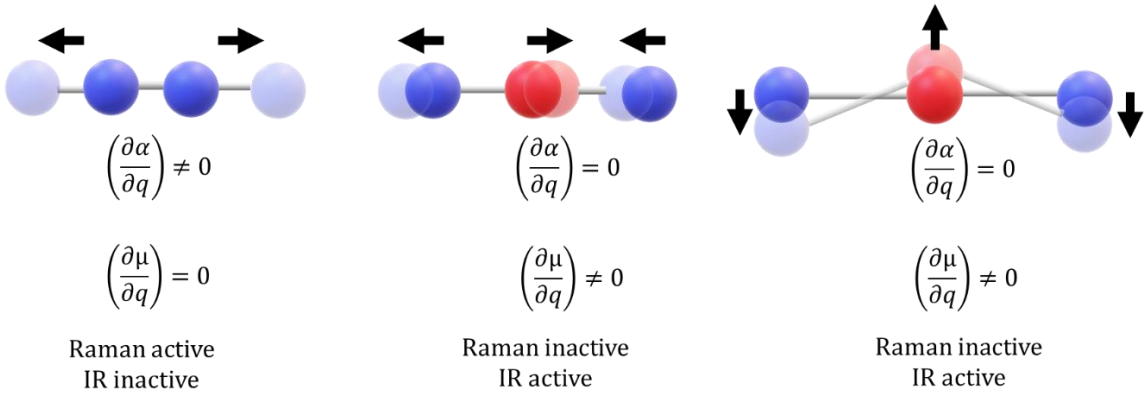

Figure VI. Scheme of Raman and IR active or inactive vibrational modes

Raman spectroscopy provides a chemical 'fingerprint' of materials and molecules. It is not an invasive technique and it doesn't require a complex sample preparation.

Confocal Raman Microscopy (CRM), is the combination of a Raman spectrophotometer with a confocal microscope allowing to analyse in the confocal plane the Raman spectra of each pixel from an image. The equipment is based in a monochromatic light source focus by the confocal microscope components to the sample. The sample (nanomaterials, cells or tissues) is scanned point-by point and line-by-line in the X-Y (lateral) or Z (depth) direction of the selected image (Fig. VII).

The light dispersed by the sample is filtered to avoid the signal from Rayleigh scattering and guided to the monochromator and the detector (CCD camera). The detector sends the information to the computer where the Raman spectra can be analysed. With the analysis is possible to generate a 3D image of the sample or a colour mapping.

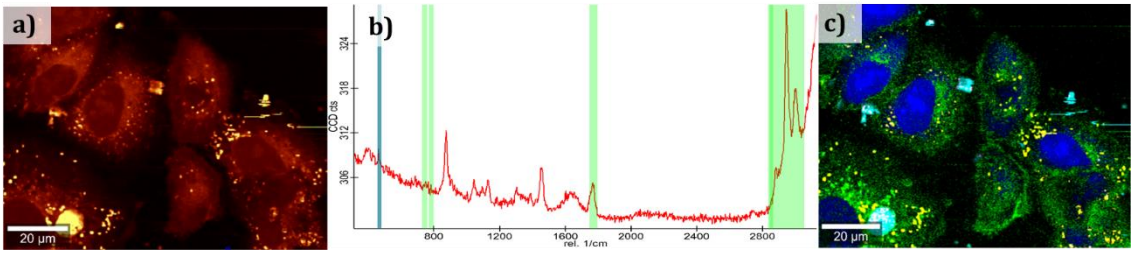

Figure VII. a) pixels in the Raman picture. b) Raman spectra of a pixel. c) mapping of the cells (green, blue and yellow) and NPs (light blue)

The used of CRM allows to study the NP uptake in fixed cells or monitoring it in real time. The different cell components as DNA, proteins or lipids have an specific spectra being possible to located the NMs in the different parts of the cell.[384,385] This process is sometimes complex due to the similar composition (i.e. chemical moieties) between cells components and organic NMs. The use of molecules with different 'fingerprint' from those components present in cells or their deuterated forms can overcome these limitations.

In this work, Confocal Raman measurements were performed with an Alpha 300 R microscope (WITec GmbH) equipped with a 785 nm laser, 300 g mm^{-1} grafting, and a CCD device cooled down to -61°C. The objective used was the 63 water immersion W Plan-Apochromat 63/1.0 Zeiss.

VIII. Nuclear magnetic resonance (NMR)

Nuclear Magnetic Resonance (NMR) is physical technique based on the perturbation in the magnetic moment of an atomic nuclei due to the existence of an external magnetic field.[386] The nuclei have magnetic spins randomly oriented in absence of a magnetic field. When the magnetic field is applied, the nuclei absorb energy promoting their spin to a different energy state. Returning to the ground state, the nuclei emit signals that the equipment record as frequency graph vs the intensity (NMR spectra). These signals depend on the energy gap between spin states, the magnetic field and the surrounding environment of each atom. In organic chemistry, the most used nuclei are: ^{1}H, ^{13}C, ^{31}P, ^{19}F y ^{15}N. This technique is employed to characterize the compounds structure, kinetic and thermodynamic studies.

In this thesis, a variation of NMR technique, the time-lapse NMR, was used which allows to monitor the NMR spectrum evolution over time under specific conditions. i,e, with changes in temperature. The technique is suitable to trace change in molecular dynamics. A decrease in rotational freedom will result accordingly to an

increase in residual dipolar coupling. Consequently, the NMR signal decays faster due to a substantially reduced spin–spin relaxation time (T_2). A significant fraction of immobilized protons generates extremely broadened NMR signals which are beyond detection by conventional high resolution NMR probes. Therefore, eventually an apparent signal intensity drop can be observed during VPT.

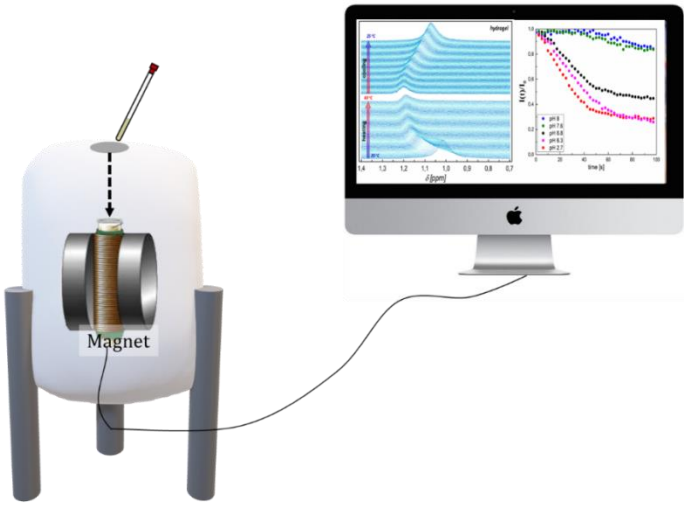

Figure VIII. NMR equipment. The sample is introduced inside the magnet where the NMR signal were obtained and sent to the computer to be analysed. With Time-Lapse NMR is possible to monitor the changes in the intensity of the peaks in order to see structural changes

The relation between the normalized integrated areas of a particular peak at certain time and the same peak at reference temperature which is the initial point ($I(t)/I_0$) are evaluated to follow some kinetics processes as function of time and temperature (Fig. I.IX).[387]

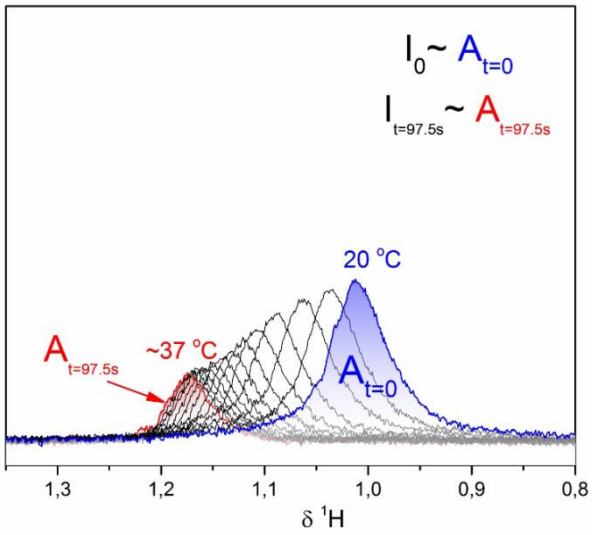

Figure IX. Temperature/time dependence of the signal of methyl protons in the case of P(NIPAM-co-MAA) hydrogel (pH 6.8).[388]

REFERENCES

1. *Nanomedicine Market Analysis By Products, (Therapeutics, Regenerative Medicine, Diagnostics), By Application, (Clinical Oncology, Infectious diseases), By Nanomolecule (Gold, Silver, Iron Oxide, Alumina), & Segment Forecasts, 2018 - 2025*. (2017).
2. Ferrari, M. Cancer nanotechnology: Opportunities and challenges. *Nat. Rev. Cancer* **5**, 161–171 (2005).
3. Kuwahara, H. *et al.* Efficient in vivo delivery of siRNA into brain capillary endothelial cells along with endogenous lipoprotein. *Mol. Ther.* **19**, 2213–2221 (2011).
4. Chandarana, M., Curtis, A. & Hoskins, C. The use of nanotechnology in cardiovascular disease. *Appl. Nanosci.* **8**, 1607–1619 (2018).
5. Dacoba, T. G., Olivera, A., Torres, D., Crecente-Campo, J. & Alonso, M. J. Modulating the immune system through nanotechnology. *Semin. Immunol.* **34**, 78–102 (2017).
6. Tautzenberger, A., Kovtun, A. & Ignatius, A. Nanoparticles and their potential for application in bone. *Int. J. Nanomedicine* **7**, 4545–4557 (2012).
7. Jiang, Y. & Pu, K. Advanced Photoacoustic Imaging Applications of Near-Infrared Absorbing Organic Nanoparticles. *Small* **13**, 1–19 (2017).
8. Wu, Y., Ali, M. R. K., Chen, K., Fang, N. & El-Sayed, M. A. Gold nanoparticles in biological optical imaging. *Nano Today* **24**, 120–140 (2019).
9. Iglesias, M. S. & Grzelczak, M. Using gold nanoparticles to detect single-nucleotide polymorphisms: toward liquid biopsy. *Beilstein J. Nanotechnol.* **11**, 263–284 (2020).
10. Priyadarshini, E. & Pradhan, N. Gold nanoparticles as efficient sensors in colorimetric detection of toxic metal ions: A review. *Sensors Actuators, B Chem.* **238**, 888–902 (2017).
11. Algar, W. R. *et al.* The controlled display of biomolecules on nanoparticles: A challenge suited to bioorthogonal chemistry. *Bioconjug. Chem.* **22**, 825–858 (2011).
12. Sapsford, K. E. *et al.* Functionalizing nanoparticles with biological molecules: Developing chemistries that facilitate nanotechnology. *Chem. Rev.* **113**, 1904–2074 (2013).
13. Park, J. *et al.* A Hierarchical Nanoparticle-in-Micropore Architecture for Enhanced Mechanosensitivity and Stretchability in Mechanochromic Electronic Skins. *Adv. Mater.* **31**, 1–10 (2019).
14. Chiari-Andréo, B. G. *et al.* Nanoparticles for cosmetic use and its application. in *Nanoparticles in Pharmacotherapy* 113–146 (Elsevier Inc, 2019).
15. Al-Naamani, L., Dobretsov, S. & Dutta, J. Chitosan-zinc oxide nanoparticle composite coating for active food packaging applications. *Innov. Food Sci.*

Emerg. Technol. **38**, 231–237 (2016).

16. De Oliveira, L. F. *et al.* Functionalized Silica Nanoparticles As an Alternative Platform for Targeted Drug-Delivery of Water Insoluble Drugs. *Langmuir* **32**, 3217–3225 (2016).
17. Sapsford, K. E. *et al.* Functionalizing Nanoparticles with Biological Molecules: Developing Chemistries that Facilitate Nanotechnology. *Chem. Rev.* **113**, 1904–2074 (2013).
18. Donahue, N. D., Acar, H. & Wilhelm, S. Concepts of nanoparticle cellular uptake, intracellular trafficking, and kinetics in nanomedicine. *Adv. Drug Deliv. Rev.* **143**, 68–96 (2019).
19. Wilhelm, S. *et al.* Analysis of nanoparticle delivery to tumours. *Nat. Rev. Mater.* **1**, 16014 (2016).
20. Anselmo, A. C. & Mitragotri, S. Nanoparticles in the clinic: An update. *Bioeng. Transl. Med.* **4**, 1–16 (2019).
21. Chabner, B. A. & Roberts, T. G. Chemotherapy and the war on cancer. *Nat. Rev. Cancer* **5**, 65–72 (2005).
22. Coates, A. *et al.* On the receiving end-patient perception of the side-effects of cancer chemotherapy. *Eur. J. Cancer Clin. Oncol.* **19**, 203–208 (1983).
23. Matsumura, Y. & Maeda, H. A New Concept for Macromolecular Therapeutics in Cancer Chemotherapy: Mechanism of Tumoritropic Accumulation of Proteins and the Antitumor Agent Smancs. *Cancer Res.* **46**, 6387–6392 (1986).
24. Bertrand, N., Wu, J., Xu, X., Kamaly, N. & Farokhzad, O. C. Cancer nanotechnology: The impact of passive and active targeting in the era of modern cancer biology. *Adv. Drug Deliv. Rev.* **66**, 2–25 (2014).
25. Danhier, F., Feron, O. & Préat, V. To exploit the tumor microenvironment: Passive and active tumor targeting of nanocarriers for anti-cancer drug delivery. *J. Control. Release* **148**, 135–146 (2010).
26. Danhier, F. To exploit the tumor microenvironment: Since the EPR effect fails in the clinic, what is the future of nanomedicine? *J. Control. Release* **244**, 108–121 (2016).
27. Sindhwani, S. *et al.* The entry of nanoparticles into solid tumours. *Nat. Mater.* **19**, (2020).
28. Yoo, J., Park, C., Yi, G., Lee, D. & Koo, H. Active targeting strategies using biological ligands for nanoparticle drug delivery systems. *Cancers (Basel).* **11**, (2019).
29. Li, Y. *et al.* Transferrin receptor-targeted redox/pH-sensitive podophyllotoxin prodrug micelles for multidrug-resistant breast cancer therapy. *J. Mater. Chem. B* **7**, 5814–5824 (2019).
30. Zwicke, G. L., Ali Mansoori, G. & Jeffery, C. J. Utilizing the folate receptor for active targeting of cancer nanotherapeutics. *Nano Rev.* **3**, 18496 (2012).
31. Chen, L. *et al.* Folic acid-conjugated magnetic ordered mesoporous carbon nanospheres for doxorubicin targeting delivery. *Mater. Sci. Eng. C* **104**, 109939

(2019).

32. Minko, T. Drug targeting to the colon with lectins and neoglycoconjugates. *Adv. Drug Deliv. Rev.* **56**, 491–509 (2004).

33. Moulari, B., Béduneau, A., Pellequer, Y. & Lamprecht, A. Lectin-decorated nanoparticles enhance binding to the inflamed tissue in experimental colitis. *J. Control. Release* **188**, 9–17 (2014).

34. Choi, K. Y. *et al.* Hyaluronic Acid–Based Activatable Nanomaterials for Stimuli-Responsive Imaging and Therapeutics: Beyond CD44-Mediated Drug Delivery. *Adv. Mater.* **31**, 1–18 (2019).

35. Liang, Y. *et al.* Smart nanoparticles assembled by endogenous molecules for siRNA delivery and cancer therapy via CD44 and EGFR dual-targeting. *Nanomedicine Nanotechnology, Biol. Med.* **15**, 208–217 (2019).

36. Chi, L. *et al.* Enhanced delivery of liposomes to lung tumor through targeting interleukin-4 receptor on both tumor cells and tumor endothelial cells. *J. Control. Release* **209**, 327–336 (2015).

37. Gocheva, G. & Ivanova, A. A Look at Receptor-Ligand Pairs for Active-Targeting Drug Delivery from Crystallographic and Molecular Dynamics Perspectives. *Molecular Pharmaceutics* vol. 16 3293–3321 (2019).

38. Miao, L. *et al.* The Binding Site Barrier Elicited by Tumor-Associated Fibroblasts Interferes Disposition of Nanoparticles in Stroma-Vessel Type Tumors. *ACS Nano* **10**, 9243–9258 (2016).

39. Stewart, M. P., Lorenz, A., Dahlman, J. & Sahay, G. Challenges in carrier-mediated intracellular delivery: moving beyond endosomal barriers. *Wiley Interdiscip. Rev. Nanomedicine Nanobiotechnology* **8**, 465–478 (2016).

40. Pérez-Campaña, C. *et al.* Biodistribution of different sized nanoparticles assessed by positron emission tomography: A general strategy for direct activation of metal oxide particles. *ACS Nano* **7**, 3498–3505 (2013).

41. Kutscher, H. L. *et al.* Threshold size for optimal passive pulmonary targeting and retention of rigid microparticles in rats. *J. Control. Release* **143**, 31–37 (2010).

42. Owens, D. E. & Peppas, N. A. Opsonization, biodistribution, and pharmacokinetics of polymeric nanoparticles. *Int. J. Pharm.* **307**, 93–102 (2006).

43. Lopez-Chaves, C. *et al.* Gold nanoparticles: Distribution, bioaccumulation and toxicity. In vitro and in vivo studies. *Nanomedicine Nanotechnology, Biol. Med.* **14**, 1–12 (2018).

44. Li, X. *et al.* The systematic evaluation of size-dependent toxicity and multi-time biodistribution of gold nanoparticles. *Colloids Surfaces B Biointerfaces* **167**, 260–266 (2018).

45. Pan, R. *et al.* Size-dependent endocytosis and a dynamic-release model of nanoparticles. *Nanoscale* **10**, 8269–8274 (2018).

46. Wang, T. *et al.* Size-Dependent Regulation of Intracellular Trafficking of

Polystyrene Nanoparticle-Based Drug-Delivery Systems. *ACS Appl. Mater. Interfaces* **9**, 18619–18625 (2017).

47. Cabral, H. *et al.* Accumulation of sub-100 nm polymeric micelles in poorly permeable tumours depends on size. *Nat. Nanotechnol.* **6**, 815–823 (2011).

48. Decuzzi, P., Pasqualini, R., Arap, W. & Ferrari, M. Intravascular delivery of particulate systems: Does geometry really matter? *Pharm. Res.* **26**, 235–243 (2009).

49. Nejati, S., Mohseni Vadeghani, E., Khorshidi, S. & Karkhaneh, A. Role of particle shape on efficient and organ-based drug delivery. *Eur. Polym. J.* **122**, 109353 (2020).

50. Geng, Y. *et al.* Shape effects of filaments versus spherical particles in flow and drug delivery. *Nat. Nanotechnol.* **2**, 249–255 (2007).

51. Kinnear, C., Moore, T. L., Rodriguez-Lorenzo, L., Rothen-Rutishauser, B. & Petri-Fink, A. Form Follows Function: Nanoparticle Shape and Its Implications for Nanomedicine. *Chem. Rev.* **117**, 11476–11521 (2017).

52. Decuzzi, P. *et al.* Size and shape effects in the biodistribution of intravascularly injected particles. *J. Control. Release* **141**, 320–327 (2010).

53. Nambara, K. *et al.* Reverse Size Dependences of the Cellular Uptake of Triangular and Spherical Gold Nanoparticles. *Langmuir* **32**, 12559–12567 (2016).

54. Champion, J. A. & Mitragotri, S. Role of target geometry in phagocytosis. *Proc. Natl. Acad. Sci. U. S. A.* **103**, 4930–4934 (2006).

55. Verma, A. & Stellacci, F. Effect of surface properties on nanoparticle-cell interactions. *Small* **6**, 12–21 (2010).

56. Blanco, E., Shen, H. & Ferrari, M. Principles of nanoparticle design for overcoming biological barriers to drug delivery. *Nat. Biotechnol.* **33**, 941–951 (2015).

57. Martinez-Moro, M., Di Silvio, D. & Moya, S. E. Fluorescence correlation spectroscopy as a tool for the study of the intracellular dynamics and biological fate of protein corona. *Biophys. Chem.* **253**, 106218 (2019).

58. Banerjee, A., Qi, J., Gogoi, R., Wong, J. & Mitragotri, S. Role of nanoparticle size, shape and surface chemistry in oral drug delivery. *J. Control. Release* **238**, 176–185 (2016).

59. Zheng, H., Mortensen, L. J., Ravichandran, S., Bentley, K. & DeLouise, L. A. Effect of nanoparticle surface coating on cell toxicity and mitochondria uptake. *J. Biomed. Nanotechnol.* **13**, 155–166 (2017).

60. Fröhlich, E. The role of surface charge in cellular uptake and cytotoxicity of medical nanoparticles. *Int. J. Nanomedicine* **7**, 5577–5591 (2012).

61. Rothen-Rutishauser, B., Bourquin, J. & Petri-Fink, A. Nanoparticle-cell interactions: Overview of uptake, intracellular fate and induction of cell responses. in *NanoScience and Technology* 153–170 (Springer International Publishing, 2019).

62. Nel, A. E. *et al.* Understanding biophysicochemical interactions at the nano-bio interface. *Nat. Mater.* **8**, 543–557 (2009).

63. Wu, L., Zhang, J. & Watanabe, W. Physical and chemical stability of drug nanoparticles. *Adv. Drug Deliv. Rev.* **63**, 456–469 (2011).

64. Moore, T. L. *et al.* Nanoparticle colloidal stability in cell culture media and impact on cellular interactions. *Chem. Soc. Rev.* **44**, 6287–6305 (2015).

65. Guerrini, L., Alvarez-Puebla, R. A. & Pazos-Perez, N. Surface modifications of nanoparticles for stability in biological fluids. *Materials (Basel).* **11**, 1–28 (2018).

66. Bagwe, R. P., Hilliard, L. R. & Tan, W. Surface modification of silica nanoparticles to reduce aggregation and nonspecific binding. *Langmuir* **22**, 4357–4362 (2006).

67. Amoozgar, Z. & Yeo, Y. Recent advances in stealth coating of nanoparticle drug delivery systems. *Wiley Interdiscip. Rev. Nanomedicine Nanobiotechnology* **4**, 219–233 (2012).

68. Li, D. *et al.* Cross-Linked Poly(ethylene glycol) Shells for Nanoparticles: Enhanced stealth effect and colloidal stability. *Langmuir* **35**, 8799–8805 (2019).

69. Fam, S. Y. *et al.* Stealth Coating of Nanoparticles in Drug-Delivery Systems. *Nanomaterials* **10**, 787 (2020).

70. Martin, A. L., Homenick, C. M., Xiang, Y., Gillies, E. & Matsuura, N. Polyelectrolyte Coatings Can Control Charged Fluorocarbon Nanodroplet Stability and Their Interaction with Macrophage Cells. *Langmuir* **35**, 4603–4612 (2019).

71. Gal, N., Schroffenegger, M. & Reimhult, E. Stealth Nanoparticles Grafted with Dense Polymer Brushes Display Adsorption of Serum Protein Investigated by Isothermal Titration Calorimetry. *J. Phys. Chem. B* **122**, 5820–5834 (2018).

72. Roosjen, A., Norde, W., Mei, H. C. & Busscher, H. J. The Use of Positively Charged or Low Surface Free Energy Coatings versus Polymer Brushes in Controlling Biofilm Formation. in *Characterization of Polymer Surfaces and Thin Films* vol. 132 138–144 (Springer-Verlag, 2006).

73. Behzadi, S. *et al.* Cellular uptake of nanoparticles: Journey inside the cell. *Chem. Soc. Rev.* **46**, 4218–4244 (2017).

74. Wang, R., Lu, K. Q., Tang, Z. R. & Xu, Y. J. Recent progress in carbon quantum dots: synthesis, properties and applications in photocatalysis. *J. Mater. Chem. A* **5**, 3717–3734 (2017).

75. Anselmo, A. C. & Mitragotri, S. A Review of Clinical Translation of Inorganic Nanoparticles. *AAPS J.* **17**, 1041–1054 (2015).

76. Giner-Casares, J. J., Henriksen-Lacey, M., Coronado-Puchau, M. & Liz-Marzán, L. M. Inorganic nanoparticles for biomedicine: Where materials scientists meet medical research. *Mater. Today* **19**, 19–28 (2016).

77. Garcia, M. A. Surface plasmons in metallic nanoparticles: Fundamentals and applications. *J. Phys. D. Appl. Phys.* **44**, (2011).

78. Grzelczak, M., Pérez-Juste, J., Mulvaney, P. & Liz-Marzán, L. M. Shape control in gold nanoparticle synthesis. *Chem. Soc. Rev.* **37**, 1783–1791 (2008).

79. Xie, X., Liao, J., Shao, X., Li, Q. & Lin, Y. The Effect of shape on Cellular Uptake of Gold Nanoparticles in the forms of Stars, Rods, and Triangles. *Sci. Rep.* **7**, 1–9 (2017).

80. Kong, F. Y. *et al.* Unique roles of gold nanoparticles in drug delivery, targeting and imaging applications. *Molecules* **22**, (2017).

81. Li, B., Wang, Y. & He, J. Gold Nanorods-Based Smart Nanoplatforms for Synergic Thermotherapy and Chemotherapy of Tumor Metastasis. *ACS Appl. Mater. Interfaces* **11**, 7800–7811 (2019).

82. Farooq, M. U. *et al.* Gold Nanoparticles-enabled Efficient Dual Delivery of Anticancer Therapeutics to HeLa Cells. *Sci. Rep.* **8**, 1–12 (2018).

83. Saha, K., Agasti, S. S., Kim, C., Li, X. & Rotello, V. M. Gold nanoparticles in chemical and biological sensing. *Chem. Rev.* **112**, 2739–2779 (2012).

84. Moros, M. *et al.* Triggering antitumoural drug release and gene expression by magnetic hyperthermia. *Adv. Drug Deliv. Rev.* **138**, 326–343 (2019).

85. Kaviyarasu, K. *et al.* Elucidation of photocatalysis, photoluminescence and antibacterial studies of ZnO thin films by spin coating method. *J. Photochem. Photobiol. B Biol.* **173**, 466–475 (2017).

86. Lewicka, Z. A., Yu, W. W., Oliva, B. L., Contreras, E. Q. & Colvin, V. L. Photochemical behavior of nanoscale TiO2 and ZnO sunscreen ingredients. *J. Photochem. Photobiol. A Chem.* **263**, 24–33 (2013).

87. Manzano, M. & Vallet-Regí, M. Mesoporous Silica Nanoparticles for Drug Delivery. *Adv. Funct. Mater.* **30**, 3–5 (2020).

88. Baeza, A., Guisasola, E., Ruiz-Hernández, E. & Vallet-Regí, M. Magnetically triggered multidrug release by hybrid mesoporous silica nanoparticles. *Chem. Mater.* **24**, 517–524 (2012).

89. Martínez-Carmona, M., Lozano, D., Colilla, M. & Vallet-Regí, M. Lectin-conjugated pH-responsive mesoporous silica nanoparticles for targeted bone cancer treatment. *Acta Biomater.* **65**, 393–404 (2018).

90. Guisasola, E. *et al.* Beyond Traditional Hyperthermia: In Vivo Cancer Treatment with Magnetic-Responsive Mesoporous Silica Nanocarriers. *ACS Appl. Mater. Interfaces* **10**, 12518–12525 (2018).

91. Zhu, Q. L. & Xu, Q. Metal-organic framework composites. *Chem. Soc. Rev.* **43**, 5468–5512 (2014).

92. Coustet, M. *et al.* Layer-by-layer assembly of polymersomes and polyelectrolytes on planar surfaces and microsized colloidal particles. *J. Colloid Interface Sci.* **421**, 132–140 (2014).

93. Romero, G. *et al.* Stepwise surface tailoring of carbon nanotubes with polyelectrolyte brushes and lipid layers to control their intracellular distribution and 'in vitro' toxicity. *Soft Matter* **7**, 6883–6890 (2011).

94. Lin, X., Clasky, A., Lai, K. & Yang, L. Carbon-based nano biomaterials: design,

fabrication and application. in *Biomedical Nanomaterials: From design to implementation* (eds. Webster, T. W. & Yazici, H. Y.) 51–61 (Institution of Engineering and Technology, 2016).

95. Lin, T. *et al.* Blood-Brain-Barrier-Penetrating Albumin Nanoparticles for Biomimetic Drug Delivery via Albumin-Binding Protein Pathways for Antiglioma Therapy. *ACS Nano* **10**, 9999–10012 (2016).

96. Pandya, A. D. *et al.* Drug-loaded Photosensitizer-Chitosan Nanoparticles for Combinatorial Chemo- and Photodynamic Cancer Therapy. *Biomacromolecules* (2020).

97. Li, K. & Liu, B. Polymer-encapsulated organic nanoparticles for fluorescence and photoacoustic imaging. *Chem. Soc. Rev.* **43**, 6570–6597 (2014).

98. Elsana, H. *et al.* Evaluation of novel cationic gene based liposomes with cyclodextrin prepared by thin film hydration and microfluidic systems. *Sci. Rep.* **9**, 1–17 (2019).

99. Knovich, M. A., Storey, J. A., Coffman, L. G., Torti, S. V. & Torti, F. M. Ferritin for the clinician. *Blood Rev.* **23**, 95–104 (2009).

100. Hirokawa, N., Noda, Y., Tanaka, Y. & Niwa, S. Kinesin superfamily motor proteins and intracellular transport. *Nat. Rev. Mol. Cell Biol.* **10**, 682–696 (2009).

101. Lee, E. J., Lee, N. K. & Kim, I. S. Bioengineered protein-based nanocage for drug delivery. *Adv. Drug Deliv. Rev.* **106**, 157–171 (2016).

102. Grove, T. Z. & Cortajarena, A. L. *Protein design for nanostructural engineering: General aspects*. *Advances in Experimental Medicine and Biology* vol. 940 (2016).

103. Scott, A. M., Wolchok, J. D. & Old, L. J. Antibody therapy of cancer. *Nat. Rev. Cancer* **12**, 278–287 (2012).

104. Fan, W. *et al.* Functional nanoparticles exploit the bile acid pathway to overcome multiple barriers of the intestinal epithelium for oral insulin delivery. *Biomaterials* **151**, 13–23 (2018).

105. Chaiwaree, S. *et al.* Doxorubicin–loaded human serum albumin submicron particles: Preparation, characterization and in vitro cellular uptake. *Pharmaceutics* **12**, 1–15 (2020).

106. Liu, X. *et al.* Low-Fouling Electrosprayed Hemoglobin Nanoparticles with Antioxidant Protection as Promising Oxygen Carriers. *Macromol. Biosci.* **20**, 1–11 (2020).

107. Lohcharoenkal, W., Wang, L., Chen, Y. C. & Rojanasakul, Y. Protein nanoparticles as drug delivery carriers for cancer therapy. *Biomed Res. Int.* **2014**, (2014).

108. Bulbake, U., Doppalapudi, S., Kommineni, N. & Khan, W. Liposomal formulations in clinical use: An updated review. *Pharmaceutics* **9**, 1–33 (2017).

109. Rideau, E., Dimova, R., Schwille, P., Wurm, F. R. & Landfester, K. Liposomes and polymersomes: a comparative review towards cell mimicking. *Chem. Soc. Rev.* **47**, 8572–8610 (2018).

110. Zhang, X. & Zhang, P. Polymersomes in Nanomedicine - A Review. *Curr. Nanosci.*

13, 124–129 (2016).

111. Che, H. & Van Hest, J. C. M. Stimuli-responsive polymersomes and nanoreactors. *J. Mater. Chem. B* **4**, 4632–4647 (2016).

112. Hu, X. *et al.* Stimuli-Responsive Polymersomes for Biomedical Applications. *Biomacromolecules* **18**, 649–673 (2017).

113. Song, Z. *et al.* Synthetic polypeptides: From polymer design to supramolecular assembly and biomedical application. *Chem. Soc. Rev.* **46**, 6570–6599 (2017).

114. Keddie, D. J. A guide to the synthesis of block copolymers using reversible-addition fragmentation chain transfer (RAFT) polymerization. *Chem. Soc. Rev.* **43**, 496–505 (2014).

115. Barbey, R. *et al.* Polymer Brushes via Surface-Initiated Controlled Radical Polymerization: Synthesis, Characterization, Properties, and Applications. *Chem. Rev.* **109**, 5437–5527 (2009).

116. Giussi, J. M. *et al.* A study of the complex interaction between poly allylamine hydrochloride and negatively charged poly(N-isopropylacrylamide-co-methacrylic acid) microgels. *Soft Matter* 799–804 (2020).

117. Proctor, C. M. *et al.* Ionic Hydrogel for Accelerated Dopamine Delivery via Retrodialysis. *Chem. Mater.* (2019).

118. Di Silvio, D. *et al.* Self-assembly of poly(allylamine)/siRNA nanoparticles, their intracellular fate and siRNA delivery. *J. Colloid Interface Sci.* **557**, 757–766 (2019).

119. Romero, G., Qiu, Y., Murray, R. A. & Moya, S. E. Study of intracellular delivery of doxorubicin from poly(lactide-co-glycolide) nanoparticles by means of fluorescence lifetime imaging and confocal raman microscopy. *Macromol. Biosci.* **13**, 234–241 (2013).

120. Soppimath, K. S., Aminabhavi, T. M., Kulkarni, A. R. & Rudzinski, W. E. Biodegradable polymeric nanoparticles as drug delivery devices. *J. Control. Release* **70**, 1–20 (2001).

121. Chen, X. & Fuchs, H. Self-Assembly of Organic Molecules into Nanostructures. in *Soft Matter Nanotechnology: From Structure to Function* (eds. Chen, X. & Fuchs, H.) 21–95 (Wiley-VCH Verlag GmbH & Co. KGaA, 2015).

122. Decher, G. & Hong, J. -D. Buildup of ultrathin multilayer films by a self-assembly process, 1 consecutive adsorption of anionic and cationic bipolar amphiphiles on charged surfaces. *Makromol. Chemie. Macromol. Symp.* **46**, 321–327 (1991).

123. Muzzio, N. E. *et al.* Enhanced antiadhesive properties of chitosan/hyaluronic acid polyelectrolyte multilayers driven by thermal annealing: Low adherence for mammalian cells and selective decrease in adhesion for Gram-positive bacteria. *Mater. Sci. Eng. C* **80**, 677–687 (2017).

124. Gregurec, D. *et al.* Stability of polyelectrolyte multilayers in oxidizing media: a critical issue for the development of multilayer based membranes for nanofiltration. *Colloid Polym. Sci.* **293**, 381–388 (2014).

125. Huang, J., Zajforoushan Moghaddam, S., Maroni, P. & Thormann, E. Swelling

Behavior, Interaction, and Electrostatic Properties of Chitosan/Alginate Dialdehyde Multilayer Films with Different Outermost Layer. *Langmuir* **36**, 3782–3791 (2020).

126. Sukhorukov, G. B. *et al.* Layer-by-layer self assembly of polyelectrolytes on colloidal particles. *Colloids Surfaces A Physicochem. Eng. Asp.* **137**, 253–266 (1998).

127. Donath, E., Sukhorukov, G. B., Caruso, F., Davis, S. A. & Möhwald, H. Novel Hollow Polymer Shells by Colloid-Templated Assembly of Polyelectrolytes. *Angew. Chemie Int. Ed.* **37**, 2201–2205 (1998).

128. Gabriela, R. *et al.* Layer by layer surface engineering of poly (lactide-co-glycolide) nanoparticles: A versatile tool for nanoparticle engineering for targeted drug delivery. *Sci. China Chem.* **56**, 1029–1039 (2013).

129. Oh, J. K., Drumright, R., Siegwart, D. J. & Matyjaszewski, K. The development of microgels/nanogels for drug delivery applications. *Prog. Polym. Sci.* **33**, 448–477 (2008).

130. Hellstrand, E. *et al.* Complete high-density lipoproteins in nanoparticle corona. *FEBS J.* **276**, 3372–3381 (2009).

131. Tenzer, S. *et al.* Rapid formation of plasma protein corona critically affects nanoparticle pathophysiology. *Nat. Nanotechnol.* **8**, 772–781 (2013).

132. Mahmoudi, M. *et al.* Protein–Nanoparticle Interactions: Opportunities and Challenges. *Chem. Rev.* **111**, 5610–5637 (2011).

133. Shen, Y. *et al.* Characterization of the human blood plasma proteome. *Proteomics* **5**, 4034–4045 (2005).

134. Gräfe, C. *et al.* Protein corona formation and its constitutional changes on magnetic nanoparticles in serum featuring a polydehydroalanine coating: effects of charge and incubation conditions. *Nanotechnology* **30**, 265707 (2019).

135. Mirshafiee, V., Kim, R., Mahmoudi, M. & Kraft, M. L. The importance of selecting a proper biological milieu for protein corona analysis in vitro: Human plasma versus human serum. *Int. J. Biochem. Cell Biol.* **75**, 188–195 (2016).

136. Walczyk, D., Bombelli, F. B., Monopoli, M. P., Lynch, I. & Dawson, K. A. What the Cell "Sees" in Bionanoscience. *J. Am. Chem. Soc.* **132**, 5761–5768 (2010).

137. Pederzoli, F. *et al.* Protein corona and nanoparticles: how can we investigate on? *Wiley Interdiscip. Rev. Nanomedicine Nanobiotechnology* **9**, 1–23 (2017).

138. Milani, S., Baldelli Bombelli, F., Pitek, A. S., Dawson, K. A. & Rädler, J. Reversible versus Irreversible Binding of Transferrin to Polystyrene Nanoparticles: Soft and Hard Corona. *ACS Nano* **6**, 2532–2541 (2012).

139. VROMAN, L. Effect of Adsorbed Proteins on the Wettability of Hydrophilic and Hydrophobic Solids. *Nature* **196**, 476–477 (1962).

140. Carrillo-Carrion, C., Carril, M. & Parak, W. J. Techniques for the experimental investigation of the protein corona. *Curr. Opin. Biotechnol.* **46**, 106–113 (2017).

141. Monopoli, M. P. *et al.* Physical–Chemical Aspects of Protein Corona: Relevance

to in Vitro and in Vivo Biological Impacts of Nanoparticles. *J. Am. Chem. Soc.* **133**, 2525–2534 (2011).

142. Mikelez-alonso, I., Aires, A. & Cortajarena, A. L. Cancer nano-immunotherapy from the injection to the target: The role of protein corona. *Int. J. Mol. Sci.* **21**, (2020).

143. Munsell, E. V., Fang, B. & Sullivan, M. O. Histone-Mimetic Gold Nanoparticles as Versatile Scaffolds for Gene Transfer and Chromatin Analysis. *Bioconjug. Chem.* **29**, 3691–3704 (2018).

144. Gebauer, J. S. *et al.* Impact of the nanoparticle-protein corona on colloidal stability and protein structure. *Langmuir* **28**, 9673–9679 (2012).

145. Ganesh, A. N. *et al.* Colloidal Drug Aggregate Stability in High Serum Conditions and Pharmacokinetic Consequence. *ACS Chem. Biol.* **14**, 751–757 (2019).

146. Bertrand, N. *et al.* Mechanistic understanding of in vivo protein corona formation on polymeric nanoparticles and impact on pharmacokinetics. *Nat. Commun.* **8**, (2017).

147. Tekie, F. S. M. *et al.* Controlling evolution of protein corona: a prosperous approach to improve chitosan-based nanoparticle biodistribution and half-life. *Sci. Rep.* **10**, 9664 (2020).

148. Palchetti, S. *et al.* Influence of dynamic flow environment on nanoparticle-protein corona: From protein patterns to uptake in cancer cells. *Colloids Surfaces B Biointerfaces* **153**, 263–271 (2017).

149. Lesniak, A. *et al.* Nanoparticle Adhesion to the Cell Membrane and Its Effect on Nanoparticle Uptake Efficiency. *J. Am. Chem. Soc.* **135**, 1438–1444 (2013).

150. Ge, C. *et al.* Binding of blood proteins to carbon nanotubes reduces cytotoxicity. *Proc. Natl. Acad. Sci.* **108**, 16968–16973 (2011).

151. Duan, G. *et al.* Protein corona mitigates the cytotoxicity of graphene oxide by reducing its physical interaction with cell membrane. *Nanoscale* **7**, 15214–15224 (2015).

152. Stan, M. S. *et al.* Dynamic analysis of the interactions between Si/SiO2 quantum dots and biomolecules for improving applications based on nano-bio interfaces. *Sci. Rep.* **8**, 91–95 (2018).

153. Wan, S. *et al.* The "Sweet" Side of the Protein Corona: Effects of Glycosylation on Nanoparticle–Cell Interactions. *ACS Nano* **9**, 2157–2166 (2015).

154. Francia, V. *et al.* Corona Composition Can Affect the Mechanisms Cells Use to Internalize Nanoparticles. *ACS Nano* **13**, 11107–11121 (2019).

155. Cox, A. *et al.* Evolution of Nanoparticle Protein Corona across the Blood-Brain Barrier. *ACS Nano* **12**, 7292–7300 (2018).

156. Sanchez-Cano, C. & Carril, M. Recent developments in the design of non-biofouling coatings for nanoparticles and surfaces. *Int. J. Mol. Sci.* **21**, 1–24 (2020).

157. Pelaz, B. *et al.* Surface Functionalization of Nanoparticles with Polyethylene Glycol: Effects on Protein Adsorption and Cellular Uptake. *ACS Nano* **9**, 6996–

7008 (2015).

158. Gref, R. *et al.* 'Stealth' corona-core nanoparticles surface modified by polyethylene glycol (PEG): Influences of the corona (PEG chain length and surface density) and of the core composition on phagocytic uptake and plasma protein adsorption. *Colloids Surfaces B Biointerfaces* **18**, 301–313 (2000).

159. Ishida, T. *et al.* Injection of PEGylated liposomes in rats elicits PEG-specific IgM, which is responsible for rapid elimination of a second dose of PEGylated liposomes. *J. Control. Release* **112**, 15–25 (2006).

160. Yang, Q. *et al.* Analysis of pre-existing IgG and IgM antibodies against polyethylene glycol (PEG) in the general population. *Anal. Chem.* **88**, 11804–11812 (2016).

161. Lubich, C. *et al.* The Mystery of Antibodies Against Polyethylene Glycol (PEG) - What do we Know? *Pharm. Res.* **33**, 2239–2249 (2016).

162. Weiss, A. C. G. *et al.* Link between Low-Fouling and Stealth: A Whole Blood Biomolecular Corona and Cellular Association Analysis on Nanoengineered Particles. *ACS Nano* **13**, 4980–4991 (2019).

163. Xia, Y. *et al.* PASylated interferon α efficiently suppresses hepatitis B virus and induces anti-HBs seroconversion in HBV-transgenic mice. *Antiviral Res.* **161**, 134–143 (2019).

164. Hu, C. M. J. *et al.* Erythrocyte membrane-camouflaged polymeric nanoparticles as a biomimetic delivery platform. *Proc. Natl. Acad. Sci. U. S. A.* **108**, 10980–10985 (2011).

165. Shi, J., Kantoff, P. W., Wooster, R. & Farokhzad, O. C. Cancer nanomedicine: Progress, challenges and opportunities. *Nat. Rev. Cancer* **17**, 20–37 (2017).

166. Estrella, V. *et al.* Acidity generated by the tumor microenvironment drives local invasion. *Cancer Res.* **73**, 1524–1535 (2013).

167. Azevedo, C., Macedo, M. H. & Sarmento, B. Strategies for the enhanced intracellular delivery of nanomaterials. *Drug Discov. Today* **23**, 944–959 (2018).

168. Francia, V., Montizaan, D. & Salvati, A. Interactions at the cell membrane and pathways of internalization of nano-sized materials for nanomedicine. *Beilstein J. Nanotechnol.* **11**, 338–353 (2020).

169. Conner, S. D. & Schmid, S. L. Regulated portals of entry into the cell. *Nature* **422**, 37–44 (2003).

170. Behzadi, S. *et al.* Cellular uptake of nanoparticles: Journey inside the cell. *Chem. Soc. Rev.* **46**, 4218–4244 (2017).

171. Doherty, G. J. & McMahon, H. T. Mechanisms of Endocytosis. *Annu. Rev. Biochem.* **78**, 857–902 (2009).

172. Henne, W. M. *et al.* FCHo proteins are nucleators of Clathrin-Mediated endocytosis. *Science (80-.).* **328**, 1281–1284 (2010).

173. Ferreira, A. P. A. & Boucrot, E. Mechanisms of Carrier Formation during Clathrin-Independent Endocytosis. *Trends Cell Biol.* **28**, 188–200 (2018).

174. Parton, R. G. Clathrin Independent Endocytosis. *Encycl. Cell Biol.* **2**, 394–400 (2016).

175. McMahon, H. T. & Boucrot, E. Molecular mechanism and physiological functions of clathrin-mediated endocytosis. *Nat. Rev. Mol. Cell Biol.* **12**, 517–533 (2011).

176. Sahay, G., Alakhova, D. Y. & Kabanov, A. V. Endocytosis of nanomedicines. *J. Control. Release* **145**, 182–195 (2010).

177. Carver, L. A. & Schnitzer, J. E. Caveolae: Mining little caves for new cancer targets. *Nat. Rev. Cancer* **3**, 571–581 (2003).

178. Shin, J.-S. CELL BIOLOGY: Caveolae--Not Just Craters in the Cellular Landscape. *Science (80-.).* **293**, 1447–1448 (2001).

179. Mout, R. *et al.* General Strategy for Direct Cytosolic Protein Delivery via Protein-Nanoparticle Co-engineering. *ACS Nano* **11**, 6416–6421 (2017).

180. Varkouhi, A. K., Scholte, M., Storm, G. & Haisma, H. J. Endosomal escape pathways for delivery of biologicals. *J. Control. Release* **151**, 220–228 (2011).

181. Smith, S. A., Selby, L. I., Johnston, A. P. R. & Such, G. K. The Endosomal Escape of Nanoparticles: Toward More Efficient Cellular Delivery. *Bioconjug. Chem.* **30**, 263–272 (2019).

182. Rayamajhi, S. *et al.* pH-responsive cationic liposome for endosomal escape mediated drug delivery. *Colloids Surfaces B Biointerfaces* **188**, 110804 (2020).

183. Thorn, C. F. *et al.* Doxorubicin pathways: pharmacodynamics and adverse effects. *Pharmacogenet. Genomics* **21**, 440–446 (2011).

184. Goh, K. Il *et al.* The human disease network. *Proc. Natl. Acad. Sci. U. S. A.* **104**, 8685–8690 (2007).

185. Whitehead, K. A., Langer, R. & Anderson, D. G. Knocking down barriers: Advances in siRNA delivery. *Nat. Rev. Drug Discov.* **8**, 129–138 (2009).

186. Hu, Q. *et al.* Engineering Nanoparticle-Coated Bacteria as Oral DNA Vaccines for Cancer Immunotherapy. *Nano Lett.* **15**, 2732–2739 (2015).

187. Zhao, W., Hou, X., Vick, O. G. & Dong, Y. RNA delivery biomaterials for the treatment of genetic and rare diseases. *Biomaterials* **217**, 119291 (2019).

188. Sousa, Â. *et al.* Optimization of peptide-plasmid DNA vectors formulation for gene delivery in cancer therapy exploring design of experiments. *Colloids Surfaces B Biointerfaces* **183**, 110417 (2019).

189. Frankiw, L., Baltimore, D. & Li, G. Alternative mRNA splicing in cancer immunotherapy. *Nat. Rev. Immunol.* **19**, 675–687 (2019).

190. Makarova, K. S. *et al.* Evolution and classification of the CRISPR-Cas systems. *Nat. Rev. Microbiol.* **9**, 467–477 (2011).

191. Fernandez-nieves, A., Wyss, H. M., Mattsson, J. & Weitz, D. a. *Microgel Suspensions*. (Wiley-VCH Verlag GmbH & Co. KGaA, 2011).

192. Shibayama, M. & Tanaka, T. *Volume phase transition and related phenomena of polymer gels*. *Advances in Polymer Science* vol. 109 (1993).

193. Pierre, A. C. *Introduction to Sol-Gel Processing*. *Introduction to Sol-Gel Processing*

(Springer International Publishing, 2020).

194. Kabiri, K., Omidian, H., Hashemi, S. A. & Zohuriaan-Mehr, M. J. Synthesis of fast-swelling superabsorbent hydrogels: Effect of crosslinker type and concentration on porosity and absorption rate. *Eur. Polym. J.* **39**, 1341–1348 (2003).

195. Peppas, N. A., Bures, P., Leobandung, W. & Ichikawa, H. Hydrogels in pharmaceutical formulations. *Eur. J. Pharm. Biopharm.* **50**, 27–46 (2000).

196. Hoare, T. R. & Kohane, D. S. Hydrogels in drug delivery: Progress and challenges. *Polymer (Guildf).* **49**, 1993–2007 (2008).

197. Vermonden, T., Censi, R. & Hennink, W. E. Hydrogels for Protein Delivery. *Chem. Rev.* **112**, 2853–2888 (2012).

198. Dadsetan, M. *et al.* A stimuli-responsive hydrogel for doxorubicin delivery. *Biomaterials* **31**, 8051–8062 (2010).

199. Cao, M. *et al.* Reversible Thermoresponsive Peptide-PNIPAM Hydrogels for Controlled Drug Delivery. *Biomacromolecules* **20**, 3601–3610 (2019).

200. Buenger, D., Topuz, F. & Groll, J. Hydrogels in sensing applications. *Prog. Polym. Sci.* **37**, 1678–1719 (2012).

201. Pinelli, F., Magagnin, L. & Rossi, F. Progress in hydrogels for sensing applications: a review. *Mater. Today Chem.* **17**, 100317 (2020).

202. Toma, M., Jonas, U., Mateescu, A., Knoll, W. & Dostalek, J. Active control of SPR by thermoresponsive hydrogels for biosensor applications. *J. Phys. Chem. C* **117**, 11705–11712 (2013).

203. Lei, Z., Wang, Q. & Wu, P. A multifunctional skin-like sensor based on a 3D printed thermo-responsive hydrogel. *Mater. Horizons* **4**, 694–700 (2017).

204. Serpe, M. J., Yarmey, K. a., Nolan, C. M. & Lyon, L. A. Doxorubicin uptake and release from microgel thin films. *Biomacromolecules* **6**, 408–413 (2005).

205. Seiffert, S. Sensitive microgels as model colloids and microcapsules. *J. Polym. Sci. Part A Polym. Chem.* **52**, 435–449 (2014).

206. Brugger, B. & Richtering, W. Emulsions stabilized by stimuli-sensitive poly(N-isopropylacrylamide)-co-methacrylic acid polymers: microgels versus low molecular weight polymers. *Langmuir* **24**, 7769–7777 (2008).

207. Schmidt, S. *et al.* Influence of microgel architecture and oil polarity on stabilization of emulsions by stimuli-sensitive core-shell poly(N - isopropylacrylamide- co -methacrylic acid) microgels: Mickering versus pickering behavior? *Langmuir* **27**, 9801–9806 (2011).

208. Serpe, M. J., Jones, C. D. & Lyon, L. A. Layer-by-Layer Deposition of Thermoresponsive Microgel Thin Films. *Langmuir* **19**, 8759–8764 (2003).

209. Spears, M. W., Herman, E. S., Gaulding, J. C. & Lyon, L. A. Dynamic Materials from Microgel Multilayers. *Langmuir* **30**, 6314–6323 (2014).

210. Xu, W. *et al.* Distribution of Ionizable Groups in Polyampholyte Microgels Controls Interactions with Captured Proteins: From Blockade and 'levitation' to Accelerated Release. *Biomacromolecules* **20**, 1578–1591 (2019).

211. Maza, E. *et al.* Layer-by-Layer Assembled Microgels Can Combine Conflicting Properties: Switchable Stiffness and Wettability without Affecting Permeability. *Langmuir* **34**, 3711–3719 (2018).

212. Kleinen, J. & Richtering, W. Rearrangements in and release from responsive microgel-polyelectrolyte complexes induced by temperature and time. *J. Phys. Chem. B* **115**, 3804–3810 (2011).

213. Walta, S. *et al.* Microgels enable capacious uptake and controlled release of architecturally complex macromolecular species. *Polym. (United Kingdom)* **119**, 50–58 (2017).

214. Islam, M. R. & Serpe, M. J. Penetration of Polyelectrolytes into Charged Poly(N -isopropylacrylamide) Microgel Layers Confined between Two Surfaces. *Macromolecules* **46**, 1599–1606 (2013).

215. Costa, E., Lloyd, M. M., Chopko, C., Aguiar-Ricardo, A. & Hammond, P. T. Tuning smart microgel swelling and responsive behavior through strong and weak polyelectrolyte pair assembly. *Langmuir* **28**, 10082–10090 (2012).

216. Dobrynin, A. V. & Rubinstein, M. Adsorption of hydrophobic polyelectrolytes at oppositely charged surfaces. *Macromolecules* **35**, 2754–2768 (2002).

217. Gelissen, A. P. H. *et al.* An anionic shell shields a cationic core allowing for uptake and release of polyelectrolytes within core-shell responsive microgels. *Soft Matter* **14**, 4287–4299 (2018).

218. Zavgorodnya, O. & Serpe, M. J. Assembly of poly(N-isopropylacrylamide)-co-acrylic acid microgel thin films on polyelectrolyte multilayers: Effects of polyelectrolyte layer thickness, surface charge, and microgel solution pH. *Colloid Polym. Sci.* **289**, 591–602 (2011).

219. Sanz, B. *et al.* Thermally-induced softening of PNIPAm-based nanopillar arrays. *Soft Matter* **13**, 2453–2464 (2017).

220. Nolan, C. M., Serpe, M. J. & Lyon, L. A. Thermally modulated insulin release from microgel thin films. *Biomacromolecules* **5**, 1940–1946 (2004).

221. Basuki, J. S. *et al.* Using fluorescence lifetime imaging microscopy to monitor theranostic nanoparticle uptake and intracellular doxorubicin release. *ACS Nano* **7**, 10175–10189 (2013).

222. Senff, H. & Richtering, W. Temperature sensitive microgel suspensions: Colloidal phase behavior and rheology of soft spheres. *J. Chem. Phys.* **111**, 1705–1711 (1999).

223. Schild, H. G. Poly(N-isopropylacrylamide): experiment, theory and application. *Prog. Polym. Sci.* **17**, 163–249 (1992).

224. Li, W. *et al.* Comparison of the Responsivity of Solution-Suspended and Surface-Bound Poly(N-isopropylacrylamide)-Based Microgels for Sensing Applications. *ACS Appl. Mater. Interfaces* **9**, 26539–26548 (2017).

225. Shin, D. S. *et al.* Synthesis of Microgel Sensors for Spatial and Temporal Monitoring of Protease Activity. *ACS Biomater. Sci. Eng.* **4**, 378–387 (2018).

226. Newsom, J. P., Payne, K. A. & Krebs, M. D. Microgels: Modular, tunable constructs

for tissue regeneration. *Acta Biomater.* **88**, 32–41 (2019).

227. Nakayama, M. *et al.* Molecular design of biodegradable polymeric micelles for temperature-responsive drug release. *J. Control. Release* **115**, 46–56 (2006).

228. Sung, B., Kim, C. & Kim, M. H. Biodegradable colloidal microgels with tunable thermosensitive volume phase transitions for controllable drug delivery. *J. Colloid Interface Sci.* **450**, 26–33 (2015).

229. Fundueanu, G., Constantin, M., Bucatariu, S. & Ascenzi, P. Poly(N-isopropylacrylamide-co-N-isopropylmethacrylamide) Thermo-Responsive Microgels as Self-Regulated Drug Delivery System. *Macromol. Chem. Phys.* **217**, 2525–2533 (2016).

230. Malmsten, M., Bysell, H. & Hansson, P. Biomacromolecules in microgels — Opportunities and challenges for drug delivery. *Curr. Opin. Colloid Interface Sci.* **15**, 435–444 (2010).

231. Smeets, N. M. B. & Hoare, T. Designing responsive microgels for drug delivery applications. *J. Polym. Sci. Part A Polym. Chem.* **51**, 3027–3043 (2013).

232. Matanović, M. R., Kristl, J. & Grabnar, P. A. Thermoresponsive polymers: Insights into decisive hydrogel characteristics, mechanisms of gelation, and promising biomedical applications. *Int. J. Pharm.* **472**, 262–275 (2014).

233. Hoare, T. & Pelton, R. Functional Group Distributions in Carboxylic Acid Containing Poly(N -isopropylacrylamide) Microgels. *Langmuir* **20**, 2123–2133 (2004).

234. Saunders, B. R., Crowther, H. M. & Vincent, B. Poly[(methyl methacrylate)- co -(methacrylic acid)] Microgel Particles: Swelling Control Using pH, Cononsolvency, and Osmotic Deswelling. *Macromolecules* **30**, 482–487 (1997).

235. Okhapkin, I. M., Nasimova, I. R., Makhaeva, E. E. & Khokhlov, A. R. Effect of Complexation of Monomer Units on pH- and Temperature-Sensitive Properties of Poly(N -vinylcaprolactam- co -methacrylic acid). *Macromolecules* **36**, 8130–8138 (2003).

236. Giussi, J. M., Velasco, M. I., Longo, G. S., Acosta, R. H. & Azzaroni, O. Unusual temperature-induced swelling of ionizable poly(N-isopropylacrylamide)-based microgels: experimental and theoretical insights into its molecular origin. *Soft Matter* **11**, 8879–8886 (2015).

237. Spěváček, J. Application of NMR Spectroscopy to Study Thermoresponsive Polymers. in *Temperature-Responsive Polymers* 225–247 (John Wiley & Sons Ltd, 2018).

238. Spěváček, J., Konefał, R., Dybal, J., Čadová, E. & Kovářová, J. Thermoresponsive behavior of block copolymers of PEO and PNIPAm with different architecture in aqueous solutions: A study by NMR, FTIR, DSC and quantum-chemical calculations. *Eur. Polym. J.* **94**, 471–483 (2017).

239. Konefał, R., Spěváček, J. & Černoch, P. Thermoresponsive poly(2-oxazoline) homopolymers and copolymers in aqueous solutions studied by NMR spectroscopy and dynamic light scattering. *Eur. Polym. J.* **100**, 241–252 (2018).

240. Loukotová, L. *et al.* Hybrid κ-carrageenan-based polymers showing

"schizophrenic" lower and upper critical solution temperatures and potassium responsiveness. *Carbohydr. Polym.* **210**, 26–37 (2019).

241. Konefał, R., Spěváček, J., Jäger, E. & Petrova, S. Thermoresponsive behaviour of terpolymers containing poly(ethylene oxide), poly(2-ethyl-2-oxazoline) and poly(ε-caprolactone) blocks in aqueous solutions: an NMR study. *Colloid and Polymer Science* vol. 294 1717–1726 (2016).
242. Yoon, J. A., Gayathri, C., Gil, R. R., Kowalewski, T. & Matyjaszewski, K. Comparison of the thermoresponsive deswelling kinetics of poly(2-(2-methoxyethoxy)ethyl methacrylate) hydrogels prepared by ATRP and FRP. *Macromolecules* **43**, 4791–4797 (2010).
243. Sun, S., Wu, P., Zhang, W., Zhang, W. & Zhu, X. Effect of structural constraint on dynamic self-assembly behavior of PNIPAM-based nonlinear multihydrophilic block copolymers. *Soft Matter* **9**, 1807–1816 (2013).
244. Ru, G., Wang, N., Huang, S. & Feng, J. H HRMAS NMR study on phase transition of poly(N-isopropylacrylamide) gels with and without grafted comb-type chains. *Macromolecules* **42**, 2074–2078 (2009).
245. Tang, H., Zhang, B. & Wu, P. On the two-step phase transition behavior of the Poly(N-isopropylacrylamide) (PNIPAM) brush: different zones with different orders. *Soft Matter* **10**, 7278–7284 (2014).
246. Zhou, S. & Chu, B. Synthesis and Volume Phase Transition of Poly(methacrylic acid- co - N -isopropylacrylamide) Microgel Particles in Water. *J. Phys. Chem. B* **102**, 1364–1371 (1998).
247. Bajpai, A. K., Shukla, S. K., Bhanu, S. & Kankane, S. Responsive polymers in controlled drug delivery. *Prog. Polym. Sci.* **33**, 1088–1118 (2008).
248. Tanaka, T., Amiya, T., Mamada, A. & Tokuhiro, T. NMR Study of Poly(N-isopropylacrylamide) Gels near Phase Transition. *Macromolecules* **24**, 2936–2943 (1991).
249. Gottlieb, H. E., Kotlyar, V. & Nudelman, A. NMR chemical shifts of common laboratory solvents as trace impurities. *J. Org. Chem.* **62**, 7512–7515 (1997).
250. Gomez, M. V. & De La Hoz, A. NMR reaction monitoring in flow synthesis. *Beilstein J. Org. Chem.* **13**, 285–300 (2017).
251. Pino, P. Del *et al.* Protein corona formation around nanoparticles - From the past to the future. *Mater. Horizons* **1**, 301–313 (2014).
252. Monopoli, M. P., Åberg, C., Salvati, A. & Dawson, K. A. Biomolecular coronas provide the biological identity of nanosized materials. *Nat. Nanotechnol.* **7**, 779–786 (2012).
253. Biga, L. M. *et al.* 18.1 Functions of Blood. in *Anatomy&Physiology* (OpenStax/Oregon State University, 2020).
254. Lundqvist, M. *et al.* Nanoparticle size and surface properties determine the protein corona with possible implications for biological impacts. *Proc. Natl. Acad. Sci. U. S. A.* **105**, 14265–14270 (2008).
255. Madathiparambil Visalakshan, R. *et al.* The Influence of Nanoparticle Shape on

Protein Corona Formation. *Small* **16**, (2020).

256. Tenzer, S. *et al.* Rapid formation of plasma protein corona critically affects nanoparticle pathophysiology. *Nat. Nanotechnol.* **8**, 772–781 (2013).

257. Vedantam, P., Huang, G. & Tzeng, T. R. J. Size-dependent cellular toxicity and uptake of commercial colloidal gold nanoparticles in DU-145 cells. *Cancer Nanotechnol.* **4**, 13–20 (2013).

258. Shahabi, S., Treccani, L., Dringen, R. & Rezwan, K. Modulation of Silica Nanoparticle Uptake into Human Osteoblast Cells by Variation of the Ratio of Amino and Sulfonate Surface Groups: Effects of Serum. *ACS Appl. Mater. Interfaces* **7**, 13821–13833 (2015).

259. Weiss, A. C. G. *et al.* Link between Low-Fouling and Stealth: A Whole Blood Biomolecular Corona and Cellular Association Analysis on Nanoengineered Particles. *ACS Nano* **13**, 4980–4991 (2019).

260. Ding, L. *et al.* Size, Shape, and Protein Corona Determine Cellular Uptake and Removal Mechanisms of Gold Nanoparticles. *Small* **14**, 1–13 (2018).

261. Schöttler, S., Landfester, K. & Mailänder, V. Controlling the Stealth Effect of Nanocarriers through Understanding the Protein Corona. *Angew. Chemie - Int. Ed.* **55**, 8806–8815 (2016).

262. Augustsson, C. *et al.* The nanoparticle protein corona formed in human blood or human blood fractions. *PLoS One* **12**, e0175871 (2017).

263. Colapicchioni, V. *et al.* Personalized liposome-protein corona in the blood of breast, gastric and pancreatic cancer patients. *Int. J. Biochem. Cell Biol.* **75**, 180–187 (2016).

264. Setyawati, M. I., Tay, C. Y., Docter, D., Stauber, R. H. & Leong, D. T. Understanding and exploiting nanoparticles' intimacy with the blood vessel and blood. *Chem. Soc. Rev.* **44**, 8174–8199 (2015).

265. Vroman, L., Adams, A. L., Fischer, G. & Munoz, P. Interaction of high molecular weight kininogen, factor XII, and fibrinogen in plasma at interfaces. *Blood* **55**, 156–159 (1980).

266. Walczyk, D., Bombelli, F. B., Monopoli, M. P., Lynch, I. & Dawson, K. A. What the Cell "Sees" in Bionanoscience. *J. Am. Chem. Soc.* **132**, 5761–5768 (2010).

267. Peng, Q. & Mu, H. The potential of protein-nanomaterial interaction for advanced drug delivery. *J. Control. Release* **225**, 121–132 (2016).

268. Luby, A. O., Breitner, E. K. & Comfort, K. K. Preliminary protein corona formation stabilizes gold nanoparticles and improves deposition efficiency. *Appl. Nanosci.* **6**, 827–836 (2016).

269. Mahmoudi, M. *et al.* Crucial role of the protein corona for the specific targeting of nanoparticles. *Nanomedicine* **10**, 215–226 (2015).

270. Mirshafiee, V., Mahmoudi, M., Lou, K., Cheng, J. & Kraft, M. L. Protein corona significantly reduces active targeting yield. *Chem. Commun.* **49**, 2557 (2013).

271. Corbo, C. *et al.* The impact of nanoparticle protein corona on cytotoxicity, immunotoxicity and target drug delivery. *Nanomedicine* **11**, 81–100 (2016).

272. Yang, Z., Hancock, W. S., Chew, T. R. & Bonilla, L. A study of glycoproteins in human serum and plasma reference standards (HUPO) using multilectin affinity chromatography coupled with RPLC-MS/MS. *Proteomics* **5**, 3353–3366 (2005).

273. Helenius, A. & Aebi, M. Roles of N-Linked Glycans in the Endoplasmic Reticulum. *Annu. Rev. Biochem.* **73**, 1019–1049 (2004).

274. Lin, B., Qing, X., Liao, J. & Zhuo, K. Role of Protein Glycosylation in Host-Pathogen Interaction. *Cells* **9**, 1–24 (2020).

275. Wan, S. *et al.* The 'sweet' Side of the protein corona: Effects of glycosylation on nanoparticle-cell interactions. *ACS Nano* **9**, 2157–2166 (2015).

276. Weis, W. I. & Drickamer, K. STRUCTURAL BASIS OF LECTIN-CARB OHYDRATE. (1996).

277. Ribeiro, A. C., Ferreira, R. & Freitas, R. *Plant Lectins: Bioactivities and Bioapplications*. *Studies in Natural Products Chemistry* vol. 58 (Elsevier B.V., 2018).

278. Immel, F. *et al.* The shell of the invasive bivalve species Dreissena polymorpha: Biochemical, elemental and textural investigations. *PLoS One* **11**, 1–28 (2016).

279. Gnanesh Kumar, B. S. & Surolia, A. Site specific N-glycan profiling of NeuAc(α2-6)-Gal/GalNAc-binding bark Sambucus nigra agglutinin using LC–MSn revealed differential glycosylation. *Glycoconj. J.* **33**, 907–915 (2016).

280. Winzen, S. *et al.* Complementary analysis of the hard and soft protein corona: Sample preparation critically effects corona composition. *Nanoscale* **7**, 2992–3001 (2015).

281. Jan Wolfgang Krieger, J. L. QuickFit 3.0. A data evaluation application for biophysics. (2015).

282. Bradford, M. M. A rapid and sensitive method for the quantitation of microgram quantities of protein utilizing the principle of protein-dye binding. *Anal. Biochem.* **72**, 248–254 (1976).

283. Burda, C., Chen, X., Narayanan, R. & El-Sayed, M. A. *Chemistry and properties of nanocrystals of different shapes*. *Chemical Reviews* vol. 105 (2005).

284. Liz-Marzán, L. M. Tailoring surface plasmons through the morphology and assembly of metal nanoparticles. *Langmuir* **22**, 32–41 (2006).

285. He, Y. Q., Liu, S. P., Kong, L. & Liu, Z. F. A study on the sizes and concentrations of gold nanoparticles by spectra of absorption, resonance Rayleigh scattering and resonance non-linear scattering. *Spectrochim. Acta - Part A Mol. Biomol. Spectrosc.* **61**, 2861–2866 (2005).

286. Zhang, T. X., Zhu, G. Y., Lu, B. Y., Zhang, C. L. & Peng, Q. Concentration-dependent protein adsorption at the nano-bio interfaces of polymeric nanoparticles and serum proteins. *Nanomedicine* **12**, 2757–2769 (2017).

287. Maley, F., Trimble, R. B., Tarentino, A. L. & Plummer, T. H. Characterization of glycoproteins and their associated oligosaccharides through the use of endoglycosidases. *Anal. Biochem.* **180**, 195–204 (1989).

288. Zhao, B. & Brittain, W. . Polymer brushes: surface-immobilized macromolecules. *Prog. Polym. Sci.* **25**, 677–710 (2000).

289. Moad, G. & Solomon, D. H. *The chemistry of Radical polimerization*. (Elsevier Science, 2006).

290. Braunecker, W. A. & Matyjaszewski, K. Controlled/living radical polymerization: Features, developments, and perspectives. *Prog. Polym. Sci.* **32**, 93–146 (2007).

291. Odian, G. *Principles of Polymerization*. *Physics and Chemistry of Glasses* vol. 37 (y John Wiley & Sons, Inc, 2004).

292. Nicolas, J. *et al.* Nitroxide-mediated polymerization. *Prog. Polym. Sci.* **38**, 63–235 (2013).

293. Cazotti, J. C. *et al.* Grafting from Starch Nanoparticles with Synthetic Polymers via Nitroxide-Mediated Polymerization. *Macromol. Rapid Commun.* **40**, 1–5 (2019).

294. Matyjaszewski, K. Advanced Materials by Atom Transfer Radical Polymerization. *Adv. Mater.* **30**, 1–22 (2018).

295. Matyjaszewski, K. & Xia, J. Atom Transfer Radical Polymerization. *Chem. Rev.* **101**, 2921–2990 (2001).

296. Perrier, S. 50th Anniversary Perspective: RAFT Polymerization - A User Guide. *Macromolecules* **50**, 7433–7447 (2017).

297. Moad, G. RAFT polymerization to form stimuli-responsive polymers. *Polym. Chem.* **8**, 177–219 (2017).

298. Keddie, D. J. A guide to the synthesis of block copolymers using reversible-addition fragmentation chain transfer (RAFT) polymerization. *Chem. Soc. Rev.* **43**, 496–505 (2014).

299. Perrier, S., Takolpuckdee, P., Westwood, J. & Lewis, D. M. Versatile Chain Transfer Agents for Reversible Addition Fragmentation Chain Transfer (RAFT) Polymerization to Synthesize Functional Polymeric Architectures. *Macromolecules* **37**, 2709–2717 (2004).

300. Byler, C. L. & Hirscher, M. M. Thermal Decomposition of Polymers. in *SFPE Handbook of Fire Protection Engineering* 110–131 (Springer New York, 2016).

301. Madelung, O. *Semiconductors. Basic Data*. (Springer, 1996).

302. Damen, T. C., Porto, S. P. S. & Tell, B. Raman effect in zinc oxide. *Phys. Rev.* **142**, 570–574 (1966).

303. Romero, G. *et al.* Surface engineered poly(lactide-co-glycolide) nanoparticles for intracellular delivery: Uptake and cytotoxicity - A confocal Raman microscopic study. *Biomacromolecules* (2010).

304. Movasaghi, Z., Rehman, S. & Rehman, I. U. Raman spectroscopy of biological tissues. *Appl. Spectrosc. Rev.* **42**, 493–541 (2007).

305. U.S. Food and Drug Administration. What is Gene Therapy? https://www.fda.gov/vaccines-blood-biologics/cellular-gene-therapy-products/what-gene-therapy (2018).

306. Jimenez-Sanchez, G., Childs, B. & Valle, D. Human disease genes. *Nature* **409**, 853–855 (2001).

307. Ylä-Herttuala, S. & Baker, A. H. Cardiovascular Gene Therapy: Past, Present, and Future. *Mol. Ther.* **25**, 1095–1106 (2017).

308. Piguet, F., Alves, S. & Cartier, N. Clinical Gene Therapy for Neurodegenerative Diseases: Past, Present, and Future. *Hum. Gene Ther.* **28**, 988–1003 (2017).

309. Adair, J. E. *et al.* Extended survival of glioblastoma patients after chemoprotective HSC gene therapy. *Sci. Transl. Med.* **4**, (2012).

310. Nóbrega, C., Mendonça, L. & Matos, C. A. *A Handbook of Gene and Cell Therapy*. *Springer* vol. 3 (Springer International Publishing, 2020).

311. Kay, M. A. State-of-the-art gene-based therapies : the road ahead. *Nat. Publ. Gr.* **12**, 316–328 (2011).

312. Sikkel, M. B., Hayward, C., Macleod, K. T., Harding, S. E. & Lyon, A. R. SERCA2a gene therapy in heart failure : an anti-arrhythmic positive inotrope. (2014).

313. Kohn, D. B. & Kuo, C. Y. Mechanisms of allergic diseases New frontiers in the therapy of primary immunodeficiency : From gene addition to gene editing. *J. Allergy Clin. Immunol.* **139**, 726–732.

314. Donnelley, M., Parsons, D. W. & Duncan, G. Gene Therapy for Cystic Fibrosis Lung Disease : Overcoming the Barriers to Translation to the Clinic. **9**, 1–8 (2018).

315. Li, Y., Glass, Z., Huang, M., Chen, Z. Y. & Xu, Q. Ex vivo cell-based CRISPR/Cas9 genome editing for therapeutic applications. *Biomaterials* **234**, (2020).

316. Lu, Y. *et al.* Safety and feasibility of CRISPR-edited T cells in patients with refractory non-small-cell lung cancer. *Nat. Med.* **26**, 732–740 (2020).

317. Boulaiz, H. *et al.* A novel double-enhanced suicide gene therapy in a colon cancer cell line mediated by gef and apoptin. *BioDrugs* **28**, 63–74 (2014).

318. Wang, D. & Gao, G. State-of-the-art human gene therapy: Part II. gene therapy strategies and clinical applications. *Discov. Med.* **18**, 151–161 (2014).

319. Smith, A. J., Bainbridge, J. W. & Ali, R. R. Prospects for retinal gene replacement therapy. (2009).

320. Fire, A. *et al.* Potent and specific genetic interference by double-stranded RNA in caenorhabditis elegans. *Nature* **391**, 806–811 (1998).

321. Napoli, C., Lemieux, C. & Jorgensen, R. Introduction of a chimeric chalcone synthase gene into petunia results in reversible co-suppression of homologous genes in trans. *Plant Cell* **2**, 279–289 (1990).

322. Zheng, M. *et al.* ROS-Responsive Polymeric siRNA Nanomedicine Stabilized by Triple Interactions for the Robust Glioblastoma Combinational RNAi Therapy. *Adv. Mater.* **31**, 1–9 (2019).

323. Kim, H. J., Kim, A., Miyata, K. & Kataoka, K. Recent progress in development of siRNA delivery vehicles for cancer therapy. *Adv. Drug Deliv. Rev.* **104**, 61–77 (2016).

324. Oh, Y. K. & Park, T. G. siRNA delivery systems for cancer treatment. *Adv. Drug Deliv. Rev.* **61**, 850–862 (2009).

325. Lei, Y. *et al.* Gold nanoclusters-assisted delivery of NGF siRNA for effective treatment of pancreatic cancer. *Nat. Commun.* **8**, 1–15 (2017).

326. Morrissey, D. V. *et al.* Potent and persistent in vivo anti-HBV activity of chemically modified siRNAs. *Nat. Biotechnol.* **23**, 1002–1007 (2005).

327. Gu, J., Al-Bayati, K. & Ho, E. A. Development of antibody-modified chitosan nanoparticles for the targeted delivery of siRNA across the blood-brain barrier as a strategy for inhibiting HIV replication in astrocytes. *Drug Deliv. Transl. Res.* **7**, 497–506 (2017).

328. Zheng, M., Tao, W., Zou, Y., Farokhzad, O. C. & Shi, B. Nanotechnology-Based Strategies for siRNA Brain Delivery for Disease Therapy. *Trends Biotechnol.* **36**, 562–575 (2018).

329. Davidson, B. L. & McCray, P. B. Current prospects for RNA interference-based therapies. *Nat. Rev. Genet.* **12**, 329–340 (2011).

330. Wittrup, A. & Lieberman, J. Knocking down disease: A progress report on siRNA therapeutics. *Nat. Rev. Genet.* **16**, 543–552 (2015).

331. Watts, J. K., Deleavey, G. F. & Damha, M. J. Chemically modified siRNA: tools and applications. *Drug Discov. Today* **13**, 842–855 (2008).

332. Cerritelli, S. M. & Crouch, R. J. Ribonuclease H: The enzymes in eukaryotes. *FEBS J.* **276**, 1494–1505 (2009).

333. Dominska, M. & Dykxhoorn, D. M. Breaking down the barriers: siRNA delivery and endosome escape. *J. Cell Sci.* **123**, 1183–1189 (2010).

334. Dong, Y., Siegwart, D. J. & Anderson, D. G. Strategies, design, and chemistry in siRNA delivery systems. *Adv. Drug Deliv. Rev.* **144**, 133–147 (2019).

335. Dong, Y. *et al.* Poly(glycoamidoamine) Brushes Formulated Nanomaterials for Systemic siRNA and mRNA Delivery in Vivo. *Nano Lett.* **16**, 842–848 (2016).

336. Jayaraman, M. *et al.* Maximizing the potency of siRNA lipid nanoparticles for hepatic gene silencing in vivo. *Angew. Chemie - Int. Ed.* **51**, 8529–8533 (2012).

337. Zatsepin, T. S. & Koteliansky, V. Lipid nanoparticles for targeted siRNA delivery – going from bench to bedside. *Int J Nanomedicine.* **11**, 3077–3086 (2016).

338. Takemoto, H. & Nishiyama, N. Functional polymer-based siRNA delivery carrier that recognizes site-specific biosignals. *J. Control. Release* **267**, 90–99 (2017).

339. Andreozzi, P. *et al.* Exploring the pH Sensitivity of Poly(allylamine) Phosphate Supramolecular Nanocarriers for Intracellular siRNA Delivery. *ACS Appl. Mater. Interfaces* **9**, 38242–38254 (2017).

340. Viricel, W. *et al.* Cationic switchable lipids: PH-triggered molecular switch for siRNA delivery. *Nanoscale* **9**, 31–36 (2017).

341. Gary, D. J., Puri, N. & Won, Y. Y. Polymer-based siRNA delivery: Perspectives on the fundamental and phenomenological distinctions from polymer-based DNA delivery. *J. Control. Release* **121**, 64–73 (2007).

342. Macháň, R. & Wohland, T. Recent applications of fluorescence correlation spectroscopy in live systems. *FEBS Lett.* **588**, 3571–3584 (2014).

343. Wöll, D. Fluorescence correlation spectroscopy in polymer science. *RSC Adv.* **4**, 2447–2465 (2014).

344. Bacia, K. & Schwille, P. Practical guidelines for dual-color fluorescence cross-correlation spectroscopy. *Nat. Protoc.* **2**, 2842–2856 (2007).

345. Schwille, P., Meyer-Almes, F. J. & Rigler, R. Dual-color fluorescence cross-correlation spectroscopy for multicomponent diffusional analysis in solution. *Biophys. J.* **72**, 1878–1886 (1997).

346. Baudendistel, M., Müller, G., Waldeck, W., Angel, P. & Langowski, J. Two-hybrid fluorescence cross-correlation spectroscopy detects protein-protein interactions in vivo. *ChemPhysChem* **6**, 984–990 (2005).

347. Larson, D. R., Gosse, J. A., Holowka, D. A., Baird, B. A. & Webb, W. W. Temporally resolved interactions between antigen-stimulated IgE receptors and Lyn kinase on living cells. *J. Cell Biol.* **171**, 527–536 (2005).

348. Kohl, T., Haustein, E. & Schwille, P. Determining protease activity in vivo by fluorescence cross-correlation analysis. *Biophys. J.* **89**, 2770–2782 (2005).

349. Tiwari, M., Oasa, S., Yamamoto, J., Mikuni, S. & Kinjo, M. A Quantitative Study of Internal and External Interactions of Homodimeric Glucocorticoid Receptor Using Fluorescence Cross-Correlation Spectroscopy in a Live Cell. *Sci. Rep.* **7**, 1–16 (2017).

350. Bacia, K., Majoul, I. V. & Schwille, P. Probing the endocytic pathway in live cells using dual-color fluorescence cross-correlation analysis. *Biophys. J.* **83**, 1184–1193 (2002).

351. Nuhn, L. *et al.* Cationic nanohydrogel particles as potential siRNA carriers for cellular delivery. *ACS Nano* **6**, 2198–2214 (2012).

352. Clamme, J. P., Azoulay, J. & Mély, Y. Monitoring of the formation and dissociation of polyethylenimine/DNA complexes by two photon fluorescence correlation spectroscopy. *Biophys. J.* **84**, 1960–1968 (2003).

353. Ohrt, T. *et al.* Fluorescence correlation spectroscopy and fluorescence cross-correlation spectroscopy reveal the cytoplasmic origination of loaded nuclear RISC in vivo in human cells. *Nucleic Acids Res.* **36**, 6439–6449 (2008).

354. Otsu, N. A Threshold Selection Method from Gray-Level Histograms. *IEEE Trans. Syst. Man. Cybern.* **9**, 62–66 (1979).

355. Schwille, P. Fluorescence Correlation Spectroscopy and Its Potential for Intracellular Applications. *Cell Biochem. Biophys.* **34**, 383–408 (2001).

356. Buyens, K. *et al.* Monitoring the disassembly of siRNA polyplexes in serum is crucial for predicting their biological efficacy. *J. Control. Release* **141**, 38–41 (2010).

357. Najafi, H., Abolmaali, S. S., Owrangi, B., Ghasemi, Y. & Tamaddon, A. M. Serum resistant and enhanced transfection of plasmid DNA by PEG-stabilized polyplex nanoparticles of L-histidine substituted polyethyleneimine. *Macromol. Res.* **23**,

618–627 (2015).

358. Madeira, C., Loura, L. M. S., Prieto, M., Fedorov, A. & Aires-Barros, M. R. Effect of ionic strength and presence of serum on lipoplexes structure monitorized by FRET. *BMC Biotechnol.* **8**, 20 (2008).

359. Suh, J.; Paik, H-J.; Hwang, B. K. Ionization of PEI and PAA at Various pH's. *Bioorg. Chem.* **22**, 318–327 (1994).

360. Wang, J., Lu, Z., Wientjes, M. G. & Au, J. L.-S. Delivery of siRNA Therapeutics: Barriers and Carriers. *AAPS J.* **12**, 492–503 (2010).

361. Clamme, J. P., Krishnamoorthy, G. & Mély, Y. Intracellular dynamics of the gene delivery vehicle polyethylenimine during transfection: Investigation by two-photon fluorescence correlation spectroscopy. *Biochim. Biophys. Acta - Biomembr.* **1617**, 52–61 (2003).

362. Brock, R., Hink, M. A. & Jovin, T. M. Fluorescence Correlation Microscopy of Cells in the Presence of Autofluorescence. *Biophys. J.* **75**, 2547–2557 (1998).

363. Dunn, K. W., Kamocka, M. M. & McDonald, J. H. A practical guide to evaluating colocalization in biological microscopy. *Am. J. Physiol. - Cell Physiol.* **300**, 723–742 (2011).

364. Manders, E. M. M., Stap, J., Brakenhoff, G. J., Van Driel, R. & Aten, J. A. Dynamics of three-dimensional replication patterns during the S-phase, analysed by double labelling of DNA and confocal microscopy. *J. Cell Sci.* **103**, 857–862 (1992).

365. MANDERS, E. M. M., VERBEEK, F. J. & ATEN, J. A. Measurement of co-localization of objects in dual-colour confocal images. *J. Microsc.* **169**, 375–382 (1993).

366. Bolte, S. & Cordelieres, F. P. A guided tour into subcellular colocalisation analysis in light microscopy. *J. Microsc.* **224**, 13–232 (2006).

367. Szydlowski, J. & Van Hook, W. A. Concentration and temperature dependence of dynamic light scattering for some polystyrene solutions in toluene, cyclohexane, methylcyclohexane and deuteromethylcyclohexane. *Macromolecules* **31**, 3266–3274 (1998).

368. Stetefeld, J., McKenna, S. A. & Patel, T. R. Dynamic light scattering: a practical guide and applications in biomedical sciences. *Biophys. Rev.* **8**, 409–427 (2016).

369. Bhattacharjee, S. DLS and zeta potential - What they are and what they are not? *J. Control. Release* **235**, 337–351 (2016).

370. Teng, X., Li, F. & Lu, C. Visualization of materials using the confocal laser. *Chem. Soc. Rev.* (2020)

371. Elson, E. L. & Magde, D. Fluorescence correlation spectroscopy. I. Conceptual basis and theory. *Biopolymers* **13**, 1–27 (1974).

372. Magde, D., Elson, E. L. & Webb, W. W. Fluorescence Correlation Spectroscopy. II. An Experimental Realization. *Biopolymers* **13**, 29–61 (1974).

373. Meseth, U., Wohland, T., Rigler, R. & Vogel, H. Resolution of fluorescence correlation measurements. *Biophys. J.* **76**, 1619–1631 (1999).

374. Weidemann, T. & Schwille, P. Fluorescence Cross-Correlation Spectroscopy. in

Encyclopedia of Biophysics (ed. Roberts, G. C. K.) 795–799 (Springer Berlin Heidelberg, 2013).

375. Mérola, F. *et al.* Quantitative live-cell imaging and 3D modeling reveal critical functional features in the cytosolic complex of phagocyte NADPH oxidase. *J. Biol. Chem.* (2019).

376. Bacia, K., Kim, S. A. & Schwille, P. Fluorescence cross-correlation spectroscopy in living cells. *Nat. Methods* **3**, 83–89 (2006).

377. Introduction to Fluorescence. in *Principles of Fluorescence Spectroscopy* (ed. Lakowicz, J. R.) 1–26 (Springer US, 2006).

378. Van Munster, E. B. & Gadella, T. W. J. Fluorescence Lifetime Imaging Microscopy (FLIM). *Adv. Biochem. Eng. Biotechnol.* **95**, 143–175 (2005).

379. Duncan, R. R., Bergmann, A., Cousin, M. A., Apps, D. K. & Shipston, M. J. Multi-dimensional time-correlated single photon counting (TCSPC) fluorescence lifetime imaging microscopy (FLIM) to detect FRET in cells. *J. Microsc.* **215**, 1–12 (2004).

380. Watson, J. V. *Introduction to flow cytometry*. (Cambridge University Press, 2004).

381. Adan, A., Alizada, G., Kiraz, Y., Baran, Y. & Nalbant, A. Flow cytometry: basic principles and applications. *Crit. Rev. Biotechnol.* **37**, 163–176 (2017).

382. McKinnon, K. M. Flow Cytometry: An Overview. *Curr. Protoc. Immunol.* **120**, 56–61 (2018).

383. Dietzek, B., Cialla, D., Schmitt, M. & Popp, and J. *Confocal Raman Microscopy*. *Confocal Raman Microscopy* (Springer International Publishing, 2018).

384. Romero, G., Rojas, E., Estrela-Lopis, I., Donath, E. & Moya, S. E. Spontaneous confocal Raman microscopy-a tool to study the uptake of nanoparticles and carbon nanotubes into cells. *Nanoscale Res. Lett.* **6**, 1–4 (2011).

385. Coelho, J. M. *et al.* Oily core/amphiphilic polymer shell nanocapsules change the intracellular fate of doxorubicin in breast cancer cells. *J. Mater. Chem. B* **7**, 6390–6398 (2019).

386. *Experimental Approaches of NMR Spectroscopy*. *Experimental Approaches of NMR Spectroscopy: Methodology and Application to Life Science and Materials Science* (Springer Singapore, 2018).

387. Marshall, C. B. & Gebregiworgis, T. Real-Time NMR. in *Encyclopedia of Byophysics* (eds. Roberts, G. C. K. & Watts, A.) (European Biophysical Societies Association, 2019).

388. Martinez-Moro, M., Jenczyk, J., Giussi, J. M., Jurga, S. & Moya, S. E. Kinetics of the thermal response of poly (N-isopropylacrylamide co methacrylic acid) hydrogel microparticles under different environmental stimuli : A time-lapse NMR study. *J. Colloid Interface Sci.* **580**, 439–448 (2020).

Curriculum Vitae

Publications

Kang N., Wang Q., Djeda R., Wang W., Fu F., **Martínez-Moro M.**, Ramírez, M., Moya S.E., Coy E., Salmon L., Pozzo J.L. and Astruc D. (2020) Visible-light acceleration of H_2 evolution from aqueous solutions of inorganic hydrides catalyzed by gold-transition-metal nanoalloys. ACS Applied Materials & Interfaces**.** Just Accepted

Andreozzi, P., Tamberi, L., Tasca, E., Giacomazzo G.E., **Martínez-Moro, M.**, Severi, Mirko, Marradi, M., Cicchi, S., Moya, S., Biagiotti, G., Richichi, B. The B & B approach: Ball-milling conjugation of dextran with phenylboronic acid (PBA)-functionalized BODIPY. *Beilstein J. Org. Chem.* 16, 2272–2281 (2020)

Wang, W., Chen, S., Guisasola Cal, E., **Martinez-Moro, M.**, Moya, S. E., Coy, E., Wang, C., Hamon, J., Astruc, D. (2020). ZIF-8-Based vs. ZIF-8-Derived Au and Pd Nanoparticles as Efficient Catalysts for the Ullmann Homocoupling Reaction. Inorganic Chemistry Frontiers, 53, 83–125.

Martinez-Moro, M., Jenczyk, J., Giussi, J. M., Jurga, S. & Moya, S. E. (2020) Kinetics of the thermal response of poly (N-isopropylacrylamide co methacrylic acid) hydrogel microparticles under different environmental stimuli : A time-lapse NMR study. J. Colloid Interface Sci. 580, 439–448.

Giussi, J. M., **Martinez-Moro, M.**, Iborra, A., Cortez, M. L., Di Silvio, D., Llarena, I., Longo, G. S., Azzaroni, O., Moya, S. E. (2020). A study of the complex interaction between poly allylamine hydrochloride and negatively charged poly(N-isopropylacrylamide-co-methacrylic acid) microgels. Soft Matter, 799–804.

Martinez-Moro, M., Di Silvio, D., & Moya, S. E. (2019). Fluorescence correlation spectroscopy as a tool for the study of the intracellular dynamics and biological fate of protein corona. Biophysical Chemistry, 253 (July), 106218.

Di Silvio, D., **Martínez-Moro, M.**, Salvador, C., de los Angeles Ramirez, M., Caceres-Velez, P. R., Ortore, M. G., Dupin, D, Andreozzi, P, Moya, S. E. (2019). Self-assembly of poly(allylamine)/siRNA nanoparticles, their intracellular fate and siRNA delivery. Journal of Colloid and Interface Science, 557, 757–766.

Wang, Q., Fu, F., Yang, S., **Martinez-Moro, M.**, Ramirez, M. de los A., Moya, S., Astruc, D. (2019). Dramatic Synergy in CoPt Nanocatalysts Stabilized by "Click" Dendrimers for Evolution of Hydrogen from Hydrolysis of Ammonia Borane. ACS Catalysis, 1110–1119.

Muzzio, N. E., Pasquale, M. A., Diamanti, E., Gregurec, D., **Martínez-Moro, M.**, Azzaroni, O., & Moya, S. E. (2017). Enhanced antiadhesive properties of chitosan/hyaluronic acid polyelectrolyte multilayers driven by thermal annealing: Low adherence for

mammalian cells and selective decrease in adhesion for Gram-positive bacteria. Materials Science and Engineering C, 80, 677–687.

Conferences

2019:

A Flow Cytometry study of the degradation of polyelectrolyte multilayers for the delivery of large therapeutics. **Poster Presentation**. Marta Martínez-Moro, Patrizia Andreozzi, Sergio Moya. Conference: XXXVII Reunión Bienal de la Real Sociedad Española de Química.

2018:

Novel approach to study the intracellular fate of siRNA/polyamine complexes by Fluorescence Cross-Correlation Spectroscopy (FCCS). **Oral presentation**. Marta Martínez-Moro, Desiré Di Silvio, Patrizia Andreozzi and Sergio Moya. Conference: European Colloid and Interface Society (ECIS) Annual Meeting, Ljubljana (Slovenia).

Tracing the intracellular Fate od siRNA/Polyamine Self Assembled Nanoparticles and siRNA Delivery: A Fluorescence Cross-Corerlation Spectroscopy Study. **Poster presentation**. Desiré Di Silvio, Marta Martínez-Moro, Paolin R. Cáceres, Joaquín Martinez, Patrizia Andreozzi and Sergio E. Moya. Conference: Workshop on Self-assembly and hierarchical Materials in Biomedicine: Drug Delivery, Tissue Engineering, Sensing and Safety Issues, Donostia-San Sebastián (Spain). Organizer: CIC biomaGUNE

Techniques & Trainings

2016:

- Flow Cytometer BD FACS Canto II training (4h) – CIC biomaGUNE, San Sebastián, Spain.
- Transmission Electron Microscopy (16h) – CIC biomaGUNE, San Sebastián, Spain.
- Nuevos Retos en Síntesis Química y Materiales Seminar (6h) - Facultad de Ciencia y Tecnología de la UPV/EHU, Leioa, Spain.

2017:

- Confocal Raman Microscope Alpha300 R (WITec) (4h) – Institut für Medizinische Physik und Biophysik, Leipzig, Germany

2018:

- Confocal microscope Zeiss LSM880 training (3h) - CIC biomaGUNE, San Sebastián, Spain.
- XPS SPECS SAGE HR 100 training (4h) - CIC biomaGUNE, San Sebastián, Spain.

2019:

- Fluorescence Lifetime Imaging training (2h) - CIC biomaGUNE, San Sebastián, Spain.
- Multicolor Panel Building by Flow Cytometry, practical workshop (3,5h) – Navarrabiomed, Navarra, Spain

Participation in R&D pojects

2019-2020 - OXYGENATED: Hemoglobin based Protein Nanocarriers for Tumour Oxygenation and a more effective Photodynamic Therapy. H2020 MSCA-RISE 2019 Project, Grant Agreement 823879. Coordinator: Sergio Moya

2018-2019 - HYMADE: Hybrid Drug Delivery Systems upon Mesoporous Materials, Self-Assembled Therapeutics and Virosomes. RISE HORIZON 2020. Marie Scklodowska-Curie grant agreement 645686. Coordinator: Sergio Moya.

2016-2017 - VIROMA: Design of a versatile and fast colloidal sensor based on virus modified particles. Marie Curie Industry-Academia Partnerships and Pathways (IAPP). Seventh Framework Programme. FP7-PEOPLE-2013-IAPP. Grant agreement 612453. Coordinator: Sergio Moya

2016-2019 - FATENANO: Translocation, biological fate, stability and effective dose of engineered nanomaterials for nanosafety. FP7 3rd ERA-NET SIINN. Coordinator: Sergio Moya